

**THE UNIVERSITY OF CALGARY**

**AG Pegasi: A Multi-shell Radio Source**

**BY**

**Harold T. Kenny**

**A THESIS**

**SUBMITTED TO THE FACULTY OF GRADUATE STUDIES  
IN PARTIAL FULFILLMENT OF THE REQUIREMENTS FOR THE  
DEGREE OF MASTER OF SCIENCE**

**DEPARTMENT OF PHYSICS AND ASTRONOMY**

**CALGARY, ALBERTA**

**October, 1989**

**© Harold T. Kenny 1989**



National Library  
of Canada

Bibliothèque nationale  
du Canada

Canadian Theses Service    Service des thèses canadiennes

Ottawa, Canada  
K1A 0N4

The author has granted an irrevocable non-exclusive licence allowing the National Library of Canada to reproduce, loan, distribute or sell copies of his/her thesis by any means and in any form or format, making this thesis available to interested persons.

The author retains ownership of the copyright in his/her thesis. Neither the thesis nor substantial extracts from it may be printed or otherwise reproduced without his/her permission.

L'auteur a accordé une licence irrévocable et non exclusive permettant à la Bibliothèque nationale du Canada de reproduire, prêter, distribuer ou vendre des copies de sa thèse de quelque manière et sous quelque forme que ce soit pour mettre des exemplaires de cette thèse à la disposition des personnes intéressées.

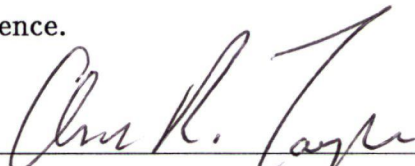
L'auteur conserve la propriété du droit d'auteur qui protège sa thèse. Ni la thèse ni des extraits substantiels de celle-ci ne doivent être imprimés ou autrement reproduits sans son autorisation.

ISBN 0-315-54255-1

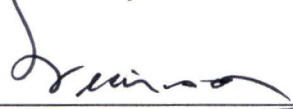
Canada

**THE UNIVERSITY OF CALGARY**  
**FACULTY OF GRADUATE STUDIES**

The undersigned certify that they have read, and recommend to the Faculty of Graduate Studies for acceptance, a thesis entitled, "AG Pegasi: A Multi-shell Radio Source" submitted by Captain Harold T. Kenny in partial fulfillment of the requirements for the degree of Master of Science.

  
\_\_\_\_\_  
Chairman, Dr. A. R. Taylor  
Department of Physics and  
Astronomy

  
\_\_\_\_\_  
Dr. R. B. Hicks  
Department of Physics and  
Astronomy

  
\_\_\_\_\_  
Dr. S. R. Sreenivasan  
Department of Physics and  
Astronomy

  
\_\_\_\_\_  
Dr. M. R. Williams  
Department of Computer  
Science

Date 6 Oct 89

## Abstract

AG Pegasi is one of about 30 symbiotic stars whose radio emission has been observed. It is also the only known symbiotic nova system to have taken longer than 100 years to return to quiescence after a major outburst (*c.*1850). The stellar components of the system include an M3III giant and a WN6 compact object (Boyarchuk 1967a). In this study, the radio emission from AG Pegasi is observed at 4 frequencies (1.5, 5, 15, 22 GHz) and in all configurations of the VLA. The observations are made at nine epochs between November 1984 and July 1987.

The observations reveal that circumstellar gas exists in four discrete components: an unresolved central source of diameter  $< 0.1''$ ; an inner nebula with diameter of  $2''$  and mass of  $3 \times 10^{-5} M_{\odot}$ ; an intermediate nebula with diameter of  $\sim 10''$  and mass of  $10^{-4} - 10^{-3} M_{\odot}$ ; and an outer bipolar nebula with an extent of  $\sim 1'$  and a mass of  $10^{-5} - 10^{-4} M_{\odot}$ .

Analysis of the observations proceeds by means of visibility modelling. "Visibilities" are the complex Fourier components of the sky's intensity distribution. They are the quantities measured by a radio interferometer and they must be processed in order to produce images of the sky. Errors associated with standard imaging packages, especially deconvolution routines, are avoided if visibilities rather than intensities are modelled. If various components of emission exist on different scales, visibility modelling facilitates their separation for independent analysis.

The existence of the outer and intermediate nebulae is significant in understanding the morphology of the system. The intermediate nebula appears to represent the pre-eruption mass loss from the giant component. The outer nebulosity is

thought to be the remnant of the 1850 outburst.

Comparison of very high resolution observations, 2.7 years apart, show that the inner nebula is expanding at several tens of kilometers per second. The nebula may arise from an interaction between pre-eruption mass loss and a fast diffuse wind which is at present emanating from the WN star. This nebula is detached from the central unresolved object and appears to be brightening with time.

It is argued that the central object is associated with mass loss currently taking place from the stellar components of the system. This conclusion is upheld by the fact that detected variations in the flux density and spectral index of the object appear to be correlated with orbital phase.

While AG Pegasi is one of the few symbiotic stars for which radio emission has been detected, the survey work of Seaquist and Taylor (1989) has shown that all symbiotic stars may be radio emitters. The general features of AG Pegasi may then have widespread applicability to the symbiotic phenomenon.

## Acknowledgements

I recognize that my own hand has brought various limitations to the present work. In setting it forth, however, I should like to acknowledge the excellence of a number of faculty members with whom I have had the pleasure to be associated: Dr. A. R. Taylor (my supervisor), Dr. S. Kwok, and Dr. S. R . Sreenivasan.

## Dedication

What spectacle confronted them when they, first the host then the guest, emerged silently, doubly dark, from obscurity by a passage from the rere of the house into the penumbra of the garden?

The heaventree of stars hung with humid nightblue fruit.

( James Joyce, *Ulysses* )

# Contents

Abstract	iii
Acknowledgements	v
Dedication	vi
<b>1 ASTROPHYSICAL BACKGROUND</b>	<b>1</b>
1.1 Symbiotic Stars	1
1.1.1 What is a Symbiotic Star?	1
1.1.2 Characteristics	4
1.1.3 Formation and Evolution	15
1.1.4 Models of Radio Emission	18
1.1.5 Directions of Research	30
1.2 AG Pegasi	32
1.2.1 History	32
1.2.2 The Binary System	40
1.2.3 Radio Emission	46
<b>2 TECHNICAL BACKGROUND</b>	<b>51</b>
2.1 Radio Telescopes	51
2.2 Radio Arrays	56
2.3 Aperture Synthesis	60
2.4 The Very Large Array	68
<b>3 OBSERVATIONS AND DATA REDUCTION</b>	<b>72</b>
3.1 Schedule of Observations	72
3.2 Calibration	74
3.3 Image Processing	75
3.4 Results	82
<b>4 ANALYSIS</b>	<b>93</b>
4.1 Modelling the Visibilities	93
4.1.1 Spherically Symmetric Models	94
4.1.2 Bipolar Models	112
4.2 Sequence of Analysis	117
4.3 The Inner Nebula	122
4.3.1 Mass and Optical Depth	123

4.3.2	Shell Detachment . . . . .	126
4.3.3	Expansion . . . . .	128
4.3.4	Nebular Flux and Electron Density . . . . .	136
4.4	The Central Source . . . . .	141
4.5	The Intermediate and Outer Nebulae . . . . .	147
4.6	Data from Epoch 2-86 . . . . .	152
<b>5</b>	<b>INTERPRETATION</b>	<b>154</b>
5.1	A Synthesis of Old and New Ideas . . . . .	154
5.2	Origin of the Outer Nebula . . . . .	157
5.3	Nature of the Inner Nebula . . . . .	161
5.4	Nature of the Intermediate Nebula . . . . .	163
5.5	Nature of the Central Source . . . . .	165
<b>6</b>	<b>CONCLUSIONS</b>	<b>168</b>
6.1	Summary . . . . .	168
6.2	Further Work . . . . .	169
<b>A</b>	<b>Tabulated Outputs from AIPS</b>	<b>172</b>
<b>B</b>	<b>Contaminating Sources</b>	<b>178</b>
<b>C</b>	<b>Tabulated Results: Data Analysis</b>	<b>180</b>
<b>D</b>	<b>Plotted Fits to Visibility Data</b>	<b>188</b>
<b>E</b>	<b>Spectral Index Determination: Inner Nebula</b>	<b>201</b>
<b>F</b>	<b>Flux Density Variations: Central Source</b>	<b>204</b>
<b>G</b>	<b>Spectral Index Determination: Central Source</b>	<b>207</b>
	<b>Bibliography</b>	<b>211</b>

## List of Tables

1.1	Spectral Development of AG Pegasi 1920-1963 . . . . .	36
1.2	Optical Components of AG Pegasi . . . . .	37
1.3	Orbital Elements of AG Pegasi . . . . .	42
1.4	Model Fits for the Hot Component of AG Pegasi . . . . .	45
1.5	Radio Observations of AG Pegasi . . . . .	47
2.1	VLA Configurations . . . . .	70
2.2	VLA Sensitivity Information . . . . .	71
3.1	Schedule of Observations . . . . .	73
4.1	Categorization of Observations . . . . .	120
4.2	Optical Depth of the Inner Nebula . . . . .	127
4.3	Spectral Index of the Inner Nebula . . . . .	127
4.4	Mass of the Inner Nebula . . . . .	128
4.5	Development of the Inner Nebula . . . . .	132
4.6	Spectral Index of the Central Source . . . . .	145
A.1	Naturally Weighted Mapping Parameters . . . . .	174
A.2	Uniformly Weighted Mapping Parameters . . . . .	175
A.3	Standard Task Outputs: Naturally Weighted Maps . . . . .	176
A.4	Standard Task Outputs: Uniformly Weighted Maps . . . . .	177
B.1	Contaminating Sources . . . . .	179

C.1	Determination of $\eta$ . . . . .	181
C.2	Determination of $\theta_c$ . . . . .	182
C.3	Determination of Nebular Flux Density . . . . .	183
C.4	Determination of Electron Density . . . . .	184
C.5	Total Flux Density Determination . . . . .	185
C.6	Central Source Flux Determination . . . . .	186
C.7	Merit Function ( $\chi^2$ ) for Fits . . . . .	187

## List of Figures

1.1	Spectrum of AG Pegasi, 1200-7000 Å . . . . .	3
1.2	Roche Lobes . . . . .	17
1.3	Interacting Winds Model . . . . .	21
1.4	Schematic of the STB Model . . . . .	23
1.5	Ionization Boundaries of The STB Model . . . . .	26
1.6	Variability of Flux and Spectral Index: STB Model . . . . .	27
1.7	Penston-Allen Model . . . . .	29
1.8	Visual Light Curve of AG Pegasi, 1822-1968 . . . . .	33
1.9	Model for the Optical Variations of AG Pegasi . . . . .	35
1.10	Nebular Model of AG Pegasi, Merrill 1959 . . . . .	39
1.11	VLA Image of AG Pegasi at 5 GHz, 1983 . . . . .	49
2.1	Example of a Beam Pattern in Two Dimensions . . . . .	52
2.2	Scanning With a Radio Telescope . . . . .	54
2.3	Beam Size and Resolution . . . . .	55
2.4	Geometry of a Two Element Array . . . . .	58
2.5	Dipole Electric Field Pattern . . . . .	59
2.6	Geometry of an n-Element Array . . . . .	59
2.7	Imaging Coordinates . . . . .	63
2.8	Phase Delay in a Simple Interferometer . . . . .	66
2.9	VLA Configurations and Instantaneous "UV Coverage" . . . . .	69
3.1	Inspection of Visibility Amplitudes . . . . .	76

3.2	Weighting of Visibility Data . . . . .	78
3.3	Closure Phase . . . . .	81
3.4	AG Pegasi: Concatenated 5 GHz Data Sets . . . . .	86
3.5	AG Pegasi: Concatenated 1.5 GHz Data Sets (Uniform) . . . . .	87
3.6	AG Pegasi: Concatenated 1.5 GHz Data Sets (Natural) . . . . .	88
3.7	Morphology of AG Pegasi . . . . .	89
3.8	Images of AG Pegasi (5 GHz): Uniform Weighing . . . . .	91
3.9	Images of AG Pegasi (5 GHz): Natural Weighing . . . . .	92
4.1	Real and Imaginary Visibilities as Output from AIPS . . . . .	96
4.2	Nebular Model: Spherical Symmetry . . . . .	98
4.3	Variation of Intensity Distribution with $\eta$ . . . . .	100
4.4	Model Visibility Curves: Homogeneous Shell . . . . .	101
4.5	Model Visibility Curves: Infinite Wind . . . . .	102
4.6	Model Visibility Curves: Truncated Wind . . . . .	103
4.7	Determination of $\eta$ . . . . .	104
4.8	Variation of Intensity Distribution with $\theta_o$ . . . . .	105
4.9	Effect of the Parameter $\theta_o$ upon the Visibility Curve . . . . .	106
4.10	Variations of Intensity Distribution with $A$ . . . . .	107
4.11	Effect of the Parameter $A$ upon the Visibility Curve . . . . .	108
4.12	Model Structure For Two Embedded Shells . . . . .	110
4.13	Visibility Curve for a Two Shell Model . . . . .	111
4.14	Nebular Model: Bipolar Features . . . . .	114
4.15	Model Visibility Curves: Bipolar Features . . . . .	115

4.16	Imaginary Visibilities: Asymmetric Features . . . . .	116
4.17	Categories of Data Sets . . . . .	119
4.18	Total Flux Density . . . . .	121
4.19	The Inner Nebula (5 GHz): Natural Weighting . . . . .	124
4.20	The Inner Nebula (5 GHz): Uniform Weighting . . . . .	125
4.21	Determination of $\eta$ for the Inner Nebula . . . . .	129
4.22	Demonstration of Expansion: Inner Nebula . . . . .	130
4.23	Expansion of the Inner Nebula: Center of Mass Radius . . .	131
4.24	Expansion of the Inner Nebula: Outer Radius . . . . .	133
4.25	Expansion of the Inner Nebula: Inner Radius . . . . .	134
4.26	Changing Thickness of the Inner Nebula . . . . .	135
4.27	Flux of the Inner Nebula . . . . .	137
4.28	Electron Density of the Inner Nebula . . . . .	138
4.29	A Comparison of Homogeneous and $1/R^2$ Density Laws . . .	140
4.30	Fitting to Homogeneous and $1/R^2$ Density Laws . . . . .	140
4.31	Central Source Flux Density: 5 GHz . . . . .	142
4.32	Flux Density versus Orbital Period: Central Source . . . . .	143
4.33	Spectral Index of the Central Source . . . . .	144
4.34	Spectral Index Variations of the Central Source . . . . .	146
4.35	Concatenated 1.5 GHz Data Sets: Real Visibilities . . . . .	148
4.36	Model Visibilities: Intermediate and Outer Nebulae . . . . .	150
5.1	Possible Evolution of AG Pegasi . . . . .	156
F.1	Central Source Flux: 15 GHz . . . . .	205

<b>F.2 Central Source Flux: 22 GHz</b>	<b>206</b>
--	------------

# Chapter 1

## ASTROPHYSICAL BACKGROUND

### 1.1 Symbiotic Stars

#### 1.1.1 What is a Symbiotic Star?

The class of symbiotic stars is defined by the basic characteristic of an optical spectrum containing both high excitation emission lines and absorption features of a late-type star. To provide a more uniform criterion for the class, Allen (1979) has further stipulated that a symbiotic star must at some time have exhibited emission lines with excitation  $E > 55$  eV (*e.g.* HeII). Such observational criteria as these fall short of defining a physically homogeneous group, and Allen (1988) notes that “more than most taxons, that of symbiotic stars has become the dustbin of stellar eccentrics”. Allen also comments that historically symbiotic stars have been considered the “platypuses of the stellar zoo”.

While one could easily object to Allen’s latter generalizations, there is in fact much to be said for them. Objects are swept into the symbiotic “dustbin” primarily according to their optical spectra: there is little to prevent physically dissimilar objects from finding their way into the class. Symbiotic stars, like platypuses, combine seemingly contradictory characteristics; although apparently single stellar objects, they display simultaneously two temperature regimes differing by a factor of 30 or more.

The spectrum of AG Pegasi, Figure 1.1, exhibits properties commonly consid-

ered representative of symbiotic stars . Features to note are listed as follows:

- Two main components are visible:
  1. a blue continuum which dominates the left of the diagram blueward of 4000 Å; and
  2. a red continuum which dominates the right of the diagram.
- Absorption features characteristic of late type giant stars are superimposed upon the red continuum. These features include among other things: TiO bands (*e.g.*  $\lambda 4955$ ); CaI lines (*e.g.*  $\lambda 4226$ ); NaI lines (*e.g.*  $\lambda 5889$ ); FeI lines (*e.g.*  $\lambda 3820$ );and CaII lines (*e.g.*  $\lambda 3933$ ).
- Strong HI (*e.g.*  $\lambda 6562$ ,  $\lambda 4861$ ) and HeI (*e.g.*  $\lambda 3888$ ) emission features are present.
- High excitation emission lines (*e.g.*  $\lambda 4686$  of HeII,  $\lambda 4363$  of OIII) are present.

These spectral characteristics point to the presence of stars of quite different properties. The red continuum of symbiotic stars and its associated absorption features are generally attributed to a late type giant star. The blue continuum is believed, at least indirectly, to be associated with a hot compact object. The high excitation (nebular) lines are thought to be of gaseous origin since they are observed regularly in planetary nebulae, but not in stellar photospheres; they arise from the recombination of atoms. The picture of symbiotic stars which emerges is of a binary system, composed of a late type giant and a hot compact object, surrounded by a gaseous nebula.

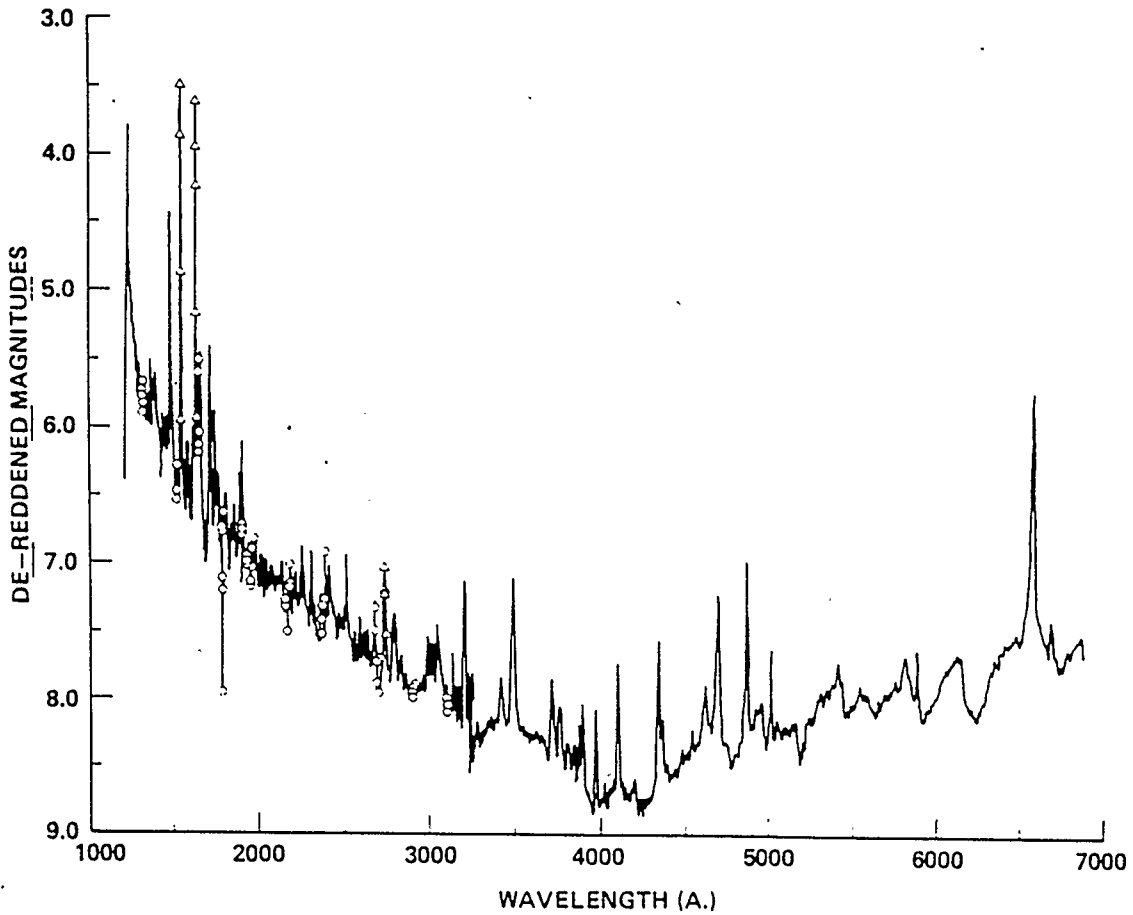


Figure 1.1: Spectrum of AG Pegasi, 1200-7000 Å

This figure is taken from Keyes and Plavec (1980a). Circles mark reseau contamination; triangles are saturated pixels. Ultraviolet observations are taken from the *International Ultraviolet Explorer* (IUE).

### 1.1.2 Characteristics

While the class of symbiotic stars may be somewhat of a “dustbin of eccentrics” there are a number of characteristics commonly held by its members. Further, there are a number of identifiable categories within the class.

The characteristics unifying symbiotic stars as a group may be listed briefly.

- Symbiotic stars are binary systems (*e.g.* Allen 1988; Kenyon 1986). This model was first suggested by Berman (1932) and Hogg (1932). Prior to 1970, however, the binary nature of symbiotic stars was very difficult to verify because of the small radial velocity amplitudes expected in a binary containing a *red giant* (RG) ( $\sim 5 - 10 \text{ km s}^{-1}$ ). Such velocities are not easily measured with photographic plates. Garcia and Kenyon (1988), using photon counting detectors and cross correlation analysis have demonstrated that all bright symbiotics are binary stars. Further, observations from the *International Ultraviolet Explorer* (IUE) have confirmed the existence of “hot components” in many systems (Keyes and Plavec 1980a, b; Slovak 1980; Johnson 1980; Michalitianos, Kafatos and Hobbs 1980; Altamore *et al.* 1981; Stencel *et al.* 1982). The “hot component” (blue continuum and emission lines) can be understood as the Rayleigh Jeans tail of a hot black body, and free-bound emission from an ionized nebula (Kenyon 1988a). In AG Pegasi, it may be inferred from the strength of the blue continuum (Figure 1.1) that a hot, compact stellar, source exists in the system. Establishing the existence of a hot compact object in a symbiotic system is generally sufficient proof that the system is binary; little doubt has ever existed that the red continuum

and absorption features were associated with an evolved giant star (Kenyon 1988a).

- The binary periods of symbiotics range from  $\sim 200$  days to  $> 10$  years (*e.g.* Kenyon 1988a). It is held by some (*e.g.* Orio 1988) that the relatively long period of symbiotic stars is the primary feature which distinguishes them from classical novae.
- Symbiotic stars have late-type giants (K-M) as one of their components (Allen 1980; Allen 1982; Feast *et al.* 1977). These giants are generally regarded as typical members of their spectral/luminosity classes (*e.g.* Kenyon and Truran 1983). As members of the old disk population, they should have masses between 1-3 *solar masses* ( $M_{\odot}$ ). This mass range is generally supported by the few systems for which spectroscopic orbits are available (*e.g.* Garcia and Kenyon 1988).
- The hot components in a majority of symbiotic systems include an object with radius characteristic of a *white dwarf* (WD) or subdwarf and temperature  $T \sim 30,000 - 150,000\text{K}$  (Kenyon 1988a). No model of hot components applicable to all symbiotic stars has yet been offered.
- Optical outbursts are characteristic of symbiotic stars. Eruptions are generally irregular and of amplitude 2-7 *magnitudes* (mag). See Section 1.2.1 for a definition of the magnitude scale. The optical spectrum of an outbursting symbiotic star usually resembles a giant (luminosity class III) of spectral type A to F. Spectral types represent a temperature sequence with order,

from highest to lowest temperature, given by: O; B; A; F; G; K; M; R; N. Outbursts are generally followed by a “quiescent phase”.

- The existence of outbursts has led to the conclusion that symbiotic stars are interacting binary systems (*e.g.* Allen 1988; Kenyon 1986; Nussbaumer and Vogel 1987). In most cases this interaction involves the accretion of matter from the RG component onto the hot companion.
- Three distinct groups of symbiotic stars are differentiated on the basis of their outburst characteristics (*e.g.* Kenyon 1986): recurrent novae; classical symbiotic stars; and symbiotic novae. Specifically, the categorization is made with reference to the duration of observed outbursts and to the spectroscopic changes which occur during outburst. Timescales for eruption are: less than several months for recurrent novae; several years for classical symbiotic stars; and many decades for symbiotic novae. Spectroscopic criteria are complex and involve the evolution of high excitation lines and the quiescent spectral features (*e.g.* absorption lines associated with the *red giant* (RG)) during outburst. Recurrent novae involve relatively large increases in flux ( $\gtrsim 7$  mag) and are associated with the ejection of a shell of matter. Classical symbiotic stars experience irregular optical variability with amplitude of variation of  $\sim 3$  mag. Symbiotic nova events involve flux increases of  $\sim 3$  mag and their light curves and spectral development strongly resemble classical novae; classical novae, however, evolve on the timescale of hundreds of days.
- Symbiotic stars possess a nebular region ionized by the ultra-violet photons of the hot star. This region gives rise to free-bound interactions observable as

emission lines (HI, HeI, HeII, and OIII) and free-free interactions observable, in some cases, as radio continuum emission.

The fundamental division of symbiotic stars into recurrent novae, classical symbiotic stars, and symbiotic novae is observational. It is naturally desirable to establish a theoretical basis for this division. To do this, it is necessary to review the two mechanisms through which eruptions are believed to occur: supercritical accretion and *thermonuclear runaway* (TNR).

Supercritical accretion involves the release of gravitational potential energy as matter falls upon a compact object. By the virial theorem, an ensemble of particles falling inward will release a portion of the gravitational potential as radiation:

$$L_{acc} = \eta \dot{M} \left( \frac{GM_c}{R_c} \right) \quad (1.1)$$

where:  $L_{acc}$  is the luminosity [erg s<sup>-1</sup>] associated with the accretion;  $\eta$  is an efficiency factor;  $\dot{M}$  is the rate of accretion [g s<sup>-1</sup>];  $G$  is the gravitational constant; and  $M_c$  and  $R_c$  are the mass and radius of the compact object respectively. The Eddington limit,  $L_{Edd}$ , is defined as the luminosity beyond which radiation pressure from  $L_{acc}$  will drive matter from the surface of an object. The condition for supercritical accretion is then given by  $L_{acc} \geq L_{Edd}$ .

A thermonuclear runaway occurs as matter collects on the surface of a compact object. Eventually, the temperature at the base of the accreted matter becomes high enough that hydrogen reactions are initiated (proton-proton chain or CNO cycle; Kutter and Sparks 1980). The result is a rapid release of energy which may be adequate to drive matter from the surface. The ejection of matter may

be particularly violent if the accreted matter is degenerate. In this case, ejection will not occur until degeneracy has been lifted by extremely high temperatures; by this time, an enormous amount of energy has accumulated which will be expended in the rapid expulsion of matter. In the limiting case of high *accretion rate* ( $\dot{M}$ ), steady burning may occur in a manner analogous to that which occurs in normal RG stars (*e.g.* Paczynski and Zytzkow 1978). The *steady burning limit* for accretion onto a compact object is given by Iben (1982):

$$\dot{M}_{steady,min} \approx 1.32 \times 10^{-7} (M_c)^{3.57} [M_\odot yr^{-1}] \quad (1.2)$$

where  $M_c$  is the mass of the compact object measured in  $M_\odot$ . For  $\dot{M} < \dot{M}_{steady,min}$  the hydrogen burning is thermally unstable (Fujimoto 1982 a,b; Iben 1982; MacDonald 1983), and mass ejection may occur. The nature of the ejection in this case depends most significantly upon the ratio  $E_{nuc}/E_{bind}$  where  $E_{nuc}$  is the amount of energy produced via nuclear reaction before the envelope expands to giant dimensions, and  $E_{bind}$  is the gravitational binding energy of the accreted envelope. Very violent runaways occur if  $E_{nuc} \gg E_{bind}$ ; matter will be ejected weakly or perhaps not be ejected at all if  $E_{nuc} \leq E_{bind}$ .

The conditions which encourage a strong TNR are those which produce a higher  $E_{nuc}/E_{bind}$  ratio. They are as follows (Kenyon 1986).

- $M_c \geq 1M_\odot$ . A more massive compact object requires less material to initiate burning ( $\rightarrow$  lower  $E_{bind}$ ) and generates relatively greater pressure at the base of the accreted material ( $\rightarrow$  higher  $E_{nuc}$ ).
- $L_c \leq L_\odot$ . A less luminous compact object will produce greater degeneracy at

the base of the accreted material. Once burning is initiated, expansion can not occur until degeneracy is lifted ( $\rightarrow$  higher  $E_{nuc}$ ).

- $\dot{M} < 10^{-9} M_{\odot} yr^{-1}$ . At low accretion rates, the kinetic energy of infalling material can be radiated away effectively and hence accumulated material will have higher degeneracy ( $\rightarrow$  higher  $E_{nuc}$ ).
- $Z_{CNO} > Z_{CNO,solar}$ . Nearly all nuclear energy, in a shell flash, is produced in the CNO cycle. In this process carbon (C), nitrogen (N), and oxygen (O) act as catalysts in the fusion of hydrogen into helium. A higher abundance of carbon, nitrogen and oxygen,  $Z_{CNO}$ , yields a higher  $E_{nuc}$  and hence a stronger shell flash.

Now that eruption mechanisms have been reviewed, the outburst categories of symbiotic stars may be considered. The following discussion is based on Kenyon (1986) and represents one attempt to systematize the phenomenon of symbiotic outbursts.

According to Kenyon, a symbiotic nova eruption takes place as a *thermonuclear runaway* (TNR) on the surface of an accreting *white dwarf* (WD). The WD ejects a shell of material at visual maximum at a high velocity and the shell interacts with material previously ejected (RG wind). The *effective black body temperature* ( $T_{eff}$ ) of the WD eventually increases from 30,000 to 40,000 K and a fast wind is initiated ( $\sim 1000 \text{ km s}^{-1}$ ) similar to that found in *Wolf-Rayet* (WR) stars. This wind, which will have velocity  $\sim 1000 \text{ km s}^{-1}$ , interacts with previously ejected material to produce X-rays (Kwok and Leahy 1984). The photosphere of the hot companion continues to contract until the WR phase and the fast wind are

terminated. At this point the eruption is effectively ended, and the system returns to quiescence.

Recurrent novae are thought to result from accretion onto *main sequence* (MS) stars. The theoretical scenario of Kenyon (1986) would have the following sequence. A blob of matter is ejected by the RG and the process through which the orbits of the ejected material are circularized collisionally around the MS star gives rise to a "primary maximum" in the visible light. Viscous processes form the circularized material into a disk which encounters the MS star to give a "secondary maximum". The disk is slowly emptied of material and a quiescent state is resumed. This scenario fails to consider the ejection of material observed to occur during recurrent nova events. The accretion mechanism is perhaps more appropriate to the optical outbursts of classical symbiotic stars.

Kenyon (1986) claims that outbursts of classical symbiotic stars may be explained by either TNR or supercritical accretion. In the case of the TNR mechanism, the stages of classical symbiotic star outburst might parallel those described above for symbiotic novae but would follow more rapidly. In the case of supercritical accretion events, classical symbiotic star outbursts might resemble those described above for recurrent novae, but a primary maximum would not occur since a steady state accretion disk is presumed to be already in place. The preceding three paragraphs represent one attempt (Kenyon 1986) to systematize symbiotics outbursts; the system does not meet the approval of all astrophysicists.

Attempts have also been made to classify symbiotic stars according to the nature of their "hot components". Kenyon and Webbink (1984) have attempted to account for the spectra of symbiotic stars in terms three classes of "hot compo-

nents”: hot stellar sources; disk accretion onto MS stars; and disk accretion onto WD stars. IUE and optical spectra were fit from 19 stars, and the following distribution was found: 8 hot stellar objects ( $\log T = 4.6 - 5.1$ ); 5 MS accretors ( $\dot{M} = 10^{-6} - 10^{-4} M_{\odot} \text{ yr}^{-1}$ ); 0 WD accretors; 3 unreliable fits (D-type systems); and 3 with appearance of none of the above. The classes of “accretors” above are so labelled to indicate that radiation is assumed to arise from disk accretion onto the specified type of object.

Another classification scheme considers the nature of the circumstellar material and places objects into two categories: stellar or S-type systems ( $\sim 75\%$ ) and dusty or D-type systems ( $\sim 25\%$ ). D-type systems tend to have long periods ( $P > 5 - 10$  yr) and the RG in these systems is a Mira-like variable which loses mass in a powerful stellar wind. Mira variables are long period variables ( $P =$  months to years) with mass  $\lesssim 2M_{\odot}$  and luminosity  $\sim 10^4 L_{\odot}$ . Mass loss in these stars is encouraged by their extended size and high luminosity, and is enhanced by radial pulsations of the star. S-type systems have shorter periods ( $P < 5 - 10$  yr), and contain a non Mira-like RG which loses mass at a considerably lower rate.

The presence of accretion disks in symbiotic stars is discussed by Nussbaumer and Vogel (1987). They find, in accordance with Paczynski and Zytlow (1978), that outburst may be attributed to accretion from RG winds ( $\dot{M}_{acc} \sim 10^{-9} M_{\odot} \text{ yr}^{-1}$ ) without hypothesizing disks. Further, they conclude that except in the case of Roche lobe overflow by the RG, disks are not expected to form in symbiotic systems. Livio *et al.* (1989) argue that outbursts resembling those of slow novae (*e.g.* AG Pegasi) are more likely to occur in systems involving wind accretion.

## Radio Properties

Of primary concern in this thesis are the radio properties of symbiotic stars, and recent work (Seaquist *et al.* 1984; Taylor and Seaquist 1984; Seaquist and Taylor 1989) has succeeded in making some useful generalization about them.

- About 25% of all known symbiotic stars are radio emitters above 0.5 mJy (1 mJy = 1 milliJansky =  $10^{-26}$  erg cm<sup>-2</sup> s<sup>-1</sup> Hz<sup>-1</sup>). This result is consistent with all symbiotic stars being radio emitters.
- Spectral index,  $\alpha$ , ( $S_\nu \propto \nu^\alpha$ , where  $S_\nu$  is flux at frequency  $\nu$ ) is found to lie in the range 0.0 to 1.0 for most symbiotic stars. This index is consistent with partially optically thick bremsstrahlung emission (see below).
- Most symbiotic stars do not vary in the radio by more than about 30% over a period of several years. This suggests that the radio emitting nebulae of most symbiotic stars exist in a quasi-steady state.
- Multifrequency observations suggest that a significant fraction of symbiotic stars become optically thin near a wavelength of 1 cm (30 GHz). Systems in this category are more likely to be D than S-type.
- Radio emission is found to be correlated with the mass outflow of the RG. This conclusion arises from the fact that radio luminosity is correlated both with the IR emission arising from dust, and with the optical spectral type of the RG. The existence of dust is sufficient (but not necessary) evidence for mass outflow since dust around RGs is considered to be ejected material, but not all ejected material is necessarily dusty. It has been shown (Allen

1980; Gehrz and Wolf 1971) that mass loss rate increases with later spectral type. Spectral types define essentially a temperature sequence with “later” spectral types implying cooler, and generally more evolved, stars. Later type stars have extended envelopes from which mass is easily driven by radiation pressure. Since luminosity is correlated both with the IR emission and with the optical spectral type of the RG one might further conclude that, in most cases, RG mass loss dominates mass loss from the hot component.

- D and S-type systems are distinguishable in their radio emission. In D-type systems radio emission is nearly optically thin and originates in the same extended volume as the  $H_\beta$  line emission. In the S-type systems, most line emitting gas is optically thick and may reside in very small dense regions such as accretion disks. D-type systems also tend to be more luminous radio emitters.

It was noted above that a spectral index in the range 0.0 to 1.0 implies partial optically thick bremsstrahlung emission; this may be demonstrated briefly. For an isothermal medium with no background sources, the radiative transfer solution is given by (*e.g.* Rohlfs 1986):

$$I_\nu = B_\nu(1 - e^{-\tau_\nu}) \quad (1.3)$$

where:  $I_\nu$  is the intensity at frequency  $\nu$  of a point on the observed surface of a source;  $\tau_\nu$  is the optical depth at frequency  $\nu$  at the same point (see below); and  $B_\nu$  is Planck’s function. For a source of uniform intensity, the flux is given by  $S_\nu = I_\nu\Omega$  where  $\Omega$  is the solid angle subtended by the source. Using Equation 1.3,

the flux may be expressed as  $S_\nu \propto B_\nu(1 - e^{-\tau_\nu})$ . The condition of optical thickness is defined by  $\tau \gg 1$ , from which it follows that flux from an optically thick source has the same frequency dependence as Planck's function; *i.e.*  $S_\nu \propto B_\nu \propto \nu^2$  ( $\alpha = 2$ ) for the case of optical thickness. Optical thinness is defined by  $\tau_\nu \ll 1$ , from which it follows that  $S_\nu \propto B_\nu \tau_\nu$ . Optical depth,  $\tau$ , is defined:

$$\tau_\nu = \int_{path} \kappa_\nu dl \quad (1.4)$$

where  $\kappa$  [ $\text{cm}^{-1}$ ] is the opacity of the medium and integration is performed along the line of sight. For thermal bremsstrahlung emission  $\kappa \propto \nu^{-2.1}$  (Equation 4.5), and hence  $S_\nu \propto \nu^{-0.1}$  ( $\alpha = -0.1$ ) for the case of optical thinness.

It has been shown that  $\alpha = 2$  implies optical thickness, and that  $\alpha = -0.1$  implies optical thinness. Spectral indices between these limits may correspond to a source which is in transition between the two extremes; or is composed of several regions, some of which are optically thin, and some of which are optically thick. A special case of considerable interest occurs for an outflowing wind whose central region is optically thick. Wright and Barlow (1975) show that an index of  $\alpha = 0.6$  results. The expression which they derive is:

$$S_\nu = 2.3 \times 10^4 \left( \frac{\dot{M}Z}{v\mu} \right)^{\frac{4}{3}} \frac{(\nu g_{ff})^{\frac{2}{3}}}{D^2} \text{ [mJy]} \quad (1.5)$$

where:  $S_\nu$  [mJy] is the flux at frequency  $\nu$  [Hz];  $\dot{M}$  [ $M_\odot \text{ yr}^{-1}$ ] is the mass loss rate;  $Z$  is the average charge of ions in the gas (in units of electron charge);  $v$  is the terminal velocity of the mass outflow;  $\mu$  is the mean atomic weight of atoms in the gas;  $g_{ff}$ , the "gaunt factor", is a dimensionless quantum mechanical correction

factor appropriate for thermal bremsstrahlung or “free-free” emission (see Equation 4.10); and  $D$  [kpc] is distance to the source. The cgs equivalent to 1 *parsec* (pc) is  $3.086 \times 10^{18}$  cm;  $1 \text{ kpc} = 10^3 \text{ pc}$ .

One further remark may be made with respect to the radio properties of symbiotic stars: there is good reason to believe that bipolar effects are widespread (Taylor 1988). The two symbiotics that lie closest to us, R Aquarii and CH Cygni include jet-like radio structures (Hollis *et al.* 1987; Sopka *et al.* 1982; Taylor *et al.* 1986; Taylor *et al.* 1988a). It is tempting to extrapolate this result since other symbiotics and related phenomena exhibit bipolar ejection when observed in radio outburst. These objects include the recurrent nova RS Ophiuchi (Bode 1987, Taylor *et al.* 1989); and the nova QU Vulpeculae (Taylor *et al.* 1988b).

### 1.1.3 Formation and Evolution

Since symbiotic stars are binary systems, the process of binary star formation must be considered; it is not understood in detail. The most popular scenario (Mouschovias 1978; Kenyon 1986) involves the collapse of a rotating interstellar cloud which is threaded by a magnetic field. The loss of angular momentum through magnetic braking allows the cloud to contract, and the instabilities arising in the early phases of the collapse result in the development of dense fragments. These fragments themselves may fission and ultimately form stars. A predictable percentage of these stars would be expected to be gravitationally bound as binaries ( $\sim 50\%$ ). Observations (*e.g.* Abt and Levy 1976, 1978) tend to confirm the distribution with binary period predicted by this model. About 50% of the stars observed in the solar neighborhood are members of binary or multiple star

systems, and, as predicted by the model of Mouschovias a single maximum in the distribution of binaries as a function of binary period appears to exist.

The primary parameters determining whether a binary system will be observed as symbiotic are the masses of the components, and the binary period. It is known that one component of a symbiotic system must be a bright evolved giant and that the approximate time required for a star to evolve to this stage is given by  $t_{MS} \approx 10^{10} M^{-3.3}$  yr (Iben 1967), where  $M$  is the mass of the star in  $M_{\odot}$ . Therefore, systems with  $M_{primary} < 1M_{\odot}$ , even if they were born at the time of galaxy formation ( $\sim 10^{10}$  yr ago), have not had time to become symbiotic. The primary, which is defined as the more massive star in the binary system, must still be on the main sequence.

Further, systems with initial binary periods of  $P \leq 50 - 100$  days cannot form symbiotic stars. Primary components in these systems would expand to fill their Roche lobes very quickly after evolving off of the main sequence. The Roche lobes of a binary system are defined in Figure 1.2. Once a star fills its Roche lobe, mass can flow freely from it, through the inner Lagrangian point onto its companion. Hence, if a star fills its Roche lobe early in the process of expansion as a giant, mass loss will prevent it becoming a bright giant. Therefore the system can not become symbiotic. On the other hand, binary stars with  $P > 10,000$  days are too far separated for interaction to occur. Hence they are also excluded from the symbiotic phenomenon.

One expects that binary systems with  $M_{primary} \sim 1 - 3M_{\odot}$  and period  $P \approx 100 - 10,000$  days will be identified as symbiotic stars when the primary becomes a giant; however, another form of symbiosis is also possible. Binary systems may

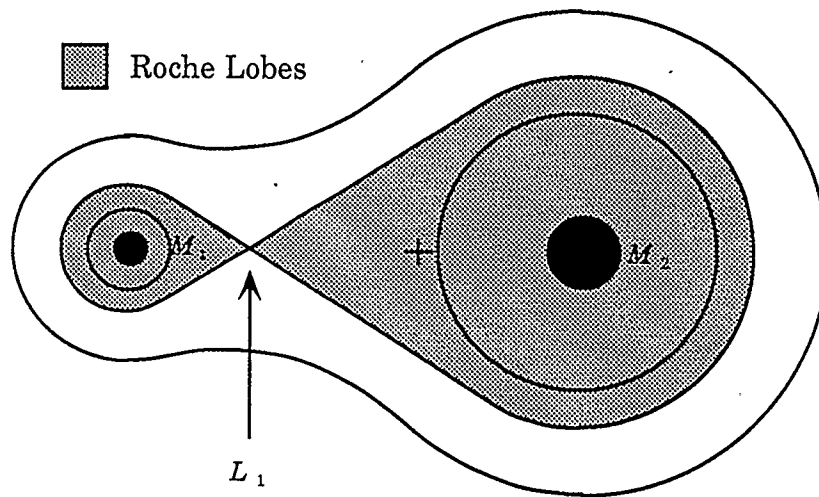


**Figure 1.2: Roche Lobes**

Contours indicate approximate equipotential surfaces in the equatorial plane of the binary system shown. The center of mass of the system is marked by an '+'.  $L_1$  defines the inner Lagrangian point.

also become symbiotic when the secondary becomes a giant; the primary by this time should have become a WD. Some of the systems which experienced the first form of symbiosis will not experience the second since, following the first symbiosis, many will undergo a “common envelope” ejection in which considerable angular momentum may be lost. Reduced angular momentum will result in a shorter binary period; if the period becomes less than  $\sim 100$  days symbiosis is not possible, as earlier noted.

The number of “original” symbiotic systems, however, that are not able to reach the second phase of symbiosis is more than compensated by the number of systems which experience *only* the second phase. Systems with  $P > 10,000$  days are not eligible for the first stage because the necessary mass loss rates from the RG can not be achieved. Material (thought to be supplied by the RG) is required to accrete onto the compact object in order to produce the optical variability typical of symbiotic stars. For a MS accretor, an accretion rate of  $\gtrsim 10^{-5} M_{\odot} \text{ yr}^{-1}$  is required to “power” a symbiotic star (Kenyon 1986), while Zuckermann(1980) estimates RG mass loss at  $10^{-5} - 10^{-7} M_{\odot} \text{ yr}^{-1}$ . Accretion rates considerably less than  $10^{-5} M_{\odot} \text{ yr}^{-1}$  are sufficient for systems containing a compact degenerate star (Kwok 1981; Willson 1981). Hence some systems may experience WD symbiosis which do not experience MS symbiosis.

#### 1.1.4 Models of Radio Emission

Radio continuum emission from symbiotic stars is attributed primarily to thermal bremsstrahlung emission (Seaquist *et al.* 1984; Seaquist and Taylor 1989). In order for this mechanism to operate, a region of ionized matter is necessary. There are

various ways in which appropriate regions might arise, and it is the purpose of this section to discuss them.

### Shell Ejection

Bath and Shaviv (1976) have proposed a model to explain the light curves of classical novae. In this model a steady outflow of matter occurs, driven by radiation pressure. The cause of luminosity  $L \geq L_{edd}$  need not be specified, although both supercritical accretion, or TNR would be possibilities. In either case, the ejection would eventually begin to decrease, leaving essentially an envelope of matter expanding from a hot central source.

Initially, the "envelope ejection" described above would be observed as a rapid rise in visible light. This would occur because the shell would initially be optically thick (optical depth,  $\tau \gg 1$ ), and expansion would result in an increase in the emitting area. Therefore flux would increase ( $S_\nu \propto I_\nu \Omega$  where  $S_\nu$  is the observed flux,  $I_\nu$  is the intensity, and  $\Omega$  is the solid angle subtended by the source). The shell would eventually, however, become optically thin ( $\tau \ll 1$ ), and from this point onward, a gradual decrease in visible light would be observed ( $S_\nu \propto B_\nu \tau_\nu$  in the case of optical thinness). The shell would become increasingly optically thin, and as this happened, the optical observer would see further and further into the nebula, revealing higher temperatures and higher excitation emission lines. The expanding nebula could remain ionized by the hot central source for a considerable time and might be observed in radio emission.

### Interacting Winds Model

Kwok and Purton (1978) have proposed a model for planetary nebulae which may be equally applicable to symbiotic stars (*e.g.* Kwok and Purton 1979): the Interacting Winds Model. This model assumes the existence of a precursor RG which loses mass in a dense, low velocity wind (mass-loss rate,  $\dot{M} \sim 10^{-5} M_{\odot} \text{ yr}^{-1}$ ; velocity,  $V \sim 10 \text{ km s}^{-1}$ ). This wind is eventually terminated and replaced, at a later time, by a diffuse, high velocity wind (mass-loss rate,  $\dot{m} \sim 10^{-8} M_{\odot} \text{ yr}^{-1}$ ; velocity,  $v \sim 2000 \text{ km s}^{-1}$ ). Interaction produces shock fronts, and a thin, dense shell of swept up material (see Figure 1.3). In a symbiotic system, the low velocity wind might be attributed to the RG in quiescence, while the high velocity wind might emerge from the hot, compact object during outburst.

Under the assumption that most of the observed shell is composed of swept up material, and that the interaction between the high velocity wind and the shell is adiabatic, the equations for conservation of mass, momentum and energy are given by (Kwok 1986):

$$\begin{aligned} \frac{dM_s}{dt} &= 4\pi R_s^2 \rho \left( \frac{dR_s}{dt} - V \right) \\ M_s \frac{d^2 R_s}{dt^2} + \frac{dM_s}{dt} \left( \frac{dR_s}{dt} - V \right) &= 4\pi R_s^2 P \\ \frac{d}{dt} (2\pi R_s^2 P) &= \frac{\dot{m} v^2}{2} - 4\pi R_s^2 \frac{dR_s}{dt} P \end{aligned} \quad (1.6)$$

where:  $\dot{M}$ ,  $V$ , and  $\rho$  are the mass-loss rate, velocity, and density of the low velocity wind respectively;  $\dot{m}$  and  $v$  are the mass-loss rate and velocity of the high velocity wind respectively;  $P$  is the pressure in the shocked region of the high velocity wind (see Figure 1.3); and  $M_s$  and  $R_s$  are the mass and radius of the shell. One radius

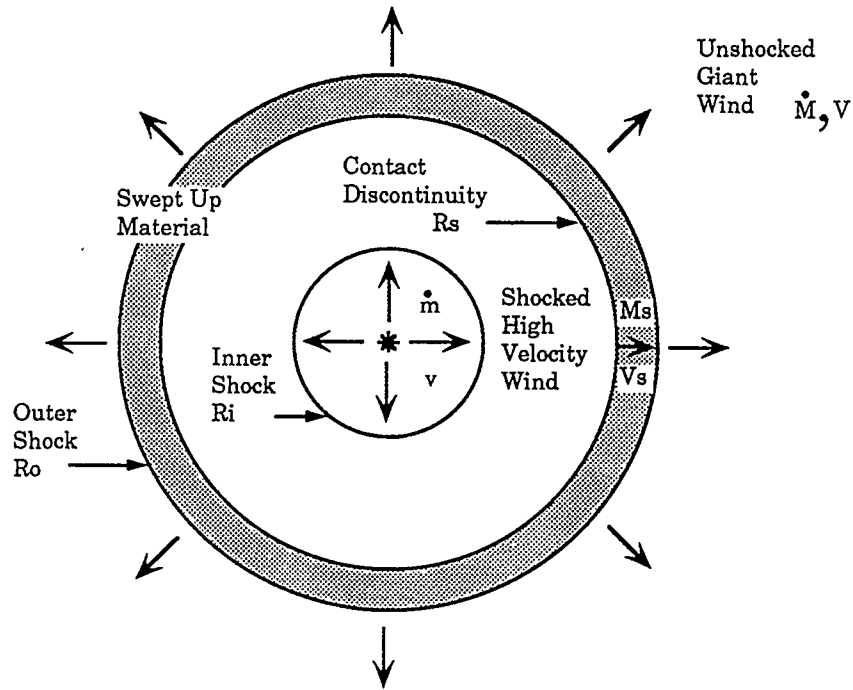


Figure 1.3: Interacting Winds Model

When the high velocity wind encounters the low velocity wind, an inner and outer shock front are set up. The Contact Discontinuity,  $R_s$ , is defined as the boundary between swept up material and the shocked high velocity wind; it is assumed that no material crosses this discontinuity.

is sufficient to describe the shell since it is considered to be thin: that is, its inner and outer radii are approximately equal.

Assuming steady mass loss (i.e.  $\frac{1}{2}\dot{m}v^2 = \text{constant}$ ) the equations of set 1.6 may be solved by similarity analysis to yield (Kwok 1986):

$$\begin{aligned}
 R_s &= V_s t \\
 M_s &= \dot{M} \left( \frac{V_s}{V} - 1 \right) t
 \end{aligned}
 \tag{1.7}$$

$$P = \frac{\frac{1}{2}\dot{m}v^3}{6\pi V_s^3}$$

where:  $V_s$  is the expansion velocity of the shell; and all other symbols are as above.  $V_s$  is in turn given by (Kwok 1986):

$$\left(\frac{\dot{M}}{V}\right)V_s^3 - 2\dot{M}V_s^2 + \dot{M}VV_s = \frac{1}{3}\dot{m}v^2. \quad (1.8)$$

Using this model, one may also predict a temperature in the “bubble” between the inner shock and the contact discontinuity. Using the ideal gas law and assuming uniform density in the bubble, the temperature is given by (Kwok 1986):

$$T = \frac{\mu m_H v^2 \epsilon}{9k} \quad (1.9)$$

where:  $\mu$  is the mean atomic weight;  $k$  is the Boltzmann constant;  $m_H$  is the mass of a hydrogen atom;  $v$  is the velocity of the high velocity wind; and  $\epsilon$  is the fractional filling factor of the bubble volume. For typical values of parameters ( $\mu \sim 0.6$ ,  $v \sim 2000\text{km s}^{-1}$ ,  $\epsilon \sim 1$ ) a temperature of  $\sim 10^7$  K is found. The low density and high temperature of material inside the bubble make it essentially undetectable in continuum emission.

### STB Model

The STB model was developed to account for the quiescent radio properties of symbiotic stars in general, and considers a cool mass-losing star associated with a hot ionizing companion (Seaquist *et al.* 1984, Taylor and Seaquist 1984). The model establishes the location of the ionization front in the cool star’s wind and

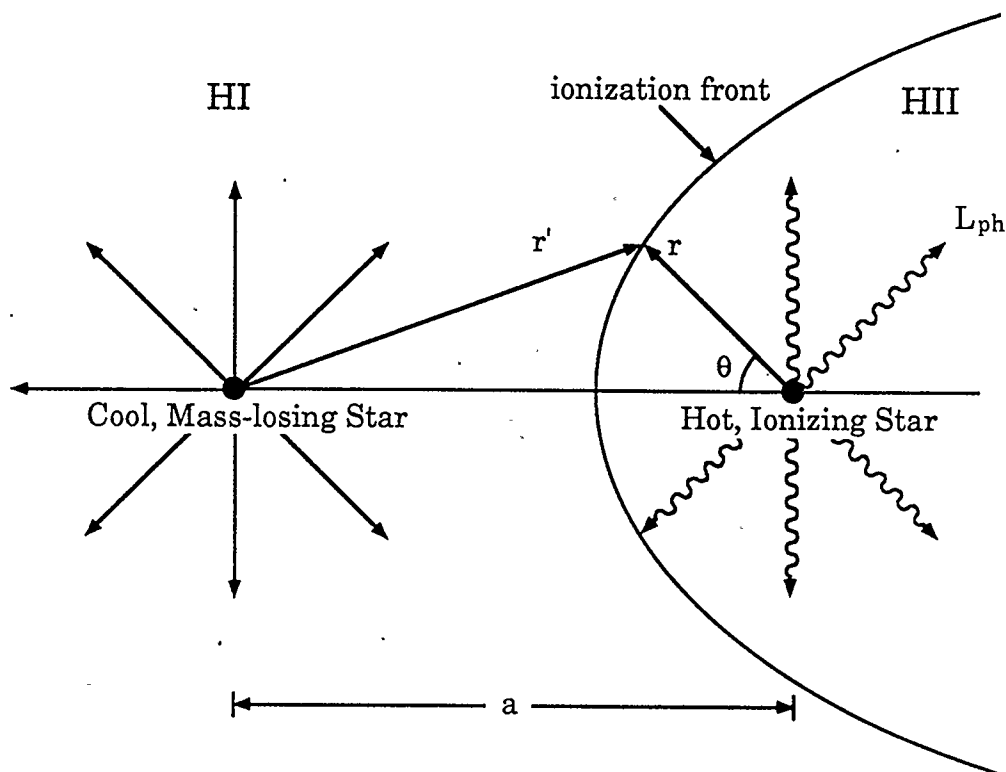


Figure 1.4: Schematic of the STB Model

predicts the geometry of the front, taking into account the binary rotation of the system. Figure 1.4 provides a schematic of the model.

The boundary of the ionization zone is defined by the condition that  $\dot{N}(r, \theta) = 0$  where:  $\dot{N}(r, \theta)$  is the luminosity of ionizing photons per unit solid angle [photons  $\text{sr}^{-1} \text{s}^{-1}$ ] at distance  $r$  from the hot component in direction  $\theta$  as shown in Figure 1.4; and the dot over  $N$  denotes a time derivative (*i.e.*  $\dot{N}$  is a luminosity). For any angle  $\theta$ , the flux of ionizing photons may then be expressed by the relationship generally applicable to Stromgren type HII regions:

$$\dot{N}(r') = \Omega L/4\pi - \alpha^{(2)}\Omega \int_0^r n^2(r')r^2 dr \quad (1.10)$$

where:  $\Omega$  is a unit of solid angle;  $L$  is the luminosity [photon  $s^{-1}$ ] of ionizing photons;  $\alpha^{(2)}$  is the hydrogen recombination coefficient [ $cm^3s^{-1}$ ] for recombination to all but the ground state; and  $n(r')$  is the density [ $cm^{-3}$ ] at distance  $r'$  from the source of mass loss (corresponding to the distance  $r$  and the angle  $\theta$  measured from the hot component). The recombination coefficient,  $\alpha^{(2)}$ , is defined  $\alpha^{(2)} = \sum_{m=2}^{\infty} \alpha_m$ , where  $\alpha_m$  is the recombination coefficient to electronic level  $m$  such that the probability of recombination is given by  $\alpha_m n(r')$ . The ionization boundary is therefore defined by:

$$\frac{L}{4\pi\alpha^{(2)}A^2} = \int_0^r \frac{r^2}{(r')^4} dr. \quad (1.11)$$

In this equation, the density  $n(r')$  has been replaced by the expression  $n(r') = A/r'^2$  appropriate to stellar winds.  $A$  is given by  $A = \dot{M}/4\pi\mu m_H v$  where:  $\dot{M}$  is the mass loss rate;  $\mu$  is the mean atomic weight of the gas;  $m_H$  is the mass of a hydrogen atom; and  $v$  is the velocity of mass loss from the cool star. The expression for  $A$  follows immediately from the assumption that mass is conserved. Qualitatively, mass lost per second at the source of mass loss is equal to mass crossing some non-overlapping boundary drawn around the source per second. For a spherical boundary of radius  $r'$ , the quantitative expression is derived as follows:

$$\begin{aligned} \dot{M} &= (\text{mass density})(\text{Area of sphere at radius } r')v \\ &= (n_e\mu m_H)(4\pi r'^2)v \end{aligned} \quad (1.12)$$

$$\begin{aligned}
&= \left(\frac{A}{r'^2} \mu m_H\right) (4\pi r'^2) v \\
&= A4\pi \mu m_H v.
\end{aligned}$$

A number of simplifying definitions may be introduced to Equation 1.11:  $X \equiv aL/4\pi\alpha^{(2)}A^2$ ; and  $f(u, \theta) \equiv \int_0^u (u^2/u'^4) du$ , where  $u \equiv r/a$ ,  $u' \equiv r'/a$  and  $a$  is the binary separation of the system. With these definitions, the ionization boundary may be expressed as:

$$f(u, \theta) = X. \quad (1.13)$$

The 2 dimensional geometry of the boundary for various values of  $X$  are shown in Figure 1.5

The orbital motion of the binary system will cause the structures of Figure 1.5 to be swept in an orbit about the center of mass with the instantaneous ionized region being defined by the volume swept out. In periods of orbital phase in which ionized material is shielded from ionizing radiation by the cool star, recombination will tend to take place. Since recombination rate decreases with density, material recombines out to radius  $R$  given by:

$$R = \left(\frac{\alpha^{(2)} \dot{M} P}{4\pi \mu m_H v}\right)^{\frac{1}{2}} \quad (1.14)$$

where  $P$  is the orbital period.

The ionized region at large distances will therefore form a ring or a “doughnut” surrounding the system. The instantaneous optical depth through the ionized material will depend upon the viewing angle, and this viewing angle will change

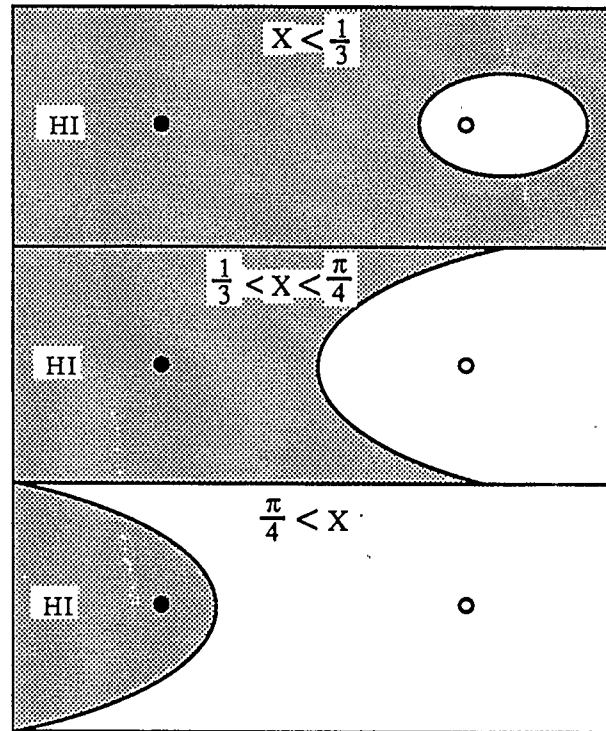


Figure 1.5: Ionization Boundaries of The STB Model

In this figure, the black dot corresponds to the cool mass losing star, and the unfilled dot corresponds to the hot ionizing source.

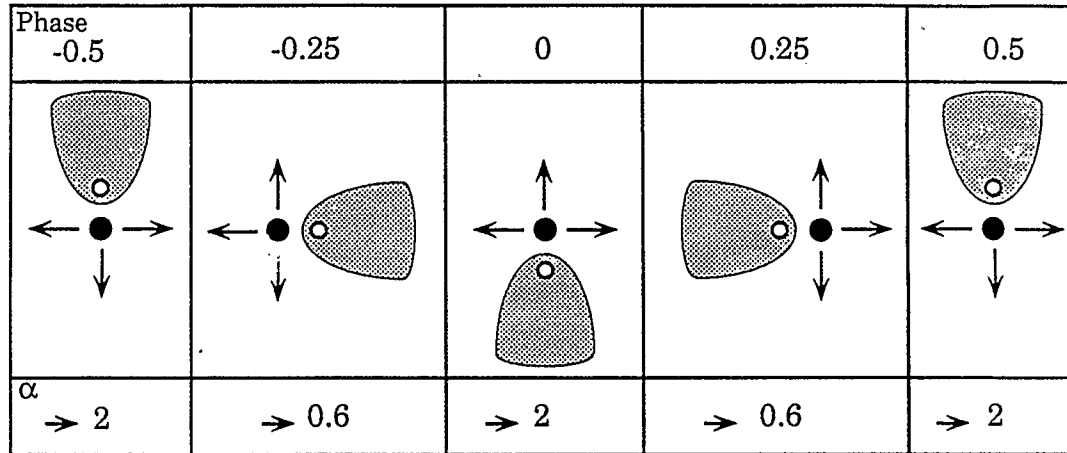


Figure 1.6: Variability of Flux and Spectral Index: STB Model

The open circle represents the hot, compact object of a symbiotic system, while the filled circle represents the giant. The case of  $1/3 < X < \pi/4$  is illustrated with the nebular region indicated by shading. The observer is positioned at the bottom of the diagram viewing upward as indicated by the arrow. The shell is considered to approach optical thickness when observed along the axis joining the two components; and to approach optical thinness when viewed perpendicular to this axis. Flux variations arise from the changing size of the optically thick surface observed, and because of shielding by the RG. The spectral index,  $\alpha$ , is defined by the relationship  $S_\nu \propto \nu^\alpha$  where  $S_\nu$  is the observed flux at frequency  $\nu$ .

with orbital phase. Variations of spectral index and flux are therefore expected with orbital phase (see Figure 1.6). By virtue of these variations with orbital phase, an STB-type phenomenon could be distinguished from either an ejected shell or an interacting winds phenomenon.

### **The Penston-Allen Model**

Penston and Allen (1985) have discussed a model which can yield radio results similar to the STB model; the physical conditions under which radio emission originates, however, are considerably different. The model, which was initially offered to describe the ultraviolet spectrum of AG Pegasi, is illustrated in Figure 1.7.

The Penston-Allen model assumes that the momentum flux which might be occurring from the RG wind is insignificant compared with that from the wind of the compact component. Mass loss from the compact component therefore dominates the physics of the system, and an ablation tail is driven from the RG. Radio emission arises both from the ablation nebula and from the "false photosphere" which is defined by the optically thick portion of the hot component wind.

The details of the Penston-Allen interaction have not yet been modelled quantitatively; however the qualitative implications for radio emission are clear. A conical nebular region is expected to develop around the cool star and this region would present a different aspect depending upon the orbital phase. Variations in flux and spectral index similar to those of the STB model are therefore predicted. Despite their apparent similarities, however, the two models are not mutually compatible: both models can not exist simultaneously in the same system. STB nebulae require an environment defined by a quiescent RG wind, while Penston-Allen neb-

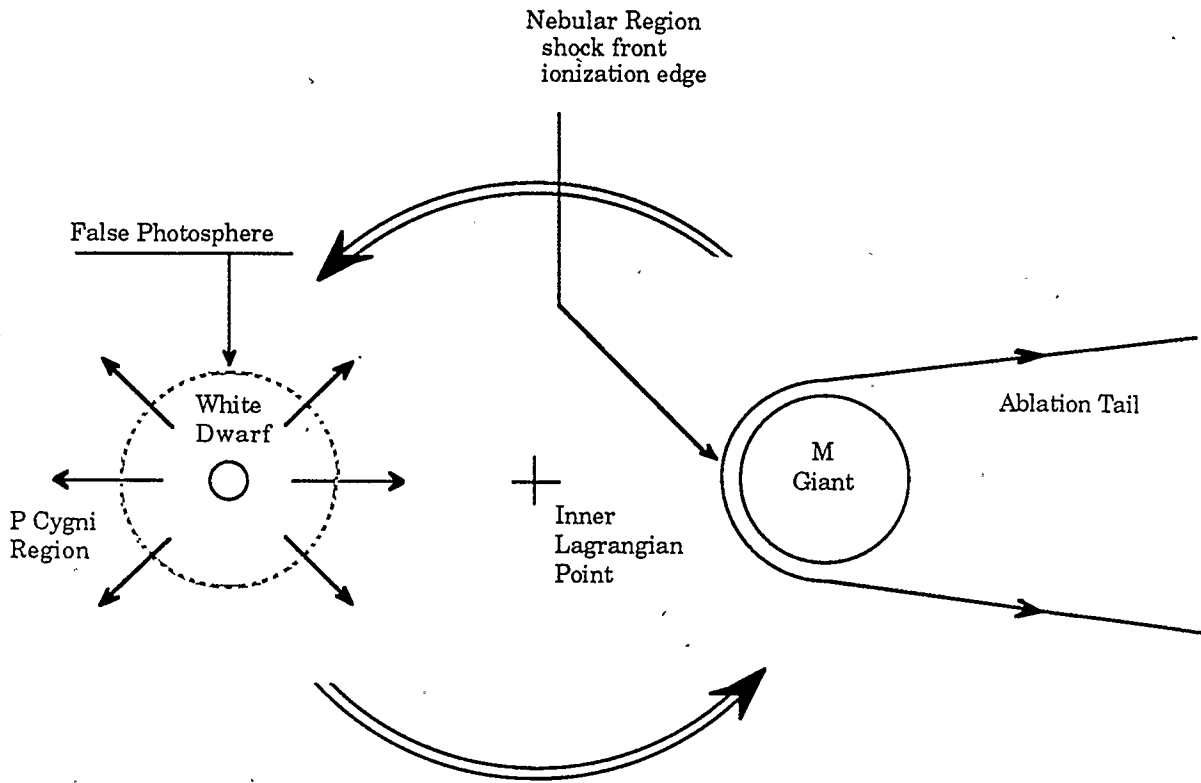


Figure 1.7: Penston-Allen Model

This Figure is based on Penston and Allen, 1985. The model was developed to explain the ultraviolet spectrum of AG Pegasi.

ulae require that this environment be disrupted by a strong wind from the hot, compact object. Independent information of the relative mass loss rates from binary components is necessary to determine which effect will dominate. Emission lines could also potentially aid in distinguishing the effects since the Penston Allen model predicts a more highly excited nebula. High velocity collisions at the surface of the RG would produce highly ionized species. This second diagnostic however is ambiguous since other forms of highly excited material such as accretion disks may conceivably exist.

#### **1.1.5 Directions of Research**

This section concludes the general discussion of symbiotic stars. Before leaving this subject it is interesting to present a few of the reasons why the study of symbiotic stars is valuable within the discipline of astrophysics. It is likewise of interest to list a few of the unanswered questions associated with current research in the field.

There are many reasons why symbiotic stars are of general interest in astrophysics. The radii and masses of components in symbiotics systems are potentially known independent of distance since the systems are binary. Such information is of intrinsic value. Further, symbiotic binaries are relatively far separated and hence their components are able to evolve in isolation from each other until their final stages. Hence, symbiotic stars are useful in the study of stellar evolution. The components of symbiotic systems do eventually interact and may provide valuable information about the processes involved. Symbiotic stars represent a limiting case of interaction and may improve our understanding of more violent phenomena such as novae and cataclysmic variables. Finally, symbiotic stars qualitatively resemble

a number of larger scale phenomena. Penston and Allen (1985) note that, in the ultraviolet, symbiotics bear a qualitative resemblance to quasars and active galaxies. They suggest that symbiotic stars may become the “laboratories” for the study of *Broad Line Radio Galaxies* (BLRG) and *Active Galactic Nuclei* (AGN). Such features as jets and accretion disks found commonly in extra galactic phenomena are also represented on a reduced scale among some symbiotic stars.

The following questions represent a few of the many problems confronting current research in the field of symbiotic stars.

- What is the nature of the “hot component” in the spectra of symbiotic stars?
- What is the nature and the cause of observed outbursts?
- What interaction occurs with the quiescent environment of a symbiotic system when an outburst occurs? How does this interaction affect the quiescent evolution following the outburst?
- What is the nature of the binary interaction within a typical symbiotic system? What are the important parameters which govern the interaction?
- What is the nature of TNRs in symbiotic systems? Does angular momentum play a significant role such as to encourage ejection in preferred directions?
- How widespread is the existence of jets and bipolar ejection?
- In how many cases does an accretion disk form around the hot compact object? Do other “blocking geometries” exist?

- How is the typical spectral index ( $\sim 0.9$ ) for thermal emission at radio frequencies among quiescent systems explained in detail?
- Do magnetic fields, especially in WDs, contribute to the symbiotic phenomenon as they do in cataclysmic variables.

## 1.2 AG Pegasi

### 1.2.1 History

AG Pegasi, the subject of this thesis, has a long and interesting history as the object of scientific investigation. Its brightness was first recorded in 1821 (Lundmark, 1921) and attention was first called to it by Fleming (1894) who noted that it was a source of bright hydrogen emission lines:  $H_\beta$ ,  $H_\gamma$ ,  $H_\delta$ . Since 1916, optical observations have taken place on a regular basis, most notably by Merrill (1929a,b; 1932; 1942; 1951a; 1951b; 1959a) and Boyarchuk (1966; 1967b; Boyarchuk *et al* 1987). The visual light curve from 1822 to 1968 is shown in Figure 1.8.

Of interest in Figure 1.8 are: the relatively steep rise in brightness by  $\sim 3$  mag between c.1850 and c.1870; a gradual decrease in brightness from c.1870 to present; and possibly a minor episode of brightening c.1945 (Arkhipova and Dokachaeva 1963; Belyakina 1968a; Kenyon 1986). The main event represented in the light curve is qualitatively reminiscent of classical novae, however it takes place on a much extended time scale. Classical novae evolve on the scale of hundreds of days, while the present eruption of AG Pegasi has extended over more than 125 years. AG Pegasi is classified as a symbiotic star by virtue of its spectrum (Figure 1.1) which includes an M giant (Penston and Allen 1985); the nature of its light curve

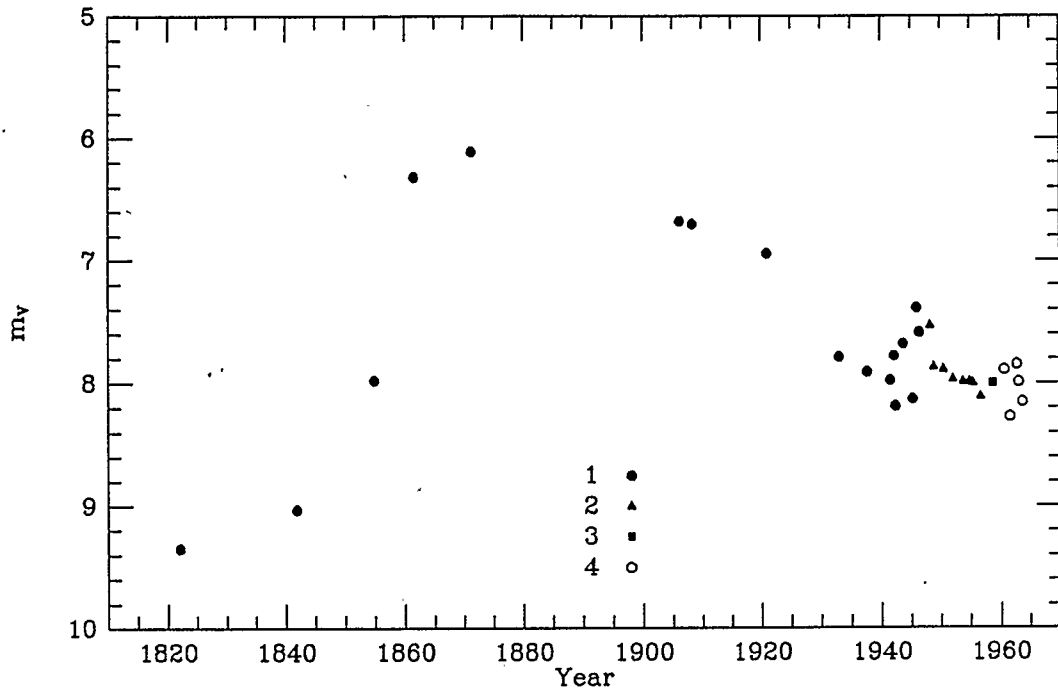


Figure 1.8: Visual Light Curve of AG Pegasi, 1822-1968

This figure is based on Belyakina 1968a. The observations corresponding to the legend above are: 1) Rigollet (1947); 2) Nord. Astron. Tidsskr. (1957); 3) AAVSO (1962); 4) Observations of Variable Stars (1963).

(Figure 1.8) justifies its subclassification as a symbiotic nova. The magnitude scale used in Figure 1.8 is defined as  $m = -2.5 \log l + K$  where:  $m$  is the apparent brightness of the source measured in "magnitudes" and is also referred to as the apparent magnitude of the source;  $l$  is the luminosity of the source (as detected at the Earth) and is measured in  $[\text{erg cm}^{-2} \text{ s}^{-1}]$ ; and  $K$  is a constant established by convention for given bands. The magnitudes scale then is a calibrated, inverse logarithmic scale for measuring brightness.

In addition to the nova-like outburst shown in Figure 1.8, the system exhibits short term photometric variations (Rigollet 1947, 1948; Stebbins, Huffer and Whitford 1940). Belyakina (1968a, 1968b, 1970) found an 800 day photometric period with an amplitude of 0.3 mag. She concludes that the variations are due to orbital motion since the photometric maximum corresponds to the maxima of a number of FeII emission lines generally associated with stellar photospheres. Figure 1.9 illustrates the mechanism by which optical variations are currently believed to occur.

The first spectrograms of AG Pegasi were obtained in 1893-1912 (Cannon 1916). From 1912 until the next observations in 1919-1920 (Merrill 1929) no major changes occurred in the spectrum, and the system was considered typical of Be stars. A Be star is a bright star of spectral type B which shows strong emission lines. The primary features in the spectrum were distinct and fairly strong emission lines of  $H_\beta$ ,  $H_\gamma$ ,  $H_\delta$ .

The next spectroscopic observations (Merrill 1929), however, revealed major changes. The neutral helium lines had greatly weakened, while the intensity of all emission lines increased several times. These facts indicated that the observed

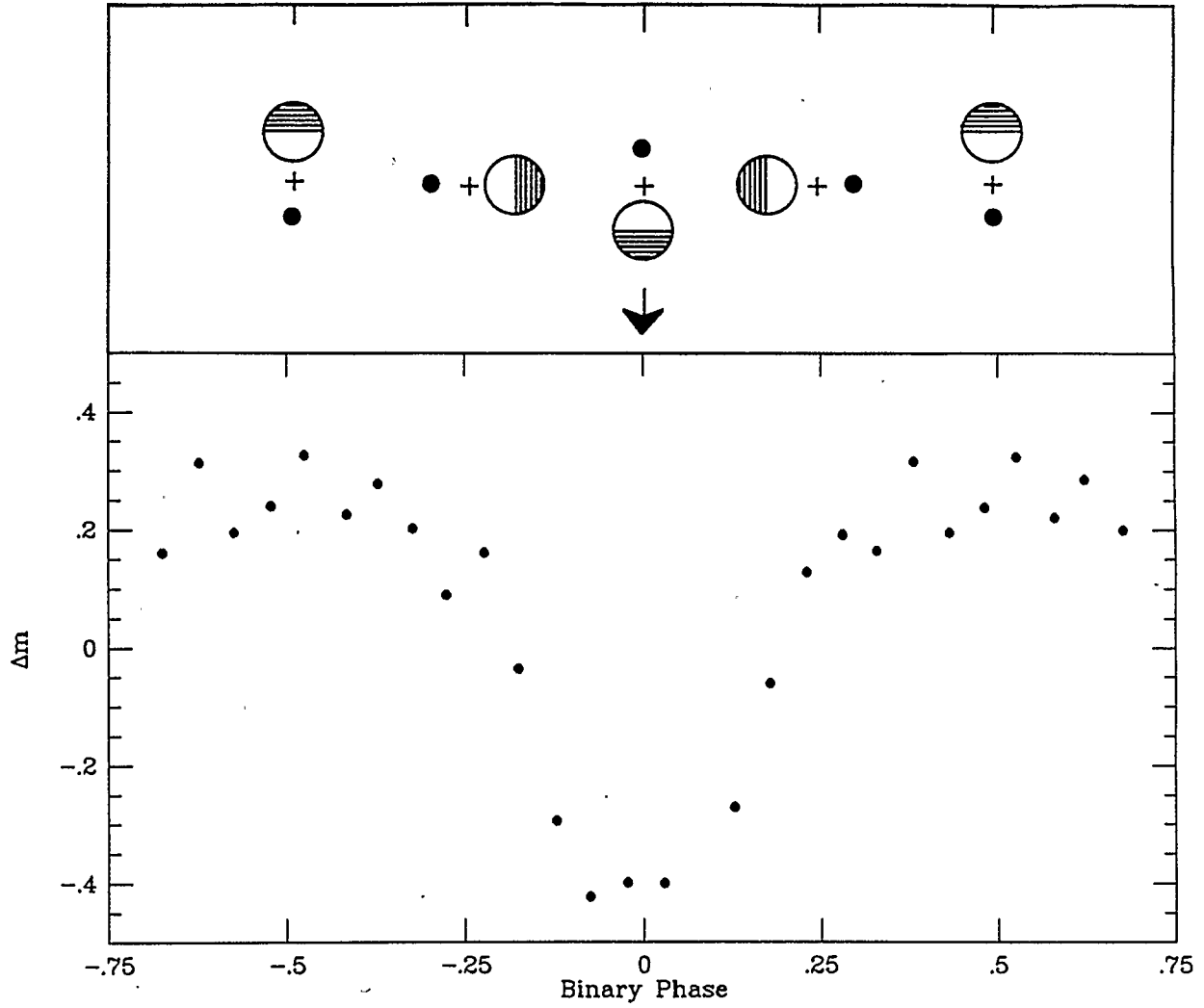


Figure 1.9: Model for the Optical Variations of AG Pegasi

This figure is based on Kenyon (1986). Heating of the surface of the giant by the hot component results in a hot spot which, depending upon the rotational orientation of the system, may or may not contribute to the observed flux.

	1920	1921	1931	1937	1941	1948	1950	1963
Appearance emission	HI	HeI NII [NII] SiIII	HeII NeIII SiIV		[OIII]		NIV CIII NeIII	CIV OIII
absorption	HI HeI NII SiIII SiIV							
Disappearance emission					SiIII	[NII]	NII	SiIV
absorption				SiIII	NII	SiIV	HI	

Table 1 1: Spectral Development of AG Pegasi 1920-1963

degree of excitation had increased; excitation has continued to increase up to the present time (see table 1.1). The intensity of high-excitation emission has also increased, and today HeII 4686 and NIV 4057 are among the strongest lines in the spectrum. While excitation continued to increase from 1921, the absorption lines corresponding to spectral type *B* experienced attenuation and disappearance. On the other hand, indications of spectral type *M* began increasingly to be exhibited. Today the signature of an *M* giant is well developed, and the overall spectrum, Figure 1.1, is typical of symbiotic stars.

Boyarchuk (1967a) analyses the development of AG Pegasi photometrically and spectroscopically. He finds the development consistent with shell ejection as discussed in the previous section. The same conclusion had been foreshadowed by Payne-Gaposchkin (1957) who noted that the development of multiple velocity

	Giant	Compact Object	Nebula
$Sp$	$M3III$	WN6	
$M_v$ [m]	-0.4	1.2	
$T_{eff}$ [K]		80,000	
$T_c$ [K]		30,000	
$T_e$ [K]			17,000
$R$ [cm]	$6 \times 10^{12}$	$6 \times 10^{10}$	$10^{16}$
$n_e$ [cm $^{-3}$ ]			$7 \times 10^6$
$M$ [ $M_\odot$ ]	7	1.5	$10^{-3}$

Table 1.2: Optical Components of AG Pegasi

This table is from Boyarchuk 1967b. Symbols are defined as follows:  $Sp$  - spectral classification;  $M_v$  - absolute magnitude (apparent magnitude if the object were located at 10 pc);  $T_{eff}$  - effective temperature (temperature of a blackbody producing the same luminosity);  $T_c$  - color temperature (temperature obtained by fitting the spectrum with a blackbody curve);  $T_e$  - electron temperature (temperature derived from velocity distribution of electrons);  $R$  - radius;  $n_e$  - electron density;  $M$  - mass;

systems in AG Pegasi was very similar to that of classical novae. Classical novae are believed to result from shell ejection driven by degenerate shell flashes on WDs (e.g. Kenyon and Truran 1983). Boyarchuk places the beginning of mass outflow from the hot component in about 1855, and the turn over to optical thinness (at optical wavelengths) in the envelope at about 1900. In about 1921 he suggests that a considerable part of the envelope had become optically thin and explains the spectral development in terms of the ability of the observer to see further and further into the nebula. With the above scheme for the flaring of the system, Boyarchuk derives the parameters for the system given in table 1.2. He also derives a distance of 600 pc to the system based on the spectral type of the giant; a binary separation of  $5.4 \times 10^{13}$  cm; and an inclination of  $\sim 36^\circ$  for the case of zero eccentricity.

The first systematic measurements of radial velocity were made by Merrill (1929) and resulted in detection of the 800 day period already discussed with reference to photometric variations. Significantly, the radial velocity variations observed in 1929 behaved differently for different elements; only the length of the period was the same for all lines. Differences included: phase; amplitude of radial velocity variations; and mean radial velocity. Lines of elements of the same ionization potentials, however, tended to behave similarly. These results suggested a complex, multifeature density structure for the system's nebular component (optical).

As an aside, distinction should be made at this point between the nebulae observed at different wavelengths. As wavelength decreases, optical depth for bremsstrahlung emission decreases; hence radio nebulae may become completely transparent in the optical. Of the four levels of radio nebulosity reported in this work only the very central, unresolved radio source is expected to make significant contribution to optical continuum flux. It should be possible, however, to detect the more extended nebulosities in optical light if forbidden lines of low ionization potential (*e.g.* [OIII]) are observed.

After 1921, new optical lines with higher degrees of ionization were identified, and these too exhibited the 800 day variations earlier identified. The only lines which did not exhibit the variations were the [OIII] 5007 and 4959 lines. Merrill (1959a) was fascinated by the fact that the [OIII] 5007 line had a velocity range of  $\sim 20 \text{ km s}^{-1}$  and no variations while the [OIII] 4363 line had a velocity range of  $\sim 70 \text{ km s}^{-1}$  and exhibited the 800 day variations. He concluded that the lines must emerge from different regions in the nebula and offered two possible models (see

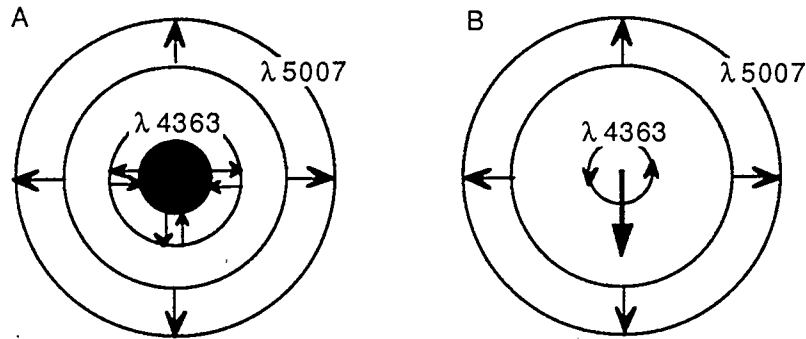


Figure 1.10: Nebular Model of AG Pegasi, Merrill 1959

Merrill (1959) offered two models to explain the disparate behavior of the [OIII] 5007 and 4363 lines. Both models involved an inner mantle emitting predominately at  $\lambda 4363$  and an other zone emitting predominately at  $\lambda 5007$ . Model A attributed the 800 day variation to pulsation. Model B attributed the 800 day variation to inner orbital motion and considered the outer region to be fed from the inner by means of "hoselike" ejection. Merrill preferred the second explanation.

Figure 1.10). It is not unusual that two different lines of the same element should behave differently in different regions. The probability of any transition occurring spontaneously is related both to the Einstein 'A' coefficient for the transition, and the density of the emitting matter. The critical density for one transition of a given atom may be higher than that of another transition of the same atom. The critical density is defined such that for densities below this value, transitions are not expected to be observed. In a given nebula, the density may be below the critical value for one transition and not for another; in this case the latter line would be observed preferentially.

Once the periodic variations of the radial velocity in AG Pegasi were discovered, it was found that other spectral characteristics shared the same periodicity.

These characteristics included: the intensity of metal lines; the intensity of TiO bandheads and late-type absorption lines; and the width of hydrogen lines. Cowley and Stencel (1973) have shown that the variations associated with the  $M$  giant occur in opposite phase to the emission line variations, reinforcing the belief that the system is binary. In addition to variations associated with the 800 day period, other systematic changes have also been noted in the spectrum. For instance, the relative displacement of absorption and emission components of HeI lines have increased dramatically since 1921 (Merrill 1929, Kenyon 1986): in 1921 the displacement implied a low expansion velocity ( $\sim 20 \text{ km s}^{-1}$ ) but in 1950 it increased to  $\approx 250 \text{ km s}^{-1}$  and has continued to increase since that time.

### 1.2.2 The Binary System

Today, the binary nature of AG Pegasi has been well established (Hutchings and Redman 1972; Cowley and Stencel 1973; Hutchings *et al* 1975). The primary component of the system is an M3III giant (Boyarchuk 1967a, Andrillat 1983) and appears to be typical for its class (Kenyon and Gallagher 1983). The secondary is classified optically as a WN6 star (Boyarchuk 1967a) and IUE spectra have confirmed this classification in the sense that they show broad emission lines that resemble those of Wolf-Rayet stars (Keyes and Plavec 1980a, b; Slovak and Lambert 1982; Penston and Allen 1985). The emission lines identified by IUE imply a wind of velocity  $\sim 1000 \text{ km s}^{-1}$  presumably flowing from the compact object. The temperature of the hot compact source has been estimated at 30,000 to 100,000 K (Gallagher *et al.* 1979; Keyes and Plavec 1980a,b; Slovak 1982a; Kenyon and Webbink 1984), although higher temperatures may be preferred in order to explain

the strength of HeII emission (Kenyon and Webbink 1984; Penston and Allen 1985; Keyes and Plavec 1980a). On the other hand, if the compact object is indeed a *Wolf-Rayet* (WR) type star, its temperature may be closer to 30,000 K than to 100,000 K (Keyes and Plavec 1980a). The system is not believed to be eclipsing (Boyarchuk 1967a). The latest determinations of the orbital elements of the system are given in table 1.3. In this table, the relative masses of the primary (most massive) and secondary components of the binary system are given by a function  $f(M)$  which is defined:

$$f(M_1, M_2, i) = \left( \frac{M_2}{M_1 + M_2} \right)^2 M_2 \sin^3 i \quad (1.15)$$

where:  $M_1$  is the mass of the primary;  $M_2$  is the mass of the secondary; and  $i$  is the angle of inclination of the orbit. If the primary in AG Pegasi has mass of  $3 M_\odot$  (Hutchings *et al.* 1975) and the inclination of the orbit is  $\sim 36^\circ$  (Boyarchuk 1967a) then according to the average value of mass function in table 1.3 (0.015) a secondary of mass  $\sim 1M_\odot$  is implied.

Infrared studies have shown AG Pegasi to be an S-type system (Roche *et al.* 1983; Feast *et al.* 1976), and Glass and Webster (1973) find it to be the least dusty of all symbiotics studied. The system was, however, detected by the *Infrared Astronomical Satellite* (IRAS) and found to be losing mass at the rate of  $\sim 2 \times 10^{-7} M_\odot \text{ yr}^{-1}$  (Kenyon 1988a). The spectral type of the giant has been confirmed in the infrared as M3 (Roche *et al.* 1983) although Kenyon and Gallagher (1983) also use infrared observations to classify it as M2. In either case, it is unlikely to fill its Roche lobe (Boyarchuk 1967a; Hutchings *et al.* 1975; Gallagher *et al.* 1979;

	Cowling and Stencel (1973)	Hutchings <i>et al.</i> (1975)	Garcia and Kenyon (1988)	Slovak and Lambert (1988)
$P$ [days]	830 $\pm 1.68$	820	796 $\pm 15$	818.72 $\pm 2.5$
$K_1$ [kms $^{-1}$ ]	5.6 $\pm 0.2$	5.5 $\pm 0.8$	6.4 $\pm 0.2$	4.98 $\pm 0.37$
$K_2$ [kms $^{-1}$ ]	-16.8 $\pm 0.2$	-16.3 $\pm 0.5$	-14 -	-16.15 $\pm 0.28$
$e$	0.25 $\pm 0.05$	0.23 $\pm 0.12$	0 -	0.28 $\pm 0.08$
$\omega$ [ $^\circ$ ]	251 $\pm 3.2$	222 $\pm 43$	-	149.9 $\pm 20.2$
$T_o$ [ $JD - 2400000$ ]	39045 $\pm 25$	40620 $\pm 19$	- -	44507.8 $\pm 33.9$
$f(m)[M_\odot]$	0.014 -	0.013 -	0.022 -	0.009 -
$a \sin i$ [ $10^{12}$ cm]	6.19 -	- -	- -	5.42 $\pm 0.13$

Table 1.3: Orbital Elements of AG Pegasi

Symbols in this table are defined as follows:  $P$  - period;  $K_1$  and  $K_2$  - semi amplitudes of radial velocity curve;  $e$  - eccentricity;  $\omega$  - longitude of periastron (Euler angle);  $T_o$  - minimum of light curve;  $f(m)$  - mass function;  $a$  - binary separation;  $i$  - inclination of orbit to line of sight.

Keyes and Plavec 1980b). An analytic approximation for the radius of a Roche lobe is given by (*e.g.* Bowers and Deeming 1984):  $r_{roche,1} = a(0.38 + 0.2\log(M_1/M_2))$  where:  $a$  is the binary separation;  $M_1$  is the mass of the component within the Roche lobe; and  $M_2$  is the mass of the other component (see Figure 1.2). Roche lobe overflow occurs if  $R > r_{roche}$  where  $R$  is the radius of the star associated with the lobe. Approximate parameters for the calculation are (Hutchings *et al.* 1975):  $M_{compact} \sim 1M_{\odot}$ ;  $M_{giant} \sim 3 - 4M_{\odot}$ ;  $R_{giant} \sim 50R_{\odot}$ ;  $a \sim 600R_{\odot}$ . It is found that  $r_{roche} \sim 300R_{\odot} \sim 6 \times R_{giant}$ . This calculation, however, assumes a circular orbit and if an eccentric orbit were invoked, overflow might perhaps exist. In this case, however, the required eccentricity would be  $e \gtrsim 0.67$  which is rather unlikely. Hutchings *et al.* (1975) consider 0.23 to be an upper limit to the orbital eccentricity. One implication of an unfilled Roche lobe is that, during quiescence, no accretion disk is expected to form (*e.g.* Nussbaumer and Vogel 1987). Another implication is that accretion must take place, or have taken place, from the *red giant* (RG) wind.

Ultraviolet studies of AG Pegasi have concentrated to a large extent upon determining the nature of the hot component; this information is necessary to place the system within the evolutionary context of symbiotics generally. Gallagher *et al.* (1979) argued that the companion to the RG was a degenerate object (*e.g.* WD) and that the 1855 event was a thermonuclear runaway on the surface of that object. These conclusions have been largely upheld in more recent work (*e.g.* Pacynski and Rudak 1980; Kenyon and Truran 1983; and Penston and Allen 1985).

Keyes and Plavec (1980a, b) found that the continuum from 1200 Å to 5000 Å could be fit by a 30,000 K Kurucz (1979) atmosphere, and obtained results

$\log(R_h/R_g) = -2.02$  and  $\log(L_h/L_g) = -0.35$  where:  $R$  is radius;  $L$  is bolometric luminosity (entire energy output at all wavelengths per second); and subscripts  $h$  and  $g$  refer to the “hot” and “giant” components respectively. Unfortunately, this solution fell critically short of predicting sufficient HeII ionizing photons and hence the authors proposed a second, tentative solution in which the near ultraviolet continuum arises from nebular emission. This solution includes a  $10^5$  K black body with  $\log(R_h/R_g) = -2.65$  and  $\log(L_h/L_g) = 0.46$ .

Kenyon and Webbink (1984), using model ultraviolet spectra produce three different fits for the hot component of AG Pegasi (See table 1.4). Their first solution, which assumes a hot stellar source, gives parameters similar to the Kurucz (1979) solution of Keyes and Plavec (1980a) and it likewise fails to produce sufficient HeII ionizing photons. Further, this first solution is suspicious because it has been possible for the authors to obtain a slightly better fit by assuming a temperature of 20,000 K (solution 3). Their second solution, a disk accreting WD, is the only one of their three alternatives which comes close to matching observed values of HeII at  $\lambda 4686$ . This solution however requires a giant of luminosity class II or brighter, while recent infrared photometry (Kenyon and Gallagher 1983) indicates unambiguously that the luminosity class is III. The authors therefore reject the second solution along with the first. They reluctantly accept the third solution which assumes a temperature of 20,000K. This solution implies the following relationships:  $\log(R_h/R_g) = -2.35 \pm 0.02$ ,  $\log(L_h/L_g) = 0.04 \pm 0.11$ . This third solution would apparently apply to an extended photosphere formed in an outflowing wind since the temperature is too low to account for the strong, high excitation emission lines.

A final detailed attempt to explain the ultraviolet continuum of AG Pegasi was

	Type	$\text{Log } \dot{M}$ [ $M_{\odot} \text{ yr}^{-1}$ ]	$\text{Log } T_h$ [K]	$E_{B-V}$
1	hs	...	$4.37 \pm 0.04$	$0.17 \pm 0.02$
2	wd	$-6.52 \pm 0.17$	...	$0.13 \pm 0.02$
3	hs <sub>1</sub>	...	$4.76 \pm 0.04$	$0.15 \pm 0.04$

Table 1.4: Model Fits for the Hot Component of AG Pegasi

This table is taken from fits to the ultraviolet spectrum by Kenyon and Webbink (1984). Solutions designated “hs” are fits which assume the hot component to be a hot star; “hs<sub>1</sub>” refers to stellar model fits for which  $T_e$  was constrained to be 20,000 K. The designation “wd” refers to modelling done for a *white dwarf* (WD) star ( $M = 1M_{\odot}$  and  $R = 0.009R_{\odot}$ ) accreting from a disk.

undertaken by Penston and Allen (1985). Their point of departure was the identification of three ultraviolet components to the system: a  $900 \text{ km s}^{-1}$  P Cygni wind; a highly ionized, high-density, low velocity domain; and a region of highly ionized absorption lines which display different velocity structure in each ion. They found typical widths of  $65 \text{ km s}^{-1}$  for the narrow emission lines which they associate with the highly ionized, low velocity region of the system. The model which they developed to explain their observations was discussed in the previous section (Penston-Allen model); it focuses primarily upon the WR wind of the hot component and attributes aspects of the ultraviolet spectrum to ablation from the surface of the RG by this wind. This application of the Penston-Allen model has the considerable virtue of providing a “stream” of matter pointing directly away from the hot star; this feature would account for the apparent flow of material identified by Hutchings *et al.* (1975). Hutchings *et al.* used high dispersion optical spectra of AG Pegasi to derive line velocities and intensities, and argued that their results suggested mass transfer from the hot to the cool component. This “illusion” could

be created by the Penston-Allen mechanism because it would provide a “stream” in the right direction.

### 1.2.3 Radio Emission

Radio study of AG Pegasi began with Wendker *et al.* (1973) who reported a null detection at the *Westerbork Synthesis Radio Telescope* (WSRT). The first reported detection was made by Woodsworth and Hughes (1977) who found a total flux of 6 - 9.4 mJy at 10.6 GHz at the *Algonquin Radio Observatory* (ARO). Table 1.5 gives the published radio observations of AG Pegasi to date. Gregory *et al.* (1977) found the system’s spectrum to be consistent with free-free emission from a circumstellar nebula, and this interpretation has been upheld by all subsequent observers (table 1.5).

While the radio emission from AG Pegasi clearly arises from circumstellar material, its nature and distribution is not well understood. Gregory *et al.* (1977) interpreted the emission as arising from an outflowing wind according to the model of Wright and Barlow (1975). They found  $\dot{M}/v = 7 \times 10^{-9} M_{\odot} \text{ yr}^{-1} \text{ km}^{-1} \text{ s}$  where  $\dot{M}$  is the mass loss rate and  $v$  is the velocity of mass loss. The implied mass of the nebula was  $7 \times 10^{-5} M_{\odot}$ . Ghigo and Cohen (1981), however, were able to resolve the nebula at the *Very Large Array Telescope* (VLA) and found a half power diameter at 5 GHz of  $1'' \pm 0.3''$ . This size was considerably larger than predicted by simple mass loss models and the authors suggested either a filling factor for the nebula of  $1/8$  to  $1/27$  or distinct optical and radio nebulae. Hjellming (1985) conducted a multifrequency radio study of AG Pegasi at the VLA. He found the system to consist of a central unresolved source and an outer nebulosity with a

Date	Instrument	HPBW	Frequency [GHz]	Total Flux [mJy]	Observer
1973	WSRT	6''	5	< 5	1
	Bonn	78''	10.69	< 10	
11 Jun 73	Bonn	78''	10.69	< 10	2
12 Feb 73	ARO	2'.8	10.6	6.0 - 9.4	3
1977	Parkes	2'.3	14.5	10 ± 3	4
		-	6.2	14 ± 6	
		4'.3	5	5 ± 3	
Oct 73	NRAO	5''	2.70	< 6	5
		-	8.09	12 ± 2	
Jun 74	ARO	2'.8	10.5	13 ± 2	
20 Jan 79	VLA	0.3''	4.9	6.2 ± 0.7	6
4 May 80	VLA	0.3''	4.9	8.0 ± 0.9	
1 Feb 82	VLA	0.6''	4.9	7.84 ± 0.95	7
Oct 83	VLA	-	1.4	3.8 ± 0.4	8
		0.3''	4.9	6.3 ± 0.4	
		0.1''	15	3.0 ± 0.4	

Table 1.5: Radio Observations of AG Pegasi

Observers: 1. Wendker *et al.* 1973; 2. Altenhoff *et al.* 1976; 3. Woodsworth and Hughes 1977; 4. Wright and Allen 1978; 5. Gregory *et al.* 1977; 6. Ghigo and Cohen 1981; 7. Seaquist *et al.* 1984 / Seaquist and Taylor 1989; 8. Hjellming 1985.

Instruments: WSRT - Westerbork Synthesis Radio Telescope; Bonn - Effelsberg 100m telescope; ARO - Algonquin Radio Observatory (46m); Parkes - Parkes Radio Telescope (64m); NRAO - National Radio Astronomy Observatory 3 element interferometer; VLA - Very Large Array Telescope. Resolution is indicated by *Half Power Beam Width* (HPBW).

high degree of spherical symmetry and a diameter of  $\sim 1.5''$  (Figure 1.11). He also noted the “suggestion” of a jet-like feature connecting the unresolved source to the outer nebulosity. He was able to separate the unresolved flux from the extended emission, and found the unresolved flux to be  $0.6 \pm 0.1$  mJy at 4.9 GHz and  $2.2 \pm 0.5$  mJy at 15 GHz. These details seemed to support the suggestion of Ghigo and Cohen that the nebula could not be described by a single component. Hjellming suggested the extended emission to be the interaction between a slow nova “wind” or shell and the pre-existing RG wind. Assuming that the initial slow nova ejection took place in 1850, he calculated an average expansion velocity of  $15 \text{ km s}^{-1}$ . The 5 GHz image produced by Hjellming is given in Figure 1.11. It is well, again to distinguish between objects observed at optical wavelengths from those observed in radio. The central unresolved source should not be confused with the binary system. Rather, it is almost certainly a gaseous nebula by virtue of its detectability in radio emission and the spectral index of 1.2 implied by the results quoted from Hjellming above. It is useful as well to have an impression of scales. The binary separation of the system is on the order of astronomical units ( $1.5 \times 10^{13}$  cm). At 600 pc, this distance would subtend an angle of about  $0.002''$  which may be compared to the the  $2''$  diameter shown for the extended nebulosity in Figure 1.11.

As a final episode in this observational history, Fuecelida *et al.* (1988) have detected further extended nebulosity from AG Pegasi in  $H_\alpha$ . Their image shows two lobes of  $\sim 2''$  diameter situated at about  $5''$  from the center of the system; the lobes are in virtually opposite directions from the center ( $\sim$  NW-SE). The separation of  $\sim 5''$  places the emission considerably further out than the  $1.5''$  emission detected

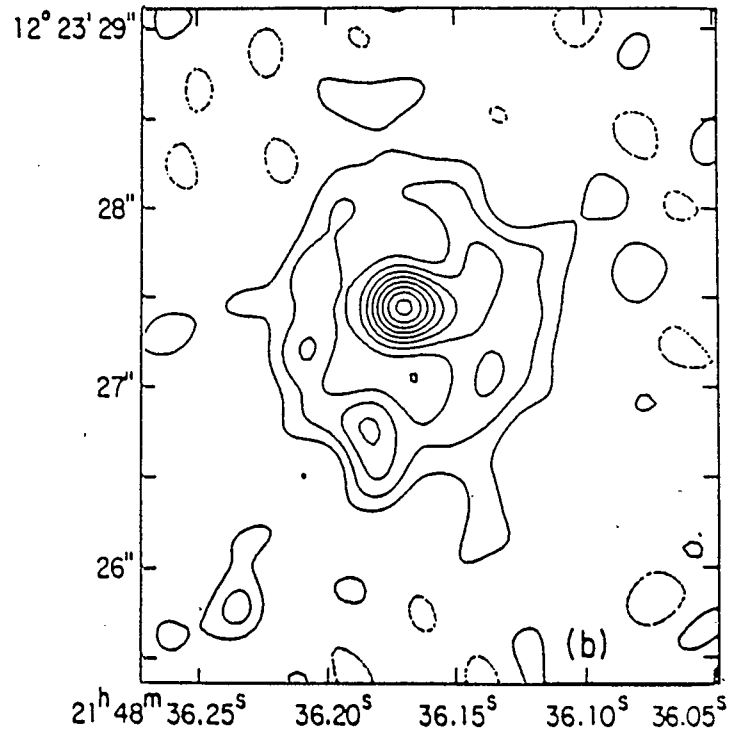


**Figure 1.11: VLA Image of AG Pegasi at 5 GHz, 1983**

This image is from Hjellming (1985). Uniform weighting as described in Section 3.3 has been applied.

by Hjellming. If this further emission exists, it is potentially detectable in radio emission at the VLA for observations of appropriate resolution and sensitivity.

## Chapter 2

### TECHNICAL BACKGROUND

The material in this section represents the technical background necessary to understand the observations of AG Pegasi which will be presented in this thesis. An elementary discussions of radio telescopes and arrays leads to a more detailed exposition of aperture synthesis. The term aperture synthesis refers to the type of radio interferometry carried out at the VLA where the observations of AG Pegasi were made.

#### 2.1 Radio Telescopes

A radio telescope is a reflector. The reflector collects radio waves from the area of the sky in which it is pointing, and focuses them upon a receiver. The receiver develops a voltage in response to the amplitude of the electric field of the focused waves. This voltage is an observable quantity, and is essentially a measure of the energy of the focused radiation. An "ideal" radio telescope has infinite directivity; that is, it is sensitive only to signals arriving from the precise direction in which it is pointing, the "pointing center". In reality radio telescopes are, in a weighted fashion, sensitive to radiation arriving from all directions. The weighing function is referred to as the "beam" and is normalized to a value of 1 at the pointing center. The normalized beam may be characterized as a function  $A(s)$ , where the vector  $s$  denotes the direction of incoming radiation relative to the pointing center of the

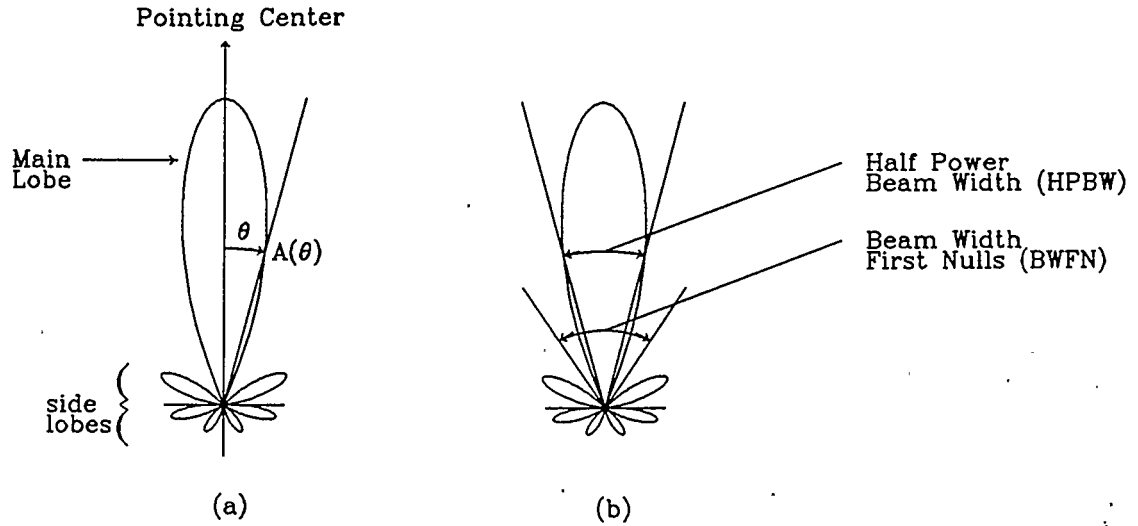


Figure 2.1: Example of a Beam Pattern in Two Dimensions

In the above figures, the angular coordinate  $\theta$  designates the direction  $s$  in real space, while the radial component  $A$  represents the weighing function (beam) which expresses the response of the antenna to radiation arriving from that direction. The plotted curve  $A(\theta)$  or  $A(s)$  is a theoretical response of a radio telescope.

telescope. Note that bold face symbols are used to denote vector quantities. A two dimensional example of a “beam pattern” is shown in Figure 2.1.

From Figure 2.1 a number of important quantities may be identified. The “main lobe” of the beam pattern is labelled in Figure 2.1a. Clearly the weighting of incoming radiation favors sources with  $\theta$  (the angular displacement from the pointing center) lying within the main lobe. The small areas of enhanced weighing surrounding the main lobe are referred to as “side lobes”. Signal contributions from the side lobes are seldom useful and serve only to contaminate the signal from the source at the pointing center. The “beam width” is a fundamental quantity which must be known in order to assign meaning to any radio observation; it indicates the area of the sky over which the telescope is primarily sensitive. A useful definition

of “beam width” is the *Half Power Beam Width* (HPBW) of the main lobe as illustrated in Figure 2.1b.

From the above description, radio telescopes may not appear to be very promising instruments. For one thing, they do not seem capable of producing images; they provide only voltages indicating energy received from an area of the sky. In reality, radio telescopes not only produce images, they produce images of better resolution than any other astronomical instruments. There are basically two ways in which radio images may be made: scanning, and aperture synthesis.

Scanning produces images by moving the pointing center of a radio telescope across a source as shown in Figure 2.2. This movement may be facilitated by the earth’s rotation. In Figure 2.2 the beam solid angle,  $\Omega_B$ , is much smaller than the solid angle subtended by the source,  $\Omega_S$ . Hence, to produce a two dimensional image of the source in Figure 2.2 a number of scans would be necessary. Notice that the profile detected by the telescope in Figure 2.2 is an imperfect representation of the true profile. The imperfection arises because the telescope beam samples “areas” on the surface of the source rather than points. The observed flux distribution is, mathematically speaking, the “convolution” of the actual intensity distribution with the telescope beam:

$$S_{obs}(l, m) = \int_{4\pi} A(l - l', m - m') I_S(l - l', m - m') d\Omega \quad (2.1)$$

where:  $l$  and  $m$  are angular coordinates on the plane of the sky;  $(l', m')$  designates the pointing center of the telescope; and  $I_S$  is the true intensity distribution of the source. An observed intensity distribution,  $I_{obs}$ , may then be defined such that  $I_{obs} \equiv \Omega_B S_{obs}$ .

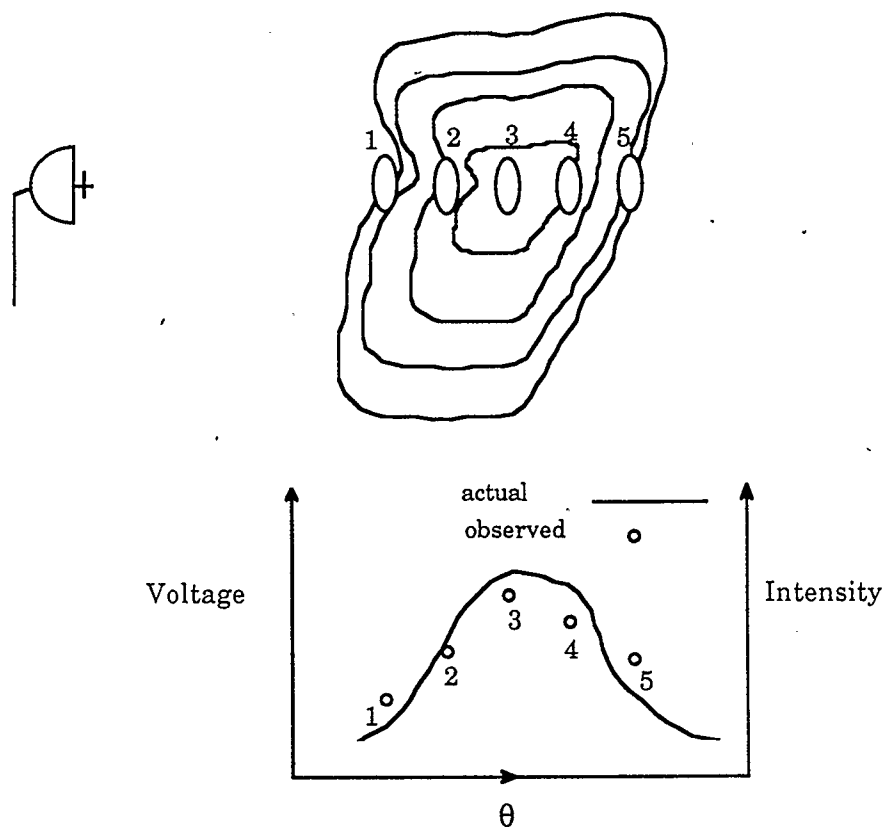


**Figure 2.2: Scanning With a Radio Telescope**

The source in the above figure is represented by contours connecting points of equal intensity. The plot shown below the source image indicates voltage measurements corresponding to the positioning of the telescope "beam" upon the image.

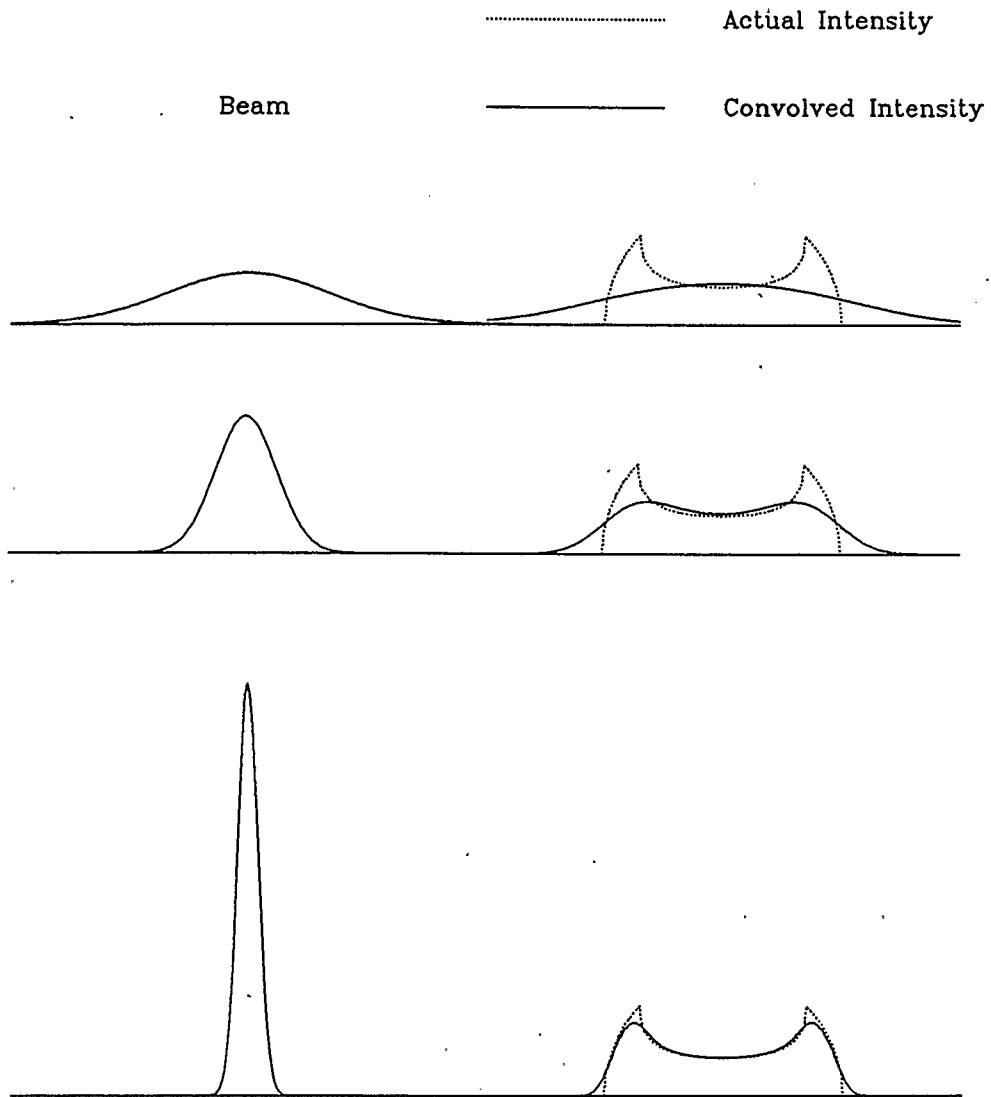


**Figure 2.3: Beam Size and Resolution**

The left hand profiles in the above sequence denote the telescope beam, and the right hand images show both the actual intensity distribution and the distribution "observed" by the telescope. It will be noted that the observed distribution becomes increasingly precise as the beam become narrower.

Scanning is a useful procedure, however its utility is limited by the relatively large beam widths of single dish antennas. The smallest beam presently achieved in centimeter wavelengths is  $1.5'$ ; this is the HPBW at 2.7 GHz of the 305 m diameter dish at Arecibo. At millimeter wavelengths, the *James Clerk Maxwell Telescope* (JCMT) has been able to achieve a resolution of  $\theta \sim 10''$ . Small beam widths are desired since it is the beam width which defines the "resolution" achievable by a given telescope. Figure 2.3 illustrates the effect of mapping an intensity distribution with progressively smaller beams. Large single dish antennas have for practical purposes reached the limits of their potential resolution; it is unlikely that construction of a dish larger than that at Arecibo will be undertaken. The technique of aperture synthesis, which makes use of arrays of many telescopes, is the key to higher spatial resolution.

## 2.2 Radio Arrays

As noted, arrays of antennas rather than larger single dishes are the key to higher resolution in radio astronomy. The resolving power,  $\theta$ , at wavelength  $\lambda$  of an array of telescopes positioned within an area of diameter  $D$  is given by  $\theta \sim \lambda/D$ ; this is the same resolution theoretically achievable by a single dish of the same diameter. The relationship  $\theta \sim \lambda/D$  will now be demonstrated for the case of  $n$  identical, evenly spaced antennas in one dimension. The arguments are generalizable to two dimensional arrays and the result is also approximately true for irregular spacing and non-identical elements. It should be noted, however, that high resolution is not the only prerequisite of a good radio telescope; it must also have high sensitivity

(*i.e.* be very sensitive). The sensitivity of a radio telescope array will always be lower than that of a single dish of equivalent diameter. The reason for this is that the array will always have a smaller collecting area.

Consider two identical point sources separated by a distance  $L$  and radiating coherently at the same wavelength,  $\lambda$  as in Figure 2.4. By the reciprocity theorem, the power pattern generated by such point sources corresponds exactly with the receiving power pattern (synthesized beam) when the array is used as a receiving antenna. For two sources (antennas) with identical electric field patterns given by  $E(\phi)$  (primary beam), the combined electric field pattern of the two element array (synthesized beam) is given by:

$$\begin{aligned} E &= E(\phi)e^{i\psi/2} + E(\phi)e^{-i\psi/2} \\ &= 2E(\phi)\cos(\psi/2) \end{aligned} \quad (2.2)$$

where:  $\phi$  is defined in Figure 2.4;  $\psi \equiv \mathbf{k} \cdot \mathbf{L} = (2\pi L/\lambda)\sin\phi$ ;  $\mathbf{k}$  points in the direction  $\phi$  and has magnitude  $2\pi/\lambda$ ; and the reference point for phase is taken half way between the two sources (antennas). The factors  $e^{i\psi/2}$  and  $e^{-i\psi/2}$  represent the phase delay caused by the displacement of the sources from the phase center.

Figure 2.5 shows the relative far-field pattern for two equal, in-phase point sources separated by one half wavelength (dipole radiation):  $E = \cos((\pi/2)\sin\psi)$ . Note that if the array in this figure is treated as an antenna located at the phase center, then a second identical "antenna" may be placed next to it to produce a "binomial" array. If this were done such that the separation of the two new "antennas" was  $L$  and the phase center were taken at the center of this new array,

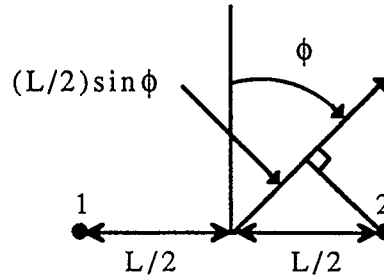


Figure 2.4: Geometry of a Two Element Array

then the resultant relative pattern would be given by  $E = \cos^2((\pi/2)\sin\psi)$ . It is possible now to extrapolate the result for binomial arrays of the  $n$ th degree:  $E = \cos^n((\pi/2)\sin\psi)$ . The net effect is that the pattern shown in Figure 2.5 becomes progressively narrower as  $n$  is increased. The width of the pattern determines the resolution of the instrument, and is measured by the quantity HPBW or BWFN (see Figure 2.1). This establishes qualitatively that larger arrays are able to produce progressively narrower beam patterns.

Consider now an array of  $n$  identical evenly spaced elements as shown in Figure 2.6. The combined electric field pattern is given by:

$$E = E_o[1 + e^{i\psi} + e^{i2\psi} + \dots + e^{i(n-1)\psi}] \quad (2.3)$$

where:  $E_o$  is the electric field pattern generated by each individual source; the phase delay between antennas is given by  $\psi = (2\pi d/\lambda)\sin\phi$ ; and  $\phi$  and  $d$  are given in Figure 2.6.

Multiplying Equation 2.3 by  $e^{i\psi}$  gives the result:

$$Ee^{i\psi} = E_o[e^{i\psi} + e^{i2\psi} + e^{i3\psi} + \dots + e^{in\psi}]. \quad (2.4)$$

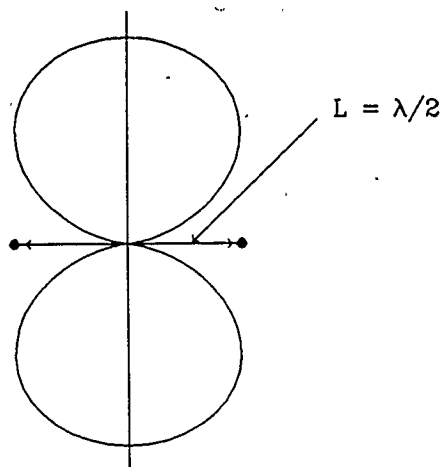


Figure 2.5: Dipole Electric Field Pattern

The above figure displays the relative electric field pattern resultant from two identical isotropic point sources radiating coherently. By the reciprocity theorem, it also represents the power pattern for the “array” in receiving mode.

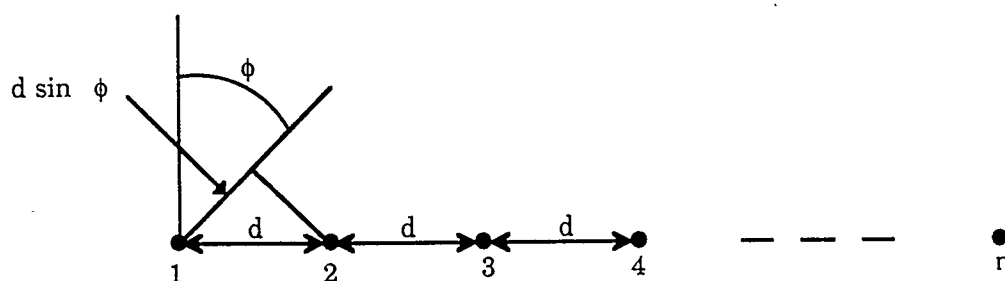


Figure 2.6: Geometry of an n-Element Array

Subtracting Equation 2.4 from Equation 2.3 yields:

$$E = E_o \frac{1 - e^{in\psi}}{1 - e^{i\psi}}. \quad (2.5)$$

The null directions of the pattern represented in Equation 2.5 are given by the condition  $e^{in\psi} = 1$  provided  $e^{i\psi} \neq 1$ . Therefore  $n\psi = \pm 2k\pi$  where  $k = 1, 2, 3 \dots$  (but  $k \neq mn$ , where  $m = 1, 2, 3 \dots$ ). This is equivalent to the condition  $\phi_o = \sin^{-1}(\pm k\lambda/nd)$ , where  $\phi_o$  represents null angles of the power pattern. Taking  $k = 1$  for the first null, and assuming array dimension larger than  $\lambda$ , the condition becomes  $\phi_o \sim \pm\lambda/D$  where  $D \equiv nd$  is the “diameter” of the array. The *Beam Width at First Nulls* (BWFN) is then given by  $BWFN = 2\phi_{o1} = 2\lambda/D$ . The more common measure of resolution is the *Half Power Beam Width*;  $HPBW \sim BWFN/2$  (Kraus 1986). The desired relationship may now be written:  $\theta \sim HPBW \sim \lambda/D$ .

### 2.3 Aperture Synthesis

Aperture synthesis is the most powerful technique available to the radio astronomer to map surface brightness on the sky with high resolution. It is also called radio interferometry because it uses the correlation of electromagnetic signals received along different paths to obtain its results. Radio interferometers consist of a number of “antenna pairs”. An antenna pair or “baseline”, consists of two radio antennas and a correlator to combine their signals. An interferometer consisting of  $n$  antennas will include  $n(n - 1)/2$  possible antenna pairs or baselines. Since the results from all baselines are only combined in the final stage of imaging, the present discussion will consider, without loss of generality, only a single antenna

pair. Similarly, only one polarization of radiation will be considered.

The aim of this section is to derive the fundamental equation of aperture synthesis:

$$I_\nu(l, m) = \int_{-\infty}^{+\infty} \int_{-\infty}^{+\infty} V_\nu(u, v) e^{2\pi i(ul+vm)} du dv. \quad (2.6)$$

The terms of this equation will be defined below; it is sufficient here to note that:  $I_\nu(l, m)$  is the desired brightness distribution on the sky; and  $V_\nu(u, v)$  is the “visibility function”, the quantity measured by an interferometer.

The autocorrelation function or visibility function for radiation at frequency  $\nu$  is defined:

$$V_\nu(\mathbf{r}_1, \mathbf{r}_2) = \langle E_\nu(\mathbf{r}_1) E_\nu^*(\mathbf{r}_2) \rangle \quad (2.7)$$

where:  $\mathbf{r}_1$  and  $\mathbf{r}_2$  are two points (antenna locations in practice);  $\mathbf{E}_\nu(\mathbf{r})$  is the monochromatic component of the electric field at frequency  $\nu$  received by an antenna at  $\mathbf{r}$  due to all sources of electromagnetic radiation; and the raised asterisk denotes complex conjugation. An expression of  $E_\nu(\mathbf{r})$  arises as follows. The electric field of some astrophysical phenomenon at location  $\mathbf{R}$  is in general both complicated and time varying:  $\mathbf{E}(\mathbf{R}, t)$ . However, it is possible to decompose the magnitude of such a field at  $R$  into the monochromatic components of a Fourier series,  $\mathbf{E}_\nu(\mathbf{R})$ . At some second point  $\mathbf{r}$  these components will be observed as  $d\mathbf{E}_\nu(\mathbf{r})$ . The wave equation for electric fields described by Maxwell’s equations for isotropic non-conducting media may be solved to provide a spherical harmonic solution for  $d\mathbf{E}_\nu(\mathbf{r})$ :

$$dE_\nu(\mathbf{r}) = \mathcal{E}_\nu(\mathbf{R}) \frac{e^{2\pi i \nu |\mathbf{R}-\mathbf{r}|/c}}{|\mathbf{R}-\mathbf{r}|} dS \quad (2.8)$$

where:  $S$  denotes the surface of the “celestial sphere” such that  $dS$  contains the discrete source giving rise to  $dE_\nu(\mathbf{r})$ ; and  $\mathcal{E}_\nu(\mathbf{R})$  gives the distribution of electric fields on the surface of the celestial sphere. For the purposes of imaging, a celestial sphere of radius  $R$  is equivalent to the external universe (see Figure 2.7b.).

The superposed magnitude of the induced field at  $\mathbf{r}$  at distance  $R$  from all sources is then given by:

$$E_\nu(\mathbf{r}) = \int_S \mathcal{E}_\nu(\mathbf{R}) \frac{e^{2\pi i \nu |\mathbf{R}-\mathbf{r}|/c}}{|\mathbf{R}-\mathbf{r}|} dS. \quad (2.9)$$

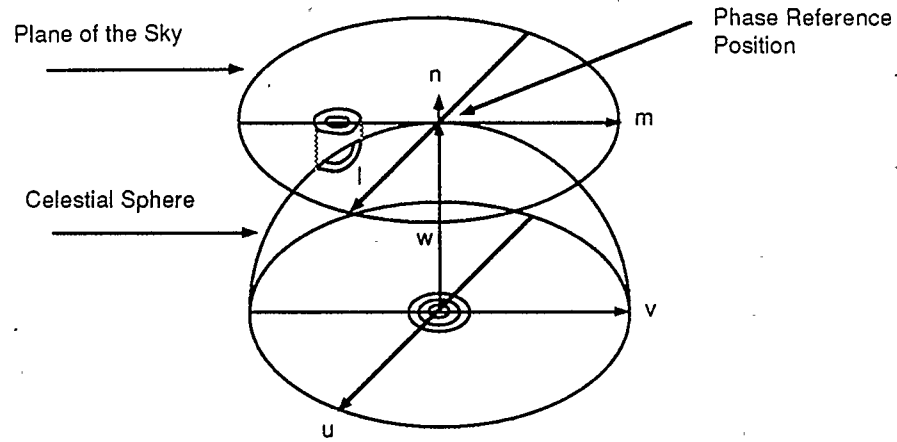
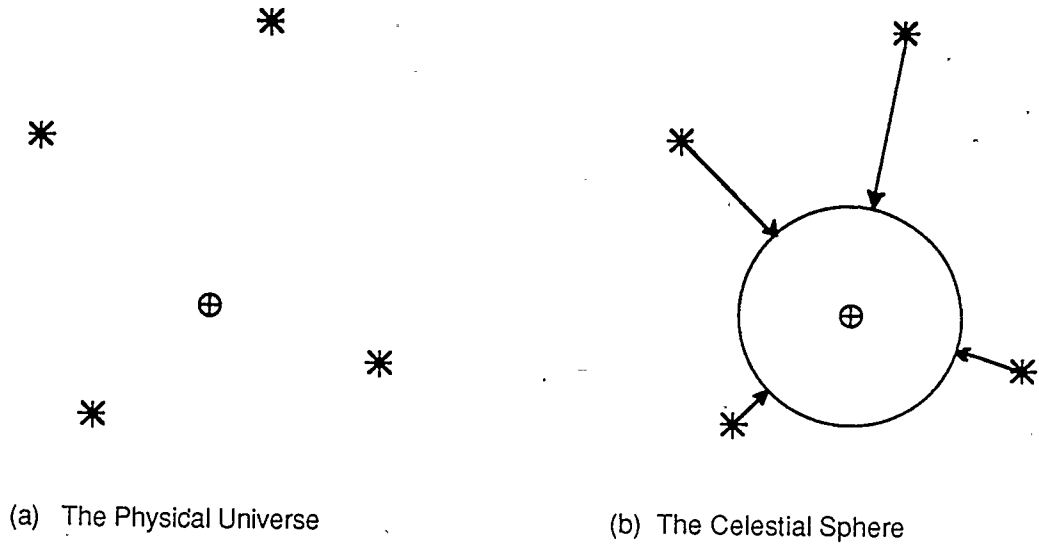
Substituting Equation 2.9 into Equation 2.7 one obtains:

$$V_\nu(\mathbf{r}_1, \mathbf{r}_2) = \langle \int_{S_1} \int_{S_2} \mathcal{E}_\nu(\mathbf{R}_1) \mathcal{E}_\nu^*(\mathbf{R}_2) \frac{e^{2\pi i \nu |\mathbf{R}_1-\mathbf{r}_1|/c}}{|\mathbf{R}_1-\mathbf{r}_1|} \frac{e^{-2\pi i \nu |\mathbf{R}_2-\mathbf{r}_2|/c}}{|\mathbf{R}_2-\mathbf{r}_2|} dS_1 dS_2 \rangle. \quad (2.10)$$

All known astronomical objects, with the possible exception of pulsars and maser line sources are believed to spatially incoherent. Under the assumption of spatial incoherence,  $\langle \mathcal{E}_\nu(\mathbf{R}_1) \mathcal{E}_\nu^*(\mathbf{R}_2) \rangle = 0$  for  $\mathbf{R}_1 \neq \mathbf{R}_2$  and Equation 2.10 may be rewritten as:

$$V_\nu(\mathbf{r}_1, \mathbf{r}_2) = \int_S \langle |\mathcal{E}_\nu(\mathbf{R})|^2 \rangle |\mathbf{R}|^2 \frac{e^{2\pi i \nu |\mathbf{R}-\mathbf{r}_1|/c}}{|\mathbf{R}-\mathbf{r}_1|} \frac{e^{-2\pi i \nu |\mathbf{R}-\mathbf{r}_2|/c}}{|\mathbf{R}-\mathbf{r}_2|} dS. \quad (2.11)$$

Notice here that integration over  $S_1$  has had the effect of identifying  $\mathbf{R}_1$  with  $\mathbf{R}_2$  so that both may now be represented as  $\mathbf{R}$ . A number of simplifications and “approximations” may be made in Equation 2.11. The unit vector  $\mathbf{R}/|\mathbf{R}|$  may be designated



(c) Plane of the Sky

Figure 2.7: Imaging Coordinates

$s$ ; and  $I_\nu(s)$  may be written for the observed intensity  $|\mathbf{R}|^2 \langle |\mathcal{E}_\nu(s)|^2 \rangle$ . The identification of  $I_\nu(s)$  with  $|\mathbf{R}|^2 \langle |\mathcal{E}_\nu(s)|^2 \rangle$  arises from the fact that the observable intensity of an electromagnetic wave is given by its time averaged Poynting vector flux and this flux, for the case of a spherical, harmonic solution to the wave equation is given by  $\langle S \rangle = |\mathbf{R}|^2 \langle |\mathcal{E}_\nu(s)|^2 \rangle$  (to within a multiplicative constant which is traditionally absorbed into  $\mathcal{E}_\nu(s)$ ). To further simplify Equation 2.11, terms of order  $|r|/|\mathbf{R}|$  may be ignored in the far field approximation and it is useful to designate the integration over an angular element,  $dS = R^2 d\Omega$ . Equation 2.11 becomes:

$$V_\nu(\mathbf{r}_1, \mathbf{r}_2) = \int_{4\pi} I_\nu(s) e^{-2\pi i \nu \mathbf{s} \cdot (\mathbf{r}_1 - \mathbf{r}_2)/c} d\Omega. \quad (2.12)$$

The practical application of Equation 2.12 requires the introduction of a coordinate system. Define a "unit" of measurement as the radius of the celestial sphere,  $R$  in order that displacements may be measured on the celestial sphere in radians. Select a point on the celestial sphere in direction  $\hat{w}$  and designate this point the "phase reference position". Define two mutually perpendicular unit vectors  $\hat{u}$  and  $\hat{v}$  which are both perpendicular to  $\hat{w}$ . Directions of observation  $\mathbf{r}$  are given in terms of  $\hat{u}, \hat{v}$  and  $\hat{w}$  by coordinates  $(u, v, w)$  measured in wavelengths. Positions on the celestial sphere are given in terms of  $\hat{u}, \hat{v}$  and  $\hat{w}$  by coordinates  $(l, m, n)$  where coordinate variables represent direction cosines. Having defined these coordinates, various substitutions may be made in equation 2.12:  $\mathbf{r}_1 - \mathbf{r}_2 = (u, v, w)$ ;  $\mathbf{s} = (l, m, n)$ ;  $d\Omega = dl dm / n$  where  $d\Omega$  is an element of solid angle on the celestial sphere; and  $n^2 = \sqrt{1 - l^2 - m^2}$  is an identity of direction cosines. Thus,

$$V_\nu(u, v, w) = \int_{-\infty}^{\infty} \int_{-\infty}^{\infty} I_\nu(l, m) e^{-2\pi i(ul+vm+w\sqrt{1-l^2-m^2})} \frac{dldm}{\sqrt{1-l^2-m^2}}. \quad (2.13)$$

It is convenient to consider the sites of measurement,  $\mathbf{r}$ , to lie in a plane defined by the vectors  $\hat{u}$  and  $\hat{v}$  because then the  $w$  component of  $\mathbf{r}_1 - \mathbf{r}_2$  becomes zero. This effect is technically achieved by introducing an instrumental delay into the signal of one antenna of a pair before correlation as shown in Figure 2.8. If further, all radiation may be considered to come from a small portion of the celestial sphere, then  $l$  and  $m$  are small and  $\sqrt{1-l^2-m^2} \sim 1$ . Equation 2.13 may then be written:

$$V_\nu(u, v) = \int_{-\infty}^{\infty} \int_{-\infty}^{\infty} I_\nu(l, m) e^{-2\pi i(ul+vm)} dldm. \quad (2.14)$$

Equation 2.14 is essentially the desired equation since Equation 2.6 follows immediately from a Fourier transform. However for practical purposes, two additional factors are introduced such that  $I_\nu(l, m)$  is written  $A_\nu(l, m)I_\nu(l, m)$  and  $V_\nu(u, v)$  is written  $S(u, v)V_\nu(u, v)$ .  $A(l, m)$  is the "primary beam" referred to in the previous section and reflects the fact that radiation arriving from directions other than the pointing center will be weighted by some factor less than unity.  $S(u, v)$  is the sampling function, and it makes explicit the fact that not all points on the " $uv$  plane" are sampled. The practical equation of aperture synthesis may now be written:

$$S(u, v)V_\nu(u, v) = \int_{-\infty}^{\infty} \int_{-\infty}^{\infty} A_\nu(l, m)I_\nu(l, m) e^{-2\pi i(ul+vm)} dldm. \quad (2.15)$$

The " $uv$  plane" is an abstraction which formalizes the fact that in terms of visibility measurements, all antenna pairs of equal separation and orientation are equivalent regardless of their absolute position. Each point on the " $uv$  plane"

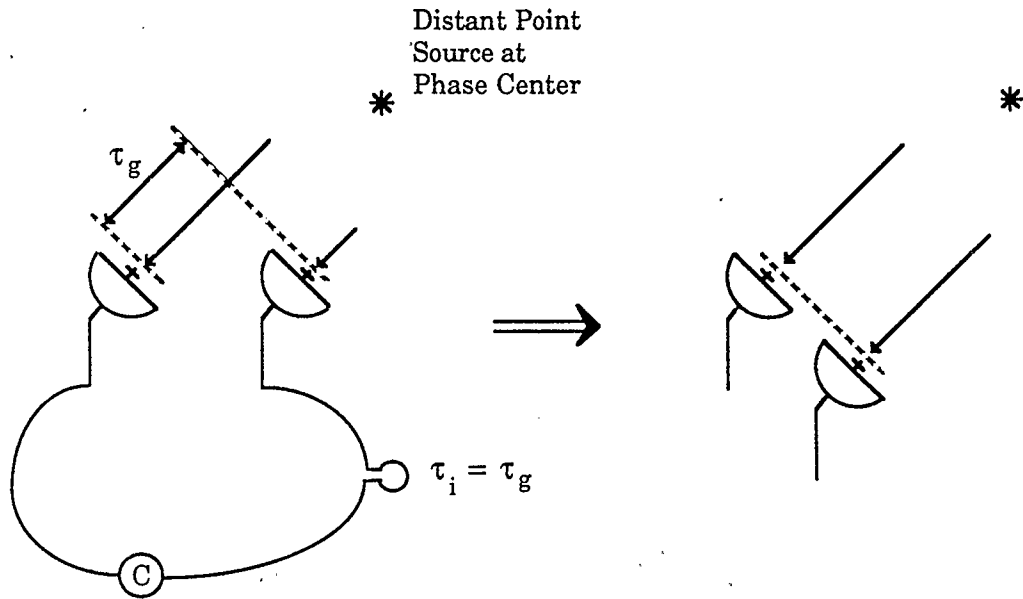


Figure 2.8: Phase Delay in a Simple Interferometer

designates an antenna pair rather than an antenna and the coordinates  $(u, v)$  refer to components of relative antenna separation,  $r_2 - r_1$ , rather than absolute antenna position. The configuration of the array will determine the sampling pattern  $S(u, v)$  on the “ $uv$  plane”, however, the rotation of the earth will cause that pattern to change with time and in effect enhance the “ $uv$  coverage”. Observers must be concerned about “ $uv$  coverage” because the sampling function is discrete and finite and hence images produced by aperture synthesis are not unique. The more complete the coverage on the “ $uv$  plane”, the better constrained becomes the observed intensity distribution on the sky.

From Equation 2.15 the formal definition of the “synthesized beam” of a radio array may be expressed. The synthesized beam is the response of the array to a point source,  $I_\nu(l, m) = \delta_\nu(l, m)$ , located at the array’s pointing center. For such a point source  $V(u, v)$  is constant, and the beam may be expressed:

$$B_\nu(l, m) = \int_{-\infty}^{+\infty} \int_{-\infty}^{+\infty} S(u, v) e^{2\pi i(ul+vm)} dudv. \quad (2.16)$$

As a conclusion to this section, it is well to summarize the assumptions which have been made explicitly and implicitly in deriving Equation 2.6. These assumptions specify the conditions under which the equation is valid. The assumptions are:

1. Observed sources are far away ( $|\mathbf{R}| \gg |\mathbf{r}|$ ).
2. Radiation may be considered to arrive from a small portion of the celestial sphere ( $l, m \ll 1$ ).
3. The space between the points of emission and detection is empty; it was this assumption which enabled the use of Maxwell’s equations for isotropic nonconducting media and led to Equation 2.8.
4. Observed sources are spatially incoherent.
5. Radiation may be considered quasi-monochromatic, *i.e.*  $\Delta\nu/\nu \ll 1$  where  $\Delta\nu$  and  $\nu$  are the bandwidth and frequency of observed radiation respectively. Thus the quantities  $I_\nu$ ,  $V_\nu$ , and  $A_\nu$ , which are all frequency dependent, are well defined.

## 2.4 The Very Large Array

The *Very Large Array* (VLA), at which observations were made for this study, represents one implementation of aperture synthesis. The instrument is a 27 element radio interferometer located on the Plains of San Augustin near Socorro, New Mexico, USA. Each of the 27 Cassegrain type shaped-reflector antennas has an “aperture” of 25 meters and the ability to operate at six separate frequencies: 0.3, 1.5, 5, 8.5, 15 and 22 GHz. The antennas may be moved along rails in a “Y” configuration to a total span of about 36 kilometers (see Figure 2.9). The array is cycled through its four main configurations (A, B, C, D) every 15 months; table 2.1 provides a few general details about the VLA configurations. The VLA supports continuum, polarization, and spectral line work; this study concerns only continuum observations.

To take fullest advantage of the continuum capabilities of the VLA, the scientist wishes to obtain observations at as many wavelengths, and in as many configurations, as possible. Multifrequency data is important in understanding the physical processes underlying the radio emission; it facilitates the calculation of spectral index,  $\alpha$  ( $S_\nu \propto \nu^\alpha$ ) which may help distinguish between thermal (bremsstrahlung) and nonthermal (*e.g.* synchrotron) emission, between optically thick and optically thin emission, and between various processes of mass loss. Multiconfiguration data is useful in improving the “ $uv$  coverage” (see Section 2.3) of observations. Observations in A configuration, for instance, sample selectively the larger ( $u, v$ ) values and hence provide the best information about small scale structure (resolution =  $\theta \sim \lambda/D$ , see Section 2.2). Observations in D configuration sample the smaller

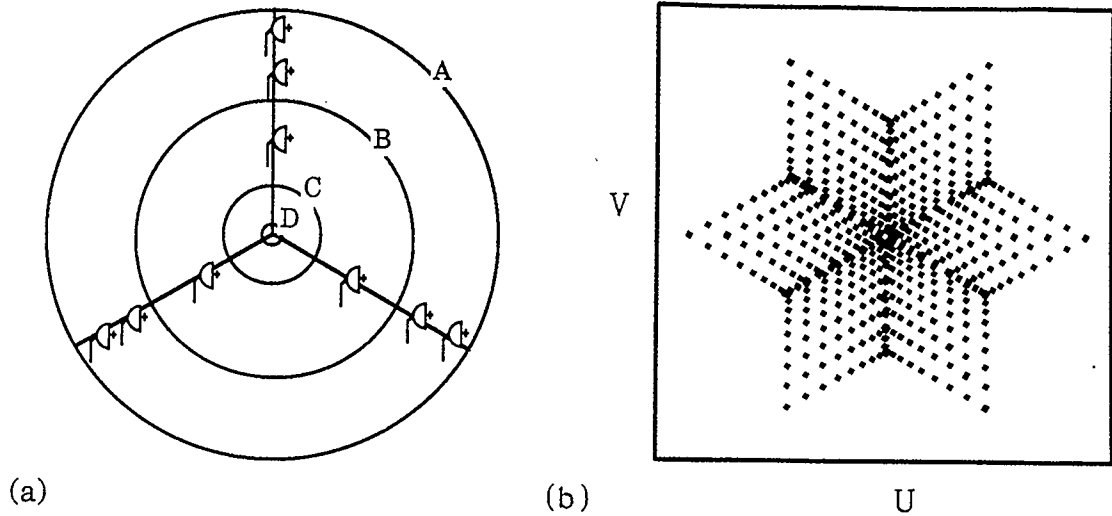


Figure 2.9: VLA Configurations and Instantaneous “UV Coverage”  
 Figure (a) illustrates the relative extents of the various VLA configurations (A,B,C,D) in real space. In each configuration, nine antenna are placed along each arm. Figure (b) shows the instantaneous pattern described by the VLA in the  $uv$  plane. Each point in the  $uv$  plane corresponds to the spacing and orientation of one antenna pair. The distinctive six pointed star arises from reflecting each branch of the VLA ‘Y’ pattern through the origin.

$(u, v)$  values and consequently yield the the best information about large scale structure.

As a further *desirable*, the observer wishes the integration time on source of his observations to be as long as possible. The sensitivity of observations improves with the square root of the integration time. Quantitatively, the sensitivity may be expressed as the *root mean square* (rms) system noise, given by the equation:

$$S_{rms} \simeq \frac{K_\nu}{\sqrt{N(N-1) \Delta t n \Delta f}} \text{ [mJy/beam]} \quad (2.17)$$

where:  $N$  is the number of antennae;  $\Delta t$  is the integration time on source in hours;  $\Delta f$  is the bandwidth in MHz (=50);  $n$  is the number of *intermediate frequency* (IF)

CONFIG	$B_{max}$ [km]	$B_{min}$ [km]	APROX HPBW ["]			
			1.5 GHz	5 GHz	15 GHz	22 GHz
A	36.4	0.68	1.4	0.4	0.14	0.08
B	11.4	0.21	3.9	1.2	0.4	0.3
C	3.4	0.063	12.5	3.9	1.2	0.9
D	1.03	0.04	44	14	3.9	2.8

Table 2.1: VLA Configurations

In the above table  $B_{max}$  and  $B_{min}$  are the maximum and minimum antenna pair separations respectively. HPBW refers to the *Half Power Beam Width* of the synthesized beam,  $B(l, m)$ .

pairs as defined below; and  $K_\nu$  is a constant which depends upon the frequency of observations ( $K_{1.5GHz} = 10$ ;  $K_{5GHz} = 7.4$ ,  $K_{15GHz} = 19$ ;  $K_{22GHz} = 33$ ). The constant  $K$  can be expressed in terms of the system temperature,  $T_{sys}$ , and the system efficiency  $\eta$  for any given frequency:  $K = 0.082T_{sys}/\eta$ . Table 2.2 summarizes the sensitivity information of the VLA.

In rough detail, the VLA performs continuum observations as follows. All 27 telescopes are pointed toward a selected source to within an accuracy of better than 15". Antenna voltages are amplified, modulated, and transmitted to a central control room where each pair of signals is correlated, and averaged over some interval (typically 10-30 s), to produce estimated complex visibilities  $V(u, v, t)$ . Following correlation, gain corrections are applied to correlator outputs so that the complex visibilities are made to reflect the fourier transform of the sky's intensity distribution. An on-line editing facility removes data which is known to be corrupt for any reason. The data is now in the form in which the observer receives it.

But the observer obtains really twice as much data as suggested above. Each

FREQUENCY [GHz]	$T_{sys}$ [K]	SENSITIVITY (RMS) [mJy]	PRIMARY BEAM [']	DYNAMIC RANGE
15	60	0.13	30	50
5	50	0.09	9	70
15	116	0.24	3	10-20?
22	350	0.88	2	10?

Table 2.2: VLA Sensitivity Information

Information in the above table is taken from the VLA Observational Status Report, December 1988. Sensitivity is expressed as *root mean square* (rms) values based upon a ten minute observation. Primary beam values are quoted as *Half Power Beam Width* (HPBW); see Figure 2.1. Dynamic range is defined as the best possible signal to noise ratio achievable before self calibration. Self calibration is discussed in section 3.3.

antenna collects data along two independent channels (A/C and B/D) separated in frequency by 50 MHz. The A/C and B/D channels are referred to as *intermediate frequency* (IF) pairs. The result of having two IFs is to double the size of the data set and hence to reduce the rms noise by a factor of  $\sqrt{2}$  according to Equation 2.17.

## Chapter 3

### OBSERVATIONS AND DATA REDUCTION

The previous two chapters discussed the observational and theoretical topics appropriate to this radio study of AG Pegasi. This chapter will describe the details through which antenna voltages measured at the *Very Large Array* (VLA) were used to produce images of AG Pegasi. The images and the quantities derived from them will also be presented.

#### 3.1 Schedule of Observations

The schedule of individual observations is given in table 3.1. The table provides specific information about each observation, including the integration time on source and the number of visibility points obtained. The observations were taken at four frequencies (1.5, 5, 15 and 22 GHz) and in all four main configurations of the VLA. Some observations took place in "hybrid" configurations: transition arrangements between main configurations. The observations spanned approximately 1000 days, during which time observations were conducted at nine epochs. The VLA went through the complete sequence of its configurations twice during this period, allowing observations to be made with a wide range of resolutions. Note that on 22 November 1984 and 27 July 1987 very sensitive observations were made at 5 GHz (109,000 visibility points) while the VLA was in 'A' configuration (maximum resolution).

DATE OF OBSERVATION	JULIAN	CONFIG	BAND [GHz]	T [min]	VIS $\times 10^{-3}$
8 Nov 84	6012	A	1.5	10	12
			5	15	16
			15	25	29
			22	40	55
22 Nov 84	6026	A	5	80	109
3 May 85	6188	B	1.5	20	27
			5	20	27
			15	35	47
			22	60	83
21 Aug 85	6298	C	1.5	15	20
			5	12	16
			15	20	28
			22	40	56
7 Nov 85	6376	D	5	15	21
			15	25	34
			22	40	53
14 Feb 86	6475	D→A	1.5	15	17
			5	15	17
			15	20	26
			22	35	46
13 Oct 86	6716	B→C	1.5	20	27
			5	16	22
			15	40	56
			22	50	64
25 Jan 87	6820	C→D	1.5	20	22
			5	20	23
			15	20	27
			22	40	51
30 Apr 87	6915	D	1.5	20	25
			5	20	22
			15	20	27
			22	30	40
27 Jul 87	7003	A	1.5	20	27
			5	80	109
			15	55	74

Table 3.1: Schedule of Observations

In this table,  $T$  is the time on source and VIS is the number of visibilities.

### 3.2 Calibration

The aim of calibration is to determine the absolute flux densities associated with the output from each correlator. This is accomplished by measuring the instrumental phase and amplitude differences per antenna pair, *i.e.* the response to a point source. For a strong point source of known flux,  $S_\nu$ , the correlated output from any two antennas should be given by:

$$V_{jk} = S_\nu e^{i2\pi\nu(\mathbf{r}_j - \mathbf{r}_k) \cdot \mathbf{s}/c} \quad (3.1)$$

where  $\mathbf{r}_j - \mathbf{r}_k$  is the base vector between antennas  $j$  and  $k$  and  $\mathbf{s}$  is the direction of the source. If the measured output does not agree with Equation 3.1, complex calibration factors  $C_{jk}(t)$  have to be introduced so that  $C_{jk}(t)V_{jk}$  agrees in amplitude and phase with the theoretically expected value of the visibility function. In practice, the net effect of calibration at the VLA is to produce a gain table which assigns to each antenna a time dependent complex gain (amplitude and phase).

Two levels of calibration are performed before a gain table is finalized: a time dependent gain calibration of amplitude and phase and; an absolute flux calibration which establishes the absolute scale of measurements. The time dependent calibration is performed with the aid of a point radio source called the “phase calibrator”. This calibrator must be located in the same vicinity of the sky as the desired source so that appropriate treatment is given to the transmission characteristics of the atmosphere. Observations of the phase calibrator take place at intervals during the observations of the desired source and occupy about 25% of the observing time. For a point source located at the phase centre, each correla-

tor should give the same visibility amplitude; therefore the relative gains of each correlator may be determined from the phase calibrator. If the absolute flux of the phase calibrator were known, absolute gains could be assigned at this stage. In general, however, the flux densities of phase calibrators vary from day to day. Therefore, a second level of calibration is necessary in which the absolute flux of the phase calibrator is established by reference to an "absolute flux calibrator". Ordinarily the absolute flux calibrator will be observed only once, at the beginning of a given observing run. The phase calibrator for the AG Pegasi observations was the radio source 2136+141 and the absolute flux calibrator was 3C286.

### 3.3 Image Processing

Image processing for the present study was accomplished using the *Astronomical Image Processing System* (AIPS) distributed by the *National Radio Astronomy Observatory* (NRAO). The "tasks" which were employed are standard and are adequately explained in the AIPS Cookbook (1986). This section will briefly review the approach taken to the AG Pegasi data base and explain the principles underlying the various steps.

#### Editing

VLA data may be edited on three levels. The first level is the on line editing of the VLA itself as previously noted. Second level editing may take place at the calibration stage. At this stage the observer may inspect his data by correlator and by time interval and flag suspect entries. Data from a correlator is considered suspect if it varies significantly from entries for other correlators expected

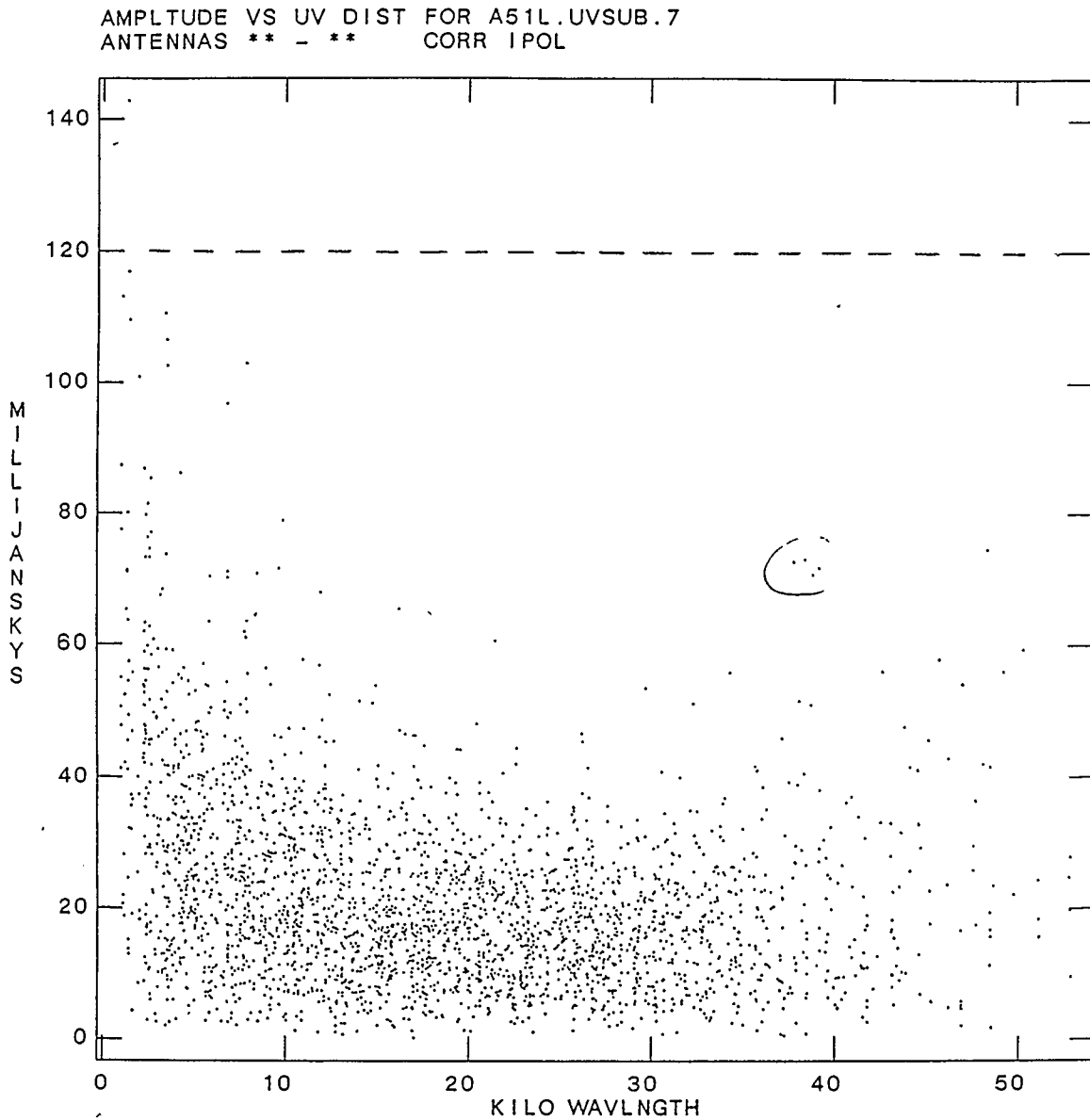


**Figure 3.1: Inspection of Visibility Amplitudes**

The AIPS task "UVPL" permits the observer to inspect his data to decide if some portion of it should be flagged. In the above figure every 28th visibility point has been plotted. The circled visibilities are suspect and should be investigated. Because erratically large visibility points sometimes find their way into data sets, it is common to clip visibilities above the  $5\sigma$  level (indicated approximately by the dotted line above).

theoretically to have similar response. Such entries stand out readily when data is tabulated for correlators by antenna. Further, most bad data is associated with individual antennae rather than correlators themselves; hence an antenna may be confirmed as providing a bad signal if many correlators to which it is connected exhibit irregular results. Bad data may arise from: radio interference both internal and external; electronics and signal transmission errors; mechanical malfunction (*e.g.* steering mechanisms for reflectors); and atmospheric irregularities (for long baselines, atmospheric variations may be very different for the two antennas of a pair).

Finally, editing may occur during image processing. AIPS permits the user to inspect his data visually, (see Figure 3.1) and decide if some portion of it should be flagged as bad. Tasks exist in AIPS to: identify portions of data by correlator; flag data by correlator or by antenna; and clip data above a given amplitude from a given range of uv distance.

## Mapping

Equation 2.15 provides the basis for creating images from visibility data. However, a number of approximations and options exist in the mapping process. As a first step in imaging, the data is ordinarily "gridded" to take advantage of the extreme efficiency of the *Fast Fourier Transform* (FFT) algorithm; this algorithm requires a regular rectangular matrix of points (see Figure 3.2). Having gridded the data, a weight may be assigned to the gridded points in a number of ways. Uniform weighting is defined by  $W_k = 1$  and natural weighting by  $W_k = N_k/N$  where  $W_k$  is the weight assigned to the  $k$ th gridded point,  $N_k$  is the number of visibility points

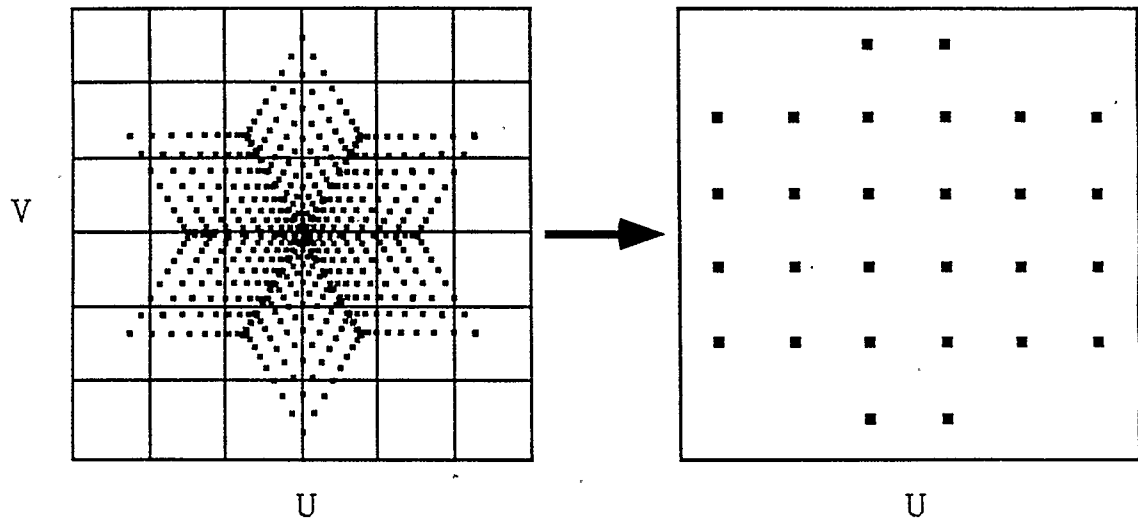


Figure 3.2: **Weighting of Visibility Data**

Visibility points in the  $uv$  plane are gridded in order to make use of the *Fast Fourier Transform* (FFT) algorithm. Visibilities are interpolated to give one gridded point at the center of each grid square. Weight may be assigned equally to each gridded point (uniform weighting) or in proportion to the number of visibility points laying within the grid square (natural weighting).

originally occupying the  $k$ th grid square, and  $N$  is the total number of visibility points. For a given data set the uniform image will in general have better resolution and the natural image will have better signal to noise ratio. This dichotomy arises because the VLA samples large  $(u, v)$  values less densely than small ones for any given configuration (see Figure 2.9b). Hence uniform weighting provides better resolution because gridded points corresponding to larger  $(u, v)$  values (smaller scale structure) are weighted the same as gridded points corresponding to smaller  $(u, v)$  values. The uniform map will, however, be expected to have a lower signal to noise ratio than the natural map because gridded points corresponding to larger  $(u, v)$  values will have larger uncertainties; they are constrained by fewer original visibility points.

### Deconvolving Images

Imaging as describe above produces “dirty” images. They are dirty in the sense that they will have defects associated with limited sampling of the  $uv$  plane. Along with the image itself, mapping routines produce a “beam”. In this context, “beam” is defined as the imaged response of a 1 *Jansky* (Jy) point source located at the phase center of the array; that is, the fourier transform of the array’s sampling function (Equation 2.16,  $B(l, m)$ ). The beam which is produced before any deconvolution takes place is referred to as the “dirty beam”. The aim of deconvolution is to remove the “dirty” characteristics from the dirty image by replacing  $B(l, m)$  by a well behaved function such as a Gaussian. This is accomplished by iteratively locating the map points of maximum intensity and subtracting, at those points, the beam  $B(l, m)$  multiplied by the peak intensity (in Jy). This process results

in: a list of locations and intensities, known as the “clean components”; and a “residual map” which includes whatever is left over once the clean components have been subtracted from the dirty map. A “clean beam” is then created by fitting the central region of the dirty beam with an appropriate model (usually a two dimensional Gaussian). The clean components are then convolved with the clean beam and returned to the residual map to yield the “cleaned” map. The entire process of deconvolution is often referred to as “cleaning a map”.

Of the two AIPS tasks capable of performing deconvolution (*i.e.* MX and APCLN), MX is preferred. It has the considerable advantage of subtracting clean components from the *ungridded* visibility data. By doing so it avoids various errors associated with gridding and aliasing noise.

### Phase Center Shifting

The method of visibility modelling employed with the AG Pegasi data base assumes that the desired source is located at the phase center of the array when observations were taken. The effect upon visibility curves of imperfect alignment of sources with the phase center is discussed in Aaquist (1985). To achieve alignment in the the AG Pegasi data sets a “shift” of the phase center was generally required. The amount and direction of the shifts were determined from deconvolved images.

### Removal of Contaminating Sources

In tight configurations (C and D) and at low frequencies (particularly 1.5 GHz) many sources were detected in the field of observation. This circumstance arose both because larger fields are being mapped ( $\theta \sim \lambda/D$ ) and because extragalactic sources, which constitute the vast majority of confusing sources, have generally

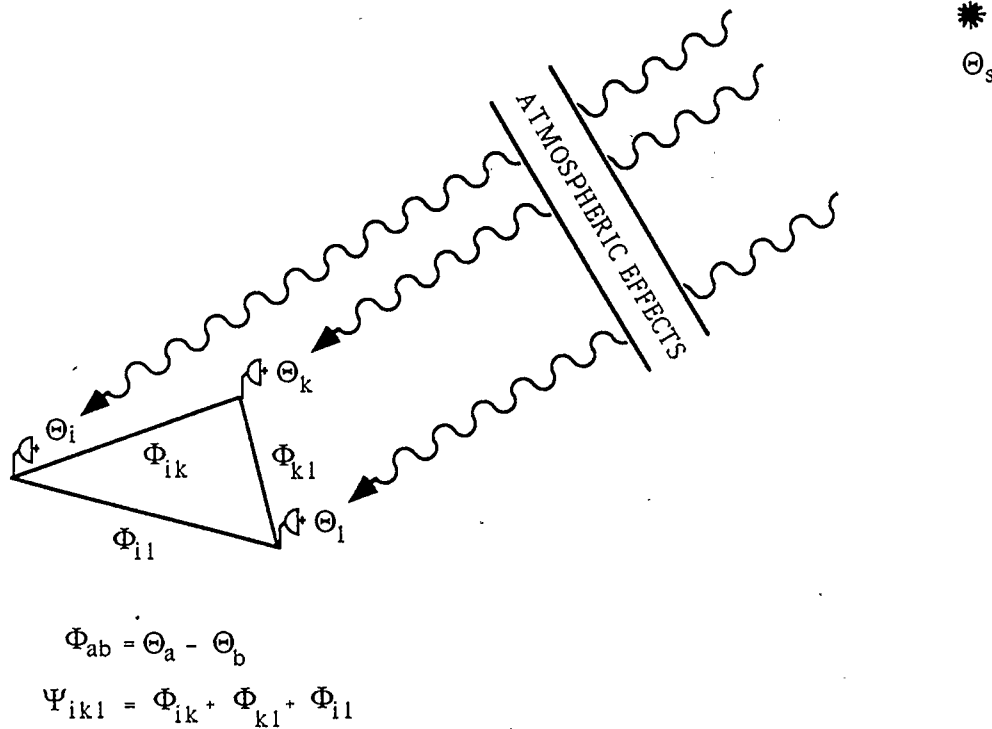


Figure 3.3: Closure Phase

higher flux at lower frequencies. In many applications, it is sufficient to simply “clean” these extraneous sources along with the source of interest. When visibility data is to be modelled, however, it is desired that the source of interest be treated in isolation and hence extraneous sources should be removed from the visibility data. In general, the procedure followed with the AG Pegasi data sets was to map the contaminating sources in individual fields using MX and to subtract their clean components from the visibility data set.

### Self Calibration

Considerable improvement in the signal to noise ratio of a mapped data set may be achieved through phase self calibration. The principle behind this calibration

is that, for a given set of three antennas, a well defined relationship exists between the phases of the wavefronts received at each antenna (see Figure 3.3). The salient quantity is termed the “closure phase” and is defined as  $\Psi_{ikl} = \phi_{ik} + \phi_{kl} + \phi_{li}$ , where  $\phi_{ab}$  denotes the observed phase difference between antennas  $a$  and  $b$ . The observed phases  $\theta$  are related to the true phases  $\psi$  by a phase noise term,  $\epsilon$ , such that  $\phi_{ab} = \psi_{ab} + \epsilon_{ab}$ . It follows directly from this identity and the definitions of  $\Psi$  and  $\phi$  (Figure 3.3) that  $\Psi$  must be zero and is hence independent of the phase errors,  $\epsilon$ . The closure phases therefore provide an array of linear equations for the determination of the true phases  $\psi$  from observed phase  $\phi$ . They provide a means through which lost phase information may be recovered. At the VLA it may be argued that there are 324 unique closure phases (Pearson and Redman, 1984) while there are 351 baselines. Therefore the closure phase information does not completely constrain the values of  $\psi$ . To carry out self calibration at the VLA, an approximate image of the source must be used in conjunction with the visibility data.

### 3.4 Results

The combined multiconfiguration, multifrequency observations obtained for this study yielded maps of the circumstellar material of AG Pegasi at various resolutions. Figures 3.4 to 3.6 present images at resolutions from 0.3" to 10". It should be noted that these images represent “average” pictures of AG Pegasi over the period of observations since they are produced from concatenated data sets from all epochs. In addition to the concatenated images shown here, individual

images for each epoch and each frequency were also made. Data for Figures 3.4 to 3.6 was concatenated in order to improve both the signal to noise ratio (Equation 2.17) and the  $uv$  coverage. At the bottom of each figure, the contour levels of the image are given as “LEVS” and a peak intensity of the image is given as “PEAK FLUX”. The unit of intensity used here and throughout radio astronomy is the *milliJansky/beam* (mJy/b), where the beam is considered to define a unit of solid angle. Dashed lines on the images designate negative contours. Scattered, irregular contours surrounding the principle object in each image are merely noise, and are plotted to give the reader an idea of the noise level of the map. A black ellipse is located in the top right hand corner of each image; it designates the synthesized beam corresponding to the image. As previously noted (Figure 2.3) the beam provides a measure of the resolution of an image.

In Figure 3.4, the concatenated data sets at 5 GHz have been used to produce a uniformly weighted map. Features to note may be listed briefly.

- An unresolved source, to be designated the “central object”, exists at the centre of the image. Its angular size is  $< 0.3''$  which is the HPBW of this image. Since the central object is also unresolved for individual maps of higher resolution (22 GHz), an upper limit of  $0.1''$  is determined for the source. The 5 GHz flux of this object is  $\sim 1.2$  mJy.
- A largely spherically symmetric nebulosity, to be designated the “inner nebula”, surrounds the central object.
  - Its angular size is  $2''$ . Note, in reference to the images, that declination is given in degrees, minutes and seconds of arc while right ascension is

given in hours, minutes and seconds of time.

- Lobe enhancements are manifest in N-S to NW-SE directions. Note that in astronomical images the top edge is north, as expected, but the right edge is west rather than east, as would be expected on a terrestrial map.

In Figure 3.5, the concatenated data sets at 1.5 GHz have been used to produce a uniformly weighted map. The beam is approximately three times larger in this image than in Figure 3.4. Features to note may be listed briefly.

- The central object and inner nebula appear to form a single, central source in this image, and that source is only barely resolved. This is due to the fact that the beam of 1" is only barely sufficient to resolve the inner nebula.
- Diffuse emission, to be designated the "intermediate nebula" surrounds the inner two objects.
  - This nebula is apparently spherically symmetric to a reasonable degree although it appears somewhat more extended in NW-SE directions.
  - The level of emission is very near the noise level of the map.

In Figure 3.6, the concatenated data sets at 1.5 GHz have been used to produce a naturally weighted map. The beam is approximately ten times larger in this image than in Figure 3.5 and thirty times larger than in Figure 3.4. It will be noted that Figure 3.6 is made from the same data set as Figure 3.5 only the weighting function is different. A discussion of the comparative merits of uniform and natural weighting was discussed in Section 3.3 under "Mapping". The effect of changing the weighting function is particularly well pronounced in this case because of the

differences in  $uv$  coverage in the visibility data sets which were combined. Features to note may be listed briefly.

- The intermediate nebula, the inner nebula, and the central object appear as a single, barely resolved source.
- Two bipolar features of total extent  $1'$  exist in NW-SE directions, and will be designated the “outer nebula”.
  - These bipolar features are unresolved, or barely resolved and hence may be considered to have “radius”  $\lesssim 5''$  which is half of the HPBW of this image.
  - The combined flux of these features is  $\sim 4$  mJy.

Only the central object and the inner nebula had been detected before this study (Section 1.2.3). The intermediate and outer nebulae are new discoveries.

Figures 3.4 to 3.6 are replotted in Figure 3.7 to give an impression of their relative scales and of the morphology of the system. It may be noted that if the binary separation ( $\sim 1$  *astronomical unit* (au) =  $1.5 \times 10^{13}$  cm) were plotted, it would subtend an angle of  $0.002''$ , many orders of magnitude smaller than the nebulae being considered here.

Apart from a general discussion of the morphology of AG Pegasi suggested in Figure 3.7, this study will concentrate largely upon the inner nebula and the central object. Most individual observations provided good information about these two nebulae, but were not sensitive enough to detect the intermediate and outer nebulosities shown in the top two images of Figure 3.7. By far the best information

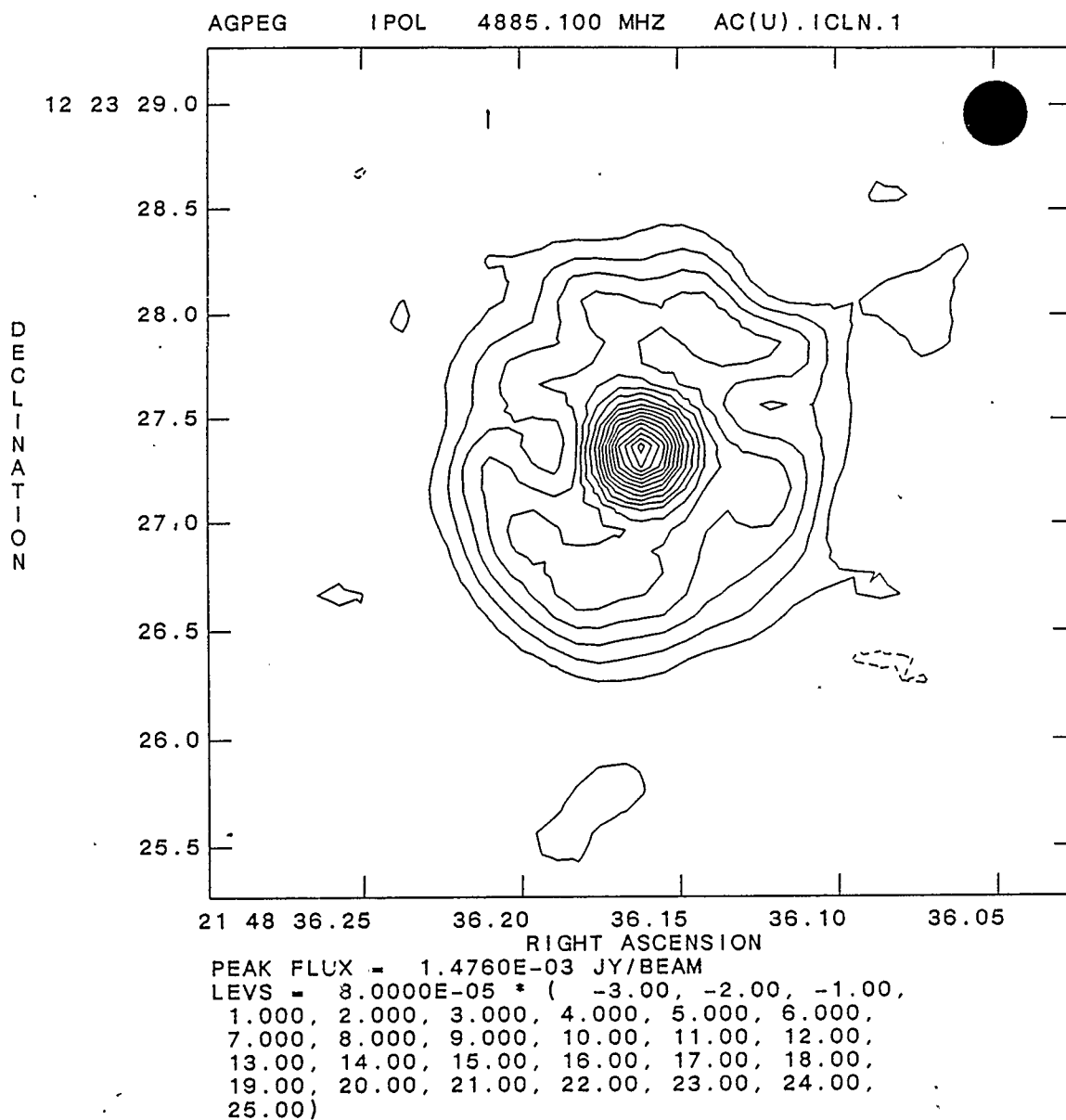
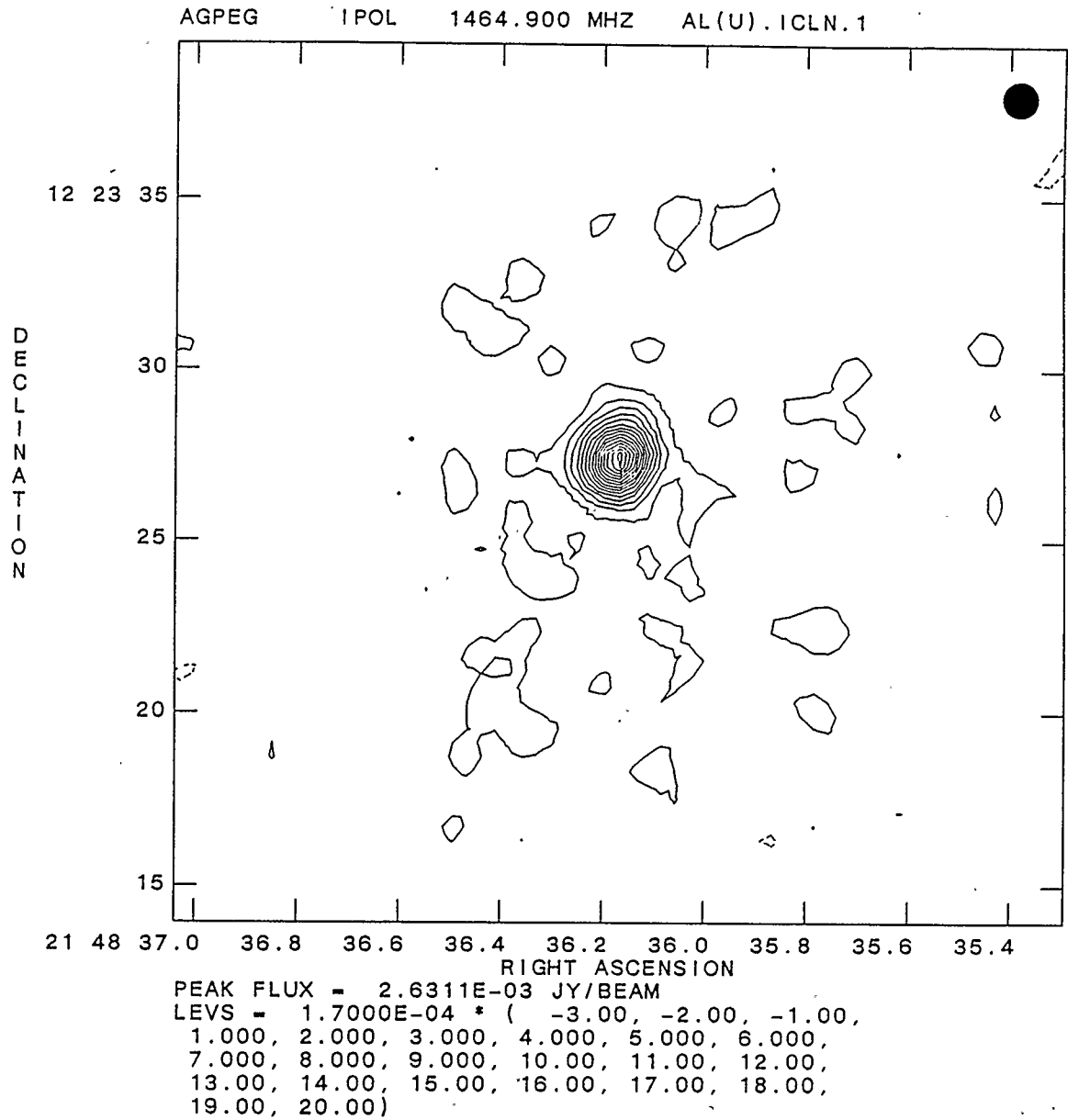
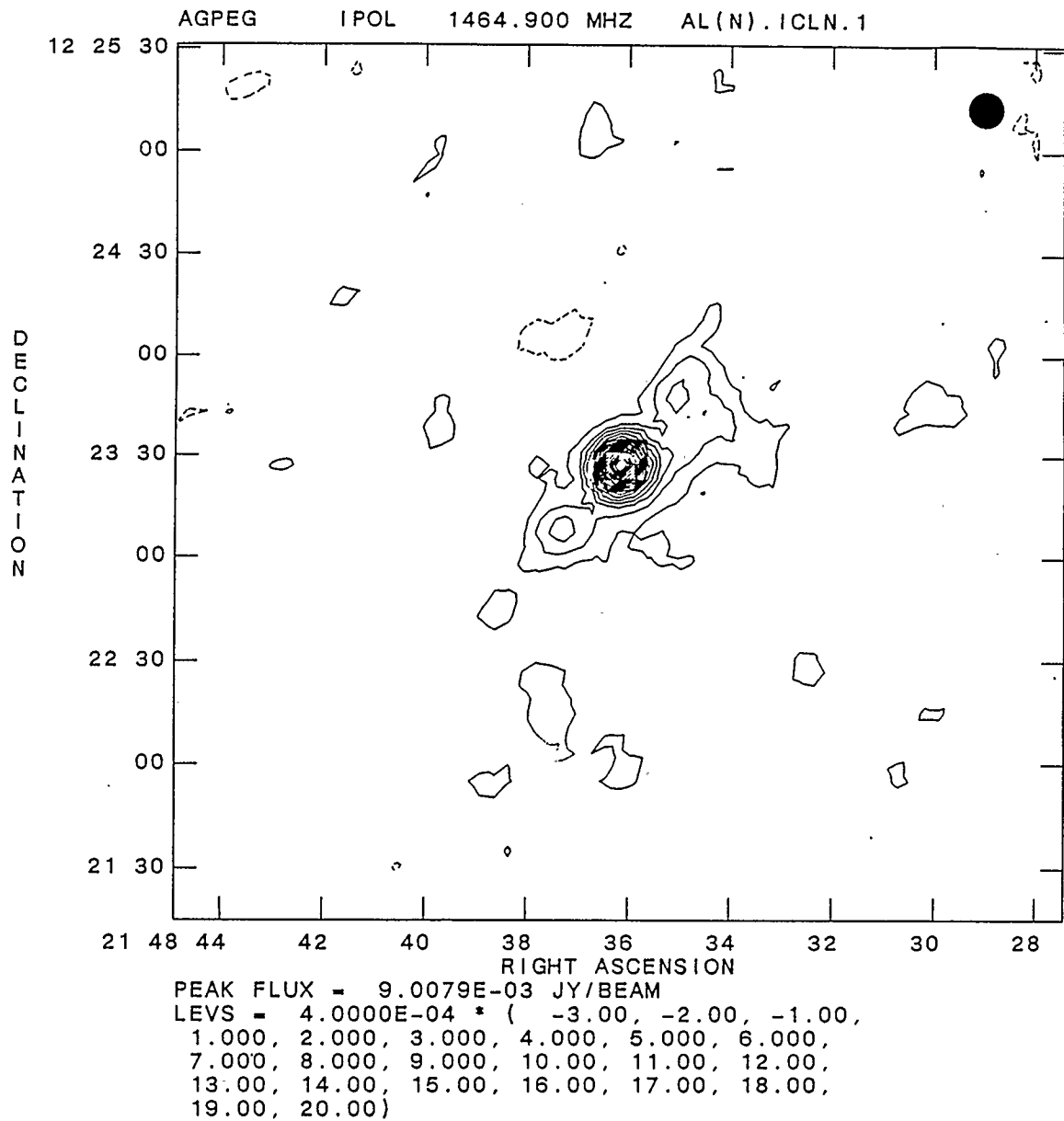


Figure 3.4: AG Pegasi: Concatenated 5 GHz Data Sets

The above image was produced from the combined 5 GHz data from all epochs. Uniform weighting was applied. Beam size is indicated in the top right hand corner.



**Figure 3.5: AG Pegasi: Concatenated 1.5 GHz Data Sets (Uniform)**  
 The above image was produced from the combined 1.5 GHz data from all epochs. Beam size is indicated in the top right hand corner.



**Figure 3.6: AG Pegasi: Concatenated 1.5 GHz Data Sets (Natural)**  
 The above image was produced from the combined 1.5 GHz data from all epochs. Beam size is indicated in the top right hand corner.

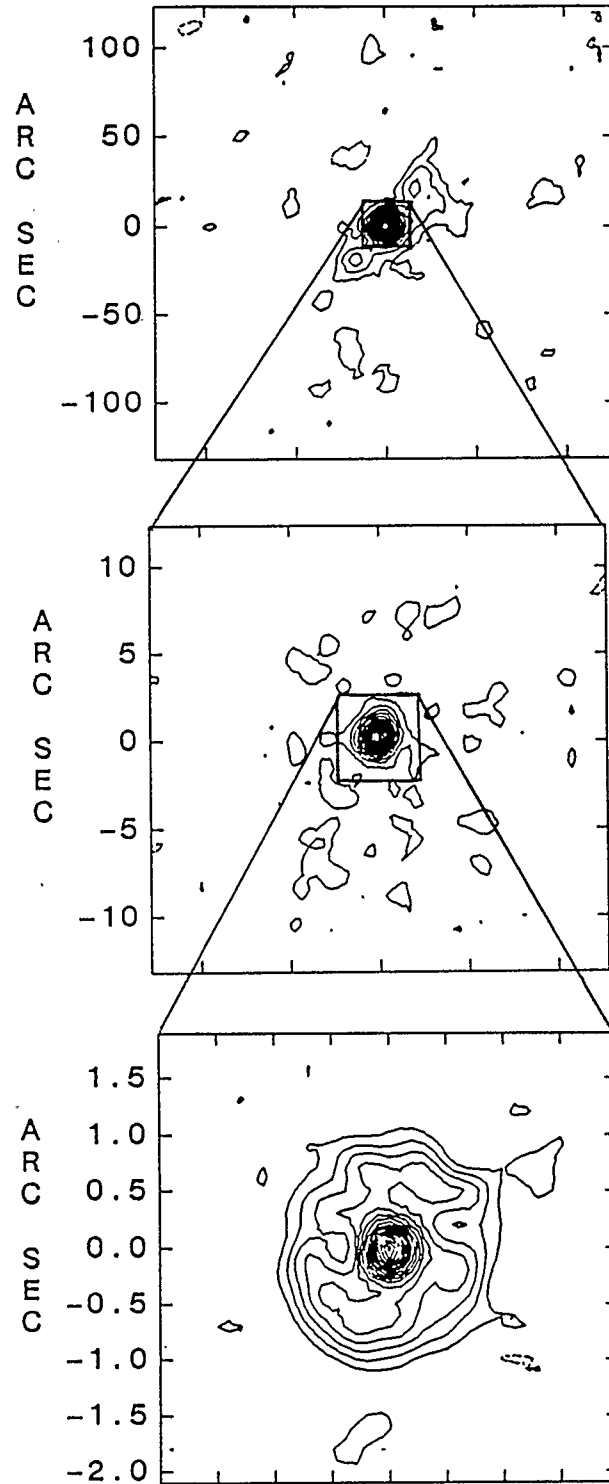


Figure 3.7: Morphology of AG Pegasi

The above images of AG Pegasi are reproduction of Figures 3.4 to 3.6 organized to show the relative scale of the various components of nebular emission. The center of each map is RA 21 48 36.164, DEC 12 23 27.42.

about the inner nebula came from the high sensitivity, A configuration, 5 GHz observations from 11-84 and 7-87. Figure 3.8 presents the uniformly weighted images from these epochs while Figure 3.9 presents the naturally weighted images. It is obvious that a number of developments have taken place between the two epochs. The 1987 images seem to have lost some of the spherical symmetry apparent in 1984. The lobe enhancements ( $\sim$  NW and SE) which are apparent in both epochs seem to have become more pronounced in 1987. It is also obvious that the total flux has increased from 1984 to 1987 and that some manner of expansion has taken place. The analysis of the next chapter will attempt to put these characteristics upon a quantitative footing.

Although images were produced for all observations listed in table 3.1, those not presented above are largely point-like in nature. Most of these images are point-like because their resolution was not sufficient to resolve the inner nebula (more compact arrays). Others, at 15 and 22 GHz had such high resolution that the inner nebula was resolved away. By "resolved away" is meant that the beam size was so small that the flux detected per beam was below the *rms* (root mean square) sensitivity. The individual 1.5 GHz observations which carried information about the intermediate and outer nebula were too noisy to produce high quality maps of these two additional features independently; that is why the data sets from all epochs were concatenated to produce Figures 3.5 and 3.6. The remaining images are well represented by their mapping parameters, and outputs from a few standard AIPS tasks. These results are given in Appendix A. Appendix B provides information about the contaminating sources which were removed from various data sets of the AG Pegasi data base.

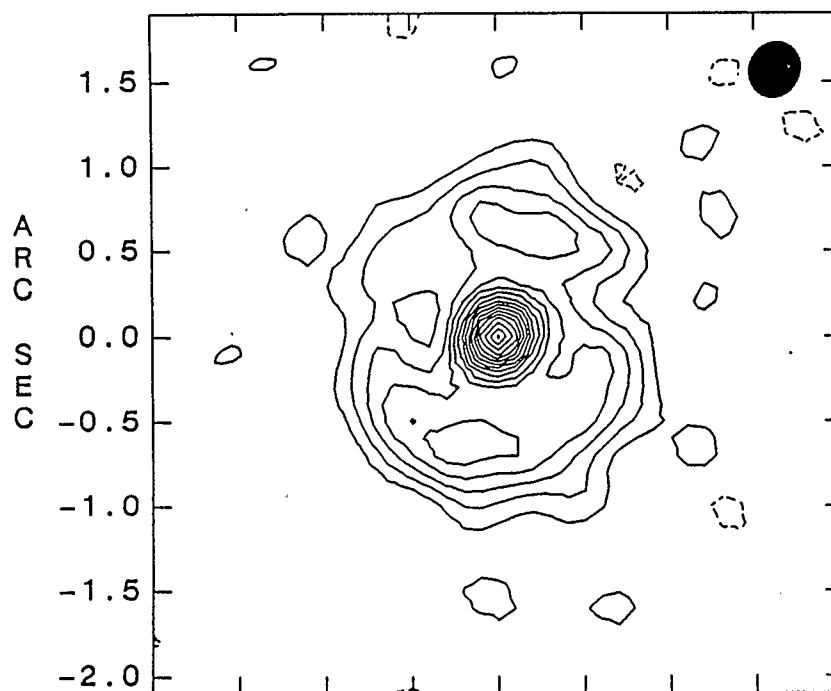
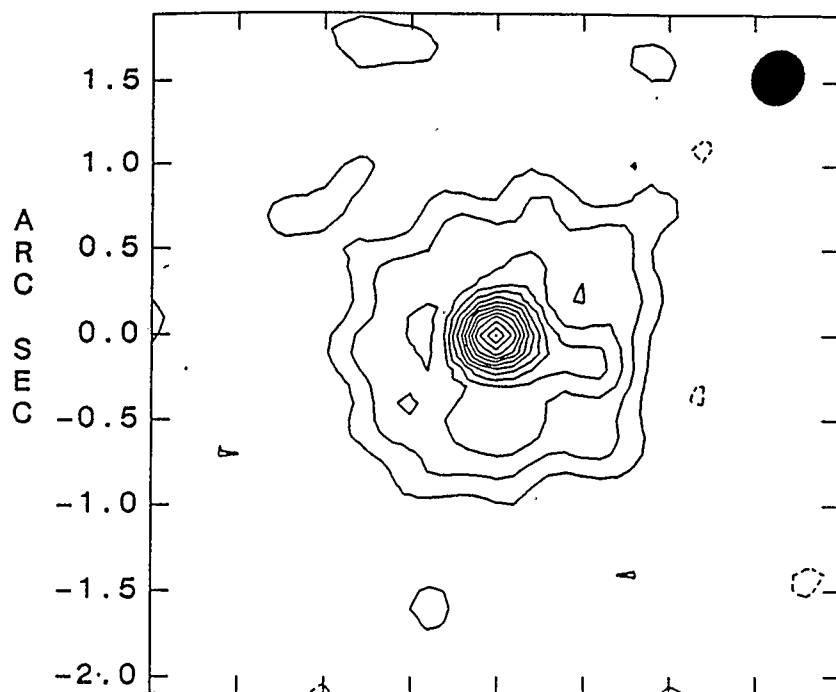


Figure 3.8: Images of AG Pegasi (5 GHz): Uniform Weighing  
The top image is from 11-84 and the bottom from 7-87. The center of each map is RA 21 48 36.164, DEC 12 23 27.42. Contours are drawn at 0.1 mJy intervals.

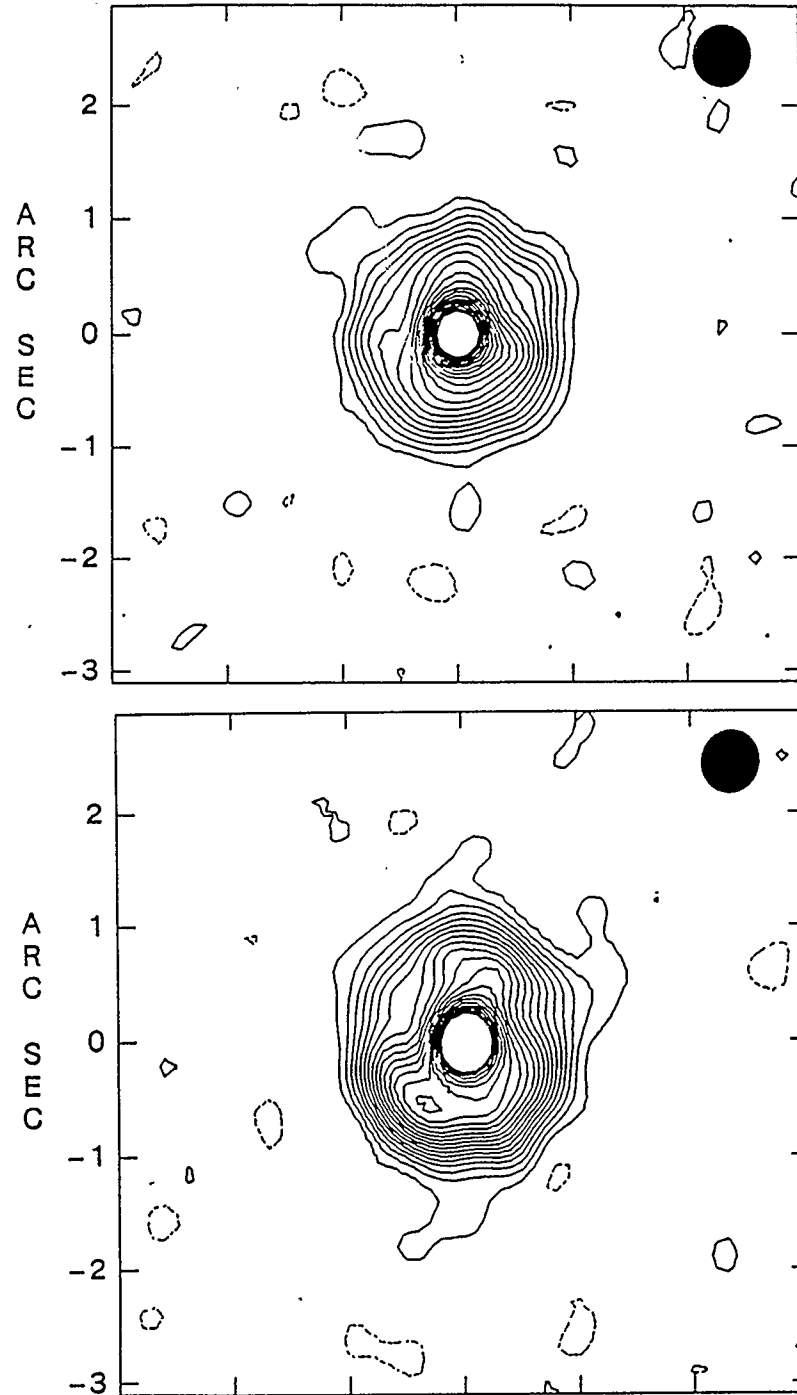


Figure 3.9: Images of AG Pegasi (5 GHz): Natural Weighing

The top image is from 11-84 and the bottom from 7-87. The center of each map is RA 21 48 36.164, DEC 12 23 27.42. Contours are drawn at 0.06 mJy intervals. The centers of these images are 'burnt out'.

## Chapter 4

### ANALYSIS

#### 4.1 Modelling the Visibilities

Modelling of the AG Pegasi data base was performed in the visibility domain. This procedure was selected because all resolved levels of nebulosity around the system revealed approximate *radial symmetry* (symmetry through the system center). In cases of considerable spherical symmetry, values of fundamental parameters such as mass and extent may be obtained from the visibility data with greater precision than from the derived images (Aaquist 1985, Aaquist and Kwok 1987). This is also true of bipolar symmetry. Greater precision is achieved because an aperture synthesis instrument like the VLA measures the complex Fourier Components of the sky's brightness distribution (visibilities) rather than directly measuring the brightness distribution itself. Information is lost in the imaging process due to the mapping algorithm and the assumptions made by deconvolution routines as described in Section 3.3. In the case of AG Pegasi the approximation of radial symmetry is well justified, as may be recognized from Figures 3.4 to 3.6. Hence visibility modelling was the most appropriate approach for the present work. In the discussion of models which follows, spherical symmetric models will be discussed first, *i.e.* all parameters will be considered a function of radius only. This will be done, however, with a view to extending the results to the bipolar case.

### 4.1.1 Spherically Symmetric Models

To facilitate modelling, the visibility function from Equation 2.15 may be expressed as:

$$V(u, 0) = \int_{-\infty}^{\infty} \int_{-\infty}^{\infty} I(l, m) e^{2\pi i l u} dl dm. \quad (4.1)$$

In order to obtain this expression the primary beam  $A(l, m)$  has been taken to be 1; this approximation is valid in cases where source structure is much smaller than the primary beam. Further,  $v$  may be set to zero because in the case of spherical symmetry all baselines of equal antenna separation will be equivalent regardless of their  $uv$  orientation. Hence the  $v$  coordinate in the following analysis will be ignored.

The visibility function,  $V(u, 0)$  may be separated into real and imaginary components,  $V_R(u)$  and  $V_I(u)$  respectively.

$$\begin{aligned} V_R(u) &= \int_{-\infty}^{\infty} Q(l) \cos(2\pi l u) dl \\ V_I(u) &= \int_{-\infty}^{\infty} Q(l) \sin(2\pi l u) dl \\ \text{where } Q(l) &= \int_{-\infty}^{\infty} I(l, m) dm. \end{aligned} \quad (4.2)$$

This separation is useful because  $V_I(u)$  will be uniformly zero in the case of a radially symmetric brightness distribution. It will be zero because  $\sin$  is an odd function and  $Q(l)$  is even for radial symmetry (*i.e.*  $I(l, m) = I(-l, -m)$ ). This implies that the product  $Q(l)\sin(2\pi l u)$  is odd and hence integration over a symmetric interval will provide a zero result for  $V_I(l)$ . The assumption of radial symmetry

may, therefore, be tested by reference to the observed imaginary visibilities. Assuming that radial symmetry does indeed exist,  $V_R(u)$  is left as the quantity to be modelled. As an aside, it may be seen from Equation 4.2 that  $V_R(0) = \int_{-\infty}^{\infty} Q(l)dl$  corresponds to the total observed flux, *i.e.* the intensity integrated over the solid angle of the source.

In practice, the quantities  $V_R(u)$  and  $V_I(u)$  are readily accessible through the AIPS software, and may be read out in graphical (Figure 4.1) or numerical form with uncertainties assigned by a binning process. The inherent assumption in binning is that values of  $V_R(u)$  and  $V_I(u)$  vary smoothly; hence, in the range of  $u$  over which visibilities are binned, the values of  $V_R(u)$  and  $V_I(u)$  change by insignificant amounts. Note that in Figure 4.1  $uv$  distance is given in units of kilowavelengths which is often abbreviated below as  $k\lambda$ .

To model  $V_R(u)$  one attempts to find the function  $Q(l)$  in Equation 4.2 which yields values of  $V_R(u)$  corresponding to those obtained in observation. The emergent intensity from an astrophysical source, obtained by solution of the radiative transfer problem (Equation 1.3) may be expressed:

$$I_\nu(l, m) = B_\nu(T)(1 - e^{-\tau_\nu(l, m)}) \quad (4.3)$$

where:  $B_\nu(T)$  is Planck's function for temperature  $T$  and frequency  $\nu$ ; and  $\tau_\nu(l, m)$  is the optical depth through the nebula at point  $(l, m)$  (Equation 1.4). Hence real visibilities may be expressed:

$$V_R(u) = \int_{-\infty}^{\infty} Q(l) \cos(2\pi lu) dl$$

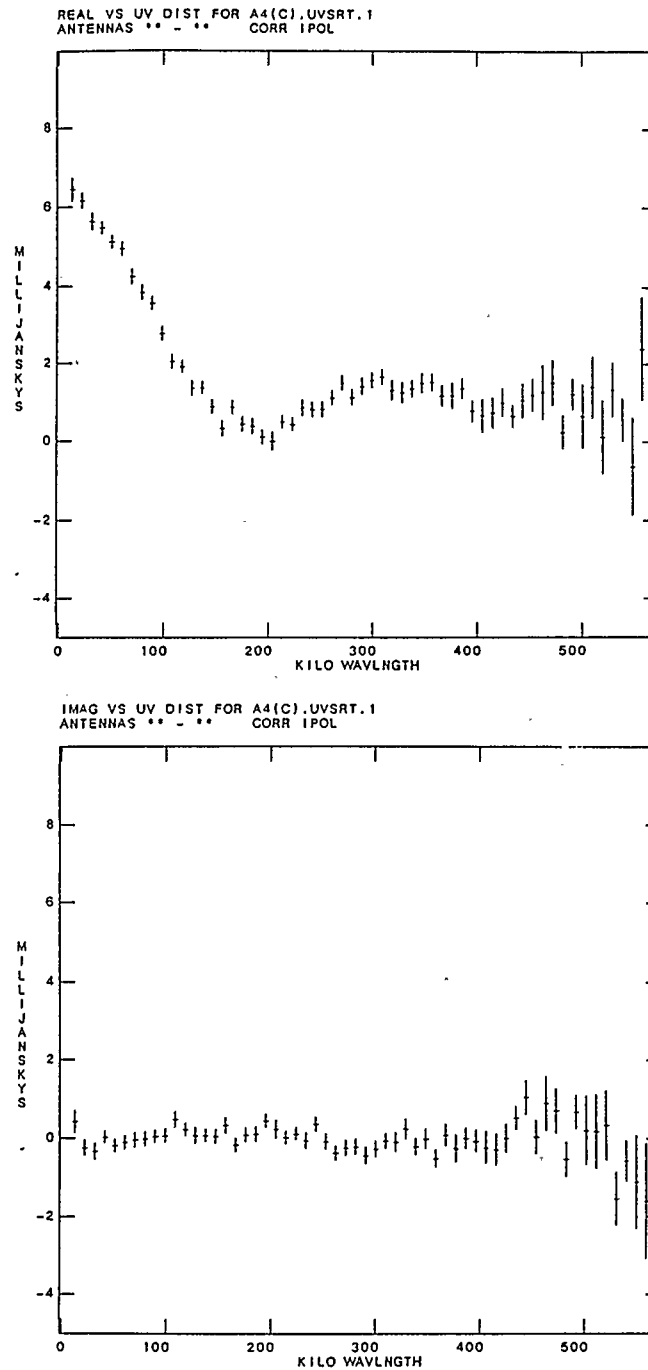


Figure 4.1: Real and Imaginary Visibilities as Output from AIPS

Real and imaginary visibilities for AG Pegasi are shown in the upper and lower plots respectively. Note that the real visibilities show considerable structure while the imaginary visibilities are approximately zero. This indicates that the observed source has considerable radial symmetry.

$$Q(l) = \int_{-\infty}^{\infty} B_{\nu}(1 - e^{-\tau_{\nu}(l,m)}) dm. \quad (4.4)$$

It remains here, then, to define optical depth,  $\tau$ , in terms of physically meaningful quantities. Consider a spherically symmetric nebula of fully ionized plasma (Figure 4.2). Let the number density of electrons be given by  $n_e = A/R^{\beta}$  [ $\text{cm}^{-3}$ ], where  $A$  and  $\beta$  are constants and  $R$  is distance measured from the centre of the nebula. If emission arises from the bremsstrahlung process, then the absorption coefficient valid in the radio regime is given by (*e.g.* Lang 1980):

$$\kappa_{\nu} = 0.0824T^{-1.35}\nu^{-2.1}(A/R^{\beta})^2 [pc^{-1}] \quad (4.5)$$

where:  $\nu$  is frequency given [GHz]; and  $T$  is the electron temperature within the shell. For the purposes of modelling,  $T$  may be taken to be  $10^4 K$ . This assumption is consistent with equilibrium of heating and cooling processes as expected in the type of nebular region under discussion (*e.g.* Spitzer 1978). Note that most of this derivation will use angular measures,  $\theta$ , for nebular distances; where linear distances are required, the distance to the source,  $D$ , must be introduced (*e.g.*  $R[\text{cm}] = D[\text{cm}] \theta[\text{rad}]$ ).

With reference to Figure 4.2 it may be shown that the optical depth through the shell material at some point of observation ( $l, m$ ) is given by:

$$\begin{aligned} \tau_{\nu}(l, m) &= 0.1648T^{-1.35}\nu^{-2.1}A^2 \int_0^{D\sqrt{\theta_o^2 - \theta^2}} \frac{dx}{[x^2 + (D\theta)^2]^{\beta}}, \quad \theta > \theta_i \\ &= 0.1648T^{-1.35}\nu^{-2.1}A^2 \int_{D\sqrt{\theta_i^2 - \theta^2}}^{D\sqrt{\theta_o^2 - \theta^2}} \frac{dx}{[x^2 + (D\theta)^2]^{\beta}}, \quad \theta < \theta_i \end{aligned} \quad (4.6)$$

where  $\theta_o$  and  $\theta_i$  are the angular outer and inner radii respectively. The quantity  $\theta$

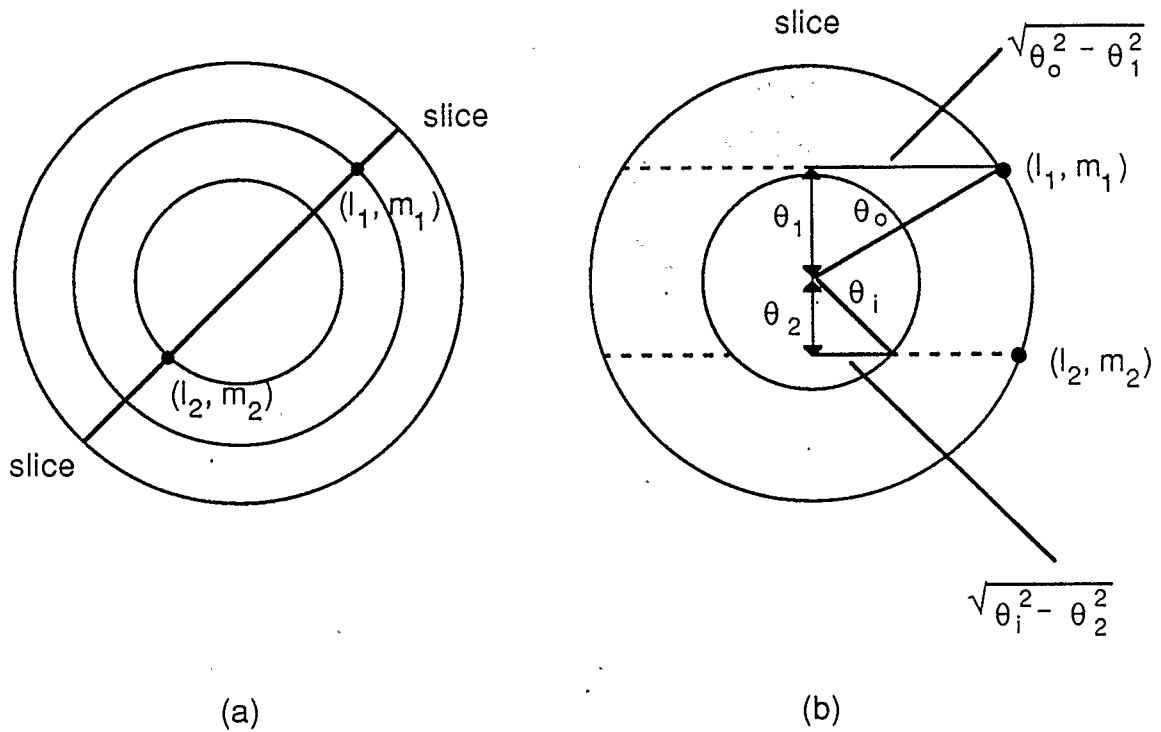


**Figure 4.2: Nebular Model: Spherical Symmetry**

Figure (a) shows the appearance of a spherically symmetric nebulosity on the plane of the sky. Contours join points of equal intensity.

Figure (b) shows a cross section of the nebulosity through the slice defined in Figure (a). Modelling parameters  $\theta_0$  and  $\theta_i$  are defined. Various distances through the nebula are computed.

is defined as  $\theta \equiv \theta(l, m) = \sqrt{l^2 + m^2}$ . The integral in Equation 4.6 has a simple analytic solution for both the case of  $\beta = 0$  (homogeneous shell) and of  $\beta = 2$  (wind). While  $\theta_i$  and  $\theta_o$  are useful parameters conceptually, the modelling process improves mathematically by replacing them with two new parameters  $\eta$  and  $\theta_c$ . The parameter  $\eta$  is defined  $\eta \equiv \theta_i/\theta_o$  and is useful because it contains all the geometry of the model. The parameter  $\theta_c$  is a “center of mass radius”; it is defined  $\theta_c \equiv \frac{1}{M} \int_{\theta_i}^{\theta_o} \theta dM$  where  $dM$  is the mass of a shell of thickness  $d\theta$  at displacement  $\theta$  from the nebular center and is dependent upon the density law assumed; and  $M$  is the total nebular mass. The parameter  $\theta_c$  is intrinsically better constrained by any given visibility data set than either  $\theta_o$  or  $\theta_i$ .

### Effects of Parameters

The fundamental parameters used to determine  $Q(l)$  and hence  $V_R(u)$  are  $\eta$ ,  $\theta_c$ , and  $A$ . If these three parameters are to be fitted, it is useful to understand what effect each has upon a model visibility curve.

The parameter  $\eta = \theta_i/\theta_o$  establishes the geometry of the source:  $\eta \rightarrow 0$  for a nebula with no central hole, and  $\eta \rightarrow 1$  for an infinitely thin shell. Figure 4.3 shows the manner in which the intensity distribution,  $I_\nu(\theta)$ , varies along the diameter of a homogeneous, spherically symmetrical nebula for different values of  $\eta$ . Figures 4.4 to 4.6 show the manner in which the real visibility curve is affected by changes in  $\eta$ . Various density laws are considered: Figure 4.4 - homogeneous shell ( $\beta = 0$ ); Figure 4.5 - infinite wind ( $\beta = 2, \theta_o = \infty$ ); Figure 4.6 - truncated wind ( $\beta = 2, \eta > 0$ ). Once  $\eta$  has been determined, the shape of the real visibility curve is completely constrained and the other parameters,  $\theta_c$  and  $A$  merely scale it in the

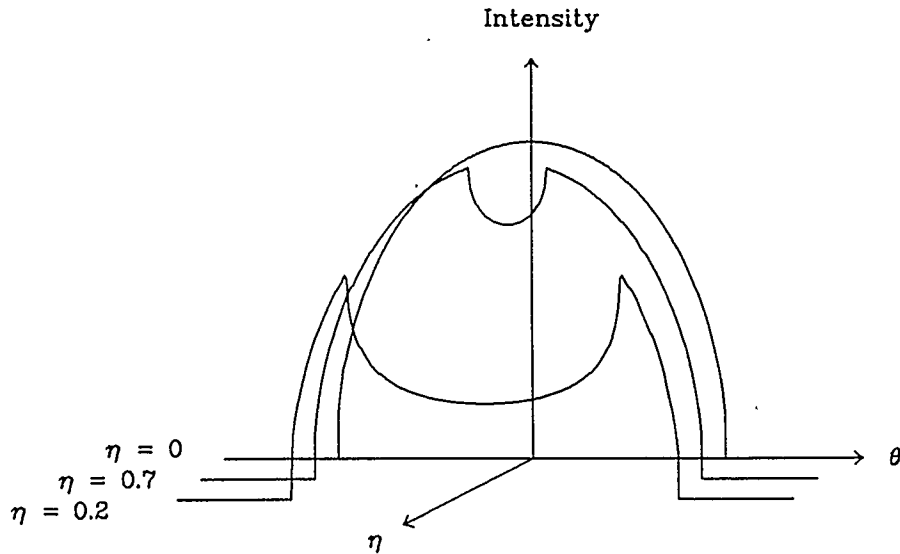


Figure 4.3: **Variation of Intensity Distribution with  $\eta$**   
 The curves above correspond to an optically thin homogeneous nebula.

x and y directions. Because of its unique effect upon the visibility curve,  $\eta$  may be determined independent of the other parameters as shown in Figure 4.7. The quantity  $\gamma$  defined in this figure may be obtained in model independent fashion by simple measurement of the first three extrema of the real visibility curve. The figure demonstrates that  $\eta$  is a monotonically increasing function of  $\gamma$  and hence if  $\gamma$  is known,  $\eta$  can be calculated.

Changes in the angular radius,  $\theta_0$ , affect the intensity distribution as shown in Figure 4.8. The affect upon the visibility curve is a simple scaling of the x-axis as shown in Figure 4.9. Y axis scaling occurs as well, however this effect is easily removed since it may be balanced by a corresponding change in  $A$ . The scaling relationship which exists, arises directly from the similarity theorem of Fourier transforms: since  $I(l)$  has the Fourier transform  $V(u)$ , it follows that  $I(al)$  has the

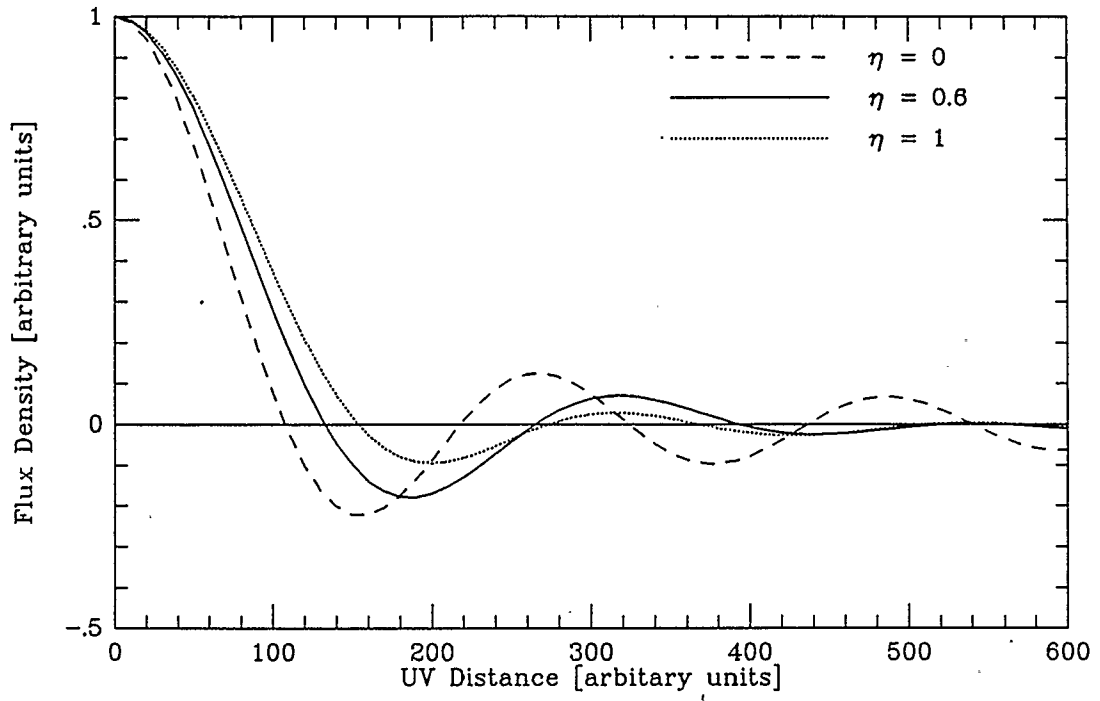


Figure 4.4: Model Visibility Curves: Homogeneous Shell

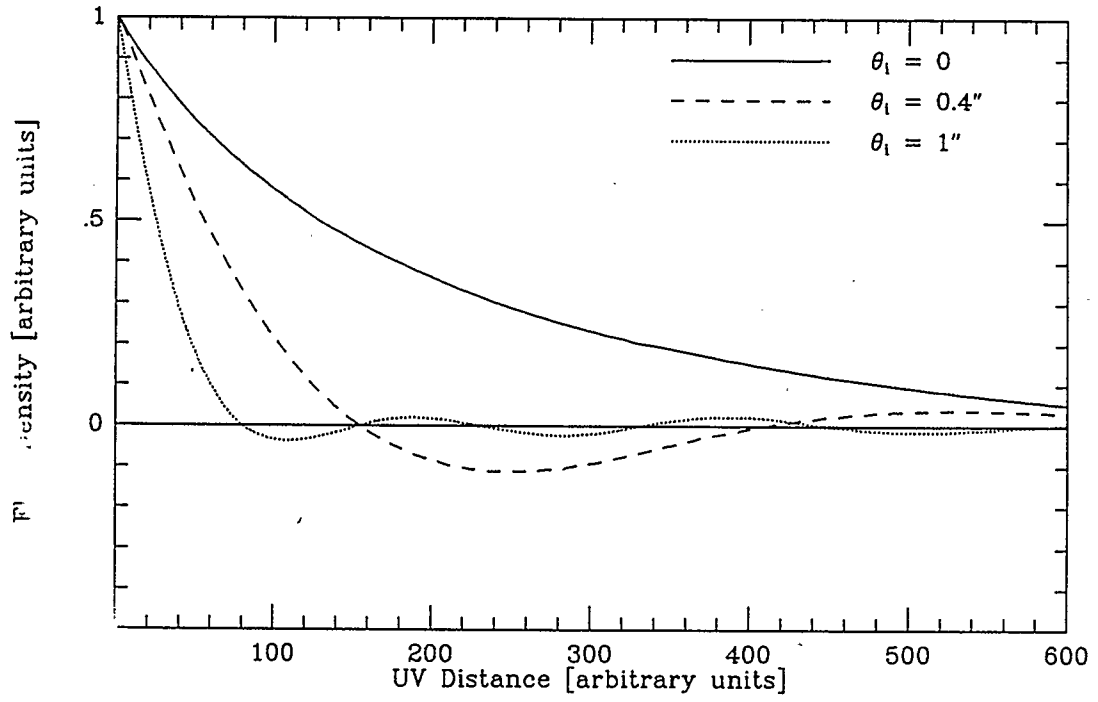


Figure 4.5: Model Visibility Curves: Infinite Wind

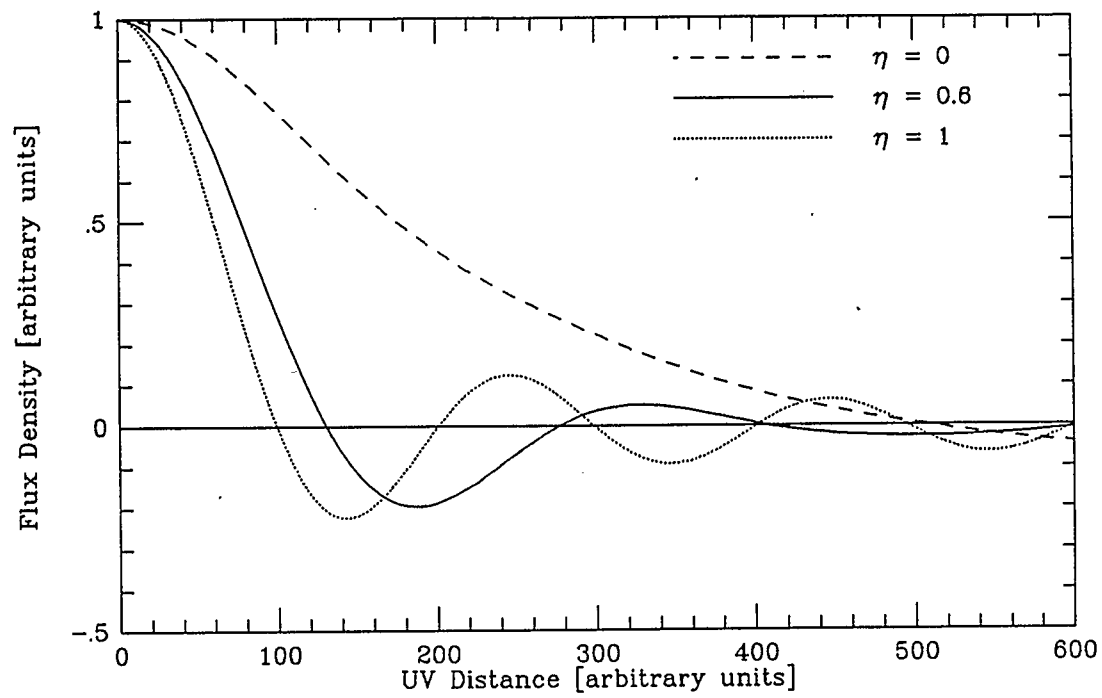


Figure 4.6: Model Visibility Curves: Truncated Wind

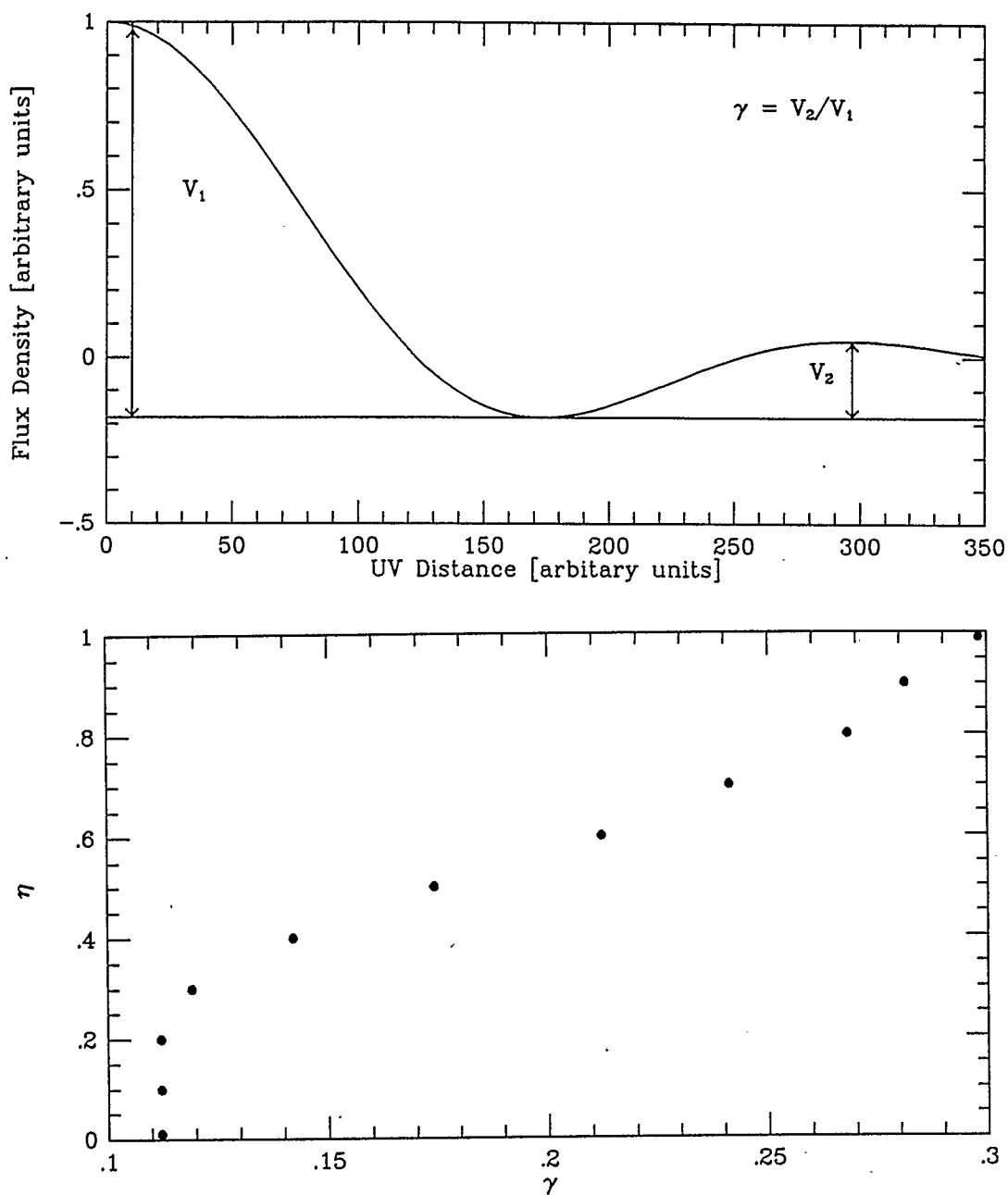


Figure 4.7: Determination of  $\eta$

The upper plot defines the parameters  $V_1$  and  $V_2$  which must be determined in order to calculate a value for  $\gamma = V_2/V_1$ . The lower plot illustrates that  $\eta$  is a monotonically increasing function of  $\gamma$  and that if  $\gamma$  is known, then  $\eta$  is easily determined. The relationship illustrated in the lower plot applies to optically thin nebulae of uniform density.

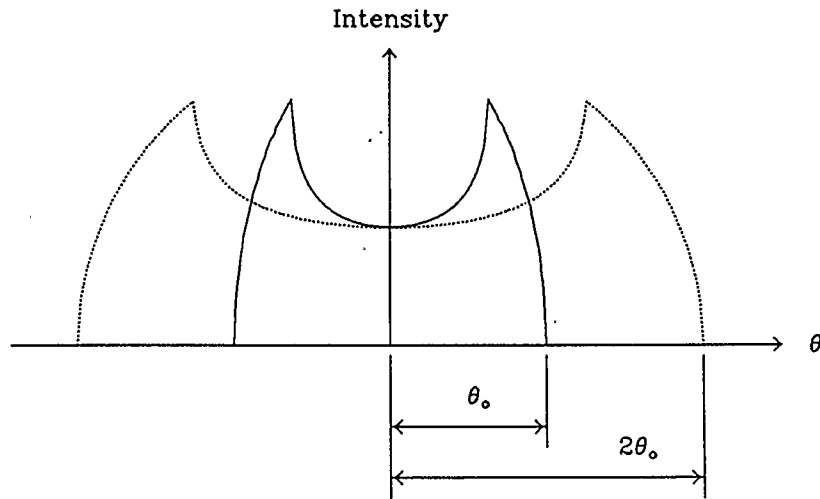


Figure 4.8: Variation of Intensity Distribution with  $\theta_0$ .

The above distributions have been scaled such that the central intensity has remained constant. The curves correspond to optically thin homogeneous nebulae.

Fourier transform  $|a|^{-1}V(u/a)$  if  $a$  is a constant (Bracewell 1986). In other words, once  $\eta$  has been determined,  $\theta_0$  may be inferred from the  $x$  coordinate (baseline value) of some well defined point on the curve such as the first minimum. It should be remembered, that  $\theta_c$  is a preferred parameter over  $\theta_0$ ; once  $\eta$  and  $\theta_0$  are known, however, and a density law has been assumed,  $\theta_c$  can be calculated.

Electron density at points within the shell is determined by the parameter  $A$ ;  $n_e = A/R^\beta$  where  $n_e$  [ $\text{cm}^{-3}$ ] is the number density of electrons;  $R$  [cm] is distance from the nebular center; and  $\beta$  is a constant. For homogeneous nebulae  $n_e = A$ , and for wind-like nebulae  $n_e = A/R^2$ . Changes in  $A$  affect the intensity distribution as shown in Figure 4.10. In the visibility domain,  $A$  scales the  $y$  axis of the curve as shown in Figure 4.11. For the optically thin case, the scaling takes a particularly

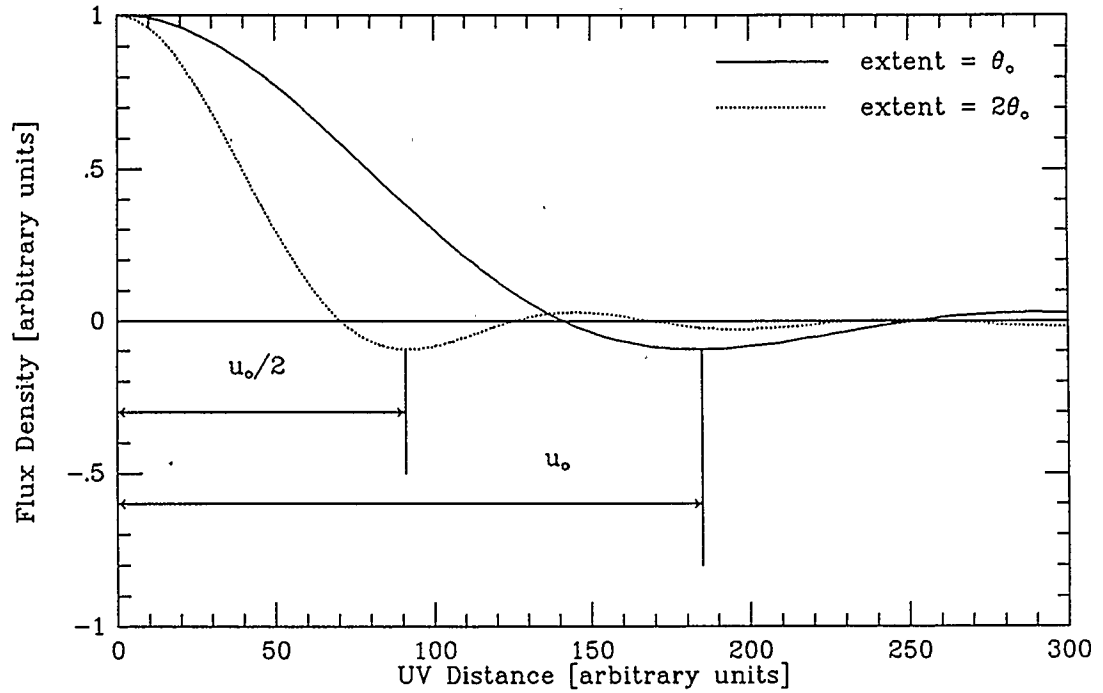


Figure 4.9: Effect of the Parameter  $\theta_0$  upon the Visibility Curve

The above distributions have been scaled such that the zero baseline flux has remained constant. The curves correspond to optically thin homogeneous nebulae. The relationship being demonstrated is that if the extent of the observed object is increased by a factor 'a' then the visibilities will be scaled inward by the factor  $1/a$ .

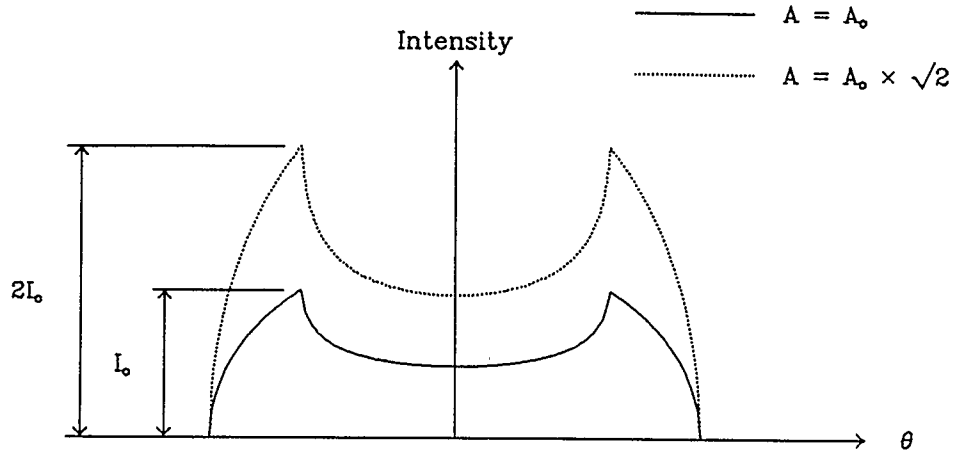


Figure 4.10: Variations of Intensity Distribution with  $A$

The above curves correspond to optically thin nebulae. For the optically thin case,  $I \propto A^2$ , so an increase in  $A$  by the factor  $\sqrt{2}$  will result in a doubling of intensity.

simple form since  $I \propto A^2$  where  $I$  is intensity. An increase in  $A$  by a constant factor ' $a$ ' will result in an increase in  $I$  by a factor  $a^2$  and in turn a scaling of  $V_R$  by the same factor (Equation 4.4).

In the case of AG Pegasi the outer levels of nebulosity enclose an unresolved central source. Such a source, if located at the phase centre, has the effect of adding to all visibilities a constant value ' $s$ ' corresponding to the flux of the unresolved source. This property arises because the Fourier transform of a point source is a d.c. level ( $\delta(l) \supset 1$ , where  $\supset$  denotes Fourier transform). The fourth parameter to enter into the fitting program, then, is this d.c. level  $s$ .

In summary to this point, visibility modelling of spherically symmetric sources may be accomplished using four parameters  $\eta$ ,  $\theta_c$ ,  $A$ , and  $s$  which represent re-

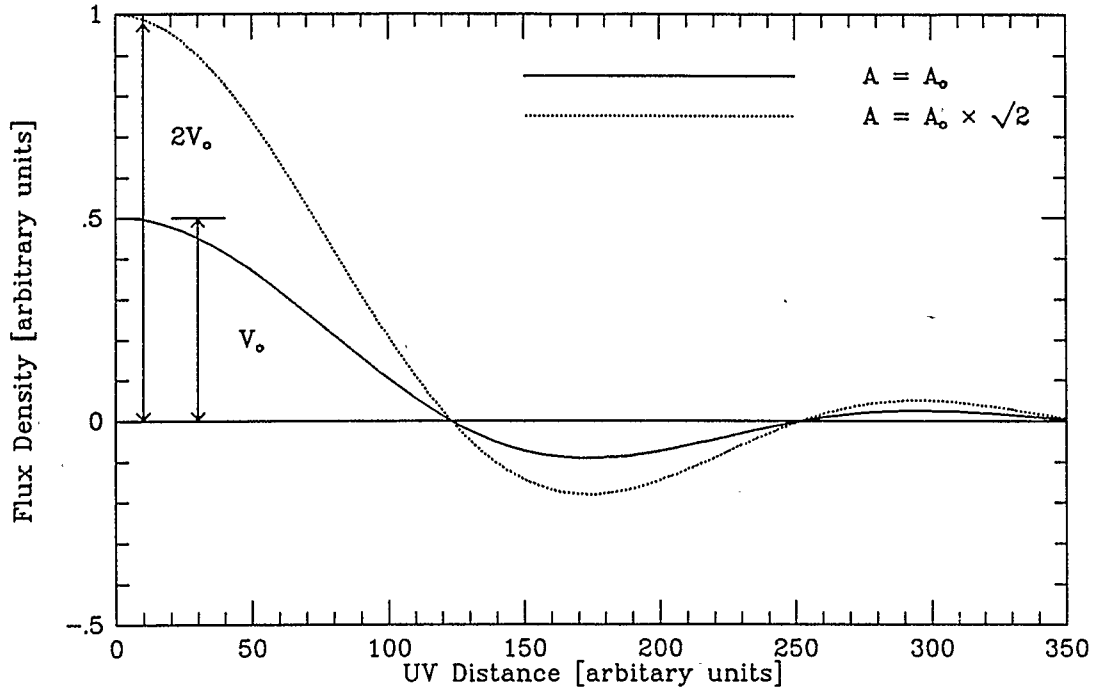


Figure 4.11: **Effect of the Parameter  $A$  upon the Visibility Curve**  
 The above curves correspond to optically thin nebulae. For the optically thin case,  $V_R \propto A^2$ , so an increase in  $A$  by the factor  $\sqrt{2}$  will result in a doubling of real visibilities.

spectively the geometry, extent, density, and point source flux of the nebula to be modelled. The parameters influence the visibility curve as follows:

1.  $\eta$  determines the curve shape;
2.  $\theta_c$  determines the x axis scaling factor;
3.  $A$  determines the y axis scaling factor; and
4.  $s$  determines the d.c. shift of the curve.

Because each parameter has a different effect upon the model curve, it is possible to determine each with high precision. The assumptions which go into this model include:

1. spherical symmetry;
2. an isothermal nebula with electron temperature of  $10^4 K$ ;
3. a density law of the form  $n = A/R^\beta$ ; and
4. emission arising from the bremsstrahlung process.

The above derivation also assumes a completely ionized plasma, however, this is not a necessary assumption. If some fraction of the nebula were not ionized, then a weighting factor,  $\gamma$ , could be introduced such that equation 4.5 is written  $\kappa_\nu = 0.0824T^{-1.35}\nu^{-2.1}(\gamma n_e^2) [pc^{-1}]$ . No other change to the equations developed would be necessary.

In the case of AG Pegasi, circumstellar nebulae take the form of a number of embedded shells around the central object. The above derivation (Equation 4.4)

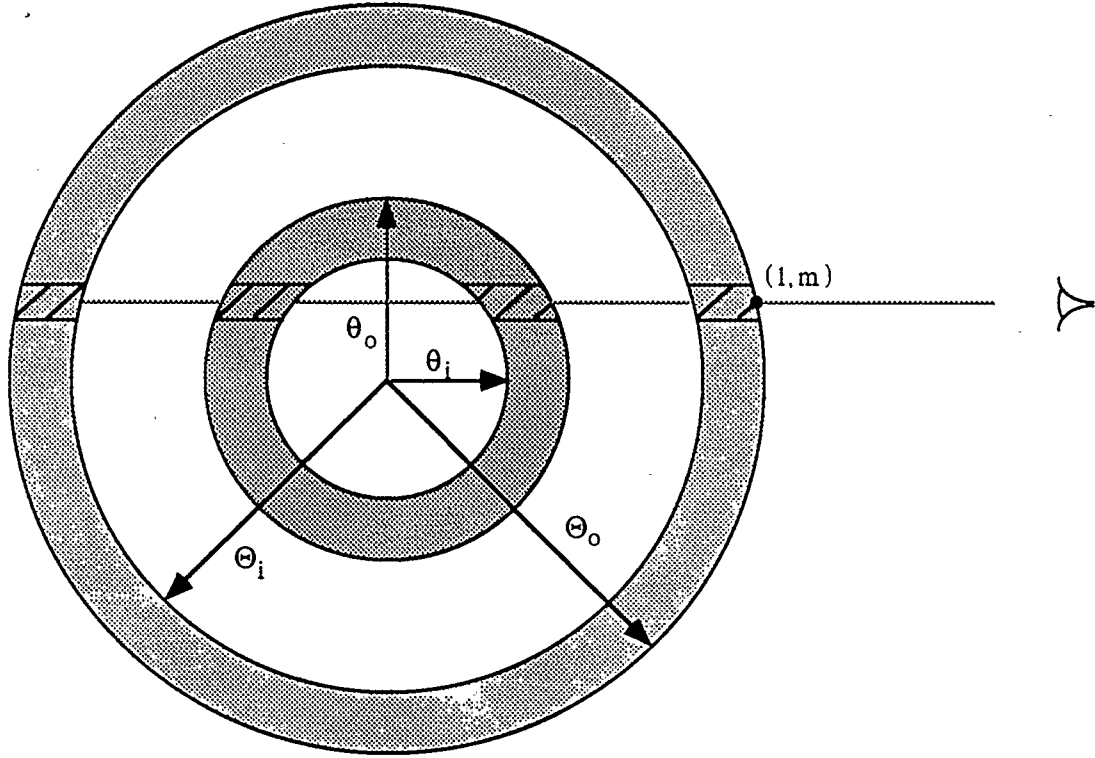


**Figure 4.12: Model Structure For Two Embedded Shells**

The optical depth along the line of sight for two embedded nebulae is given by  $\tau = \tau_{inner} + \tau_{outer}$ . In the case of optical thinness,  $I \propto \tau$ , hence  $I = I_{inner} + I_{outer}$ .

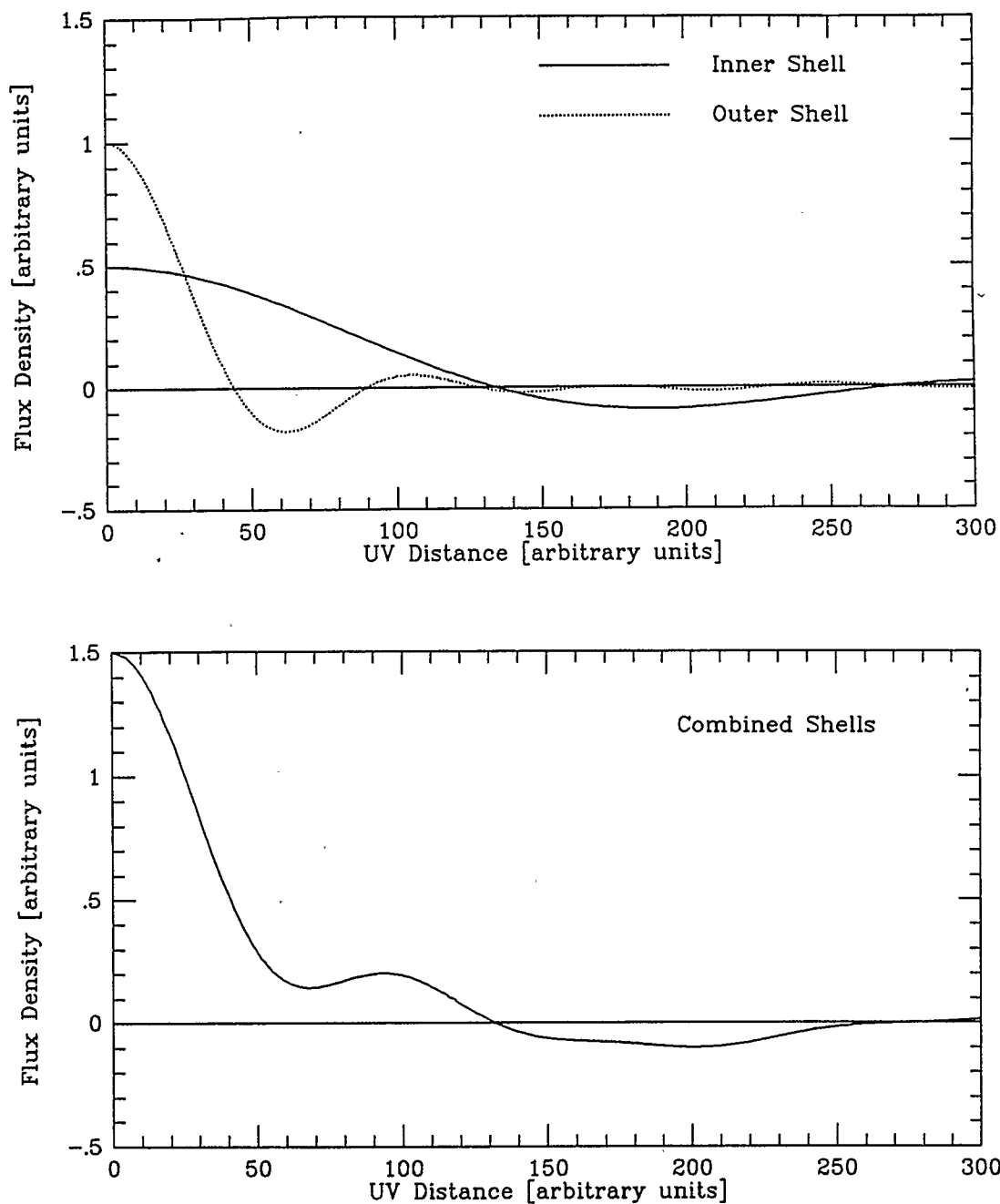


Figure 4.13: Visibility Curve for a Two Shell Model

The top figure gives the visibility curve of two spherical nebulae as they would appear in isolation from each other. The lower figure shows the resultant curve if the smaller shell is embedded inside the larger one and the resultant nebula is optically thin. The resultant curve is a superposition of the two curves shown in the top figure.

is general enough to address this problem, however the optical depth given by Equation 4.6 must be rewritten to accommodate the additional shells. Figure 4.12 shows that for the case of two shells, the optical depth at some point  $(l, m)$  is given by  $\tau = \tau_{inner} + \tau_{outer}$ . A model visibility curve for the case of two shells is given in Figure 4.13.

#### 4.1.2 Bipolar Models

The results obtained for spherically symmetric nebulae may be generalized to the bipolar case. The bipolar model used for this purpose is illustrated in Figure 4.14. All of the approximations made in deriving Equations 4.4 remain appropriate for the bipolar model except for the manner in which  $v$  was set to zero. In the case of spherical symmetry, all antenna pairs of equal baseline separation obtain, in principle, equal visibility measurements; hence  $v$  becomes a redundant parameter. In the case of bipolar symmetry, however, different visibilities may be obtained for different orientations of the baseline vector. When real visibilities are binned, in the case of bipolar symmetry, an average is taken over all baseline orientations. Let the real visibility for an antenna pair of separation  $b$  and orientation angle  $\xi$  with respect to  $\hat{u}$  be given by  $V_R(b, \xi)$ . Then, for a set of  $n$  antenna pairs with baseline separation  $b$ , the binned average of  $V_R(b, \xi)$  is given by:

$$\langle V_R(b) \rangle_{binned} = \frac{1}{n} \sum_{i=1}^n V_R(b, \xi_i). \quad (4.7)$$

If  $n$  is large, and the  $uv$  coverage is uniform (*i.e.* for all values of  $b$ ,  $\xi$  is uniformly sampled), Equation 4.7 may be replaced by the equation:

$$\langle V_R(b) \rangle_{\text{binned}} = \frac{1}{2\pi} \int_0^{2\pi} V_R(b, \xi) d\xi \quad (4.8)$$

Note that the angular dependence has been integrated out of  $V_R$  in equation 4.8. This means that, through binning, the data is rendered insensitive to the orientation of the bipolar features on the sky.

To determine  $V_R(b, \xi)$ , the function  $Q(l)$  may be evaluated according to Equation 4.2 with the qualification described below. Note that for any given antenna pair, the measured value of the real visibility function, is coordinate independent since the original visibility equation (Equation 2.12) was a vector relationship. For any given baseline  $k$ , therefore, coordinates may be redefined such that  $\hat{u}_k$  coincides with the the baseline vector and hence  $v_k$  is effectively zero. By defining the  $\hat{u}$  and  $\hat{v}$  directions in this way, the  $l$  and  $m$  axis on the plane of the sky will also be different for each antenna pair. The advantage of this arrangement is that  $Q(l)$  can be evaluated as it was in the spherically symmetric case. Namely, this function may be considered to execute strip integrations of intensity along the  $m$  axis:  $Q(l) = \int_{\theta_i}^{\theta_o} I(l, m) dm$ . For different orientations,  $\xi$ , intensities from bipolar features project at different positions along the  $l$  axis but, because the bipolar features are spherical, the shape of the projected intensity distribution for each feature will not change.

In bipolar models, a parameter  $\zeta$  may be defined as  $\theta_b/\theta_c$  where  $\theta_b$  and  $\theta_c$  are given in Figure 4.14. In this way,  $\zeta$  contains all of the geometry of the system as did  $\eta$  for the spherically symmetric case. Figure 4.15 illustrates the effect of  $\zeta$  upon visibility curve shape.

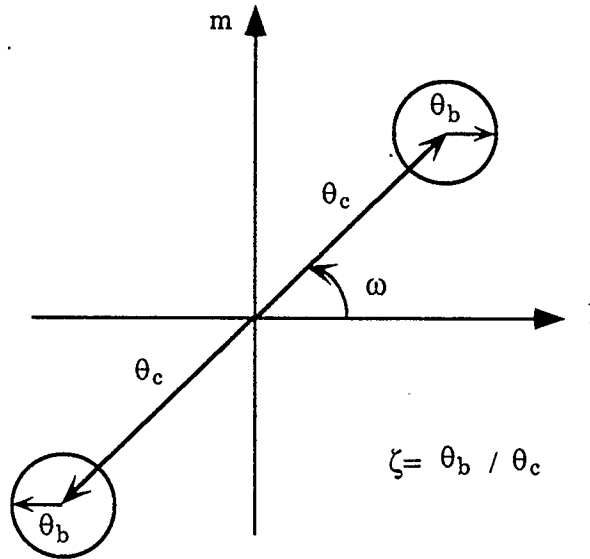


Figure 4.14: Nebular Model: Bipolar Features

A bipolar model requires slightly different parameters than a spherically symmetric one. A parameter  $\zeta$  may be defined which completely constrains the geometry as  $\eta$  did in the spherically symmetric case. Note that  $\theta_c$ , as defined above has the same meaning as for spherically symmetric models; it is the “center of mass” radius. A parameter  $\omega$  is also defined which describes the angle between the “bipolar axis” and the direction vector  $\hat{u}$ .

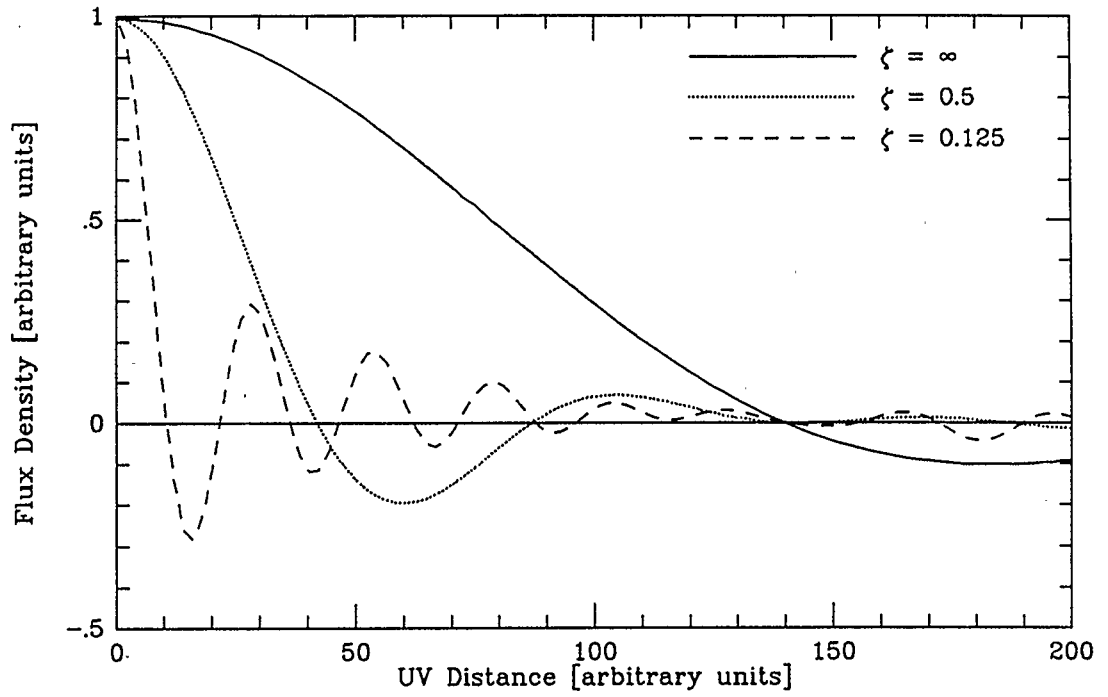


Figure 4.15: Model Visibility Curves: Bipolar Features

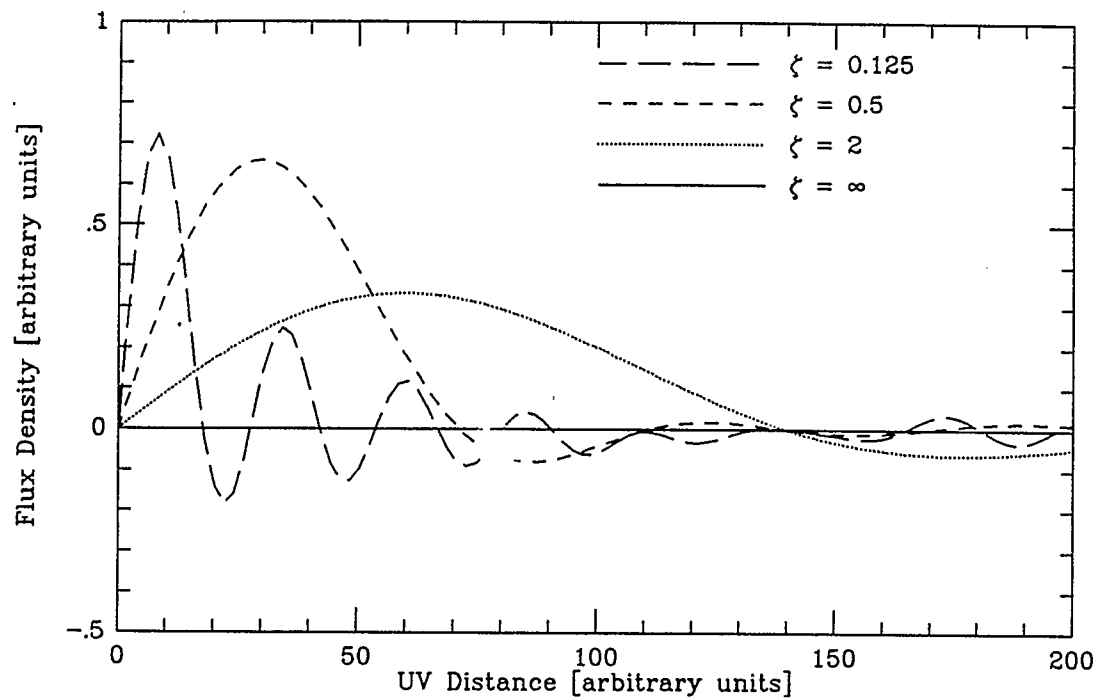


Figure 4.16: **Imaginary Visibilities: Asymmetric Features**  
The parameter  $\zeta \equiv \theta_b/\theta_c$  is illustrated in Figure 4.14.

It has been pointed out that imaginary visibilities go to zero in all cases of radial symmetry. It is possible to put this fact upon a more quantitative framework now that modelling concepts have been introduced. Figure 4.16 illustrates the effect on imaginary visibilities of moving an optically thin, homogeneous sphere progressively further from the phase center, causing an increasing level of asymmetry. The parameter  $\zeta$  used in this figure is defined in the same way as it was for bipolar symmetry (see Figure 4.14). Even small departure from radial symmetry,  $\zeta \simeq 0.1$ , causes large imaginary signals; therefore imaginary visibilities are a good test of asymmetry. The object being considered in Figure 4.16 has a flux of 1 mJy. The effect of increasing the flux of the source would be to increase the “amplitude” of the imaginary curve in precisely the same way that it did for the real visibilities.

While the imaginary visibilities provide a quantitative measure of the radial symmetry of an observed object, they do not completely constrain the geometry. It is significant, for instance that the observer distinguish between spherically symmetric and bipolar sources. To do this, recourse must be taken to the images.

## 4.2 Sequence of Analysis

Deconvolved images and final visibility data for the AG Pegasi data base were produced using the reduction procedures described in the previous chapter. When the reduction was complete, the visibility data sets from individual observations were found to fall roughly into four categories, examples of which are shown in Figure 4.17. Sets of categories 1 to 3 detected only the inner nebula and the central object; they represent the same visibility curve at different scales of  $uv$

distance. In category 1 sets, the first three extrema of the real visibilities are well defined. In category 2 sets, smaller  $(u, v)$  values are sampled; only the first maximum can be determined, but the decrease of the visibility curve toward the first minimum is well constrained. Category three sets have flat visibility curves: in subcategory 3a only very small  $(u, v)$  values are sampled and hence the decrease of the visibility curve toward the first minimum is not detected; in subcategory 3b large  $(u, v)$  values are sampled such that the oscillatory nature of the visibility curve has “damped” to zero for practically the entire range of  $(u, v)$  values measured. Category 4 sets sample very small  $uv$  values at low frequency (1.5 GHz) and detect not only the inner nebula and central source, but also the intermediate and outer nebulae. Category 4 sets are characterized by the complexity of their visibility curves which reveal their multicomponent nature.

In terms of model parameters, only category 1 sets were able to constrain  $\eta$  for the inner nebula since only in these sets were the first three extrema measurable (see Figure 4.7). Once  $\eta$  was determined, however, the other sets could provide information about the inner nebula and the central object. The complexity of the category 4 sets made them difficult to model; modelling could only be undertaken once the contributions from the inner nebula and central object were determined from analysis of sets of the other categories.

Since not all data sets provided information about all the quantities of interest, it was necessary to follow a definite sequence of analysis. Category 1 sets were analyzed first and yielded values of  $s$ ,  $\eta_{inner}$ ,  $\theta_{c,inner}$ , and  $A_{inner}$ . The subscript “inner” refers to the inner nebula. From the results,  $\eta_{inner}(t)$  was determined and used as input for the category 2 data sets. These sets in turn yielded values

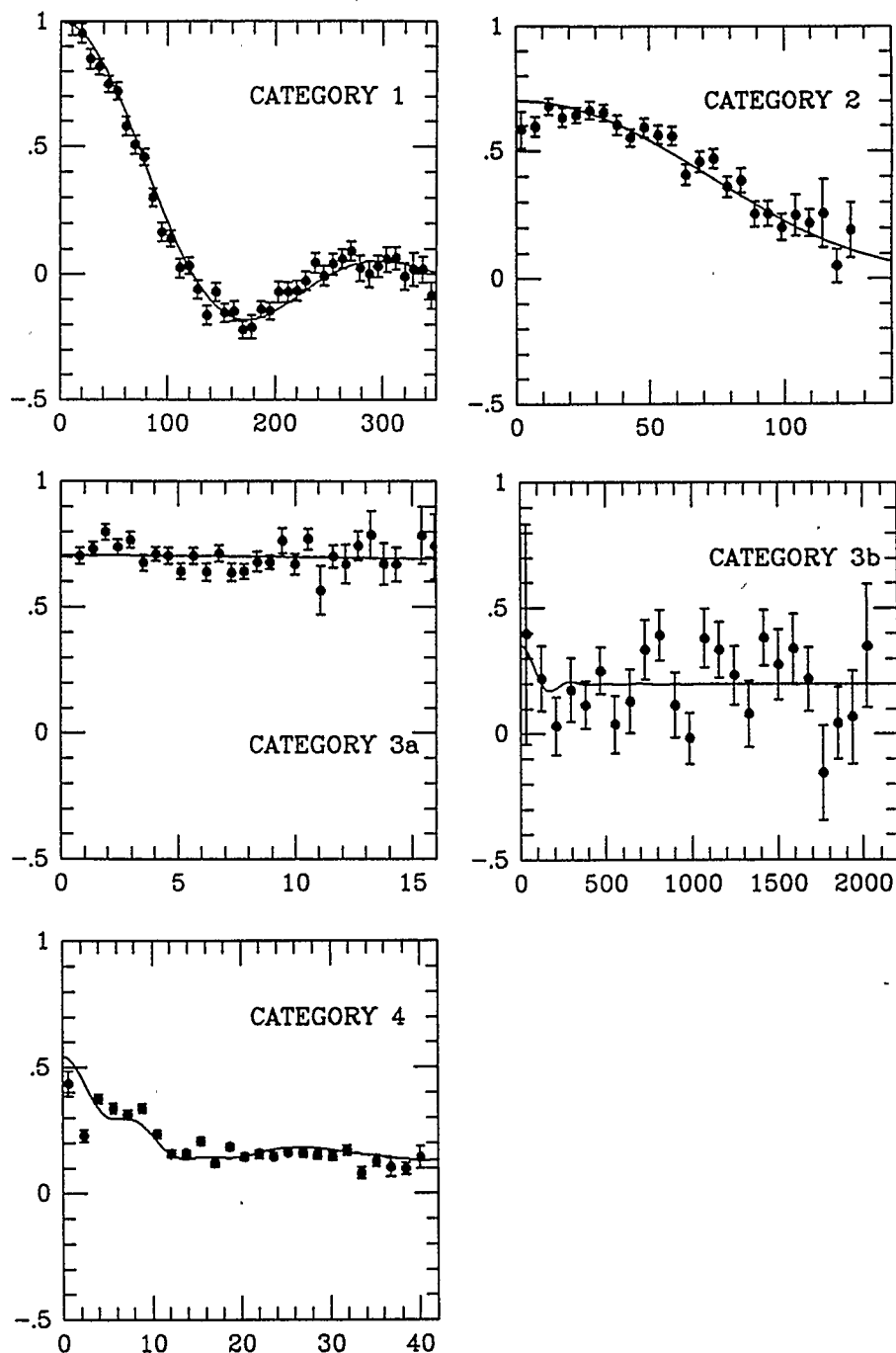


Figure 4.17: Categories of Data Sets

Real Visibilities are plotted above against  $uv$  distance. X coordinates are given in  $[k\lambda]$  and are representative of the categories being defined; y coordinates are arbitrary. Category 1: The function  $\eta_{inner}$  is well constrained. Category 2: Decreasing visibilities indicate the presence of the inner nebula. The function  $\eta_{inner}$  is not well constrained. Category 3: Data may be fitted only with a simple d.c. level. Category 4: Visibilities show a complex structure due to contributions from the outer and intermediate nebulae.

EPOCH	1.5 GHz	5 GHz	15 GHz	22.5 GHz
11-84	2	1	1	3b
	-	1	-	-
5-85	4	2	1	3b
8-85	4	3a	2	1
11-85	4	3a	3a	3a
2-86	2	1	1	3b
10-86	4	2	1	1
1-87	4	3a	2	2
4-87	4	3a	3a	3a
7-87	2	1	1	-

Table 4.1: Categorization of Observations

Data set of the AG Pegasi data base are categorized above according to the scheme defined in Figure 4.17.

of  $s$ ,  $\theta_{c,inner}$  and  $A_{inner}$ . From the combined results of the category 1 and 2 sets  $\theta_{c,inner}(t)$ , and  $A_{inner}(t)$  were fixed. Using  $\eta_{inner}(t)$ ,  $\theta_{c,inner}(t)$ , and  $A_{inner}(t)$  as input, the category 3 sets were analyzed to yield values of  $s$ . This completed the determination of parameters for the inner nebula.

Category 4 data sets contained recoverable information about emission beyond the inner nebula. The observed imaginary visibilities suggested that the distribution of the extended emission was radially symmetric. See Figure 4.1 for an example of an imaginary visibility curve corresponding to radial symmetry. The images (Figures 3.5 and 3.6) upheld the suggestion of radial symmetry. These figures indicated also that the outer nebulosity was bipolar while the intermediate nebula was more nearly circularly symmetric. The individual category 4 data sets, all of which represented 1.5 GHz observations, were too noisy to model independently. Hence all 1.5 GHz data sets were combined to form one large set for

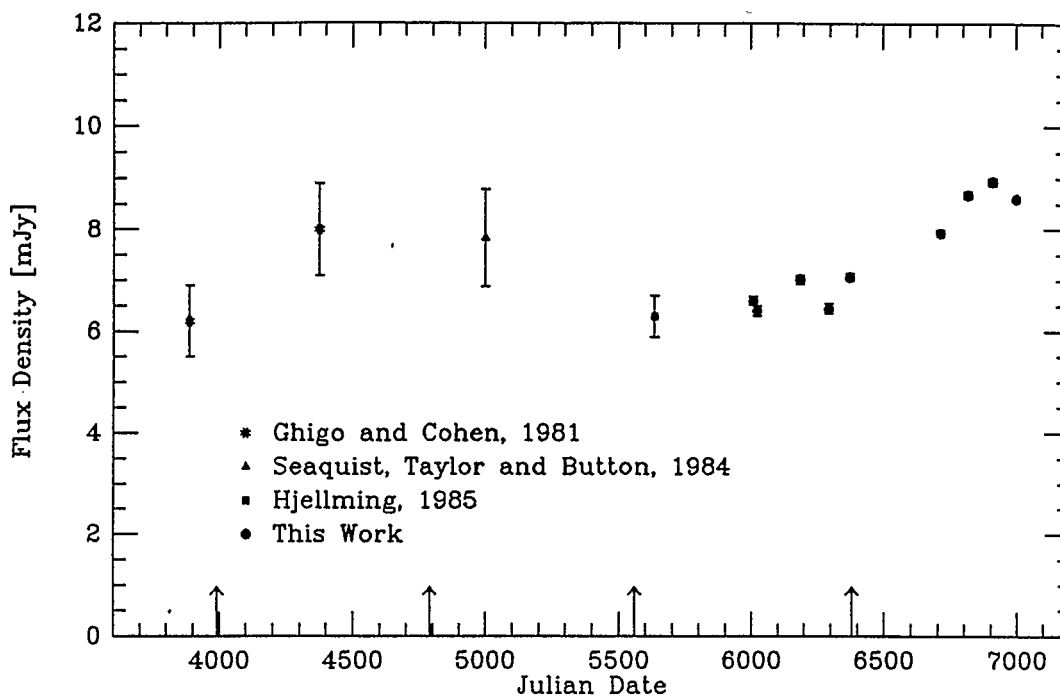


Figure 4.18: **Total Flux Density.**

Arrows in the above figure indicate optical minima (orbital phase 0).

analysis. Fits were then made to obtain appropriate parameters for the intermediate and outer nebulosities (see Figures 4.35 and 4.36). At this point, analysis of the inner, intermediate and outer nebulae was complete, and it was possible to return to the individual category 4 sets in order to determine a point source flux.

Results of analysis are tabulated in Appendix C and each of the various nebular components are discussed, in turn, below. Sample fits to the various individual data sets may be found in Appendix D. Before discussing the individual components of the system, however, it is well to consider the overall pattern, *i.e.* the total flux. Figure 4.18 shows the 5 GHz flux observed from AG Pegasi in this and previous studies. It will be remembered that total flux is determined by a simple

extrapolation of real visibilities to the zero  $(u, v)$  value ( $S_{Total} = V_R(0)$ ), and hence its values are virtually model independent. Due to large errors, little may be said from the observations made before this work except perhaps that the data was consistent with a constant total flux of about 6.5 mJy. During the observations for this study, the total flux rose progressively from 6.5 to 9 mJy. In addition, shorter term fluctuations are apparent in the total flux. It will be shown in the later discussion that these shorter term fluctuations are associated with the central object.

### 4.3 The Inner Nebula

Most observations for this study (*i.e.* data categories 1, 2, and 3) detected only the inner nebula and the central object. It has been possible to separate these two components by reference to the real visibility data, because the central source contributes merely a d.c. shift. Figure 4.19 shows the image of the inner nebula at 5 GHz for epochs 11-84 and 7-87 (natural weighting) with the point source removed. Figure 4.20 shows the same data sets mapped with uniform weighting. Features to note in the figures include: a generally circular symmetry; an increase in flux and angular size between 1984 and 1987; and, the existence of bipolar enhancements.

Sample fits to individual data sets can be found in Appendix D. For all cases, fits to the visibilities were carried out for:

- a spherically symmetric, homogeneous shell;
- a spherically symmetric wind-like shell (*i.e.*  $n_e \sim 1/R^2$ ); and

- a bipolar source (see Figure 4.14).

Spherically symmetric fits were consistently  $\sim 15\%$  better than the bipolar fits in terms of the  $\chi^2$  merit function. This implies, as do the images, that the nebula is more nearly spherically symmetric than it is bipolar. It is clear, however, from Figures 4.19 and 4.20 that bipolar enhancements do exist in the nebula and thus a completely rigorous analysis would require a two component model. Unfortunately, the real and imaginary visibility data do not suggest an obvious separation into two components; this is not surprising since the features are of about the same scale and therefore make very similar contributions to the real and imaginary visibilities. Fortunately, one-component fits produced similar results regardless of the type of model adopted. Hence, the results obtained from these one component fits may be considered accurate to a good approximation.

The results of analysis for homogeneous and wind-like shells are tabulated in Appendix C. It was found that the inner nebula is: optically thin; detached from the central source; expanding at several tens of  $\text{km s}^{-1}$ ; possibly becoming geometrically thinner with time; and brightening. The nebular mass was determined to be  $\sim 10^{-5}M_{\odot}$  and possibly increasing. These results are discussed below.

#### 4.3.1 Mass and Optical Depth

Optical depth and nebular mass may be calculated for the inner nebula from the parameters,  $\eta$ ,  $\theta_c$ , and  $A$  obtained by fitting. Optical depth through the nebular center is calculated from Equation 4.5 and table 4.2 compares the values of  $\tau$  obtained in the two extreme epochs (11-84 and 7-87). It is found that the nebula is generally optically thin and is only beginning to turn over to optical thickness

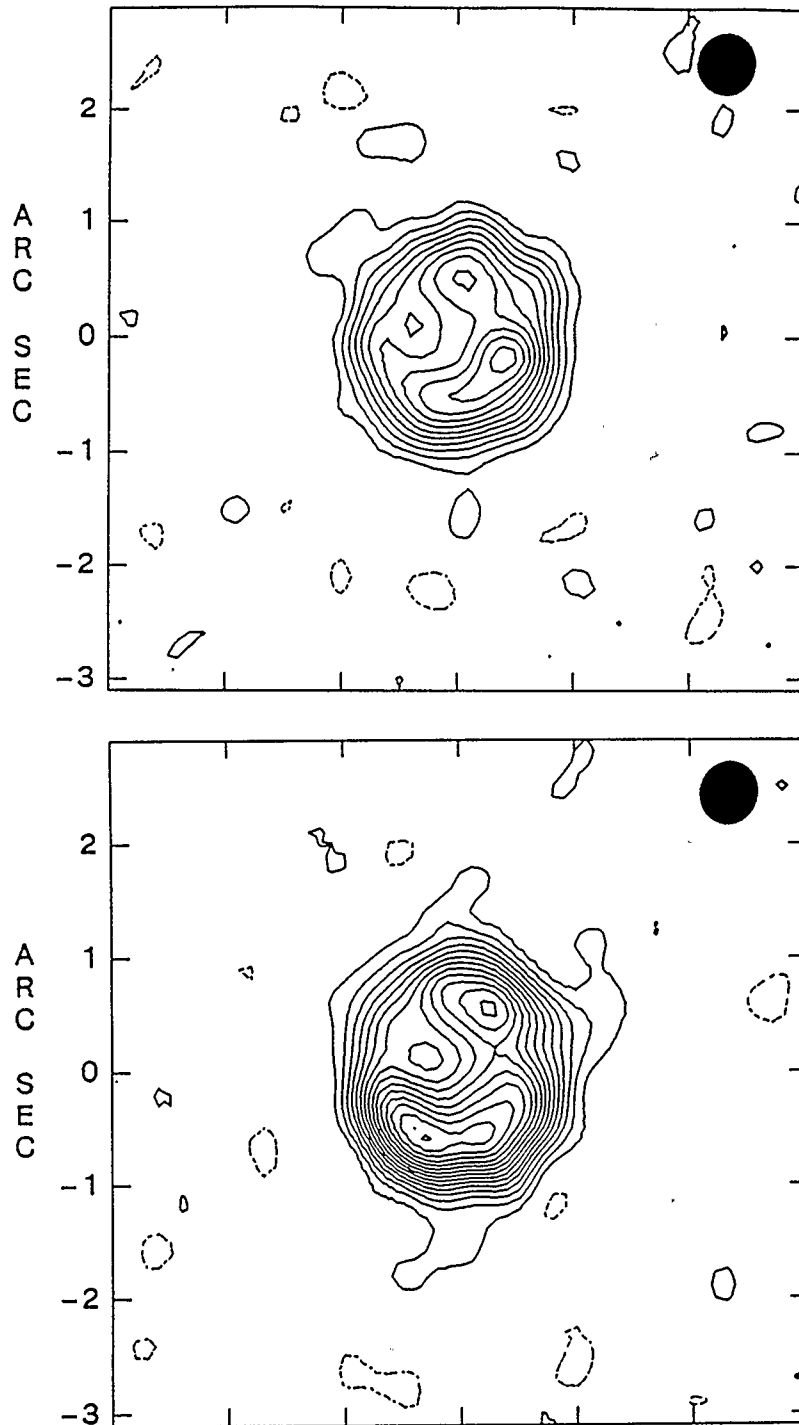


Figure 4.19: **The Inner Nebula (5 GHz): Natural Weighting**

The upper image is from epoch 11-84, and the lower from 7-87. The centres of both images are located at *Right Ascension* (RA) 21 48 36.162 and *Declination* (DEC) 12 23 27.36. Contours are drawn at intervals of 0.06 mJy/b with no contours being drawn beyond 1.2 mJy. The peak intensity is 1.623 mJy/b in 1984 and 1.804 mJy/b in 1987.

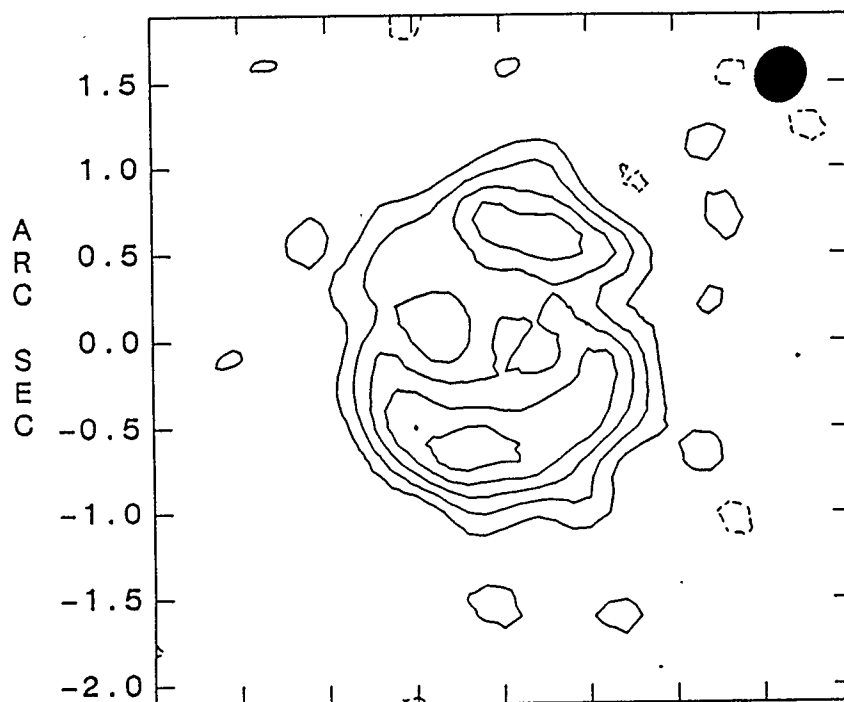
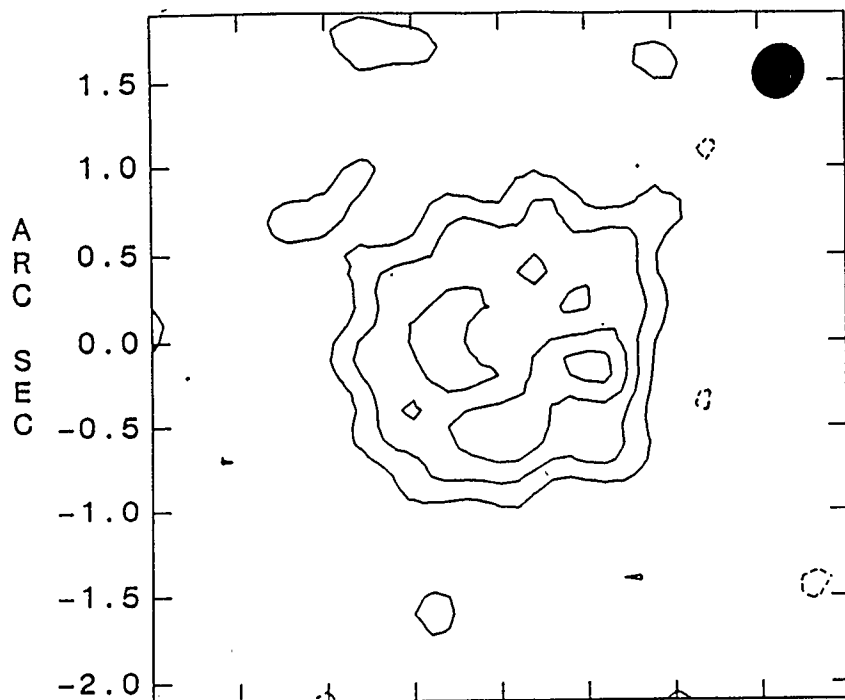


Figure 4.20: The Inner Nebula (5 GHz): Uniform Weighting

The upper image is from epoch 11-84, and the lower from 7-87. The centres of both images are located at *Right Ascension* (RA) 21 48 36.162 and *Declination* (DEC) 12 23 27.36. Contours are drawn at intervals of 0.1 mJy/b. The peak intensity is 1.409 mJy/b in 1984 and 1.628 mJy/b in 1987.

at 1.5 GHz. This result is confirmed by the average value of spectral index ( $\alpha = 0.01 \pm 0.02$ ) given in table 4.3. In this table spectral index is calculated from the fluxes at various frequencies from given epochs. Table 4.3 presents the spectral index determinations for the inner nebula. It will be remembered from Section 1.1.2 that  $\alpha = 2$  implies optical thickness;  $\alpha = -0.1$  implies optical thinness; and  $\alpha = 0.6$  implies an optically thick wind. Thus the spectral index of the inner nebula suggests optical thinness. Appendix E plots the spectral index determination for the relevant epochs.

The mass of a spherically symmetric object may be calculated by the equation:

$$M = 4\pi\mu m_H \int_{R_i}^{R_o} R^2 n_e dR \quad (4.9)$$

where:  $R_o$  and  $R_i$  are the outer and inner radii respectively;  $n_e$  is the number density of electrons;  $\mu$  is the mean molecular weight;  $m_H$  is the mass of a hydrogen atom; and  $R$  is the distance measured from the center of the object. Masses obtained for the inner nebula by the various models are shown in table 4.4, and rates of mass increase are also given. The total mass is found to be only weakly dependent upon the model assumed, and is a few  $\times 10^{-5} M_\odot$ . No increase in nebular mass has been detected to the an upper limit of  $\dot{M} \lesssim 5 \times 10^{-6} M_\odot \text{ yr}^{-1}$ .

#### 4.3.2 Shell Detachment

Analysis of the category 1 data sets indicated that the inner nebula is detached from the central object. It will be recalled that in the case of spherical symmetry  $\eta \rightarrow 0$  implies an attached nebula; *i.e.* a nebula with no central hole. The average value obtained for  $\eta$  in this analysis, was  $\bar{\eta} = 0.63 \pm 0.02$  (see table C.1), which

BAND [GHz]	EPOCH	OPTICAL DEPTH ( $\tau$ )		
		HOMO	$1/R^2$	BIPOLAR
1.5 GHz	11-84	$1.08 \times 10^{-1}$ $\pm 0.09$	$1.04 \times 10^{-1}$ $\pm 0.02$	$7.27 \times 10^{-1}$ $\pm 0.96$
	7-87	$1.23 \times 10^{-1}$ $\pm 0.09$	$1.26 \times 10^{-1}$ $\pm 0.09$	1.12 $\pm 0.01$
5 GHz	11-84	$9.03 \times 10^{-3}$ $\pm 0.8$	$8.66 \times 10^{-3}$ $\pm 0.2$	$6.07 \times 10^{-2}$ $\pm 0.8$
	7-87	$1.03 \times 10^{-2}$ $\pm 0.07$	$1.06 \times 10^{-2}$ $\pm 0.02$	$9.33 \times 10^{-2}$ $\pm 0.08$
15 GHz	11-84	$8.54 \times 10^{-4}$ $\pm 0.7$	$8.19 \times 10^{-4}$ $\pm 0.2$	$5.74 \times 10^{-3}$ $\pm 0.8$
	7-87	$9.70 \times 10^{-4}$ $\pm 0.7$	$9.98 \times 10^{-4}$ $\pm 0.2$	$8.83 \times 10^{-3}$ $\pm 0.8$
22 GHz	11-84	$3.63 \times 10^{-4}$ $\pm 0.3$	$3.48 \times 10^{-4}$ $\pm 0.07$	$2.44 \times 10^{-3}$ $\pm 0.3$
	7-87	$4.12 \times 10^{-4}$ $\pm 0.3$	$4.24 \times 10^{-4}$ $\pm 0.07$	$3.75 \times 10^{-4}$ $\pm 0.3$

Table 4.2: Optical Depth of the Inner Nebula

The designation "HOMO" above refers to fits performed with spherically symmetric models of homogeneous density. Optical depth,  $\tau$  is calculated along a line of sight through the center of the inner nebula.

EPOCH	NEBULAR FLUX [mJy]				SPECTRAL INDEX	$\chi^2/\text{pt}$
	1.5 [GHz]	5 [GHz]	15 [GHz]	22 [GHz]		
11-84	5.708 $\pm 0.4$	4.91 $\pm 0.3$	1.67 $\pm 1.3$	15.72 $\pm 13$	-0.083 $\pm 0.05$	1.71
5-85	-	5.04 $\pm 0.3$	5.03 $\pm 0.6$	6.05 $\pm 3.2$	0.015 $\pm 0.11$	0.164
10-86	-	6.73 $\pm 0.3$	5.79 $\pm 0.3$	9.22 $\pm 1.3$	-0.05 $\pm 0.06$	4.17
7-87	6.826 $\pm 0.3$	7.62 $\pm 0.1$	5.27 $\pm 0.8$	-	0.060 $\pm 0.03$	2.85

Table 4.3: Spectral Index of the Inner Nebula

MODEL	EPOCH	MASS [ $M_{\odot} \times 10^{-5}$ ]	$\dot{M}$ [ $M_{\odot} \text{ yr}^{-1} \times 10^{-6}$ ]
HOMOGENEOUS	11-84	$3.17 \pm 1.30$	$2.20 \pm 5.3$
	7-87	$3.76 \pm 0.64$	
$1/R^2$	11-84	$3.34 \pm 0.58$	$2.13 \pm 2.5$
	7-87	$3.91 \pm 0.32$	
BIPOLAR	11-84	$1.15 \pm 0.13$	$0.094 \pm 0.06$
	7-87	$1.40 \pm 0.11$	

Table 4.4: Mass of the Inner Nebula

is not consistent with an attached shell. For bipolar fits,  $\zeta$  is defined in a manner similar to  $\eta$  (see Figure 4.14) and attachment is implied by the condition  $\zeta \rightarrow 1$ . Bipolar fits, however yield an average value of  $\bar{\zeta} = 0.52 \pm 0.02$  which again is not consistent with an attached nebula. Figure 4.21 plots  $\eta$  for homogeneous shell fits. The best fit line gives  $\bar{\eta} = 2 \pm 1 \times 10^{-4}$ ; this is not a statistically significant result.

### 4.3.3 Expansion

One of the most exciting results of this study is that the inner nebula has been shown to be expanding, and an expansion velocity has been measured. The growth in extent of the inner nebula is illustrated in Figure 4.22. In this figure high resolution, A configuration, 5 GHz data is plotted for epochs 11-84 and 7-87. The central object has been removed from both data sets and the nebular flux has been scaled so that  $V_R(0)$  is the same for both epochs. As demonstrated in Figure 4.9 the effect of increasing the angular size of a nebula by a factor,  $a$ , is to scale the  $uv$ -distance axis inward by a factor  $1/a$ . The inward scaling of the visibility curve between 1984 and 1987 is clearly manifest in Figure 4.23.

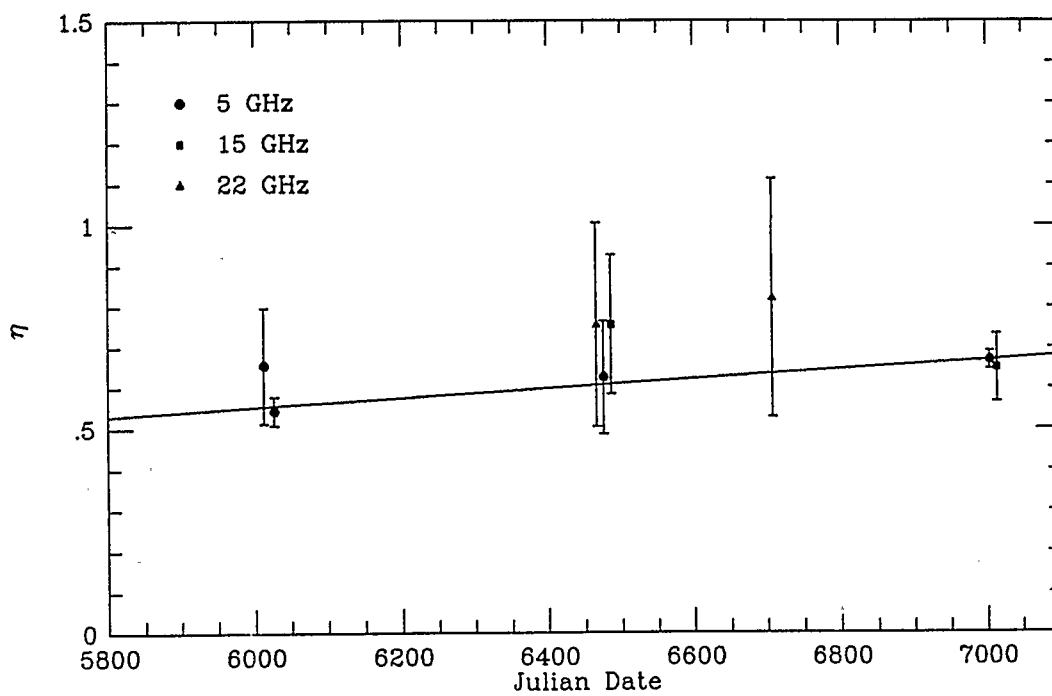


Figure 4.21: Determination of  $\eta$  for the Inner Nebula

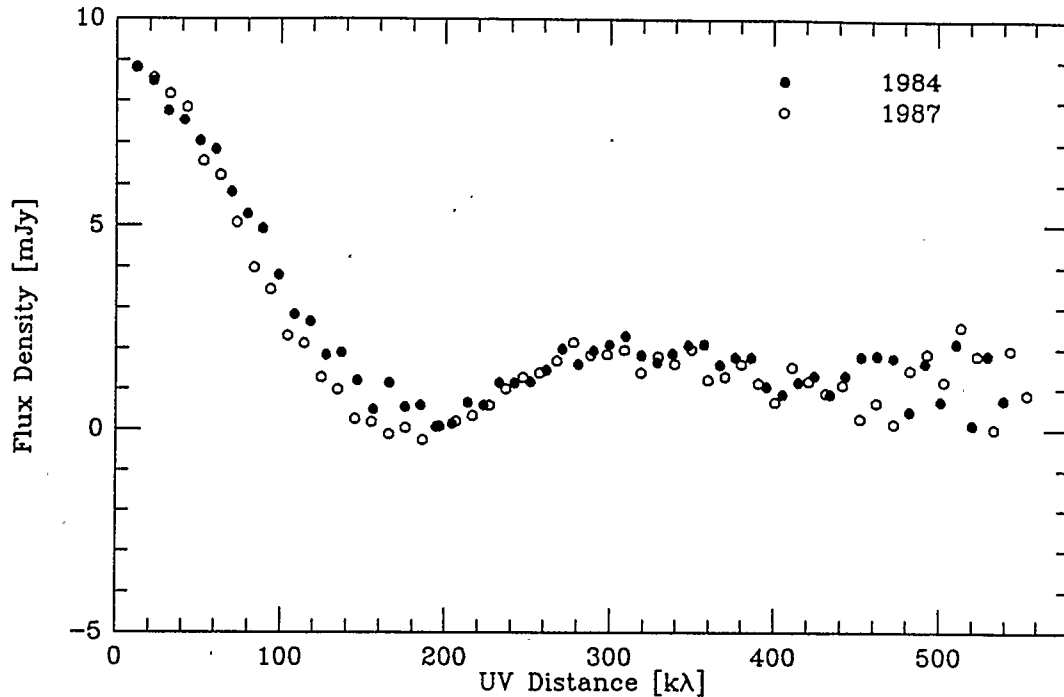


Figure 4.22: **Demonstration of Expansion: Inner Nebula**

In the two 5 GHz data sets plotted above from 11-84 and 7-87, the central object has been removed and the nebular flux has been scaled to the 1987 value. The scaling inward of the  $uv$ -distance axis indicates that expansion has taken place between the two epochs. Individual curves are plotted (with error bars) in Figures D.2 and D.9.

The details of nebular development are summarized in table 4.5. This table considers spherically symmetric and bipolar models and tabulates expansion velocities for  $\theta_e$ , the center on mass radius, and the rate of change of nebular thickness  $\Delta\theta$ . Velocities for inner and outer radii,  $\theta_i$  and  $\theta_o$ , respectively, are also calculated for spherically symmetric models.

In the case of spherically symmetric models, the inner radius seems to be expanding more quickly than the outer radius, giving rise to a narrowing shell;  $\frac{d(\Delta\theta)}{dt} \sim -100 \text{ km s}^{-1}$ . Bipolar models, however, suggest that the nebular thickness

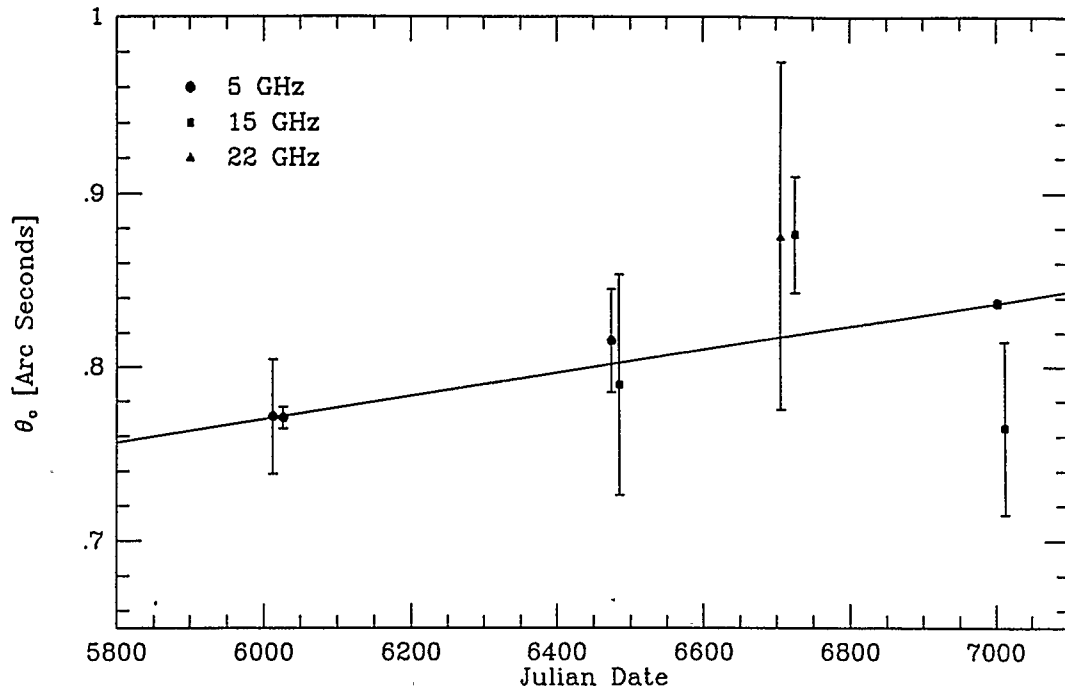


Figure 4.23: **Expansion of the Inner Nebula: Center of Mass Radius**  
 A homogeneous shell model is assumed for the data points plotted in this figure.

is remaining constant. Both types of model, however, indicate that the “center of mass” of the nebula is moving outward at several tens of  $\text{km s}^{-1}$ ; this result, then, possesses a degree of model independence. The average value of expansion is  $\dot{\theta}_c = 65 \pm 12 \text{ km s}^{-1}$ .

In practice, the measurements of expansion were constrained almost exclusively by the two data sets quoted in table 3.5. Figures 4.23 to 4.26 demonstrate that the less sensitive data sets provided results which were consistent with those given in table 3.5.

Before leaving the topic of expansion a number of interesting points may be raised. One will note from Figures 4.19 and 4.20 that while the overall structure

PARAMETER	MODEL	["] 11-84	["] 7-87	VELOCITY		< t > [yr]
				$\frac{\text{milli}''}{\text{yr}}$	km s <sup>-1</sup>	
$\theta_c$	HOMO	0.771 ± 0.006	0.837 ± 0.002	24 ± 2	69 ± 7	35 ± 3
	1/R <sup>2</sup>	0.82 ± 0.02	0.86 ± 0.008	14 ± 8	40 ± 20	63 ± 36
	BIPOLAR	0.646 ± 0.008	0.704 ± 0.005	21.72 ± 3.5	66 ± 11	32 ± 5.2
$\Delta\theta$	HOMO	0.42 ± 0.03	0.32 ± 0.02	-42 ± 9	-120 ± 30	7.7 ± 1.7
	1/R <sup>2</sup>	0.46 ± 0.02	0.37 ± 0.02	-35 ± 9	-100 ± 25	10.8 ± 2.8
	BIPOLAR	1.73 ± 0.56	1.711 ± 0.5	-	-	-
$\theta_o$	HOMO	0.94 ± 0.02	0.98 ± 0.01	12 ± 7	33 ± 20	84 ± 49
	1/R <sup>2</sup>	1.03 ± 0.04	1.03 ± 0.02	-	-	-
$\theta_i$	HOMO	0.52 ± 0.03	0.65 ± 0.02	40 ± 10	120 ± 30	15.2 ± 3.8
	1/R <sup>2</sup>	0.65 ± 0.02	0.74 ± 0.01	30 ± 7	84 ± 20	25 ± 5.8

Table 4.5: Development of the Inner Nebula

In the above table:  $\theta_c$  refers to the "center of mass" of the nebula;  $\Delta\theta$  to the thickness of the nebula;  $\theta_o$  to the outer radius; and  $\theta_i$  to the inner radius. The column < t > gives the kinematic age for  $\theta_c$ ,  $\theta_o$ , and  $\theta_i$ ; for  $\Delta\theta$  it gives the time required for nebular thickness to go to zero if the current "expansion" continues. The homogeneous shell model is designated "HOMO".

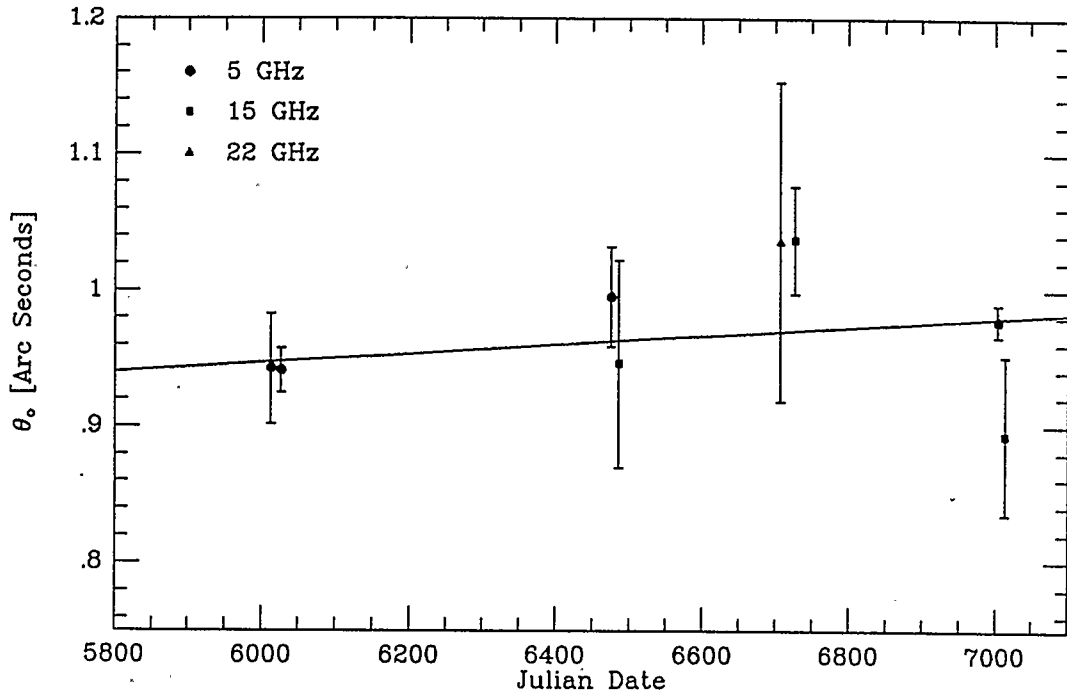


Figure 4.24: Expansion of the Inner Nebula: Outer Radius  
A homogeneous shell model is assumed for the data points plotted in this figure.

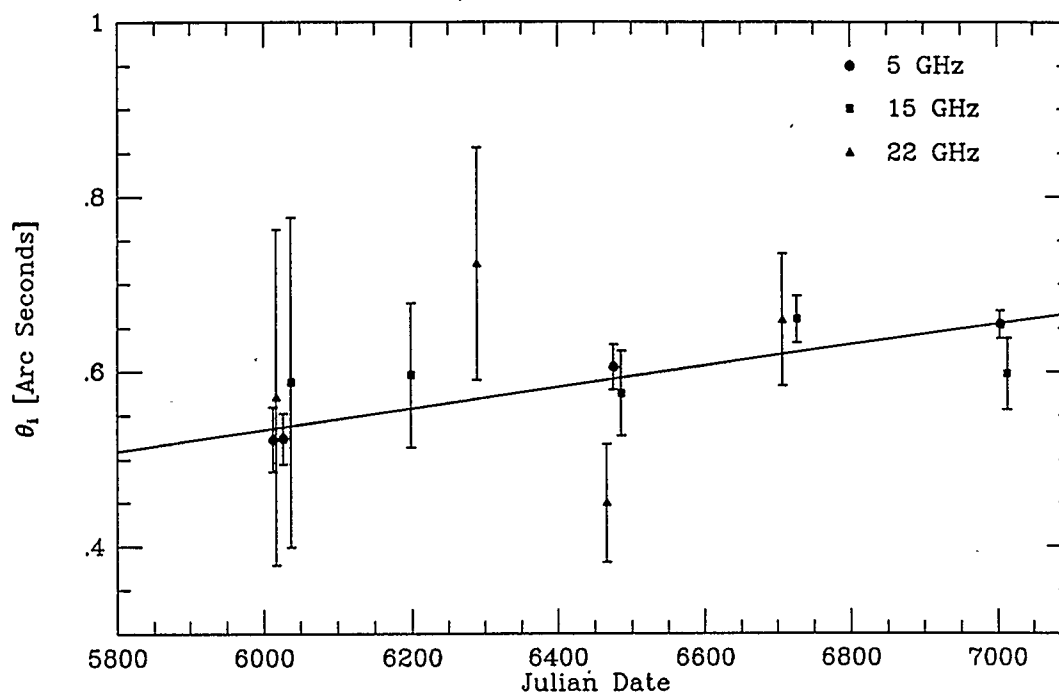


Figure 4.25: Expansion of the Inner Nebula: Inner Radius  
A homogeneous shell model is assumed for the data points plotted in this figure.

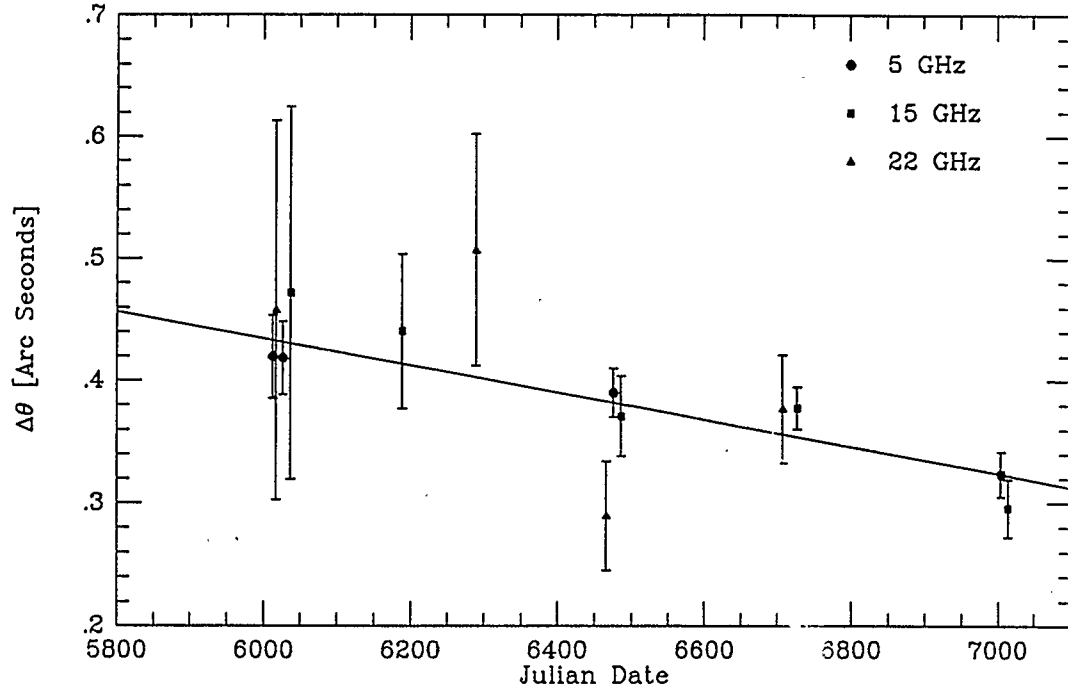


Figure 4.26: Changing Thickness of the Inner Nebula

A homogeneous shell model is assumed for the data points plotted in this figure. Bipolar fits suggest that the nebular thickness is remaining constant.

of the nebula in 1984 and 1987 appears largely circularly symmetric, the expansion seems to be bipolar. Further, the “axis of expansion” lies almost directly in line with the lobe enhancements (NW-SE) of the nebula. Finally, although radial symmetry seems to have been maintained between 1984 and 1987, the lobe enhancements apparent in both epochs appear to have shifted.

#### 4.3.4 Nebular Flux and Electron Density

The determined values of nebular flux are given in table C.3. These values were obtained by subtracting the point source flux,  $s$ , from the total flux determined by a fitted curve (Total flux =  $V_R(0)$ ). The values obtained at 5 GHz are plotted in Figure 4.27 along with the result obtained earlier by Hjellming (1985). During the period of this study’s observations, the flux has increased from 5 to 8 mJy.

Nebular flux may increase for a number of reasons, including (*e.g.*): a decrease in temperature; an increase in ionized mass; or an increase in density. It has already been argued that the electron temperature is  $\sim 10^4$  K (Section 4.1.1), and the observations do not contradict this assumption. On the other hand the nebular mass may be increasing (see table 4.4), although results suggest that  $\dot{M} <$  a few  $\times 10^{-6} M_{\odot} \text{ yr}^{-1}$ . If mass is increasing this would certainly contribute to an increasing flux. Modelling suggests that increasing density also contributes to the increased flux (see table C.4). Note that an increasing density is not presupposed even by the spherically symmetric models. The spherical models indicate that the nebula is becoming thinner, but the nebula is also expanding, and so the nebular thickness could be decreasing while the volume is increasing. It will be remembered that the number density of electrons is given by  $n_e = A/B^{\beta}$  where  $A$  is a model

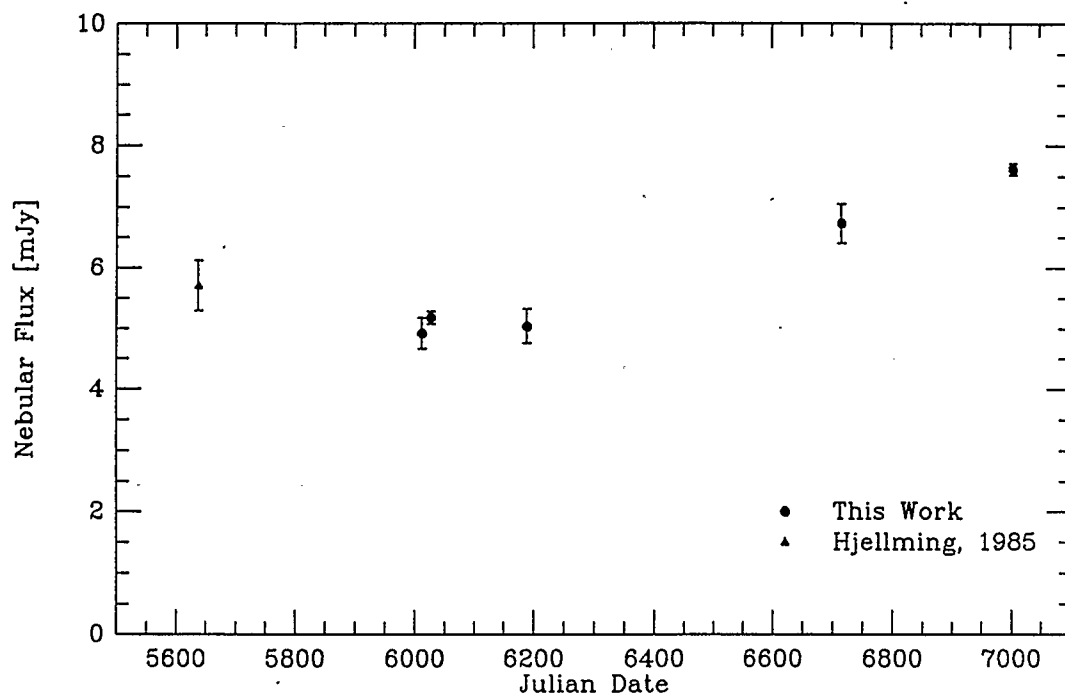


Figure 4.27: Flux of the Inner Nebula

Data points correspond to 5 GHz observations with modelling performed to a homogeneous spherically symmetric shell.

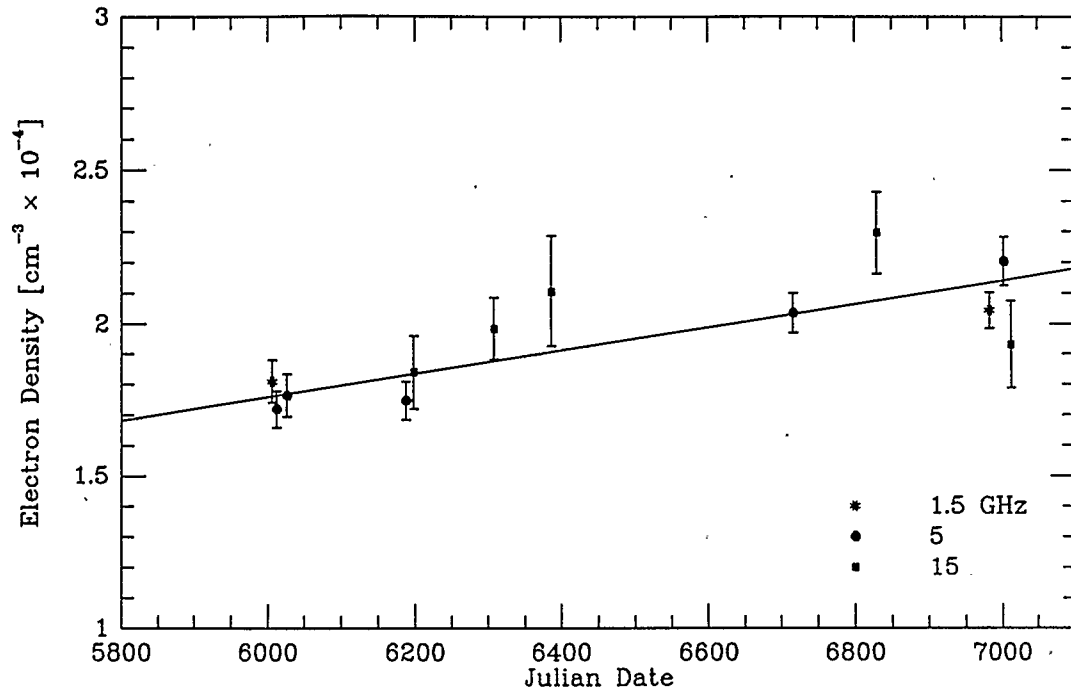


Figure 4.28: **Electron Density of the Inner Nebula**

Data points correspond to 5 GHz observations with modelling performed to a homogeneous spherically symmetric shell.

parameter,  $R$  is distance measured from the nebular center, and  $\beta$  is a constant ( $\beta = 0$  for homogeneous nebulae and  $\beta = 2$  for wind-like nebulae). Figure 4.28 shows the evolution of electron density in the inner nebula under the assumption of spherical symmetry. Bipolar fits suggest a density which is 2-3 times higher than that of spherical fits, however, a similar increase in density ( $\sim 25\%$ ) is still found.

A very important detail about the inner nebula which one might hope to determine in a study such as this is the density law. It has already been noted, for instance, that spherically symmetric models provide fits  $\sim 15\%$  better than bipolar ones; this implies that the spherically symmetric nature of the nebula is dominant.

If one wishes to go further and determine whether the nebula is homogeneous ( $\beta = 0$ ) or wind-like ( $\beta = 2$ ) the problem intensifies.

Figure 4.29 compares curves produced by homogeneous and  $1/R^2$  density laws for spherically symmetric nebulae with the same inner and outer radii. While these curves are distinguishable, it will be remembered that the parameter  $\theta_c$  may be used to scale the x axis, and hence the curves may be brought to very close correspondence by adjustment of  $\theta_c$ . When curves are fitted by a  $\chi^2$  analysis, this is precisely what happens. Figure 4.30 shows two curves which are fitted to the same data set; the two density laws are able to produce essentially identical curves. There are, however, small differences; the  $1/R^2$  laws, for instance, provides a somewhat more extended second maximum. In some cases such subtle differences might have a small effect upon the ability to fit a curve. Table C.7 compares the ability of homogeneous and  $1/R^2$  laws to fit the inner nebula. Only marginal differences are indicated and these favor the homogeneous model slightly. It must be concluded that this study has been unable to distinguish between density laws.

If spherical symmetry is assumed, a  $1/R^2$  density law is difficult to explain. It has been shown that the nebula appears to be becoming thinner. In this case, it must be supposed that some manner of compression is being exerted. The necessary pressure could arise from the inside or the outside edge of the nebula, or from both. It has also been shown that density is increasing significantly and in the case of a homogeneous nebula, a compression could account for this effect. It is improbable that a  $1/R^2$  density law could persist under such circumstances. For the law to be maintained, the constant  $A$  in the equation  $\text{density} = A/R^2$  would somehow have to be increased; it is not obvious how this might occur. The compression

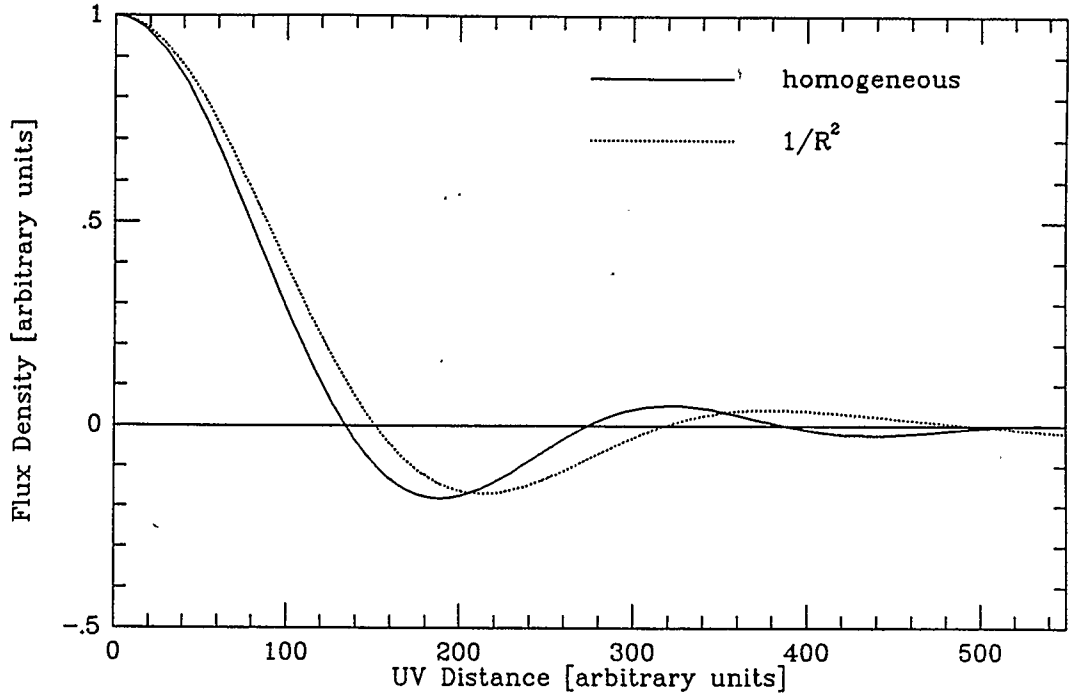


Figure 4.29: A Comparison of Homogeneous and  $1/R^2$  Density Laws

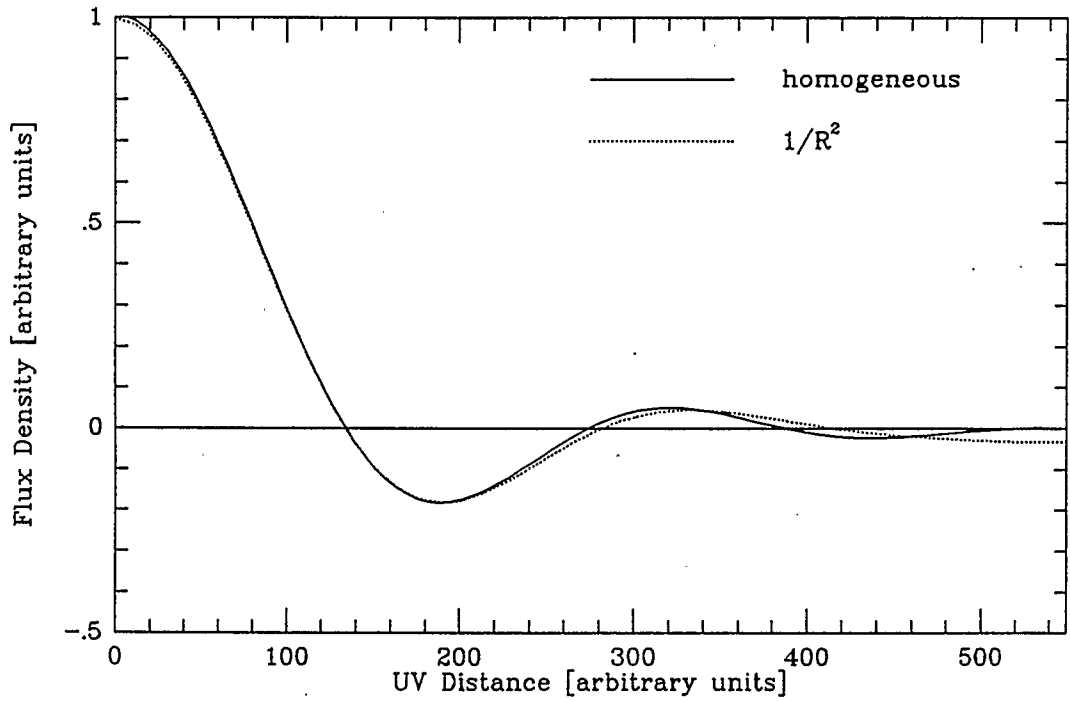


Figure 4.30: Fitting to Homogeneous and  $1/R^2$  Density Laws

would, rather, tend to destroy a  $1/R^2$  density law even if it originally existed. This argument would predict that the inner nebula is more nearly homogeneous than wind-like. The argument itself, however, involves interpretations and it must be admitted that the observations themselves are not able to distinguish between density laws. The implications of the dynamics of the inner nebula will be discussed in the context of models for the system in Chapter 5.

#### 4.4 The Central Source

While discussion of the inner nebula of AG Pegasi has dominated this chapter, the central source is interesting in its own right. The central source coincides with the portion of the symbiotic system that underlies most of the optical emission. Table C.6 reveals that the central source is variable, and this result is plotted in Figure 4.31 for the 5 GHz data sets. Plots for 15 and 22 GHz are given in Appendix F. In all of these plots a periodicity is suggested which corresponds to the orbital period of  $\sim 800$  days. The optical minimum in 1985 occurred at *Julian Date* (JD) 244 6379 (Boyarchuk *et al.* 1987) and agrees well with the minimum suggested by the radio curves. To test the validity of the suggested periodicity, the data are folded into the appropriate period and plotted as a function of orbital phase. The 5 GHz result is shown in Figure 4.32 and the remainder are given in Appendix F. In these plots, the periodic pattern is reinforced suggesting that radio emission from the inner nebula does in fact vary in phase with optical light and orbital motion.

Another interesting characteristic of the central source is the spectral index,  $\alpha$ , defined by the relationship  $S_\nu \propto \nu^\alpha$  where  $S_\nu$  is the flux at frequency  $\nu$ . Spectral

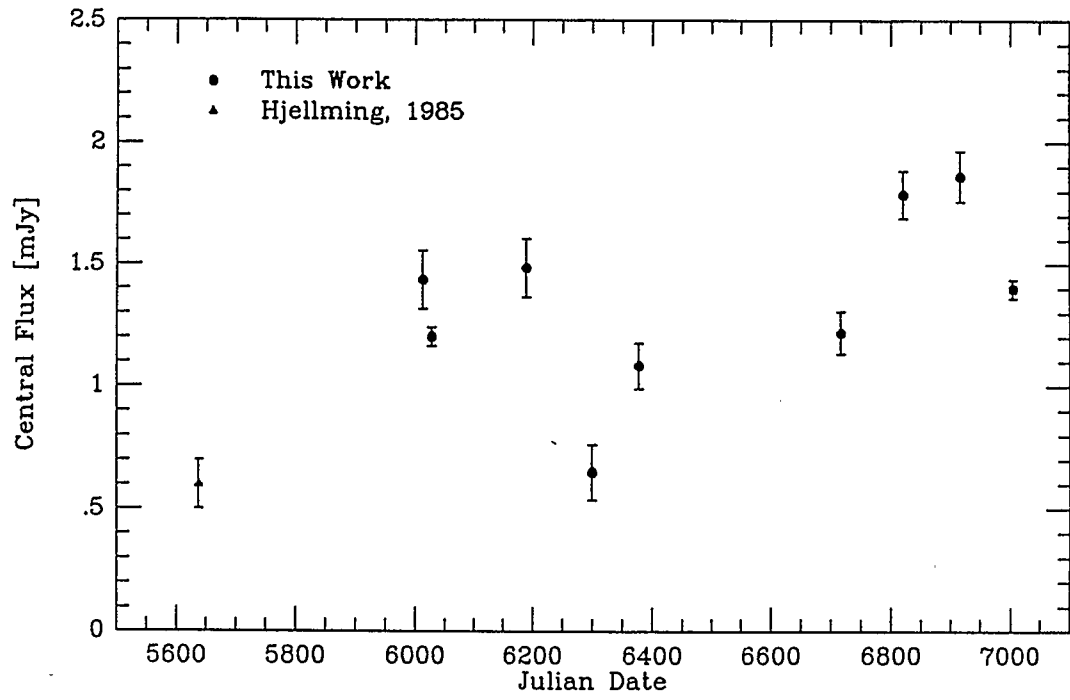


Figure 4.31: Central Source Flux Density: 5 GHz

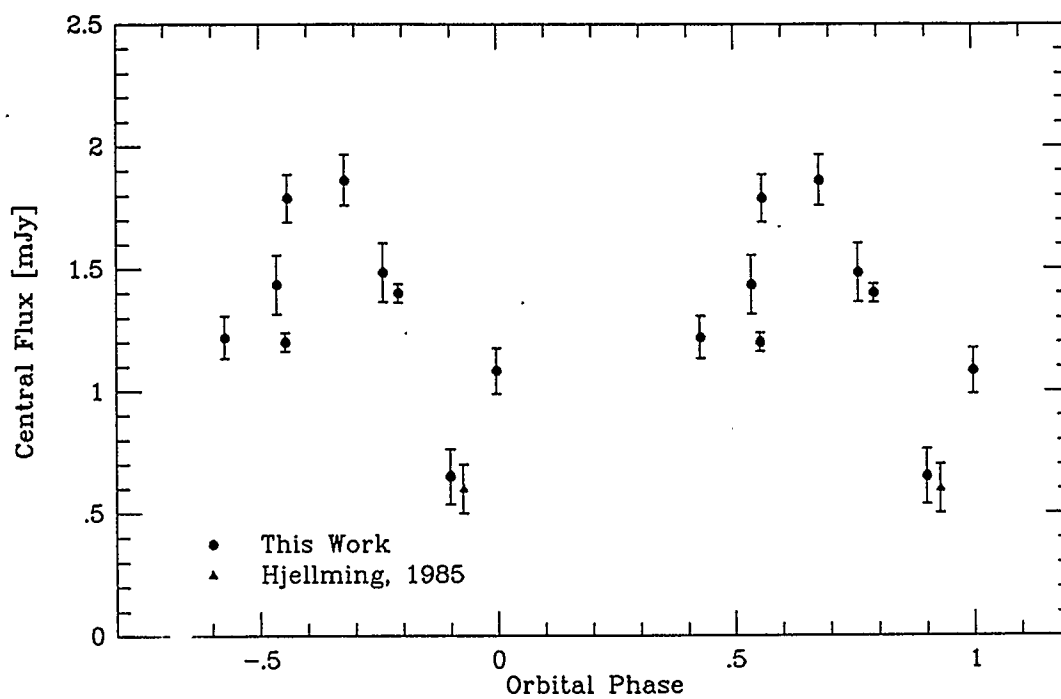


Figure 4.32: Flux Density versus Orbital Period: Central Source

In this figure, the central source flux density at 5 GHz is folded into the orbital period of the binary system. The period is taken to be 796 days (Garcia and Kenyon 1988) and the minimum is taken at JD 244 6379 (Boyarchuk *et al.* 1987).

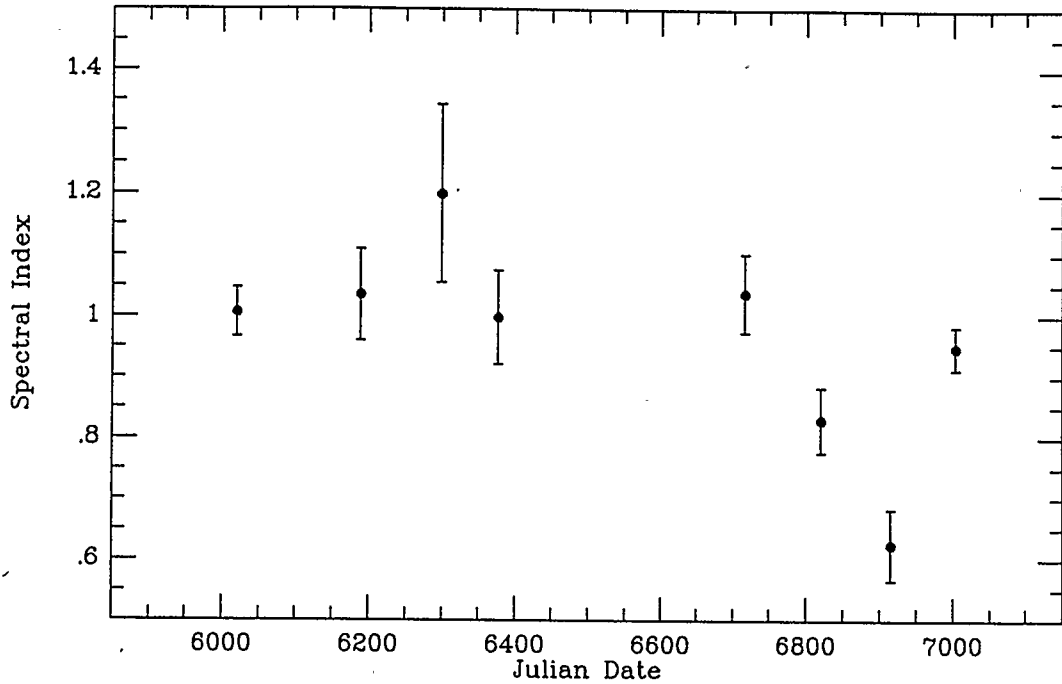


Figure 4.33: Spectral Index of the Central Source

index is determined, in practice, by fitting a line to a log-log plot of flux density vs frequency;  $\alpha \propto \log(S_\nu)/\log(\nu)$ . Table 4.6 and Figure 4.33 show the determination of  $\alpha$  for all epochs. The average value of  $\alpha$  is  $\sim 1.1$  which suggests a source which is partially optically thick:  $\alpha = 2$  implies optical thickness;  $\alpha = -0.1$  implies optical thinness; and  $\alpha = 0.6$  implies an optically thick wind. Variations in the spectral index may correspond to orbital phase as they did for flux. Figure 4.34 folds the spectral index curve into the orbital period. An effect is weakly suggested, however, it is not nearly so convincing as the flux density variation. Only the point at phase 0.7 (or -0.3) shows significant departure from a constant value.

The central radio object is presumed to be another nebula too small to be

EPOCH	CENTRAL FLUX [mJy]				SPECTRAL INDEX	$\chi^2$
	1.5 [GHz]	5 [GHz]	15 [GHz]	22 [GHz]		
11-84	0.509 $\pm 0.136$	1.434 $\pm 0.120$	3.818 $\pm 0.175$	6.004 $\pm 6.766$	1.01 $\pm 0.04$	1.26
	-	1.200 $\pm 0.033$	-	-		
5-85	-	1.485 $\pm 0.120$	5.070 $\pm 0.227$	5.657 $\pm 0.861$	1.04 $\pm 0.08$	1.54
8-85	-	0.650 $\pm 0.113$	2.877 $\pm 0.153$	2.082 $\pm 0.635$	1.20 $\pm 0.14$	3.14
11-85	-	1.083 $\pm 0.094$	3.607 $\pm 0.146$	3.829 $\pm 0.537$	1.00 $\pm 0.08$	2.25
2-86	-	0.456 $\pm 0.078$	4.265 $\pm 0.188$	-0.80 $\pm 0.647$	2.00 $\pm 0.20$	-
10-86	-	1.220 $\pm 0.088$	4.233 $\pm 0.131$	4.644 $\pm 0.523$	1.04 $\pm 0.06$	3.12
1-87	-	1.788 $\pm 0.097$	4.498 $\pm 0.165$	6.597 $\pm 0.729$	0.83 $\pm 0.05$	0.06
4-87		1.863 $\pm 0.103$	3.842 $\pm 0.168$	4.128 $\pm 0.736$	0.63 $\pm 0.06$	0.40
7-87	0.437 $\pm 0.114$	1.400 $\pm 0.033$	4.050 $\pm 0.138$	-	0.95 $\pm 0.04$	0.12

Table 4.6: Spectral Index of the Central Source

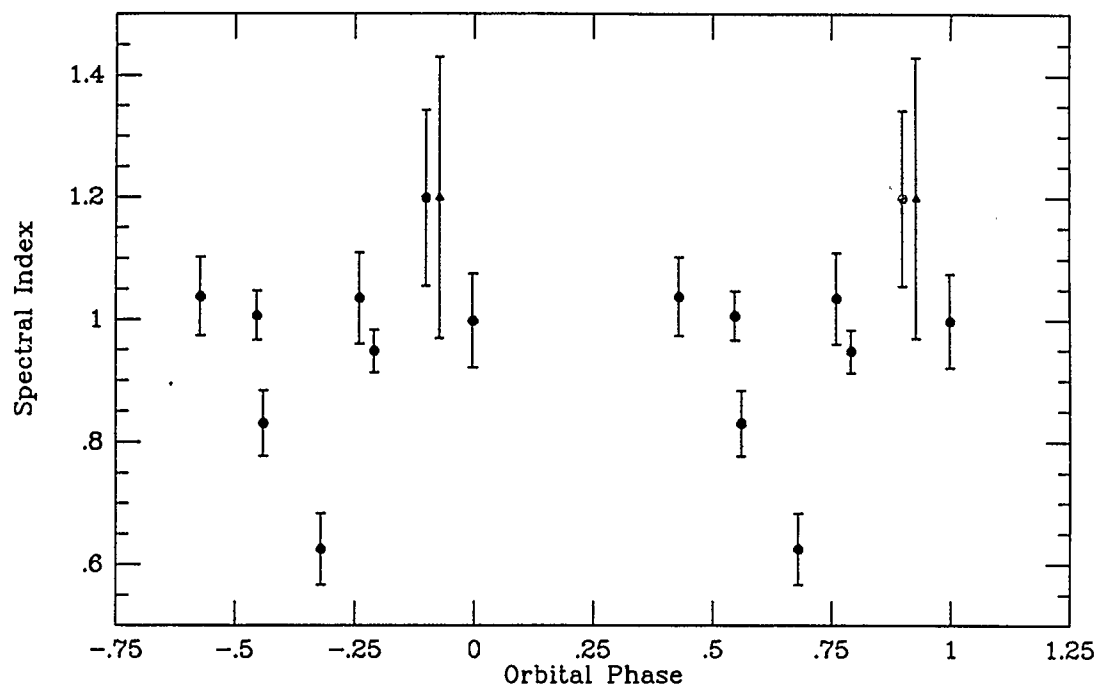


**Figure 4.34: Spectral Index Variations of the Central Source**

In this figure, the spectral index curve is folded into the orbital period of the binary system. The period is taken to be 796 days (Garcia and Kenyon 1988) and the minimum is taken at JD 244 6379 (Boyarchuk *et al.* 1987). The triangular point is from Hjellming (1985).

resolved by the VLA. It is however tightly associated with the stellar components, and has remained unresolved since 1983 (Hjellming 1985). If this nebula were completely optically thick ( $\tau \rightarrow \infty$ ), with a temperature of  $2 \times 10^4$  K as suggested by Boyarchuk (1967b), it would have a radius of  $\sim 0.017''$ . This angular size gives a linear distance of  $1.8 \times 10^{14}$  cm at 600pc, or approximately four times the binary separation ( $a \sim 4.2 \times 10^{13}$  cm, Hutchings *et al.* 1975). An object of that radius would be unresolved even at 22 GHz in A configuration at the VLA (HPBW =  $0.08''$ ) and this is indeed what is observed. It may also be noted that if the object is expanding, it must have a velocity of  $< 70$  km s $^{-1}$  so as to have remained unresolved for the last 3.5 years. It appears that this central nebulosity exists in some sort of steady state.

#### 4.5 The Intermediate and Outer Nebulae

The intermediate and outer nebulae were only detected in the category 4 data sets where data at small  $(u, v)$  values was obtained. All of these data sets were concatenated to produce the real visibility curve shown in Figure 4.35. The real visibilities of the concatenated data set provided the best information about the intermediate and outer nebulae since individual type 4 sets were too noisy to model independently. The concatenated imaginary visibilities were approximately zero indicating that the observed source possessed either circular or bipolar symmetry. An example of imaginary visibility data which suggests radial symmetry may be found in Figure 4.1.

The solid line in Figure 4.35 corresponds to the inner nebula, and for the

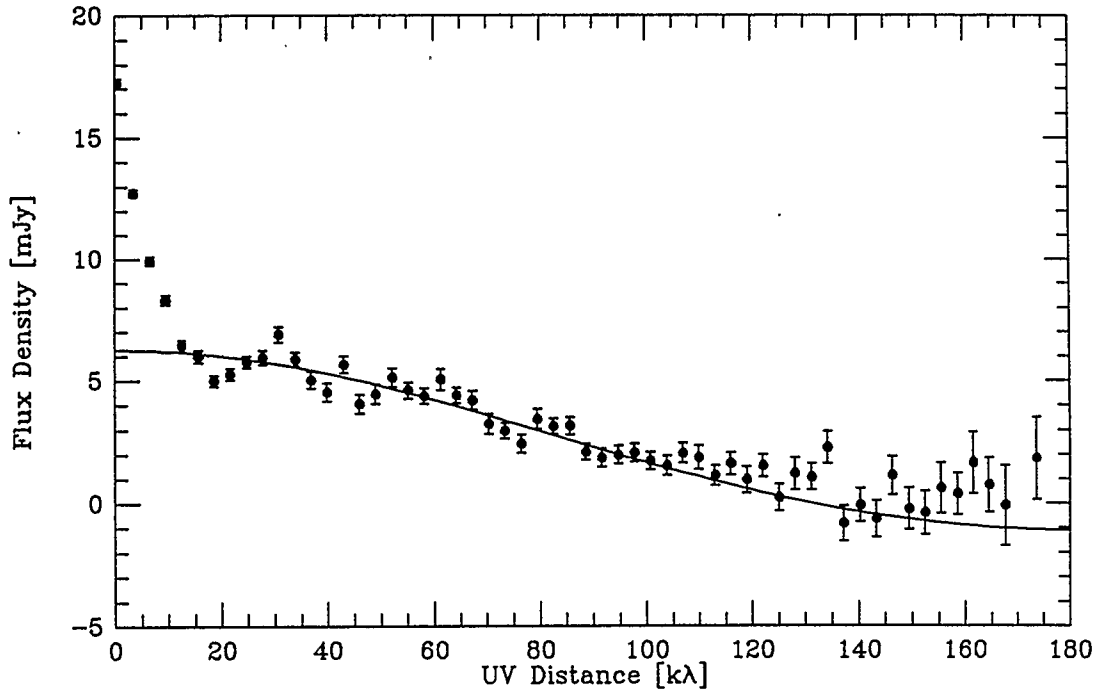


Figure 4.35: Concatenated 1.5 GHz Data Sets: Real Visibilities

In the above figure, plotted points correspond to the real visibilities of the combined 1.5 GHz data. The solid line corresponds to the contribution from the inner nebula. The sharp rise in amplitude at low  $uv$  distance, and the ripple about the solid line arise from the intermediate nebula and the outer, bipolar nebula.

purposes of modelling it was easily subtracted from the visibilities. In order to fit a model visibility curve, it was necessary to refer to the images (Figure 3.5 and 3.6) to obtain an approximate solution for the outer nebula. The outer nebula was taken to consist of two spheres of radius  $5''$  separated from each other by  $50''$  and contributing a combined flux of 4 mJy. When transformed to the visibility domain, the outer nebula accounted for the sharp peak at short baselines ( $uv$  distance). With this approximate solution for the outer nebula, spherical and bipolar fits were then performed for the intermediate nebula. Spherical models resulted in nebular shells detached from the inner nebula. The fit to a homogeneous shell yielded an outer radius of  $9''$  and an inner radius of  $6''$ . A bipolar model for the intermediate nebula is undetached; *i.e.* the inner edge of the intermediate nebula coincides with the outer edge of the inner nebula. The best bipolar fit gives the inner and outer edges of the bipolar features at  $2''$  and  $7''$  respectively. Both model fits are shown in Figure 4.36. There is evidence outside of this study that bipolar features exist with dimensions of the intermediate nebula. Fuensalida *et al.* (1988, see Section 1.2.1) have found significant bipolar  $H_\alpha$  emission arising at  $\sim 5''$  displacement from the system center and having position angle in rough agreement with the apparent enhancements of the intermediate nebula in Figure 3.5. The mass calculated for the intermediate nebula is  $10^{-4} - 10^{-3} M_\odot$ .

To estimate a mass for the outer nebula a number of constraints may be inferred. First of all, the nebula must be optically thin since otherwise it would be difficult to explain the inability of self calibrated 5 GHz observations to detect it at the expected level; it is believed that the smaller beam at 5 GHz resolves the nebula away. An upper limit of  $5''$  may be set for the radius of the bipolar features because

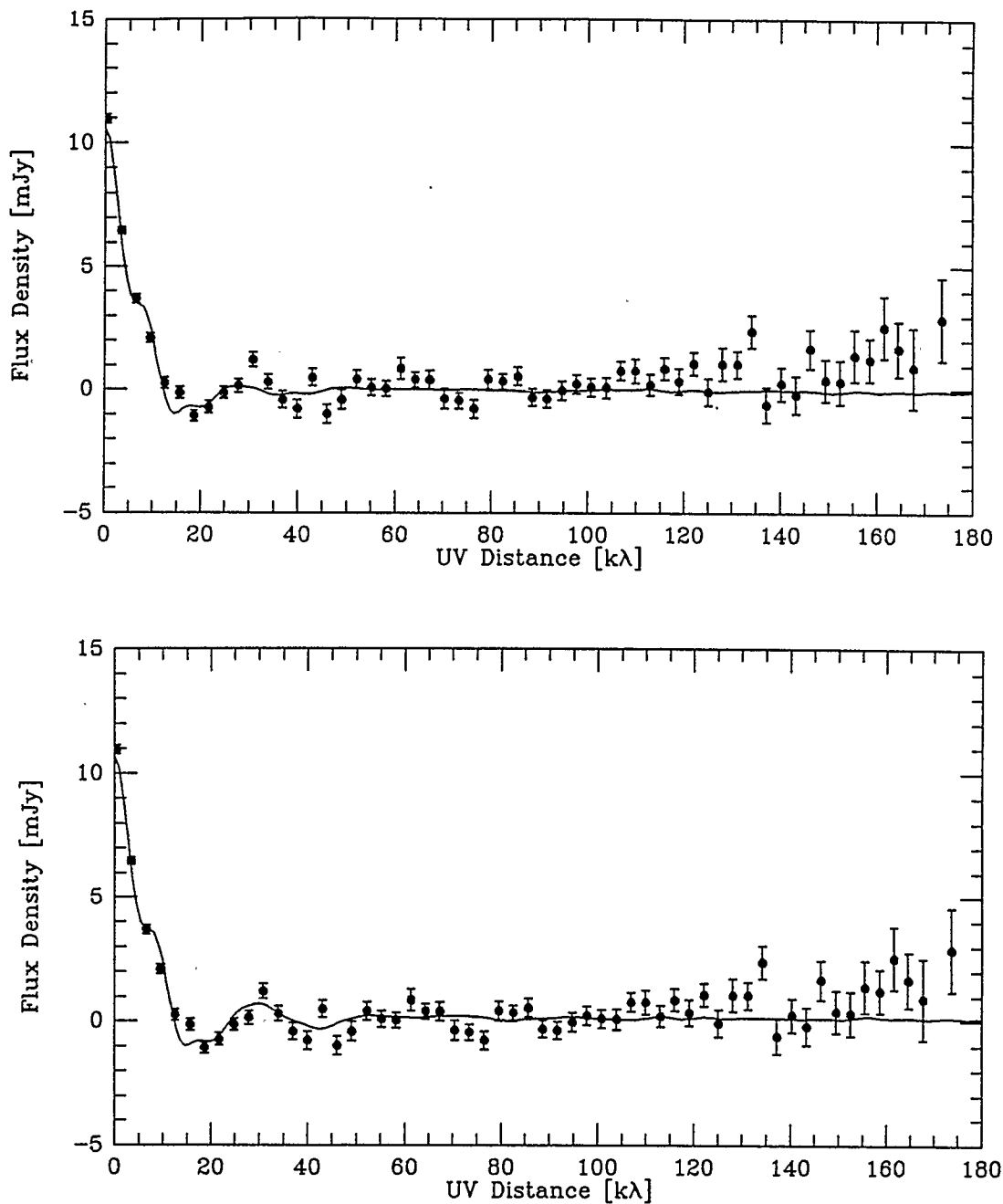


Figure 4.36: Model Visibilities: Intermediate and Outer Nebulae

The upper plot corresponds to a bipolar fit to the intermediate nebula and indicates that the data is consistent with a bipolar wind which extends inward to the inner nebula. The lower plot corresponds to a spherically symmetric fit to the intermediate nebula and suggests that under this geometry the nebula must be detached from the inner nebula.

they are unresolved, or barely resolved by a  $10''$  beam at 1.5 GHz. A lower limit to the radius of the features may be set at  $1''$  since a smaller size would imply that 5 GHz observations should not suffer from resolution effects. Finally, the 1.5 GHz flux of the nebula is known to be approximately 4 mJy. The total flux of an optically thin nebula is given by the expression:

$$S_\nu = 5.7 \times 10^{-56} T^{-1/2} g_{ff}(\nu, T) E D^{-2} \quad (4.10)$$

where  $g_{ff}(\nu, T) = \frac{\sqrt{3}}{\pi} \left[ 17.7 + \ln \left( \frac{T^{3/2}}{\nu} \right) \right]$

and  $E = \int_{source} n_e^2 dV$

where:  $S_\nu$  [mJy] is the observed flux at frequency  $\nu$  [Hz];  $T$  [K] is electron temperature;  $D$  [kpc] is distance to the nebula;  $g_{ff}$ , the gaunt factor, is a dimensionless quantum mechanical correction factor corresponding to thermal bremsstrahlung (free-free) emission; and  $E$  [ $\text{cm}^{-3}$ ] is known as the emission measure.

Knowledge of the flux density, temperature and extent of a source yields an estimate of the average electron density, which in turn provides an estimate of the total mass. The density implied for a homogeneous, spherically symmetric, optically thin nebula of radius  $3'' \pm 2''$  and flux (bremsstrahlung) of 4 mJy, at 1.5 GHz, located at 0.6 kpc is  $1.6 \times 10^3 \text{ cm}^{-3}$ . The implied mass is then  $1.2 \pm 0.9 \times 10^{-4} M_\odot$ .

## 4.6 Data from Epoch 2-86

While the data sets of the AG Pegasi data base generally showed regular development from one epoch to the next, the data from the 2-86 epoch did not fit the pattern. It differed so strongly from the other epochs in fact that it was not included in the general analysis.

The 2-86 data sets might have been expected to have been of better than average quality. The observations were taken when the VLA was essentially in A configuration, and no observing complications were recorded. The array was, however, in the process of changing from D to A configurations and this was apparently the root of some difficulties. The imbalance of the  $uv$  coverage, for instance resulted in an ill-behaved  $B(l, m)$  which made the 1.5 GHz confusion overwhelming. This data set had to be discarded. At 22 GHz a null detection was recorded possibly because of atmospheric transmission problems which are most pronounced in extended configurations and at high frequencies.

The remaining data sets of this epoch (5 GHz and 15 GHz) were used judiciously and in some instances completely discarded as well. The 5 GHz data set, for instance, provided consistent results for  $\eta$  and  $\theta_c$  and yielded a map which was qualitatively similar to previous A configuration maps at 5 GHz. Some corruption had clearly taken place, however, since the set indicated a total flux of only 3.6 mJy, well below any previous observations (see Figure 4.18). Further, the 5 GHz flux did not even agree with the 15 GHz flux as expected for an optically thin nebula; the 15 GHz flux corresponded well with the flux obtained at previous epochs.

The non-usability of much of the epoch 2-86 data set is unfortunate. It provided

the only information about the system in orbital phase  $\sim 0.1$ . Possibly something interesting was occurring at AG Pegsai during these observations which contributed to the sense of corruption of the set. Further observations are required to settle this question.

## Chapter 5

# INTERPRETATION

### 5.1 A Synthesis of Old and New Ideas

AG Pegasi is a much studied object, and many well supported conclusions about it precede the present work. To complement these conclusions, this radio study has revealed a number of significant details. The task remains to attempt to incorporate these new details into a consistent overall picture of the system.

The accepted characteristics of the AG Pegasi system may be listed briefly. It is a long period ( $\sim 800$  day) S-type symbiotic binary system consisting of a normal M3III giant, a hot compact object of temperature between 30,000 and 100,000K, and a nebular region. The giant does not fill its Roche lobe. A symbiotic nova event occurred *c.*1850, reached maximum light *c.*1875 and has generally undergone a slow decline to quiescent level in present times. Progressively higher levels of excitation have been observed in the system since the turn over of the optical light curve *c.*1875 (see Figure 1.8 and table 1.1). A brightening by  $\sim 0.5$  mag *c.*1950 may represent a lesser "event". At present the hot component manifests WR features, and IUE observations show evidence of a hot wind at  $\sim 900$  km s<sup>-1</sup> presumably arising from the hot component.

A number of ambiguities have defied explanation in present models of the system. Chief among these is an unusually high HeII flux. Disk accretion onto a WD is suggested by the HeII flux, but a better fit to the overall spectrum is achieved by

invoking a “false photosphere” formed in an outflowing wind (Kenyon and Webbink 1984).

The conclusions supported by the present work include the following. The nebular region of AG Pegasi is very complex and may be resolved into a number of discrete components: a central unresolved source coincident with the binary system; an inner nebula of  $2''$  extent; an intermediate nebula of extent  $\sim 20''$ ; and a outer bipolar nebula of extent  $\sim 1'$ . The nebular complex extends to  $\sim 0.2$  pc which is on the order of  $10^4 - 10^5$  times larger than the underlying binary system. The inner nebula has an average expansion velocity of  $\sim 65$  km s $^{-1}$ . The expansion appears to be taking place largely in a bipolar manner on a N-S axis. Lobe enhancements are apparent in this nebulae and they lie roughly in line with the axis of expansion. The brightness of the inner nebula increased significantly between 1984 and 1987. The central source is partially optically thick and appears variable both in flux density and possibly in spectral index. The variability correlates with the orbital phase of the system.

The following hypothesis (and speculation) is offered to account for, and unify, the above details (see Figure 5.1).

Previous to 1850, the RG of AG Pegasi was losing mass ( $\sim 10^{-7}M_{\odot}$  yr $^{-1}$ ) in a steady outflow, providing matter for what is now the intermediate nebula. The compact object at this time was accreting matter from the wind at a rate of  $\sim 10^{-9}M_{\odot}$  yr $^{-1}$ . The accreted matter underwent a thermonuclear shell flash, c.1850, which resulted in a bipolar

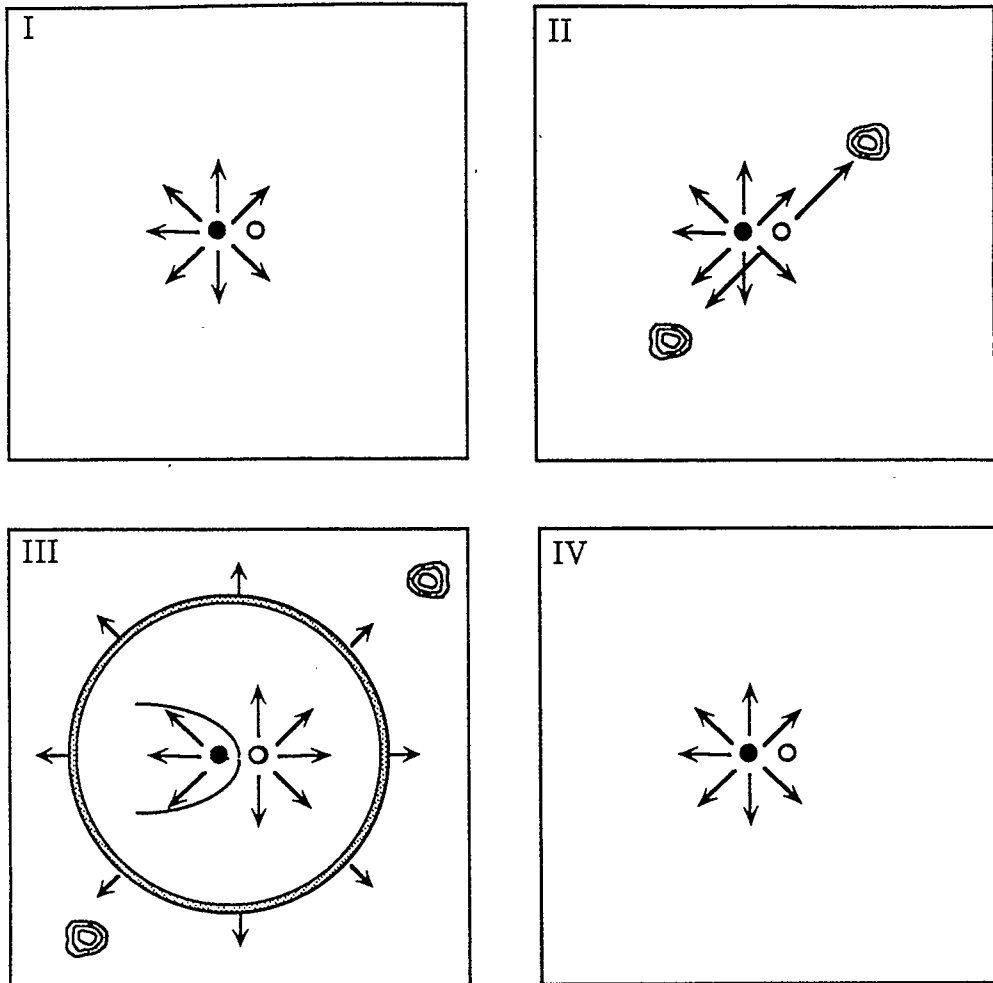


Figure 5.1: Possible Evolution of AG Pegasi

(Not to Scale)

- I. Quiescent system: mass loss from RG.
- II. Nova-like outburst from the hot companion with bipolar ejection ( $\sim 1850$ ).
- III. Onset of WR wind from hot companion ( $\sim 1950$ ).
- IV. Return to quiescence (some time in the future).

ejection of material (now visible as the outer nebula). The ejected material passed through the intermediate nebula leaving it largely intact. At a later date (possibly *c.*1950) a WR wind was initiated from the surface of the compact object. This wind quickly came into contact with the pre-eruption RG wind (intermediate nebula) creating shock fronts and sweeping up material. The zone of interaction between the WR wind and the pre-existing RG wind is now identified as the inner nebula. At the center of the system, the dynamics are, at present, dominated by the WR wind. This wind becomes optically thin at a radius of  $\sim 10^{14}$  cm and the central, optically thick region of the wind is identified as the central unresolved object. The WR wind may also be ablating material from the RG in the manner suggested by Penston and Allen (1985); this material could also give rise to radio emission.

This evolutionary scenario neatly accounts for many of the observed properties of AG Pegasi. However, the interpretation may not be unique, and arguments may be raised against the interpretation at each of its stages. In the following sections, those arguments will be presented and an attempt will be made to put the interpretation upon a more quantitative footing.

## 5.2 Origin of the Outer Nebula

It may be argued that the outer nebula is not the remnant of the 1850 outburst.

- a. The optical light curve (Figure 1.8) and spectral development (table 1.1) of AG Pegasi may be explained simply in terms of an expanding shell. The shell

gradually passes to optical thinness during which time the high temperature radiation from the central object becomes visible, resulting in a higher excitation spectrum (Boyarchuk 1967b, Section 1.2.1). However, if the ejection is bipolar then the ejecta will not obscure the central source and the region of high excitation will remain continuously observable.

- b. Hjellming (1985) has suggested that the inner nebula is the 1850 remnant. The mass of this nebula is comparable to masses associated with classical novae ejecta,  $\sim 10^{-5} M_{\odot}$ . Its kinetic energy,  $\sim 3 \times 10^{42}$  ergs, is somewhat low for symbiotic nova outbursts but not unreasonably so. Therefore the 1850 eruption may be explained without reference to the outer nebula.
- c. The existence of a bipolar outburst implies the existence of a disk around the outbursting source to channel the outburst. Disks, however, are not expected to form during quiescence in systems whose evolved component does not fill its Roche lobe. The RG in AG Pegasi does not fill its Roche lobe and therefore bipolar outbursts are not expected. Further, the spherical symmetry of the inner nebula does not support the present existence of a disk. Whatever the origin of the outer nebula, its bipolarity argues against its association with the 1850 eruption.

On the other hand, observational evidence suggests that bipolar outbursts may be widespread among symbiotic stars (see Section 1.1.2). Virtually all symbiotics with known outbursts that are imaged with sufficient resolution show evidence for bipolar geometry (Taylor *et al.* 1988). It is therefore not surprising, from a purely observational perspective, that the 1850 outburst should have been bipolar.

Objection (c) does not argue against an association of the bipolar nebula with the 1850 outburst, but perhaps points out that the process by which the ejecta is channelled is ill understood.

It has been demonstrated that in systems such as AG Pegasi, disks are not expected to form in quiescence, however, the possibility of formation is ever present in spite of average "expectations". Fluctuations in mass loss rate from the RG or eccentricity of orbit, for instance, could encourage disk formation. It is true that the inner nebula possesses a large degree of circular symmetry, however, this need not argue against the existence, or previous existence of a disk. It is possible, for instance, for mass loss to occur from a disk as well as from a stellar object. It is also possible that the eruption in 1850 would have caused considerable dissipation of a disk if it existed at that time. Further, there is evidence for bipolarity in the inner nebula which may be consistent with the existence of a disk (although a simpler explanation is also possible). The inner nebula bipolarity is perhaps most simply explained by the solid angle presented by the RG to mass loss from the compact object (0.04 sr for a  $86 R_{\odot}$  RG at 3.6 a.u.). Particles travelling at velocity  $v$  will be gravitationally captured by a body of mass  $M$  if their motion brings them to within a distance of  $R = 2GM/v^2$  to it ( $G$  is the gravitational constant). Finally, a disk has already been postulated for the system on the basis of other considerations (HeII flux, Boyarchuk *et al.* 1987).

The light curve and spectral development of AG Pegasi are as easily explained in terms of a bipolar outburst as a spherically symmetric one (argument a.). Provided that the jets of material are optically thick, the total flux of the system will initially exhibit a steep rise and will continue to increase as long as ejection continues.

When ejection terminates, or decreases significantly, the size of the optically thick region will decrease and the extended material will dissipate. The total flux of the system will consequently exhibit a long slow decline. It is true that the material ejected in bipolar fashion will not itself mask the central object unless ejection occurs along the line of sight, however, activity is expected to occur over the entire surface of compact object. Therefore, the source of high excitation will be obscured from view at least as far out as the source of collimation (disk?). If ejection decreases gradually, then progressively higher levels of excitation will be observed as obscuration of the compact object diminishes.

There are problems with associating the inner nebula with the 1850 eruption. First of all, if it were ejected in 1850 its average velocity would have to be  $\sim 15 \text{ km s}^{-1}$  for it to be located in its present position ; this velocity is about two orders of magnitude too slow for escape from a WD. Further, this velocity does not agree with the measured velocity of the nebula,  $65 \pm 15 \text{ km s}^{-1}$ . It must be concluded either that the inner nebula has been accelerated since its ejection in 1850, or that it has a more recent origin. The kinematic age of the nebula ( $R/v$ ) is about 40 years which would imply that it was ejected c.1950. Additionally, the characteristics of the inner nebula are not consistent with the light curve (Figure 1.8). Assuming a spherically symmetric development, the mass of  $\sim 3 \times 10^{-5} M_{\odot}$  would have been optically thick to (electron scattering) at a radius of  $\sim 5 \times 10^{14} \text{ cm}$ . At an average velocity of  $\sim 15 \text{ km s}^{-1}$ , the rise time of the light curve would be  $\sim 12 \text{ yr}$ . But the observed rise time is  $> 20 \text{ yr}$ . To explain the light curve, the inner nebula would have had to travel at  $\sim 7 \text{ km s}^{-1}$  between 1850 and 1875. Such a velocity is far too low to be associated with mass loss from a compact object. It is difficult, therefore,

to associate the inner nebula with the 1850 eruption.

A number of points favor the association of the outer nebula with the 1850 event. The kinematics of the outer nebula are consistent with an origin in the 1850 eruption. Assuming that the bipolar features were ejected *c.*1850, their average velocity would be  $900 \text{ km s}^{-1}$  for a distance of 600 pc and an inclination angle (Boyarchuk 1967a) of  $36^\circ$ . This result agrees well with escape velocities expected from WDs ( $\sim 1000 \text{ km s}^{-1}$ ), and with the current outflow velocity from the compact object,  $900 \text{ km s}^{-1}$  (Penston and Allen 1985); it is also similar to velocities seen in other novae and nova-like eruptions. The bipolar features may originally have had a somewhat higher velocity since considerable deceleration would presumably have taken place since their ejection. They would, for instance, have had to blast through the intermediate nebula. The mass of the outer nebula  $\sim 10^{-5} - 10^{-4} M_\odot$ , and the implied kinetic energy of  $\sim 10^{44}$  ergs are both appropriate for nova-like eruptions.

### 5.3 Nature of the Inner Nebula

It may be argued that the inner nebula does not represent an interacting winds phenomenon.

- This study has demonstrated that the inner nebula may be adequately fitted as a homogeneous shell or a wind. It is therefore unnecessary to postulate an interaction of winds since a simple ejection or a truncated wind can adequately explain the observations.

On the other hand, there are several factors which favor the interpretation of the inner nebula as an interaction of winds. It was argued in Section 4.3.4 that a homogeneous density law was preferred on the basis of the observed spherical symmetry and the physical difficulty of maintaining a  $1/R^2$  density law in the presence of the compressing forces implied by the model fits. The interacting winds interpretation predicts the existence of compressing forces which give rise to a homogeneous density law. These compressing forces are created by the pressure of a fast wind on the inside edge, and resistance to the shell expansion by a slow wind on the outside edge. Ultraviolet observations of AG Pegasi unambiguously identify a WR wind of velocity  $\sim 900 \text{ km s}^{-1}$  and possibly a very copious mass loss rate,  $\dot{M} \sim 10^{-5} M_{\odot} \text{ yr}^{-1}$  (Penston and Allen 1985). Such a wind could not itself constitute the inner nebula since it would be too fast and diffuse, but it must certainly be coming into contact with the inner nebula since its travel time to the nebula would be only  $\sim 3 \text{ yr}$ . The intermediate nebula would apparently represent pre-ejection mass loss and provides the necessary material with which the WR wind may interact. Finally, the velocity of the inner nebula,  $\sim 65 \text{ km s}^{-1}$  is typical of shell velocities for wind interaction (Kwok 1986) while it is far below the escape velocity from a compact object.

There is a problem with explaining the inner nebula as a shell ejection. As noted above in Section 5.2, the mass of the inner nebula is typical of that associated with novae. The inner nebula was not considered to be associated with the 1850 eruption because of its slow speed and because it would produce a rise in the light curve on too short a time scale. If it were ejected as a shell sometime later than 1850, however, it would have produced a sharp rise in the light curve on as large a scale

as the 1850 event ( $\sim 3$  mag). Such a rise was not observed.

If it is supposed that the intermediate nebula represents pre-eruption RG mass loss (as is argued in the next section) and that the outer nebula represents ejecta from the 1850 outburst, then the outer nebula must certainly have passed through the intermediate nebula en route to its present location. It should therefore have made a hole in the intermediate nebula. While no evidence for such a hole exists there are a number of ways that such a feature could evade detection. First of all, this hole was not necessarily large; Figure 3.6, gives the impression that the original ejection was fairly tightly directed. Further, the nature of the rising light curve (Figure 1.8) would suggest that matter was continuously ejected over a period of  $\sim 20$  yr and so the hole could have been partially filled by the later ejecta. Finally, the intermediate nebula would not tolerate a vacuum. If a hole had been blasted through it, the thermal motions of the nebular particles would cause the hole eventually to be filled.

#### 5.4 Nature of the Intermediate Nebula

It has been suggested that the intermediate nebula represents pre-eruption (before 1850) RG mass loss. There is little to argue against this hypothesis except perhaps the impression of its detachment from the inner nebula; this impression arises if the intermediate nebula is modelled as a spherically symmetric object. If detachment were to exist, then the interpretation of the inner nebula would become problematic since the WR wind would have found no material with which to interact beyond the inner nebula. This would suggest either that the intermediate nebula is not

spherically symmetric, or that it is not a RG wind. This argument, however, must not be weighted too heavily; the detection of the intermediate nebula is at the limit of sensitivity and hence observations can not place strong constraints on the geometry at this time.

There are several reasons to favor an interpretation of the intermediate nebula as an RG wind. RGs are expected to lose mass (*e.g.* Zuckerman 1980), and in a binary system this mass loss may tend toward bipolarity because of the capture cross section presented by the companion. An RG wind with bipolar enhancements is then likely to have preceded the 1850 eruption. The mass of the intermediate nebula is  $10^{-4} - 10^{-3}M_{\odot}$  and the "thickness" is  $\sim 4.5 \times 10^{16}$  cm. If the mass were lost from the RG with a velocity of  $20 \text{ km s}^{-1}$ , the implied mass loss rate would be  $5.3 \times 10^{-7}M_{\odot} \text{ yr}^{-1}$  which is typical of an M giant star (Knapp and Morris 1985).

The survey work of Seaquist and Taylor (1989) demonstrates, quite apart from the general belief that RGs lose mass, that mass loss is expected to occur from RGs in quiescent symbiotic systems. The work indicates that radio emission correlates with mass outflow from the RG and that in most cases the radio emission from symbiotic stars must originate from the ionized component of the RG's mass outflow. In the case of AG Pegasi, the present existence of a WR wind may appear to contradict their finding, but it must be remembered that AG Pegasi has not yet returned to a state of quiescence. It appears that all symbiotic novae go through a phase during which they resemble more luminous WR stars (Kenyon 1986) and AG Pegasi is in this stage at present. The systems V1016 Cyg, V1329 Cyg, HM Sge, and RR Tel have all gone through this stage in their most recent outbursts, and quiescence should not be considered complete until this stage has ended. Once

the WR wind ends, it is expected that mass loss from the RG in AG Pegasi will again dominate the inner system.

Finally, if no era exists in which mass loss from the RG is dominant, then the 1850 outburst is unexpected since all models of outburst require accretion upon a compact object. The nature of the accretion in the case of AG Pegasi is likely to be mass loss from the RG. This may be argued both on the basis of the binary separation (no Roche lobe overflow) and on the basis of the light curve (TNRs of long duration imply a low accretion rate, Section 1.1.2).

## 5.5 Nature of the Central Source

The central unresolved object in AG Pegasi has a size of  $0.1'' > \Theta > 0.04''$  and appears to exist in a steady state. The variations of flux and spectral index would tend to support its interpretation as an STB phenomenon (see Section 1.1.4), however this model assumes that the inner dynamics of the system are dominated by a RG wind and such does not appear to be the case at present. Ultraviolet observations have unambiguously identified a WR wind in the system ( $v \sim 900 \text{ km s}^{-1}$ ) and it has been shown above that this wind is necessary to explain the inner nebula. Penston and Allen (1985) have determined the mass loss rate for this wind to be  $\dot{M} = 6.0 \pm 0.2 \times 10^{-6} M_{\odot} \text{ yr}^{-1}$  for a distance of 600 pc and this value agrees well with the apparent, although not statistically significant, rate of mass increase of the inner nebula obtained in this work ( $\sim 2 \times 10^{-6} M_{\odot} \text{ yr}^{-1}$ ). If this value is correct, then the dynamics of the inner system should be dominated by the WR wind and not the RG wind. In this case the prerequisite conditions for the STB

model do not exist.

The ablation tail model of Penston and Allen (1985), Section 1.1.4, would seem appropriate for AG Pegasi since it assumes a strong WR wind from the hot component. Further, this model is capable of producing variations in flux and spectral index with orbital phase; the ablation nebula may present different sizes of optically thick surface at different viewing angles. Therefore variations are expected with orbital phase. Further, the RG itself may occult, during some phases of orbit, the region of high excitation existing between the two stars.

If a WR wind is responsible for the inner nebula, it is interesting to consider the implied mass loss rate. According to the formula of Wright and Barlow (1975), Equation 1.5, a fully ionized, spherically symmetric, hydrogen nebula with a flux of 1.2 mJy at 5 GHz, a terminal outflow velocity of  $900 \text{ km s}^{-1}$  (Penston and Allen 1985) and a distance of 0.6 kpc will lose mass at the rate of  $1.6 \times 10^{-6} M_{\odot} \text{ yr}^{-1}$ . This result is in reasonable agreement with the mass loss rate obtained by Penston and Allen (1985) of  $6 \pm 2 \times 10^{-6} M_{\odot} \text{ yr}^{-1}$ . Equation 1.5 assumes a simple, spherically symmetric outflow; in the case of AG Pegasi this assumption is obviously heuristic. The spectral index of the point source, for instance, is approximately 1.1 as opposed to 0.6 as expected for a spherically symmetric wind. It may be concluded either that the phenomenon observed is not a pure wind (*e.g.* part of the flux may arise from an ablation tail), or that the wind is not spherically symmetric.

The calculated mass loss rate of  $\sim 10^{-6} M_{\odot} \text{ yr}^{-1}$  is somewhat higher than expected for early M giants (typically  $\sim 10^{-7} M_{\odot} \text{ yr}^{-1}$ ). This fact lends support to the suggestion of Penston and Allen (1985) that the inner system is dominated by a WR wind and not an RG wind. If, however, the RG happens to be losing mass

at rate on the order of  $\sim 10^{-6}M_{\odot} \text{ yr}^{-1}$ , a more complex interplay between the STB and Penston Allen effects may result. The details of such an interplay have yet to be investigated.

## Chapter 6

# CONCLUSIONS

### 6.1 Summary

This study of AG Pegasi has ascertained that the system consists of four distinct radio components: a central unresolved object of diameter  $< 0.1''$ ; an inner nebula of  $2''$  diameter and mass  $3 \times 10^{-5} M_{\odot}$ ; an intermediate nebula of diameter  $\sim 20''$  and mass  $10^{-4} - 10^{-3} M_{\odot}$ ; and an outer bipolar nebula of extent  $\sim 1'$  and mass  $10^{-5} - 10^{-4} M_{\odot}$ . The outer nebula has been associated with the symbiotic nova event c.1850, and the intermediate nebula has been associated with pre-eruption mass loss from the RG. The inner nebula has been measured to be expanding at  $65 \pm 12 \text{ km s}^{-1}$  and appears to arise from the interaction between a RG wind ejected before 1850 and the present WR wind from the compact object. The flux from the central object appears to vary with orbital phase and is believed to be associated with a “false photosphere” produced by the WR wind.

The new results arising from the work include:

- the discovery of the intermediate and outer nebulae;
- the detection of variability in the central point source;
- the measurement of expansion of a nebula by reference to radio visibility data.

## 6.2 Further Work

There are several areas in which further work falls naturally from the present study. Further observations will provide more detailed maps of the system morphology and permit further measurements of the kinematics of the various components. They may also improve the current data base so that stronger constraints are placed on models of the system. Theoretical study is required to explain the existence of bipolar ejection in a system whose evolved component does not appear to fill its Roche lobe. Radiative transfer solutions are required for the STB and Penston-Allen models in order to clarify the variations of the central object.

If the suggested scenario for the evolution of AG Pegasi since the 1850 event is correct, a number of observable predictions may be made. The inner nebula should continue to expand at  $\sim 60 \text{ km s}^{-1}$  and its flux and mass should increase. The WR wind should subside as quiescence is completely achieved. When this happens, the RG wind should reassert itself in the central region, and a standard STB nebula should develop with outer radius defined by depletion of ionizing photons. The peculiarly high HeII flux should vanish as quiescence is regained, whether it is associated with a disk or an ablation tail; the differences between the HeI and HeII lines velocities should then be reconciled. The inner, intermediate, and outer nebulae should eventually cease to be visible, both because they will dissipate outward and because they will recombine in the absence of ultraviolet illumination from the compact object.

The data base employed for this study can be improved by further radio observations. Only a limited number of high resolution (*A* Configuration) 5 GHz

observations are now available; these observations are the most useful type in measuring the expansion characteristics of the inner nebula. No high resolution (*A* Configuration) 15 GHz observations with integration times  $\geq 2$  h have been made to date; such observations are potentially capable of imaging the inner nebula with greater detail, providing for instance, a more accurate estimate of expansion velocity. Further 1.5 GHz observations are needed to permit a more convincing study of the outer and intermediate nebulae. Observations of all kinds are required at binary phase 0 - 0.1 (phase 0 defined by optical minimum) to establish whether the epoch 2-86 observations reported in this study are altogether corrupt, or if they are recording an interesting aspect of the system. Further high sensitivity observations, particularly at 5 GHz are needed to verify the periodic variations of the central source.

It is desirable that observations be taken in other wavelength regimes as well. Imaging observations in [OIII] and  $H_{\alpha}$  may be particularly useful since they can potentially detect and resolve the nebular components of the system. Such observations could also measure expansion velocities of the outer and intermediate nebulae from the Doppler effect.

Toward an observing scheme at radio wavelengths, a number of points may be raised. Since many shortfalls of the current data base are related to resolving power, *Very Long Baseline Array* (VLBA) or *Very Long Baseline Interferometer* (VLBI) observations may be appropriate at such time as detection is possible for brightness temperatures of  $\sim 10^4$  K. Proposed extension to the VLA may provide higher resolution at that site, and observations with the Bonn-Westerbork-Jodrell Bank triangle of telescopes in Europe may also provide images of higher resolution.

Problems of sensitivity can be addressed by observations at the VLA with longer integration times. Optimally the observing scheme would be arranged to sample evenly throughout the orbital period of the system; unfortunately, changing configurations at the VLA will make equivalent sampling at all phases difficult at that site.

This concludes the present study of AG Pegasi. Its radio structure has turned out to be far more complex than may have originally been anticipated. As the prototype of symbiotic novae, it is interesting to speculate whether its characteristics will prove widespread.

## Appendix A

### Tabulated Outputs from AIPS

Mapping parameters for each observation are given in tables A.1 and A.2 for naturally weighted and uniformly weighted maps respectively. BMAJ, BMIN and BPA are used to describe the clean beam, and refer to the major axis, minor axis, and position angle (measured clockwise from north) respectively. CLEAN FLUX gives the sum of clean components used to produce the clean map. MAX RES is the peak intensity of the residual map. EXTREMA refers to the maximum and minimum intensities of the clean map. See Section 2.2 for a description of the mapping process. The unit  $[\frac{\text{mJy}}{\text{b}}]$  is mJy per beam where the beam is understood as defining a unit of solid angle.

Standard task outputs are given at tables A.3 and A.4 for naturally weighted and uniformly weighted maps respectively. The task “JMFIT” fits a Gaussian function to a source’s intensity distribution and read out: a “peak intensity” corresponding to the peak of the Gaussian; and an “integral intensity” value corresponding to the flux under the Gaussian curve. For an unresolved source JMFIT will yield equal values for peak and integral intensity. JMFIT has not been performed on images in which the source is clearly resolved and not well described by a Gaussian function. The task “MAXFIT” fits a quadratic function to the intensity distribution and reads out a peak value of intensity and a position. The task “IMEAN” performs several measurements: the results given under “FLUX” reflect a total flux for the source observed in the map; the results under “RMS” reflect

the noise level of the map.

In most cases, both naturally and uniformly weighted images have been made for each data set. In the case of the 22 GHz sets, however, signal could not be distinguished from noise for uniformly weighted maps; hence no uniformly weighted results are given. Further, in some cases clean beams could not be fitted to dirty beams at 1.5 GHz and 5 GHz. This effect was particularly pronounced when uv coverage was complicated by hybrid array configurations. In these cases no results are given for the uniformly weighted maps.

EPOCH	BAND [GHz]	BEAM			CLEAN FLUX [mJy]	MAX RES [ $\frac{mJy}{h}$ ]	EXTREMA	
		BMAJ ["]	BMIN ["]	BPA [°]			MAX [ $\frac{mJy}{h}$ ]	MIN [ $\frac{mJy}{h}$ ]
11-84	1.5	1.26	1.20	-1.29	6.50	-	3.37	-0.64
	5	0.43	0.40	-6.20	5.30	0.078	1.83	-0.37
	5	0.49	0.45	-8.88	6.22	-	1.62	-0.15
	15	0.16	0.14	17.7	4.58	0.211	3.70	-0.68
	22	0.11	0.10	-57.9	8.42	-1.81	5.06	-2.72
5-85	1.5	9.42	9.42	45.0	9.57	-	5.73	-1.10
	5	1.51	1.42	-36.9	5.96	0.071	4.98	-0.48
	15	0.53	0.48	-8.30	8.33	0.286	5.60	-0.86
	22	0.34	0.32	14.9	12.3	0.703	5.48	-3.99
8-85	1.5	16.8	15.5	-1.60	18.4	0.448	11.0	-1.48
	5	5.11	4.54	8.70	6.55	0.083	6.17	-0.66
	15	3.52	2.40	-52.8	8.80	0.122	7.36	-0.71
	22	1.47	1.31	-51.6	11.9	0.346	4.69	-3.42
11-85	5	16.1	14.8	-32.5	6.95	0.074	6.97	-0.64
	15	5.39	4.79	-20.1	8.33	-	8.75	-0.77
	22	2.56	2.54	-57.1	8.00	0.701	7.64	-3.91
2-86	1.5	1.67	1.64	-47.6	14.7	0.217	3.46	-1.07
	5	0.48	0.46	-27.9	2.61	0.069	1.21	-0.29
	15	0.18	0.13	-8.50	8.60	0.134	4.29	-0.93
	22	0.10	0.09	10.8	5.12	0.020	3.28	-3.85
10-86	1.5	18.8	13.4	-67.4	25.2	0.602	10.5	-1.64
	5	4.73	4.55	40.7	7.35	0.064	7.51	-0.40
	15	1.56	1.25	-10.1	9.80	0.148	7.37	-0.52
	22	0.83	0.80	-42.4	14.4	0.469	5.77	-2.45
1-87	1.5	64.8	39.9	-7.30	9.86	0.530	16.0	-2.71
	5	16.1	12.4	19.5	9.53	0.083	8.56	-0.38
	15	4.88	4.04	24.5	12.3	0.132	10.3	-0.87
	22	3.00	2.22	-17.1	11.8	0.614	11.6	-4.49
4-87	5	20.7	20.2	-46.5	10.5	0.047	8.89	-0.37
	15	4.84	4.77	-43.1	9.93	0.054	9.95	-0.75
	22	3.14	3.03	-39.7	4.79	0.280	9.93	-3.31
7-87	1.5	1.26	1.20	-1.29	8.75	-	4.61	-0.93
	5	0.49	0.42	-13.3	8.84	-	1.77	-0.146
	15	0.16	0.14	17.7	6.28	0.182	4.12	-0.51

Table A.1: Naturally Weighted Mapping Parameters

EPOCH	BAND [GHz]	BEAM			CLEAN FLUX [mJy]	MAX RES [ $\frac{mJy}{b}$ ]	EXTREMA	
		BMAJ ["]	BMIN ["]	BPA [°]			MAX [ $\frac{mJy}{b}$ ]	MIN [ $\frac{mJy}{b}$ ]
<b>11-84</b>	1.5	1.14	1.09	52.9	6.11	-	3.03	-0.64
	5	0.34	0.32	80.8	3.63	0.094	1.62	-0.48
	5	0.36	0.34	-57.5	5.34	-	1.41	-0.206
	15	0.11	0.11	-37.6	3.16	-	3.69	-0.98
<b>5-85</b>	1.5	3.80	3.73	39.2	8.99	0.157	5.21	-1.11
	5	1.38	1.26	-56.8	5.74	0.112	4.48	-0.56
	15	0.40	0.39	49.1	7.47	0.456	5.29	-1.37
<b>8-85</b>	1.5	13.6	13.5	46.9	15.1	0.375	9.84	-1.70
	5	3.85	3.84	45.0	5.70	0.125	6.23	-0.67
	15	2.31	1.78	-54.4	9.09	0.175	6.75	-0.98
<b>11-85</b>	15	3.88	3.84	36.3	7.38	0.205	8.73	-0.96
<b>2-86</b>	15	0.12	0.11	12.3	6.05	0.200	4.14	-1.12
<b>10-86</b>	15	1.47	0.42	-84.7	8.72	0.122	5.50	-0.84
<b>1-87</b>	1.5	32.3	29.6	38.8	20.3	0.400	13.9	-2.86
	5	5.88	5.86	44.9	8.56	0.082	8.27	-0.49
	15	1.88	1.88	45.0	9.81	0.168	8.78	-1.15
<b>4-87</b>	1.5	51.9	48.56	-63.7	20.2	0.339	16.3	-2.92
	5	14.3	12.6	87.2	9.81	0.045	8.85	-0.50
	15	4.32	4.11	-67.4	10.4	0.068	9.76	-1.10
<b>7-87</b>	1.5	1.14	1.09	52.9	8.75	-	3.77	-0.51
	5	0.33	0.329	28.5	7.17	-	1.61	-0.21
	15	0.11	0.111	-37.6	4.53	0.278	3.92	-0.75

Table A.2: Uniformly Weighted Mapping Parameters

EPOCH	BAND [GHz]	JMFIT		MAXFIT FLUX [ $\frac{mJy}{h}$ ]	IMEAN	
		PEAK [ $\frac{mJy}{h}$ ]	INT [mJy]		FLUX [mJy]	RMS [ $\frac{mJy}{h}$ ]
<b>11-84</b>	1.5	3.32	6.59	3.31	6.33	0.127
	5	-	-	1.76	6.95	0.081
	5	-	-	1.62	6.50	0.030
	15	3.55	3.55	3.49	3.73	0.136
	22	5.80	5.75	5.19	3.93	0.650
<b>5-85</b>	1.5	4.99	9.83	5.60	12.3	0.240
	5	4.99	6.83	4.88	6.33	0.089
	15	5.34	7.30	5.29	10.5	0.198
	22	5.36	7.91	5.46	9.53	0.853
<b>8-85</b>	1.5	10.2	15.5	10.5	26.4	0.357
	5	6.16	6.16	5.99	6.07	0.109
	15	7.52	8.35	7.19	8.64	0.136
	22	4.91	5.60	4.75	10.3	0.654
<b>11-85</b>	5	6.77	7.38	6.77	7.33	0.106
	15	8.86	8.80	8.37	8.99	0.134
	22	7.89	7.78	7.35	6.95	0.888
<b>2-86</b>	1.5	2.73	11.6	3.38	11.6	0.207
	5	-	-	1.17	4.38	0.062
	15	4.30	4.30	4.14	4.61	0.163
	22	null	detection			
<b>10-86</b>	1.5	8.86	18.1	10.1	22.6	0.335
	5	7.05	7.57	7.21	7.26	0.081
	15	7.56	9.89	7.26	10.4	0.114
	22	5.21	13.7	5.58	14.0	0.532
<b>1-87</b>	1.5	15.5	20.0	15.7	20.1	0.502
	5	8.70	8.70	8.24	8.84	0.082
	15	10.1	11.6	9.94	11.1	0.155
	22	11.5	13.8	11.2	12.7	0.756
<b>4-87</b>	5	8.90	9.03	8.43	9.65	0.079
	15	9.88	10.1	9.33	10.0	0.143
	22	10.1	9.35	9.40	9.61	0.689
<b>7-87</b>	1.5	4.61	8.03	2.82	5.52	0.076
	5	-	-	1.77	9.26	0.031
	15	4.28	4.28	3.94	5.57	0.103

Table A.3: Standard Task Outputs: Naturally Weighted Maps

EPOCH	BAND [GHz]	JMFIT		MAXFIT	IMEAN	
		PEAK [ $\frac{mJy}{b}$ ]	INT [mJy]	FLUX [ $\frac{mJy}{b}$ ]	FLUX [mJy]	RMS [ $\frac{mJy}{b}$ ]
<b>11-84</b>	1.5	2.93	6.12	2.98	5.77	0.141
	5	-	-	1.54	5.53	0.111
	5	-	-	1.39	6.38	0.048
	15	3.46	3.46	3.47	3.29	0.208
<b>5-85</b>	1.5	4.85	7.65	4.94	10.7	0.198
	5	4.68	6.48	4.37	5.91	0.120
	15	5.26	5.26	4.95	10.7	0.313
<b>8-85</b>	1.5	9.39	13.2	9.61	19.5	0.372
	5	6.22	6.21	5.97	5.96	0.138
	15	6.74	8.55	6.51	8.40	0.212
<b>11-85</b>	15	8.84	8.55	8.22	8.06	0.222
<b>2-86</b>	15	4.12	4.12	3.95	4.67	0.250
<b>10-86</b>	15	5.12	7.70	5.49	9.78	0.187
<b>1-87</b>	1.5	13.7	17.2	13.8	15.3	0.403
	5	7.98	8.88	7.72	9.13	0.109
	15	8.72	10.4	8.29	10.3	0.228
<b>4-87</b>	1.5	16.0	20.7	15.6	18.5	0.458
	5	9.02	9.02	8.41	9.2	0.103
	15	9.58	10.1	9.26	9.37	0.226
<b>7-87</b>	1.5	4.07	7.19	2.50	5.43	0.077
	5	-	-	1.77	9.26	0.031
	15	4.04	4.04	3.75	4.30	0.162

Table A.4: Standard Task Outputs: Uniformly Weighted Maps

## Appendix B

### Contaminating Sources

The following table documents the approximate fluxes and positions of confusing sources found within the field of AG Pegasi. RA(1950) and DEC(1950) refer to the right ascension and declination respectively of the indicated sources in 1950 coordinates. For sources with fluxes measured at both 5 and 1.5 GHz, a spectral index  $\alpha$  ( $S_\nu \propto \nu^\alpha$ ) is calculated. These spectral indices are large and negative which indicates that the emission is likely nonthermal and the sources are likely extragalactic. The indices are believed to be anomalously large (negatively) as a result of the diffuse nature of the sources. Diffuse emission may be resolved away by the smaller beams achieved at higher frequencies. Diffuse emission of this sort is typical of extragalactic sources.

SOURCE	RA(1950)	DEC(1950)	FLUX		SPECTRAL INDEX, $\alpha$
			1.5 GHz [mJy]	5 GHz [mJy]	
1	21 48 40	12 14 24	178	4.64	-3.03
2	21 48 39	12 05 16	315	4.00	-3.64
3	21 48 57	12 27 06	43.0	2.77	-2.28
4	21 48 36	12 15 03	19.5	-	-
5	21 48 08	12 12 52	6.97	-	-
6	21 48 30	12 15 21	4.19	-	-
7	21 47 54	12 33 04	22.1	-	-
8	21 48 38	12 17 37	28.1	-	-
9	21 48 08	12 16 40	2.90	-	-
10	21 48 20	11 59 18	~ 5	-	-
11	21 49 06	12 42 50	5.08	-	-
12	21 50 39	12 26 08	8.88	-	-
13	21 51 42	12 23 02	4.68	-	-
14	21 49 20	11 42 45	2.07	-	-
15	21 50 16	12 27 05	7.63	-	-
16	21 48 13	12 08 27	7.09	-	-
17	21 48 38	12 32 08	~ 5	-	-

Table B.1: Contaminating Sources

## Appendix C

### Tabulated Results: Data Analysis

This appendix presents the results of model fitting for data sets of categories 1 to 3 as defined in Section 4.2. These data sets detect only the inner nebula and the central source. Spherically symmetric models are considered with both homogeneous and  $1/R^2$  density laws. Table C.1 presents values of the geometry factor,  $\eta$ , obtained from category 1 data sets. Table C.2 presents values obtained for the “center of mass radius”,  $\theta_c$ , obtained from the same sets. Table C.3 presents the nebular flux density determination obtained from category 1 and 2 data sets, and table C.4 gives the electron density at  $\theta_c$  implied by the same sets. Tables C.5 and C.6 present the total and central source flux densities, respectively, for category 1,2 and 3 data sets. Table C.7 compares the values of the merit function  $\chi^2$ , for the best fits and final fits of data sets in categories 1 to 3. Best fits are achieved by simply allowing a model curve to fit the data. Final fits are achieved by using information from the entire data base to determine some of the parameters. Values entered for epoch 2-86 in the tables below are included for completeness, however, the results are suspect, as noted in Section 4.6.

BAND [GHz]	EPOCH	HOMOGENEOUS		$1/R^2$	
		$\eta$	$\pm$	$\eta$	$\pm$
5	11-84	0.655	0.142	0.589	0.060
		0.543	0.035	0.585	0.037
	2-86	0.625	0.139	0.585	0.086
	7-87	0.667	0.022	0.666	0.022
15	11-84	0.784	0.695	0.710	0.336
	5-85	0.329	0.279	0.343	0.139
	2-86	0.755	0.171	0.670	0.098
	10-86	0.631	0.421	0.647	0.202
	7-87	0.649	0.084	0.645	0.067
22	11-84	0.500	2.820	0.745	0.462
	5-85	0.515	0.539	0.329	0.143
	8-85	0.729	1.807	0.616	1.203
	2-86	0.755	0.251	0.456	0.220
	10-86	0.820	0.292	0.756	0.647

Table C.1: Determination of  $\eta$

BAND [GHz]	EPOCH	HOMOGENEOUS		$1/R^2$	
		$\theta_c$ ["]	$\pm$	$\theta_c$ ["]	$\pm$
5	11-84	0.822	0.571	0.771	0.033
		0.817	0.018	0.771	0.006
	2-86	0.863	0.046	0.815	0.030
	7-87	0.860	0.008	0.837	0.002
15	11-84	0.853	0.364	0.868	0.275
	5-85	0.913	0.108	0.855	0.113
	2-86	0.840	0.082	0.790	0.064
	10-86	0.901	0.050	0.876	0.033
	7-87	0.781	0.066	0.765	0.050
22	11-84	0.687	0.387	0.842	0.280
	5-85	1.051	0.361	1.105	0.366
	8-85	1.067	0.222	1.019	0.185
	2-86	0.629	0.109	0.617	0.092
	10-86	0.919	0.123	0.875	0.100

Table C.2: Determination of  $\theta_c$ .

BAND [GHz]	EPOCH	HOMOGENEOUS		$1/R^2$	
		Flux [mJy]	$\pm$	Flux [mJy]	$\pm$
1.5	11-84	5.708	0.366	5.492	0.352
	7-87	6.826	0.260	6.507	0.248
5	11-84	4.914	0.261	4.880	0.260
		5.178	0.090	5.149	0.083
	5-85	5.035	0.287	4.980	0.284
	2-86	2.986	0.168	2.998	0.481
	10-86	6.726	0.321	6.603	0.315
	7-87	7.616	0.094	7.648	0.093
15	11-84	1.670	1.272	1.586	1.264
	5-85	5.032	0.628	5.003	0.624
	8-85	5.863	0.549	5.777	0.541
	2-86	6.574	1.097	6.596	1.093
	10-86	5.792	0.283	5.733	0.280
	1-87	7.624	0.826	7.566	0.820
	7-87	5.270	0.752	5.283	0.750
22	11-84	15.72	12.85	10.23	12.66
	5-85	6.048	3.213	5.827	3.194
	8-85	8.247	1.640	8.145	1.620
	2-86	16.77	6.680	16.48	6.596
	10-86	9.222	1.286	9.189	6.596
	1-87	8.125	2.236	8.080	2.220

Table C.3: Determination of Nebular Flux Density

BAND [GHz]	EPOCH	HOMOGENEOUS		$1/R^2$	
		$[\text{cm}^{-3} \times 10^4]$	$\pm$	$[\text{cm}^{-3} \times 10^4]$	$\pm$
1.5	11-84	1.809	0.070	1.54	0.05
	7-87	2.044	0.059	10.76	0.03
5	11-84	1.718	0.059	1.49	0.035
		1.763	0.070	1.53	0.016
	5-85	1.745	0.062	1.52	0.05
	2-86	1.343	0.048	1.15	0.10
	10-86	2.035	0.065	1.83	0.05
	7-87	2.203	0.079	2.01	0.016
15	11-84	1.056	0.403	0.886	0.35
	5-85	1.840	0.121	1.76	0.114
	8-85	1.984	0.102	1.74	0.086
	2-86	2.105	0.181	1.89	0.15
	10-86	1.990	0.065	1.80	0.05
	1-87	2.296	0.134	2.07	0.11
	7-87	1.931	0.144	1.76	0.13
22	11-84	3.307	1.354	2.30	1.4
	5-85	2.058	0.548	1.7	0.51
	8-85	2.401	0.244	2.07	0.17
	2-86	3.431	0.687	3.03	0.67
	10-86	2.563	0.187	2.31	0.165
	1-87	2.419	0.337	2.33	0.36

Table C.4: Determination of Electron Density

Values given in the above table correspond to the density predicted at the "center of mass radius",  $\theta_c$ .

BAND [GHz]	EPOCH	HOMOGENEOUS		$1/R^2$	
		Flux [mJy]	$\pm$	Flux [mJy]	$\pm$
1.5	11-84	5.947	0.105	5.912	0.105
	7-87	7.868	0.078	7.953	0.078
5	11-84	6.604	0.084	6.515	0.084
		6.407	0.092	6.327	0.031
	5-85	7.022	0.084	7.034	0.084
	8-85	6.453	0.094	6.459	0.096
	11-85	7.068	0.072	7.068	0.072
	2-86	6.661	0.053	6.770	0.053
	10-86	7.928	0.064	7.959	0.064
	1-87	8.680	0.069	8.684	0.069
	4-87	8.933	0.070	8.934	0.067
	7-87	8.598	0.031	8.692	0.031
15	11-84	8.466	0.153	8.386	0.153
	5-85	10.05	0.216	10.06	0.216
	8-85	8.097	0.139	8.119	0.139
	11-85	8.990	0.133	8.996	0.133
	2-86	9.847	0.180	9.904	0.180
	10-86	10.27	0.116	10.36	0.116
	1-87	10.70	0.151	10.73	0.151
	4-87	10.21	0.150	10.21	0.150
	7-87	10.53	0.110	10.65	0.120
22	11-84	10.47	0.761	10.38	0.761
	5-85	10.44	0.858	10.45	0.858
	8-85	7.096	0.632	7.132	0.632
	11-85	8.999	0.534	9.012	0.534
	2-86	4.562	0.644	4.613	0.644
	10-86	10.44	0.519	10.52	0.519
	1-87	12.56	0.726	12.60	0.726
	4-87	10.24	0.732	10.26	0.732

Table C.5: Total Flux Density Determination

BAND [GHz]	EPOCH	HOMOGENEOUS		$1/R^2$	
		Flux [mJy]	$\pm$	Flux [mJy]	$\pm$
1.5	11-84	0.509	0.136	0.589	0.129
	7-87	0.437	0.114	0.387	0.114
5	11-84	1.434	0.120	1.459	0.112
		1.200	0.033	1.234	0.033
	5-85	1.485	0.120	1.515	0.105
	8-85	0.650	0.113	0.651	0.110
	11-85	1.083	0.094	1.063	0.091
	2-86	0.456	0.078	0.522	0.076
	10-86	1.220	0.088	1.159	0.089
	1-87	1.788	0.097	1.657	0.097
	4-87	1.863	0.103	1.730	0.101
	7-87	1.400	0.033	1.330	0.033
15	11-84	3.818	0.175	3.838	0.170
	5-85	5.070	0.227	5.106	0.225
	8-85	2.877	0.153	2.901	0.150
	11-85	3.607	0.146	3.595	0.144
	2-86	4.265	0.188	4.284	0.188
	10-86	4.233	0.131	4.242	0.133
	1-87	4.498	0.165	4.403	0.166
	4-87	3.842	0.168	3.730	0.168
	7-87	4.050	0.138	4.050	0.146
	22	11-84	6.004	0.766	5.685
5-85		5.657	0.861	6.013	0.860
8-85		2.082	0.635	2.120	0.635
11-85		3.829	0.537	3.825	0.537
2-86		-0.80	0.647	-0.78	0.646
10-86		4.644	0.523	4.640	0.523
1-87		6.597	0.729	6.527	0.729
4-87		4.128	0.736	4.024	0.736

Table C.6: Central Source Flux Determination

BAND [GHz]	EPOCH	BEST $\chi^2$		FINAL $\chi^2$	
		Homo	1/R <sup>2</sup>	Homo	1/R <sup>2</sup>
1.5	11-84	1.31	1.30	1.31	1.31
	7-87	1.79	1.79	2.10	2.23
5	11-84	0.71	0.77	0.75	0.79
		0.77	0.85	0.78	0.86
	5-85	1.12	1.13	1.25	1.27
	8-85	1.37	1.39	1.37	1.39
	11-85	1.45	1.45	1.45	1.45
	2-86	1.25	1.32	1.43	1.54
	10-86	1.78	1.78	1.78	1.79
	1-87	1.95	1.96	1.95	1.96
	4-87	3.38	3.38	3.38	3.38
	7-87	1.16	1.15	1.53	1.35
15	11-84	0.82	0.81	1.04	1.05
	5-85	0.96	0.90	1.05	1.04
	8-85	0.73	0.72	0.78	0.76
	11-85	2.36	2.36	2.36	2.23
	2-86	0.82	0.81	0.90	0.88
	10-86	0.84	0.85	0.96	1.01
	1-87	1.62	1.62	1.73	1.70
	4-87	1.58	1.59	1.58	1.59
	7-87	0.93	0.86	1.15	1.14
22	11-84	1.21	0.97	1.24	1.02
	5-85	0.95	0.82	0.96	1.20
	8-85	1.65	1.65	1.86	1.85
	11-85	0.70	0.70	0.70	0.70
	2-86	1.41	1.40	1.60	1.60
	10-86	0.75	0.76	1.06	1.05
	1-87	1.09	1.09	1.13	1.12
	4-87	0.81	0.81	0.81	0.81

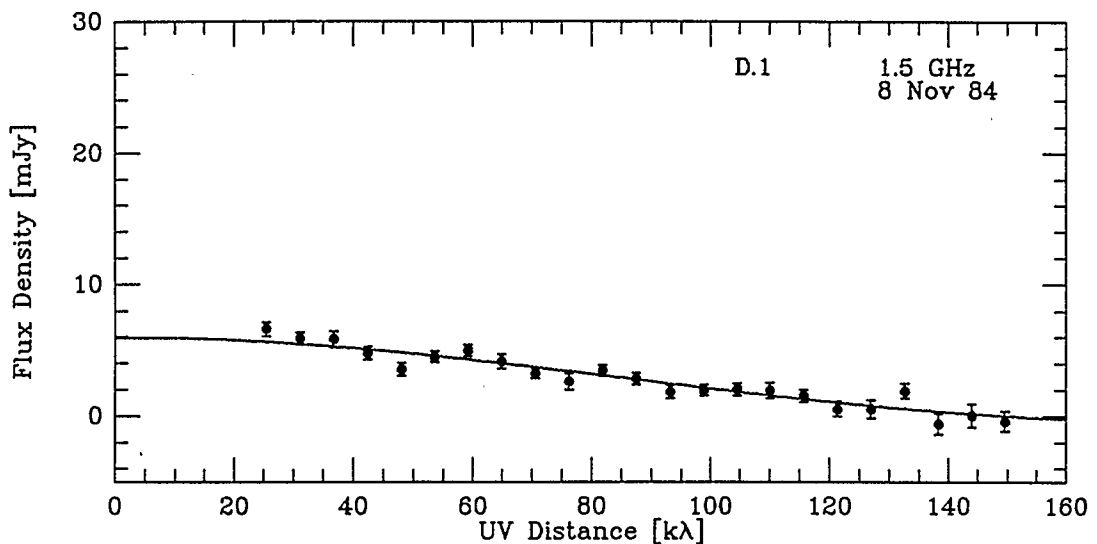
Table C.7: Merit Function ( $\chi^2$ ) for Fits

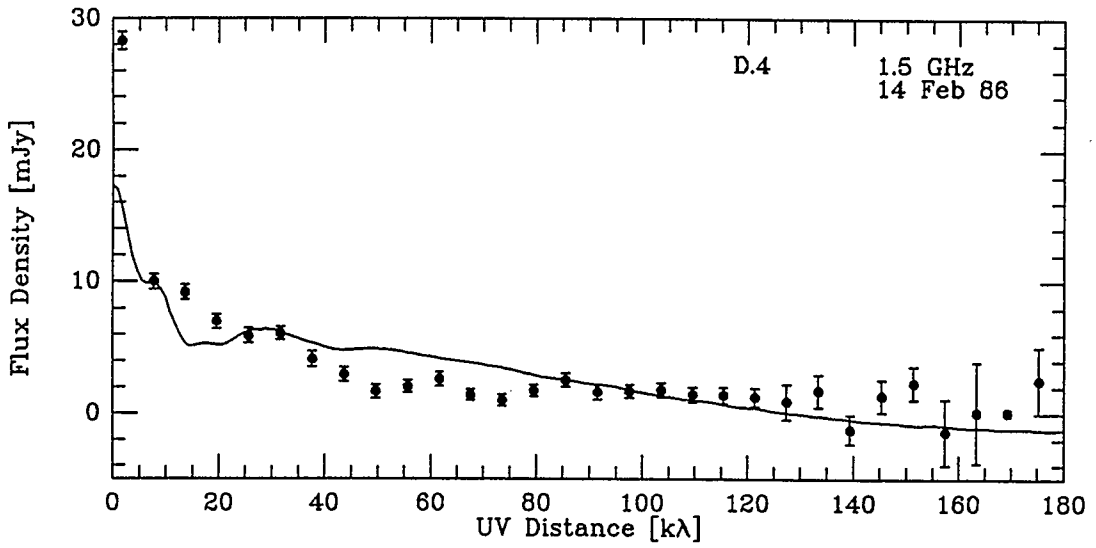
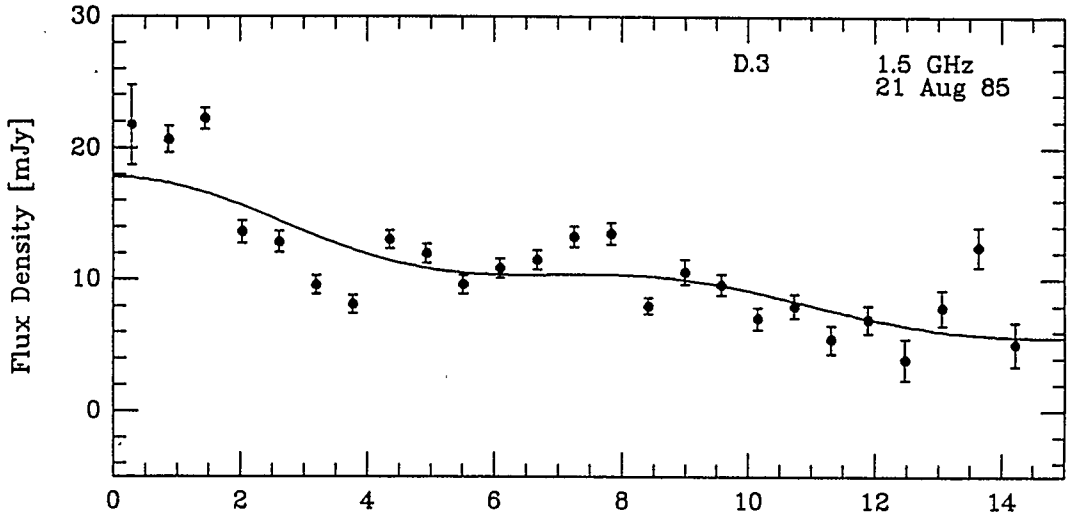
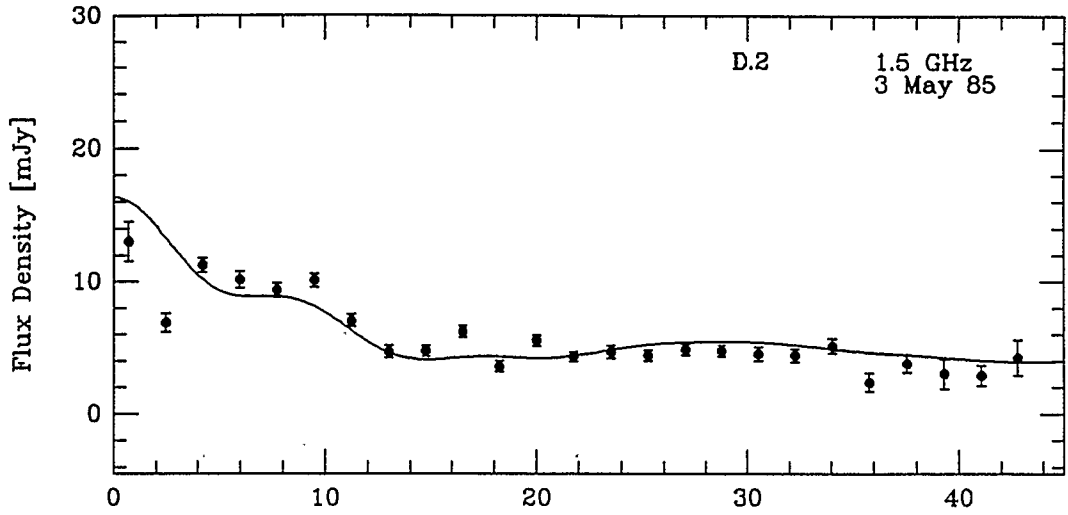
Values of  $\chi^2$  per data point are given in the above table.

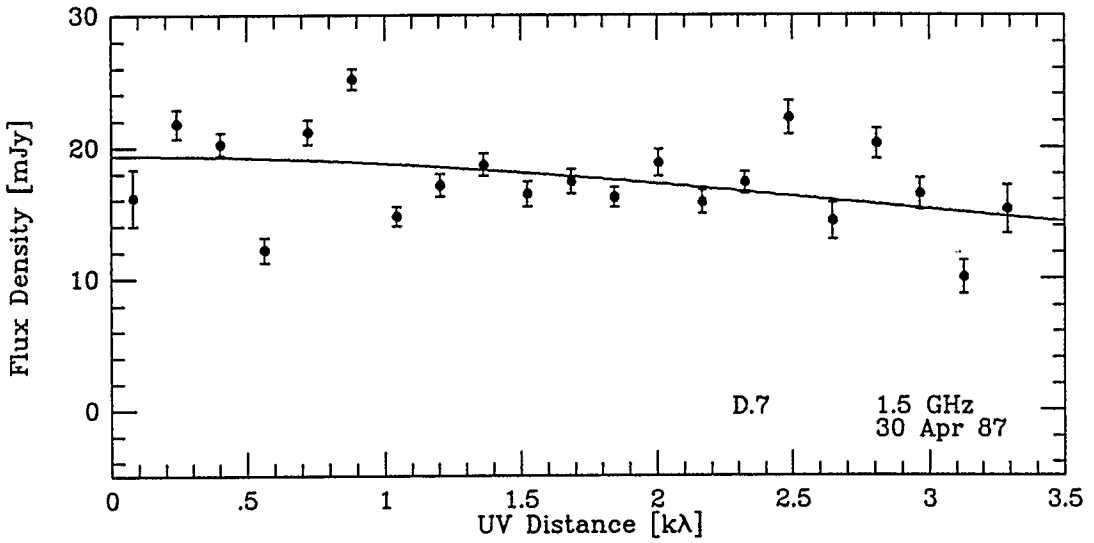
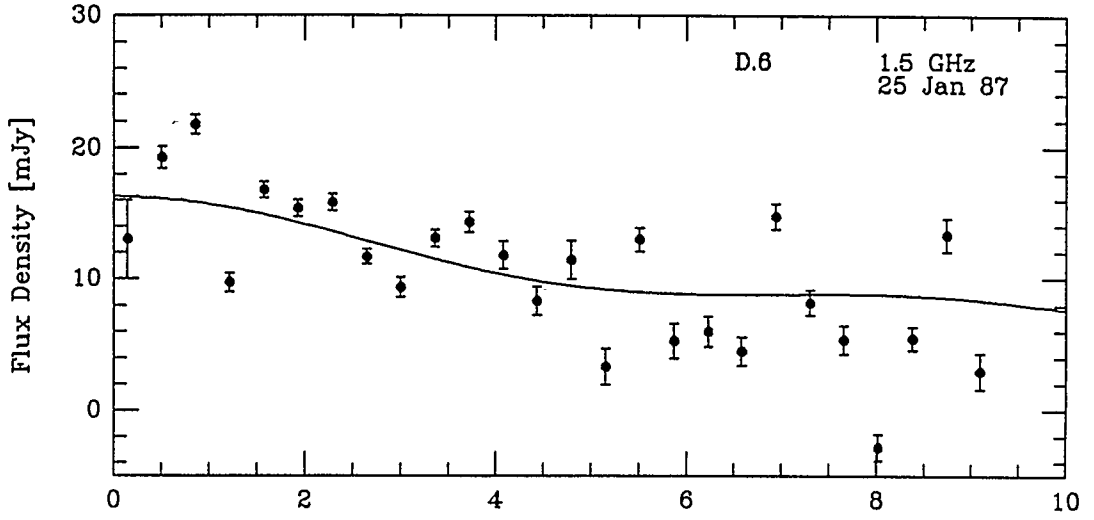
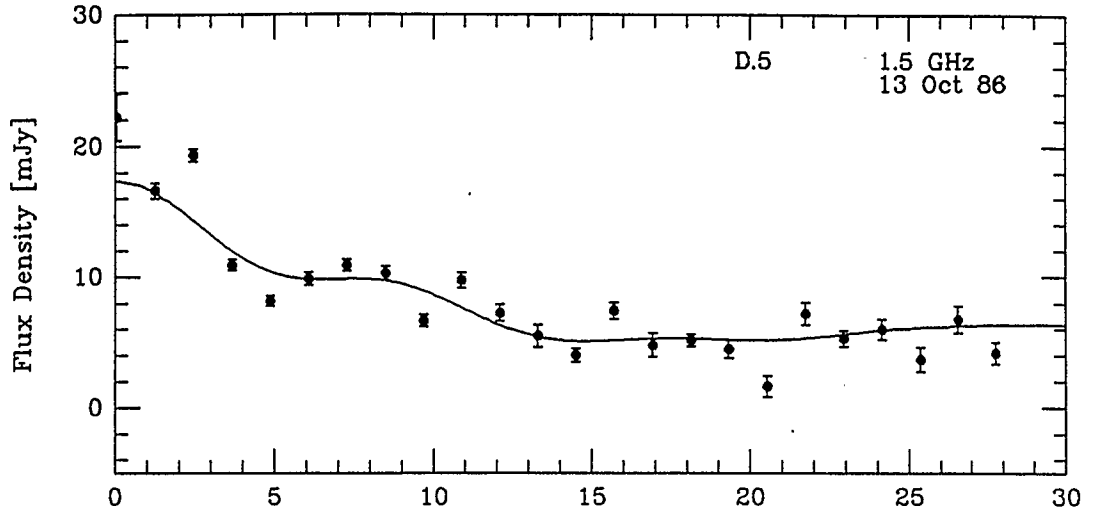
## Appendix D

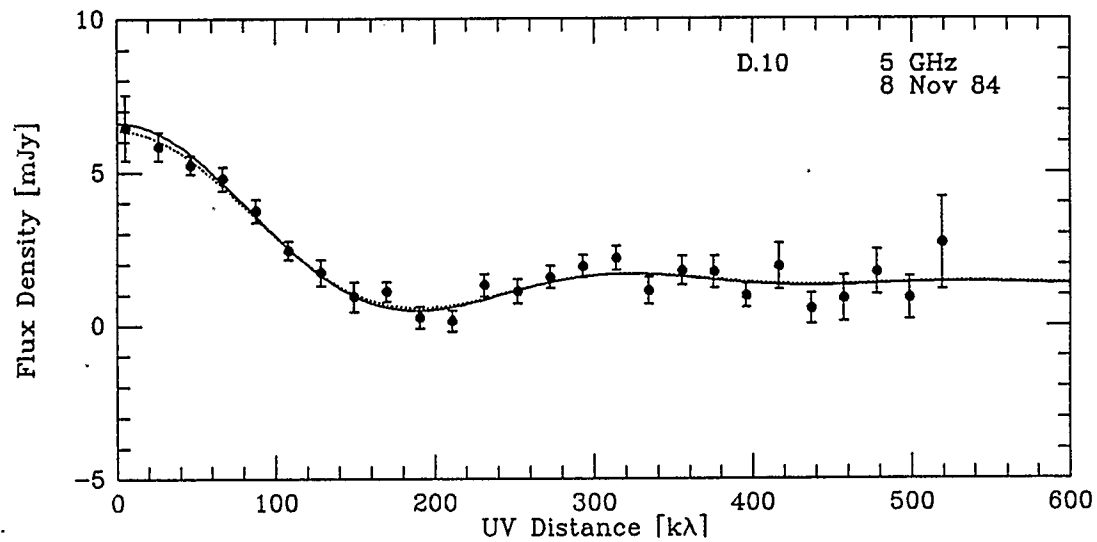
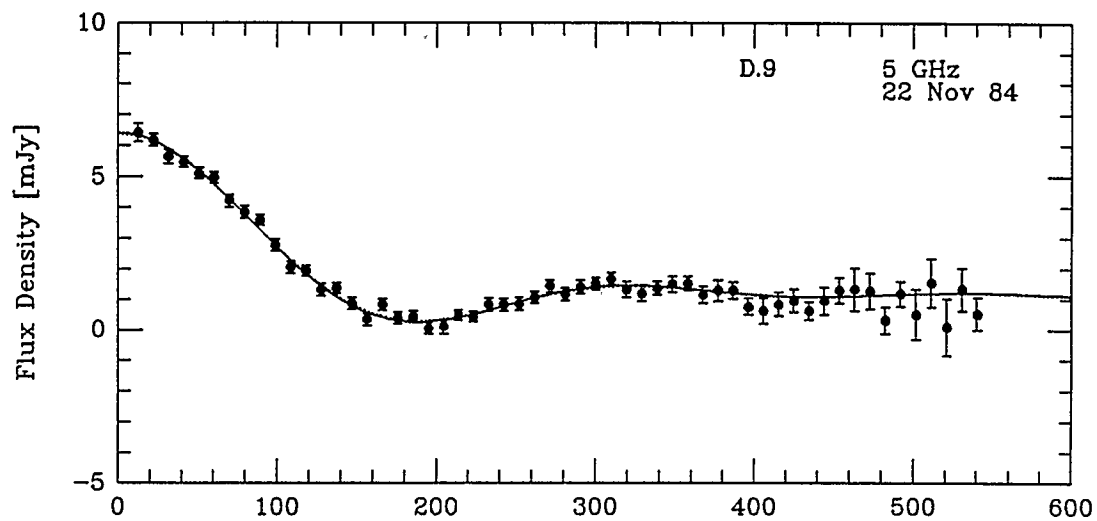
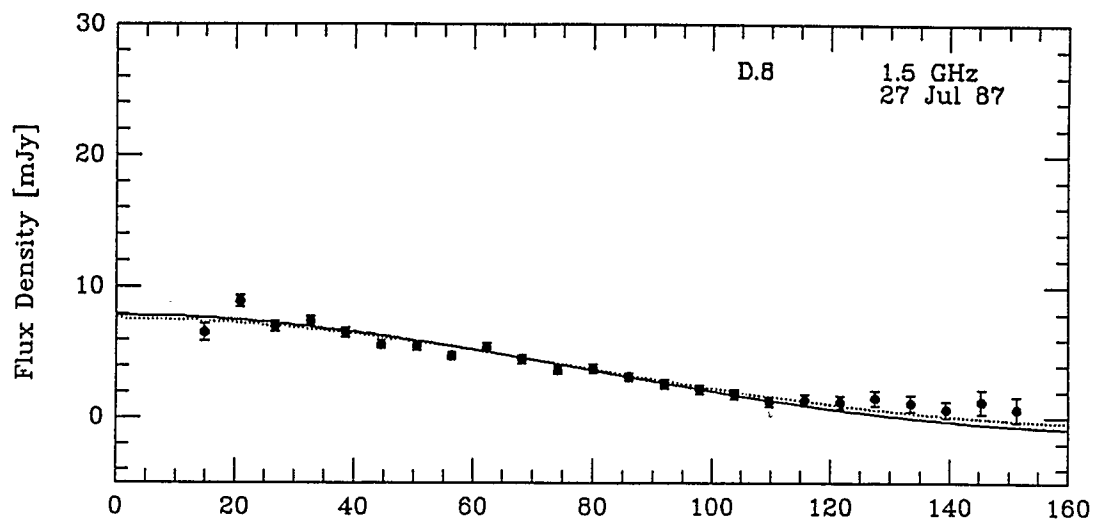
### Plotted Fits to Visibility Data

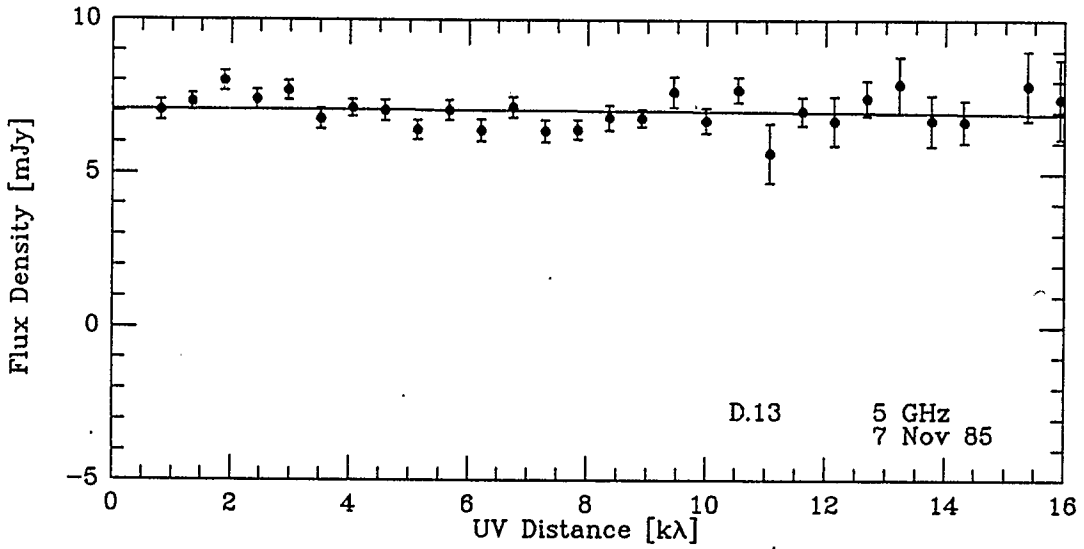
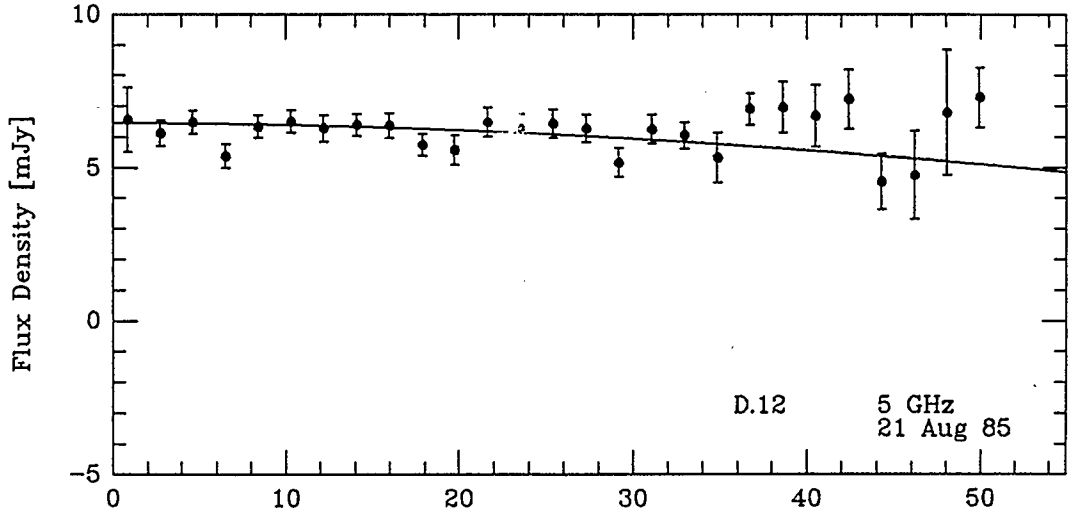
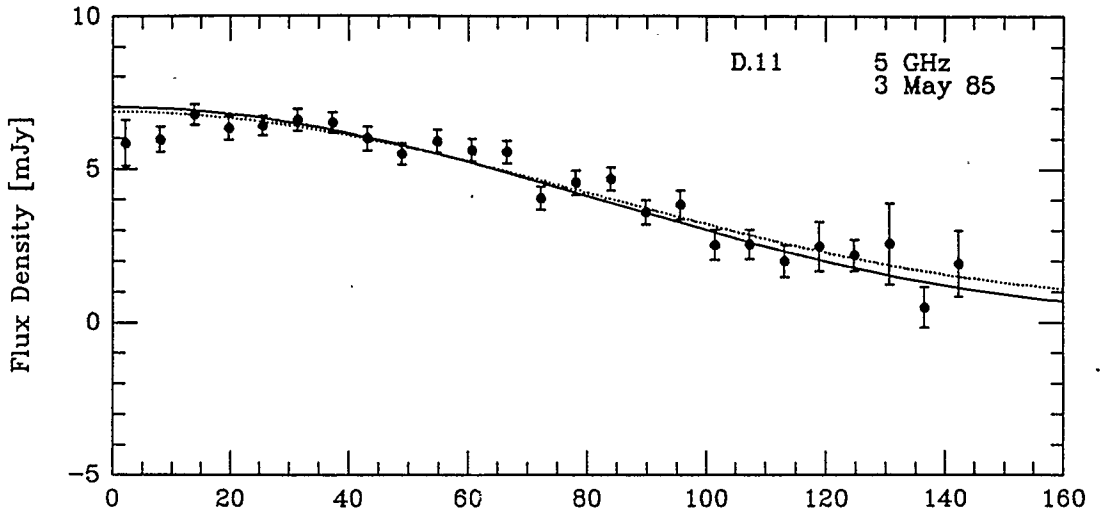
In this appendix real visibilities are plotted for each data set with dotted lines indicating best fits and solid lines indicating final fits. Best fits are achieved by leaving all parameters free to fit a model curve the data from an individual data set. Final fits are achieved by using information from the entire data base to determine some of the parameters. The fits shown assume a spherically symmetric, homogeneous shell for the inner nebula, a bipolar "wind" for the intermediate nebula, and detached bipolar features for the outer nebula. Plots are arranged from lower to higher frequency and by epoch within each frequency.

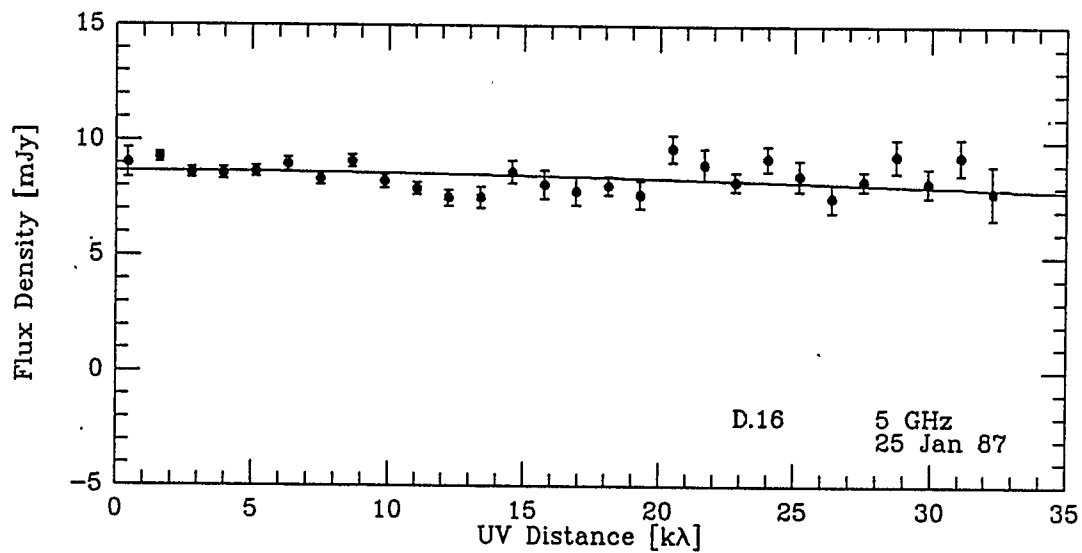
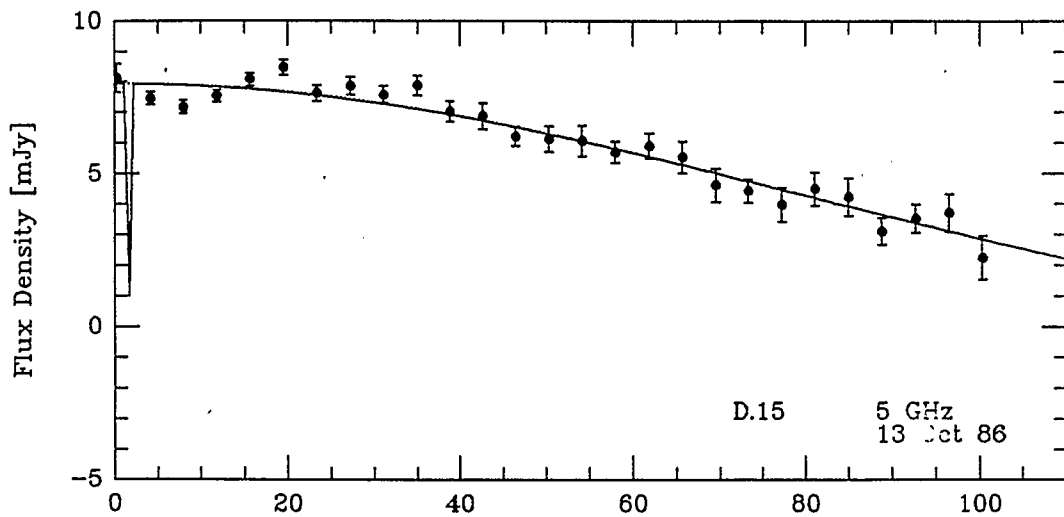
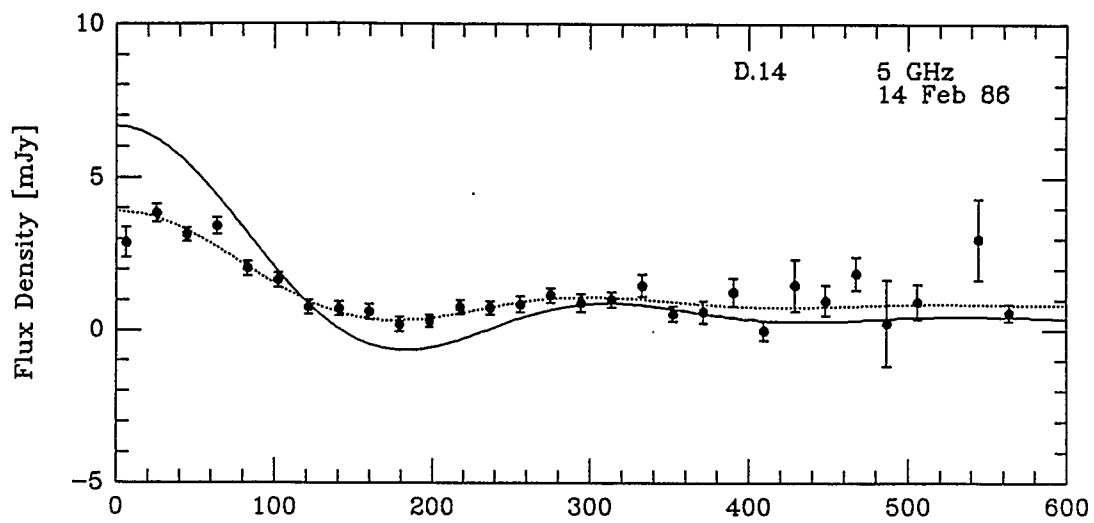


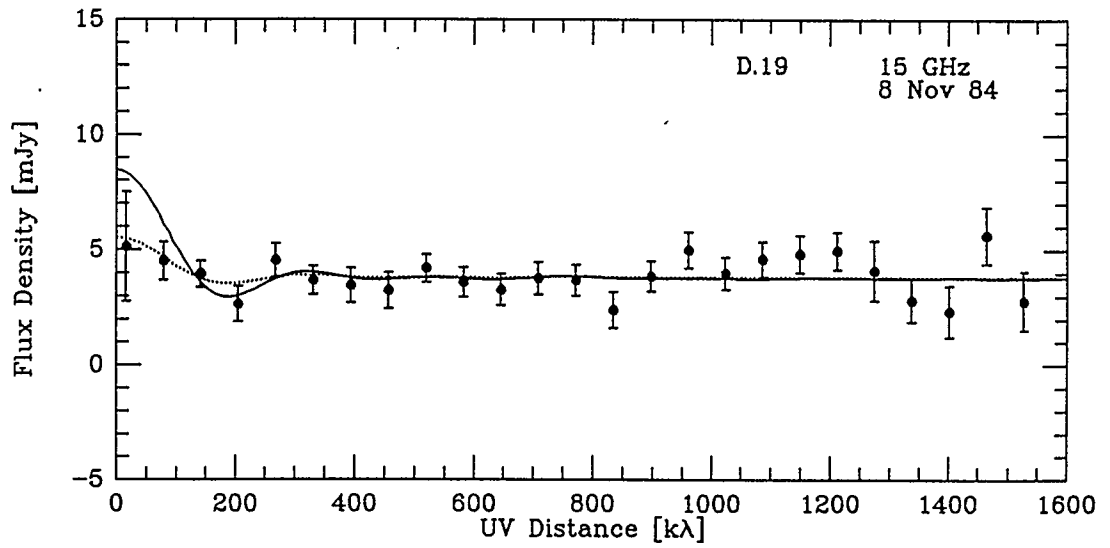
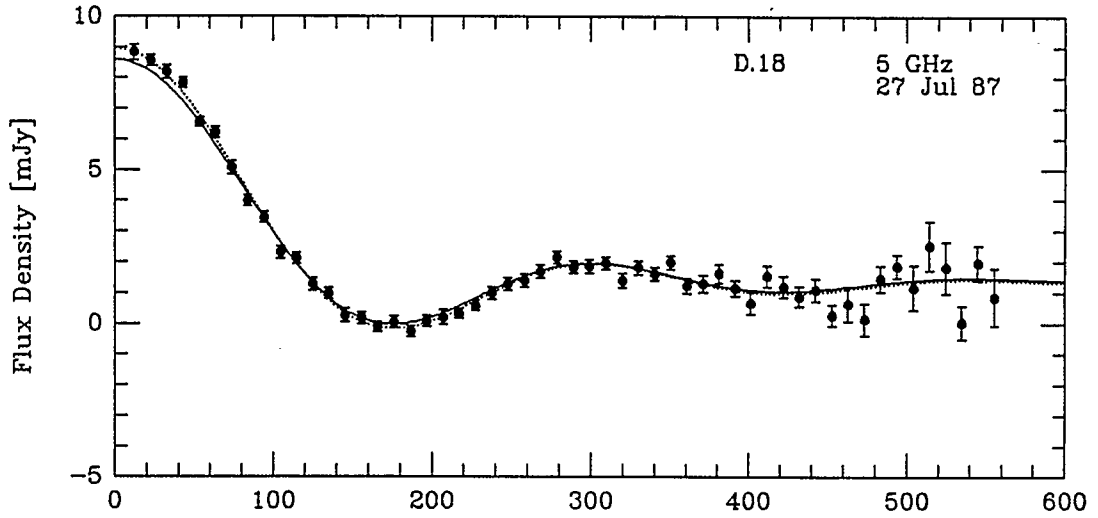
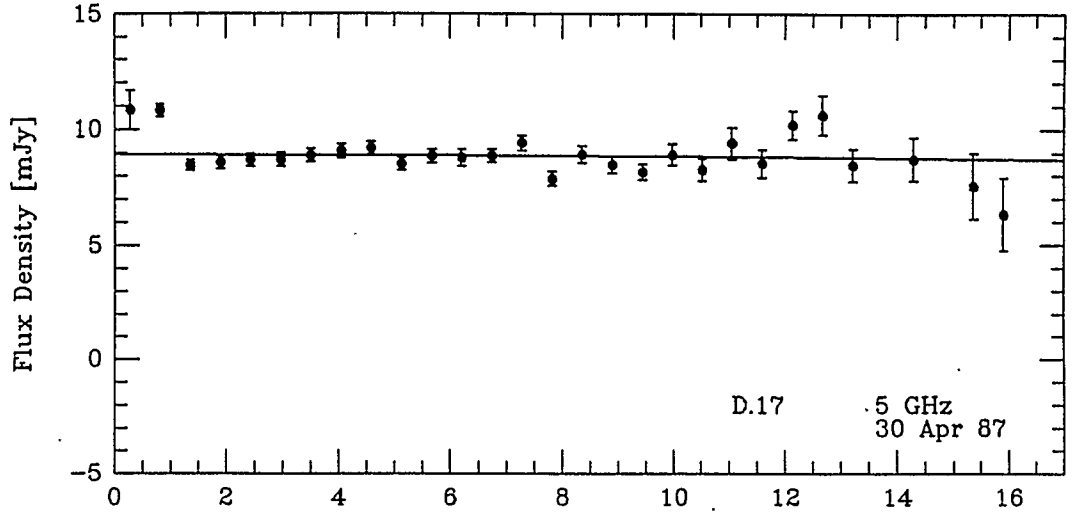


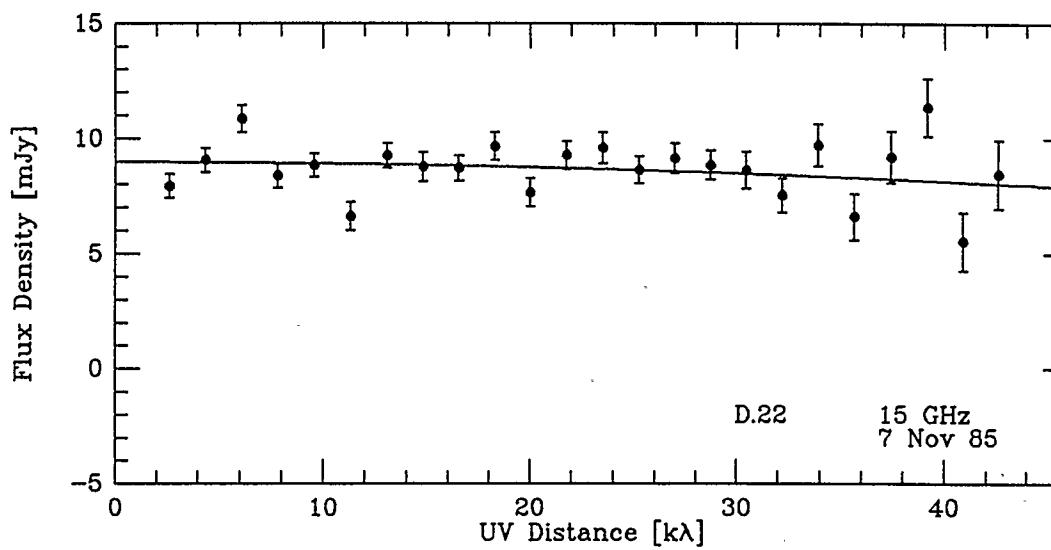
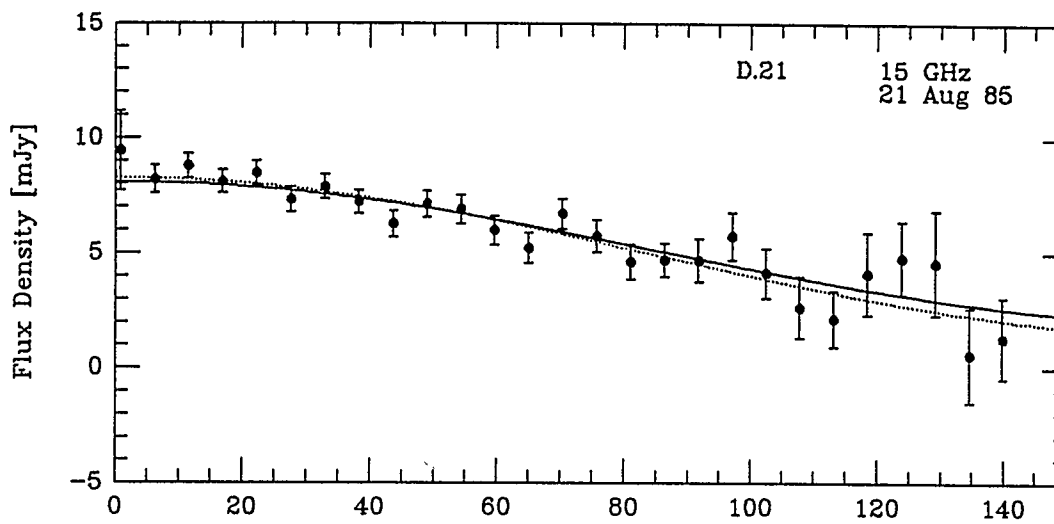
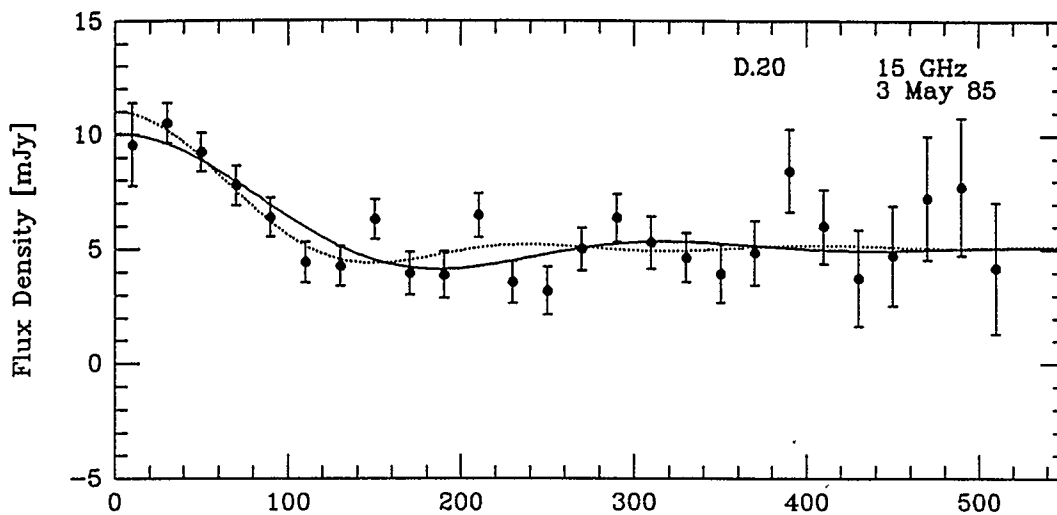


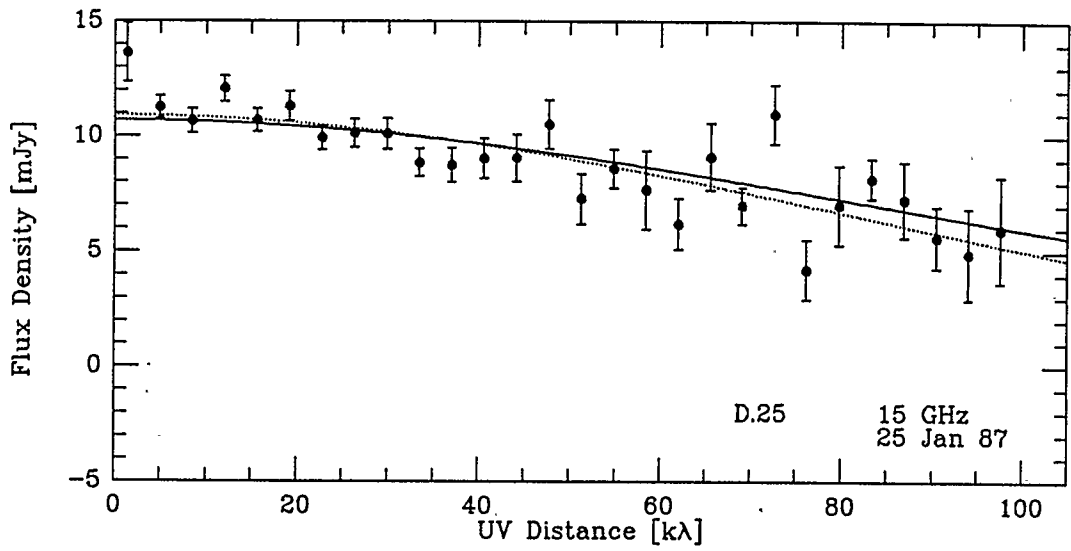
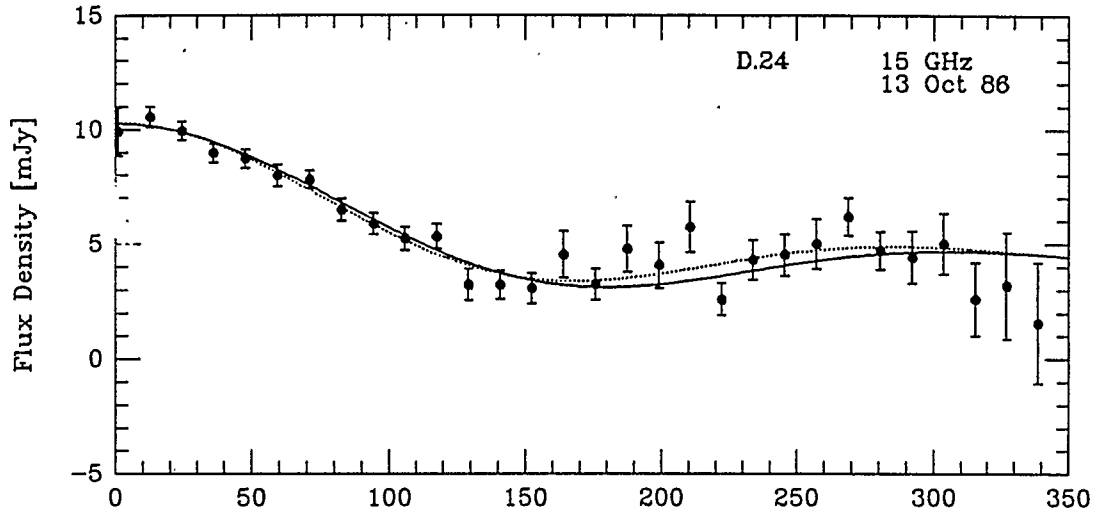
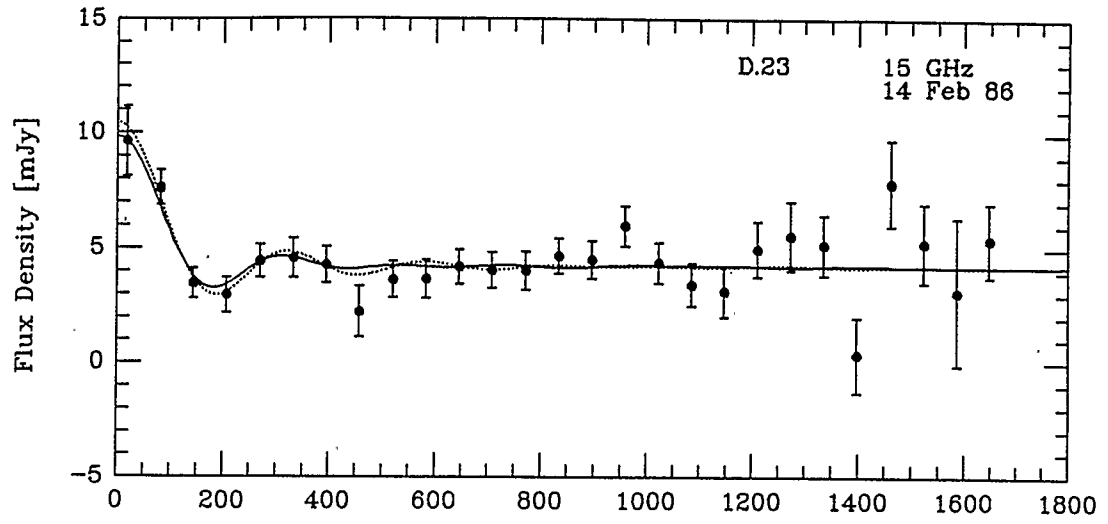


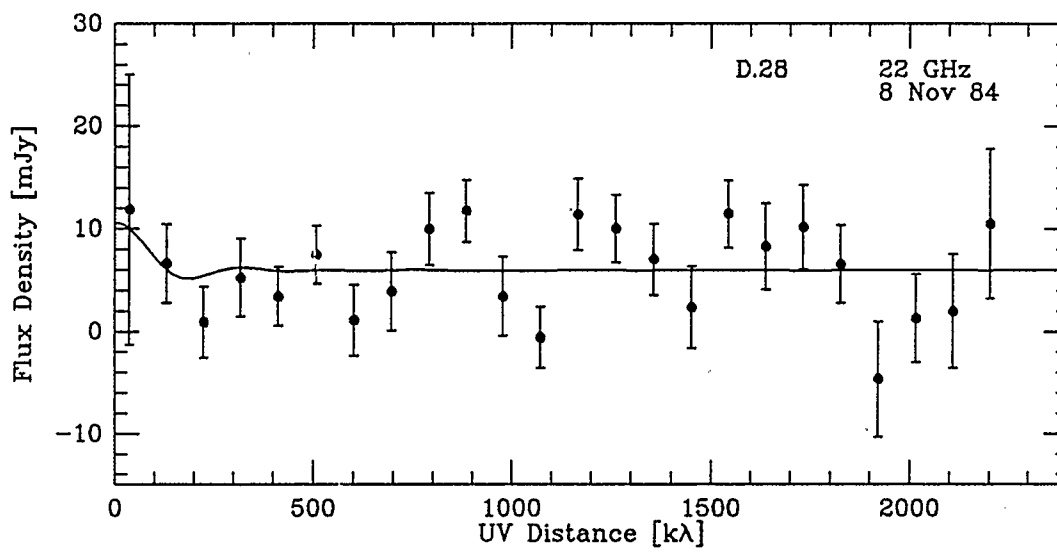
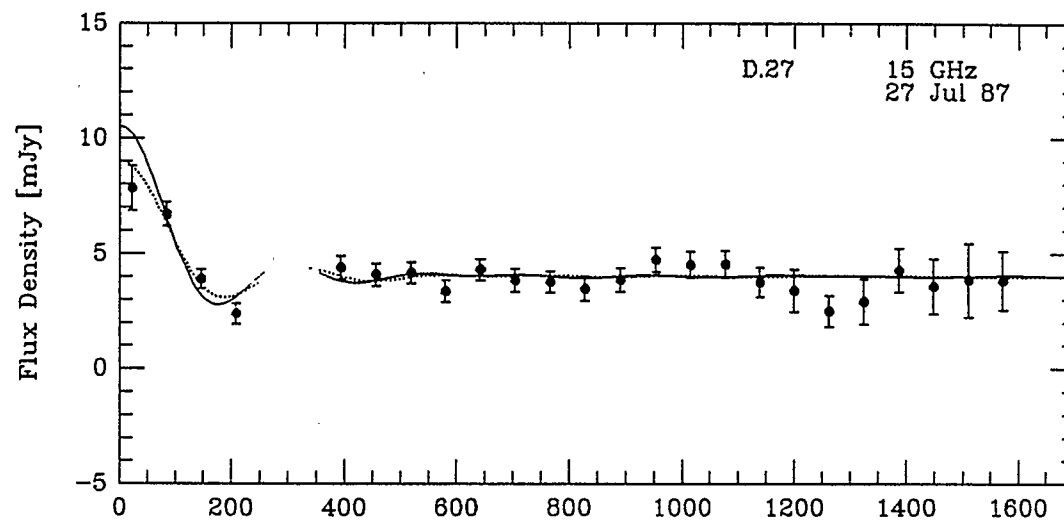
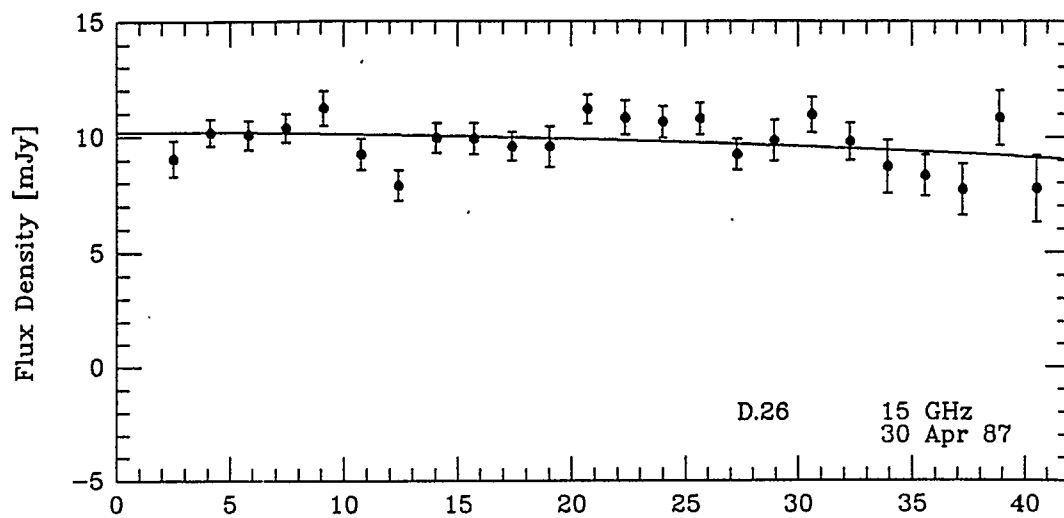


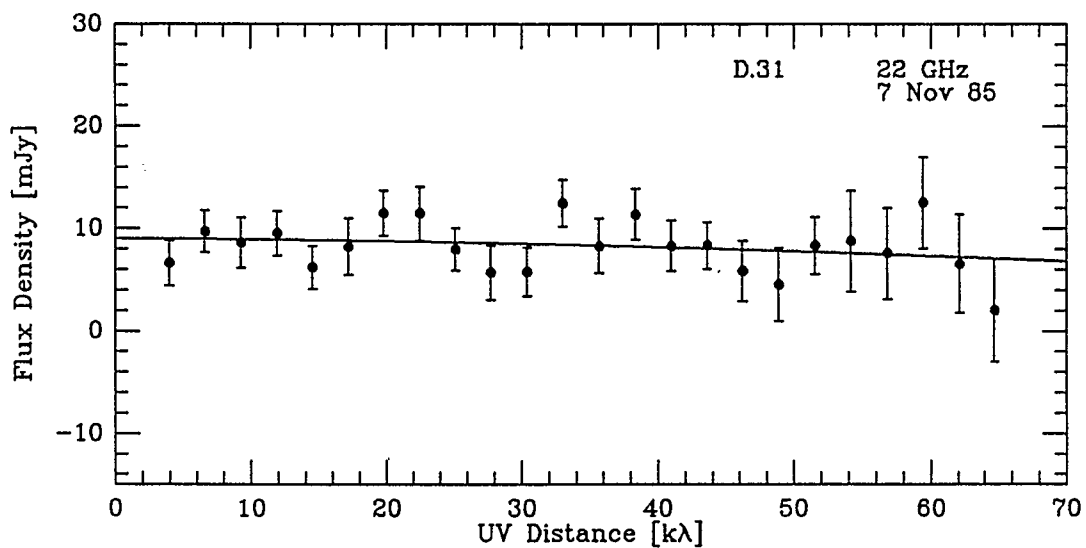
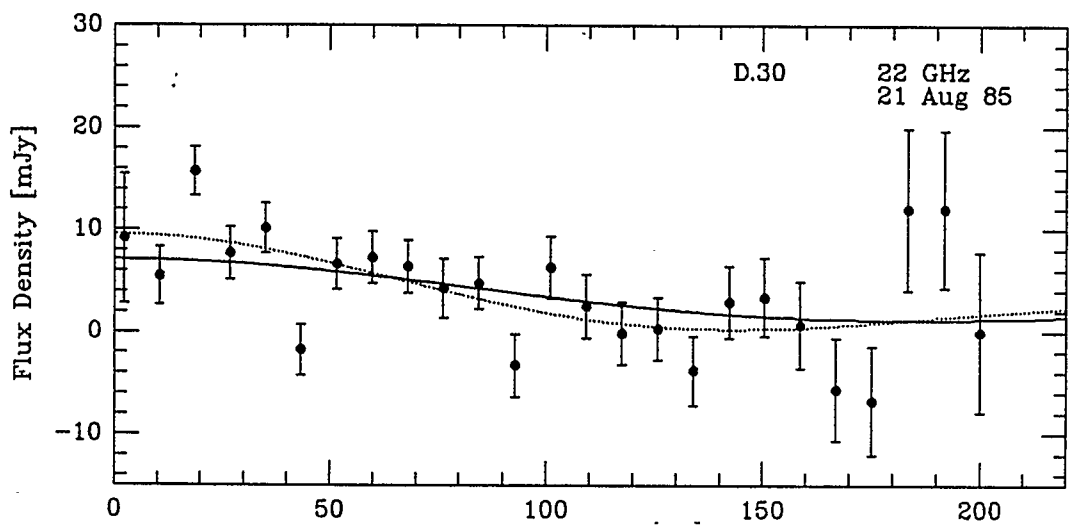
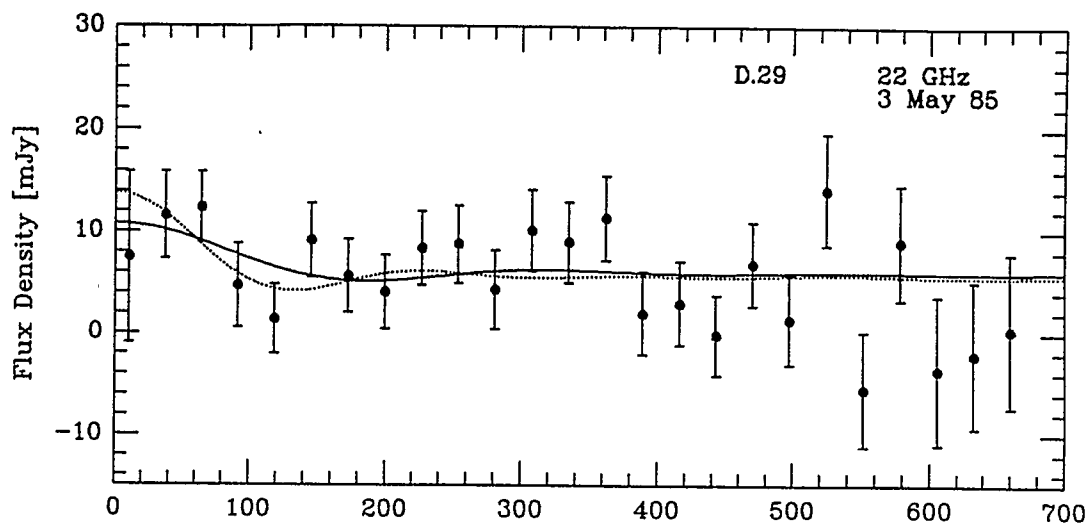


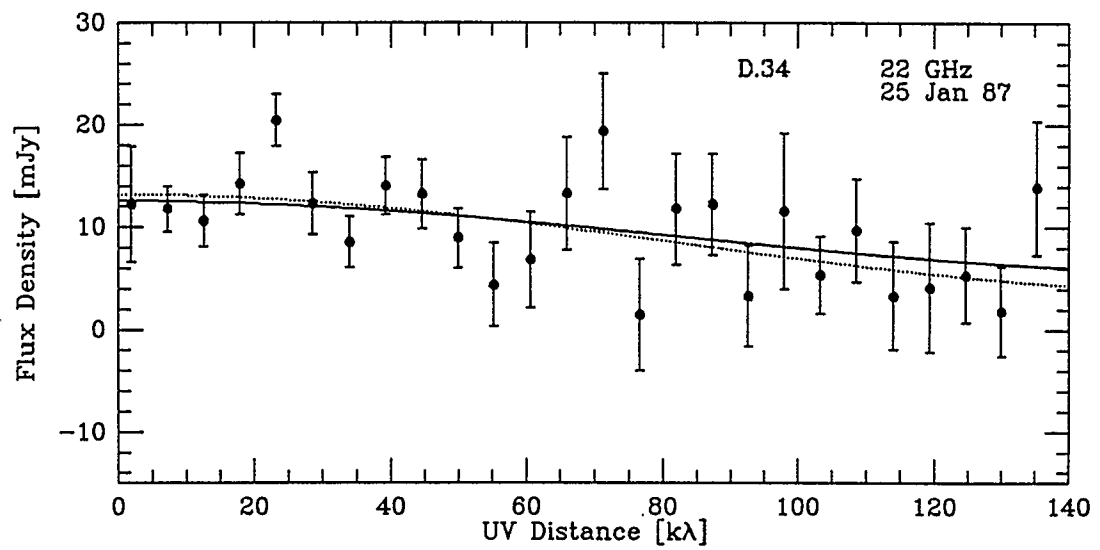
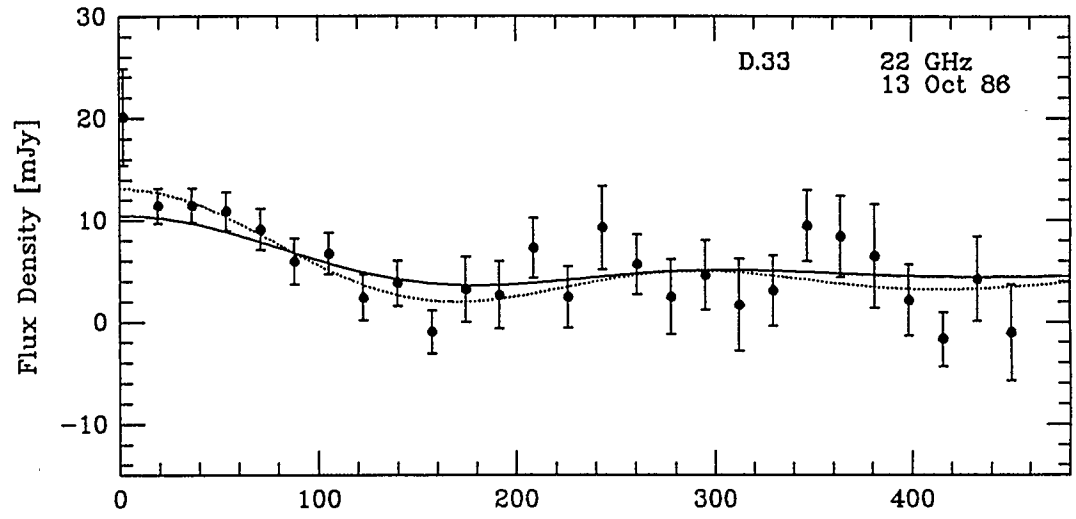
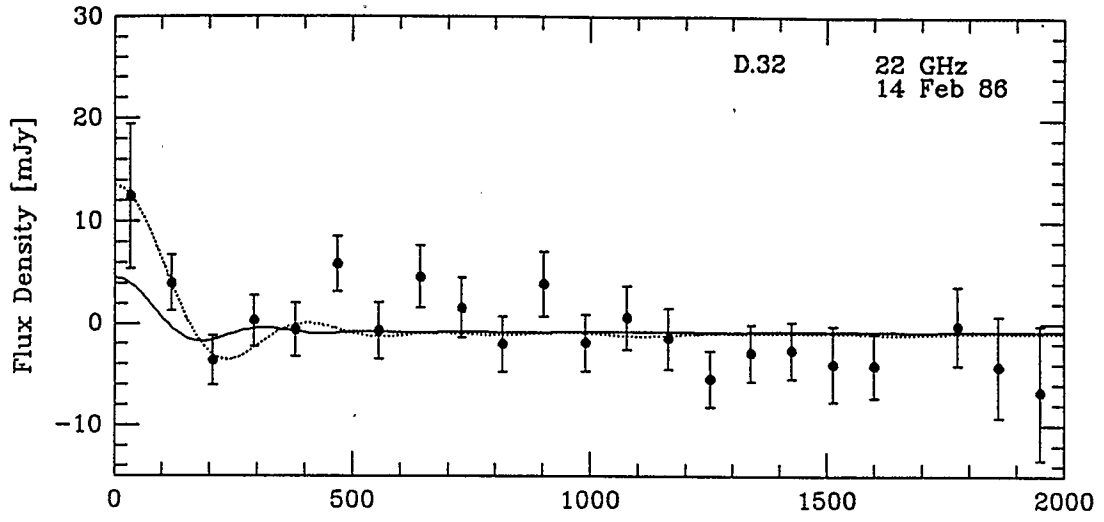


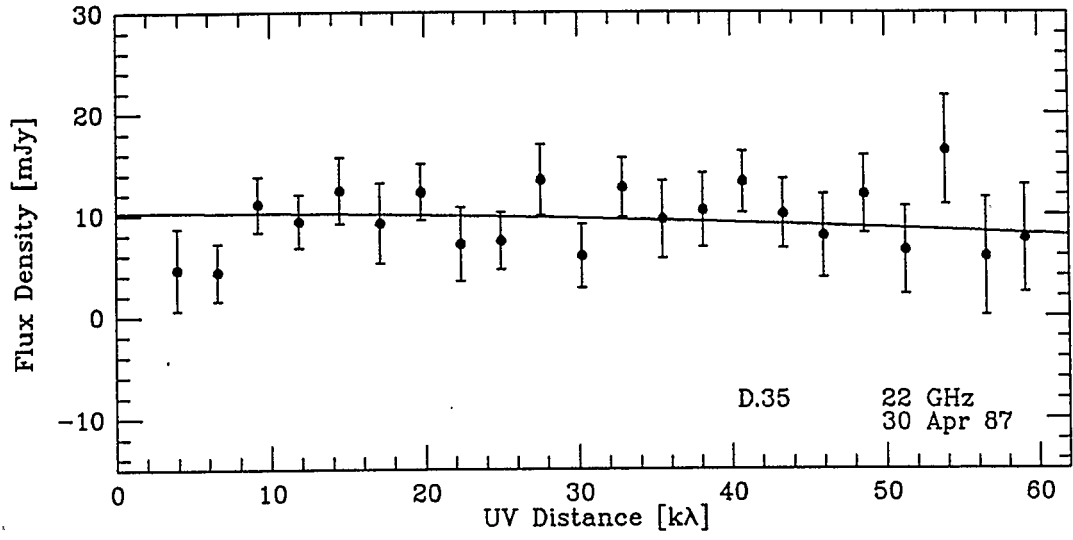








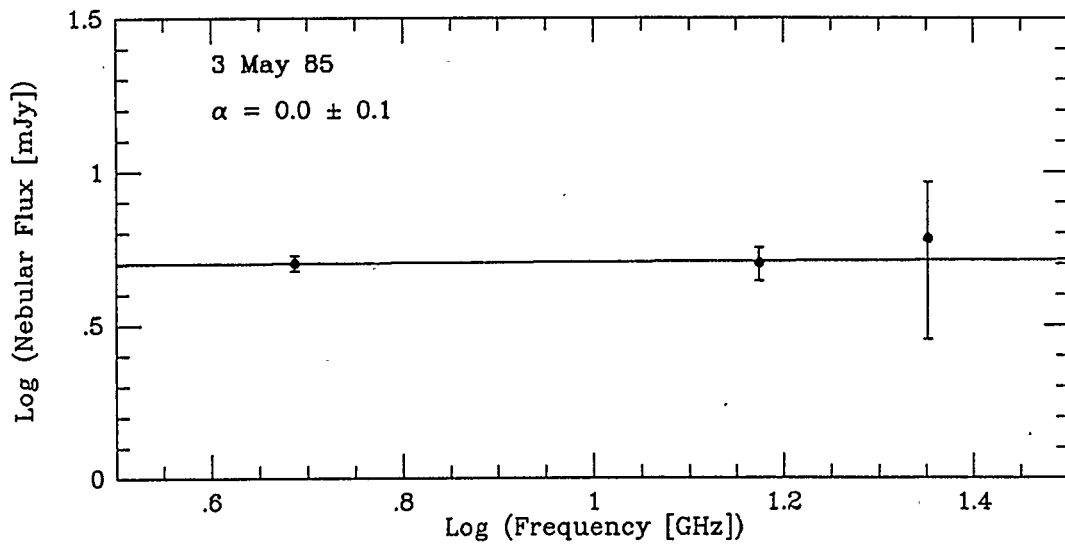
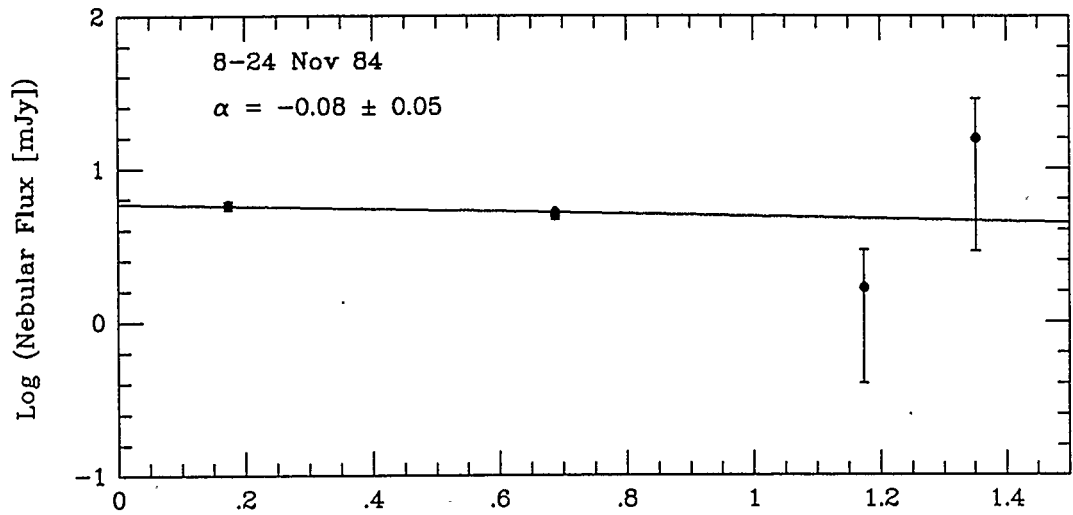


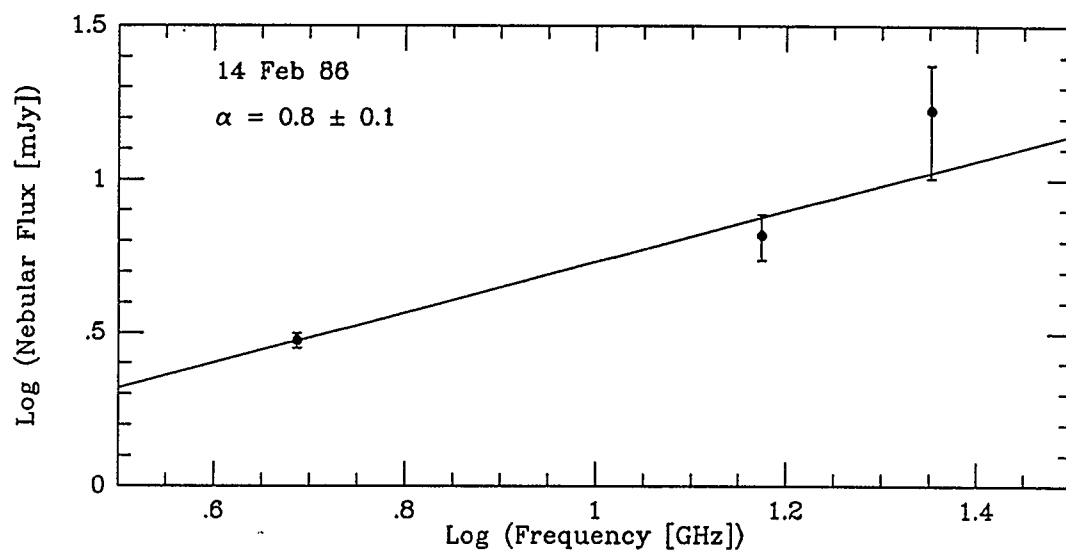
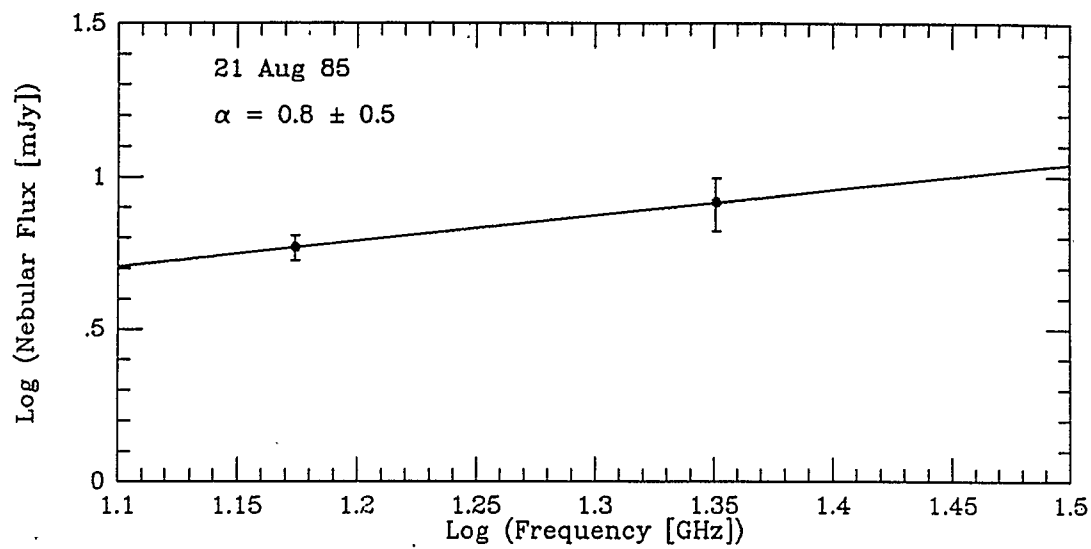


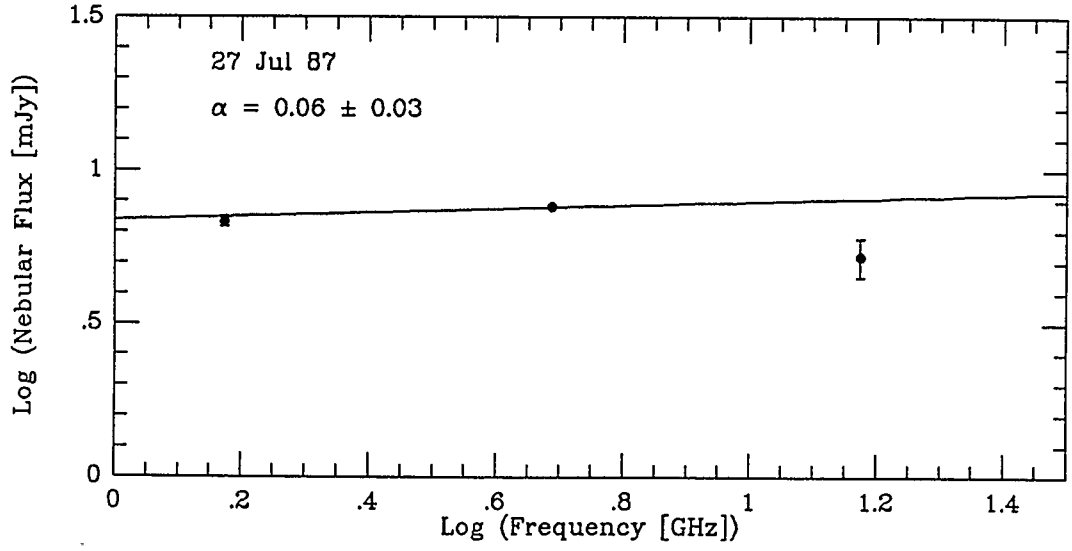
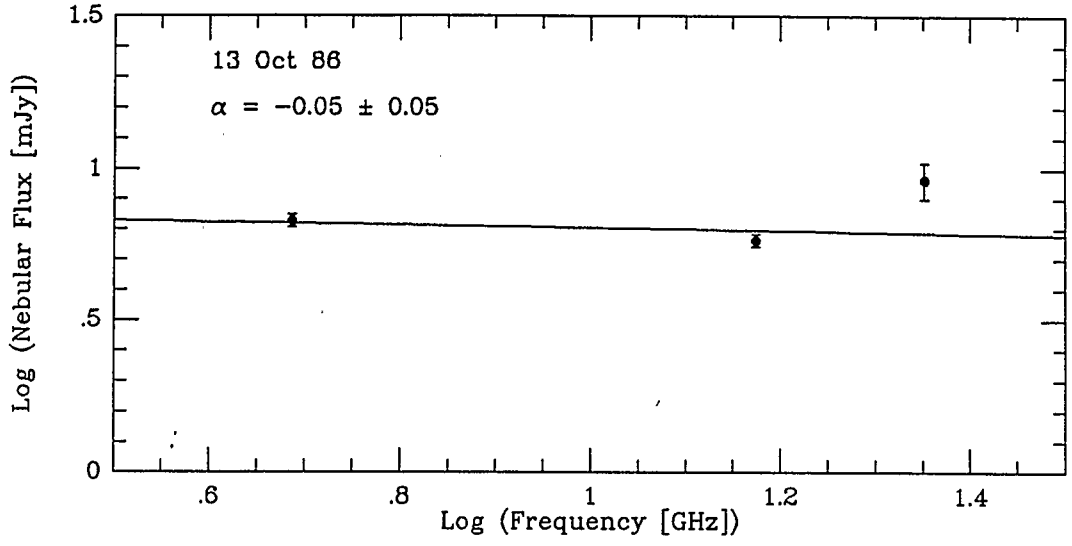
## Appendix E

### Spectral Index Determination: Inner Nebula

The plots below show the determination of spectral index,  $\alpha$ , for epochs at which the necessary information was obtained. While it has been argued that the result from epoch 2-86 is suspect (Section 4.6), it is presented here for completeness.







## Appendix F

### Flux Density Variations: Central Source

The plots below show the central source flux 15, and 22 GHz. Data is plotted both as a function of time and as a function of orbital phase. The 5 GHz results are given in Figures 4.31 and 4.32.

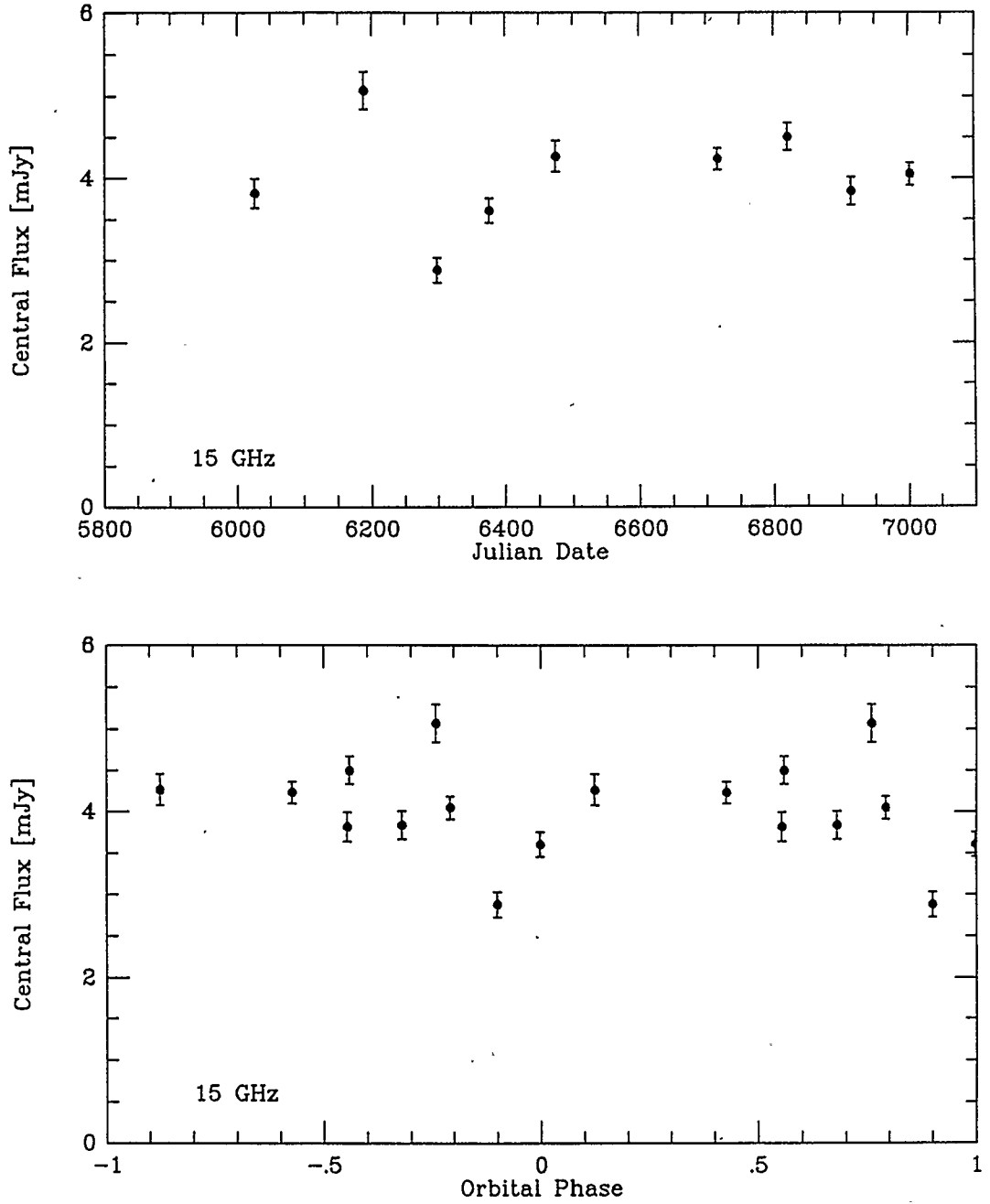


Figure F.1: Central Source Flux: 15 GHz

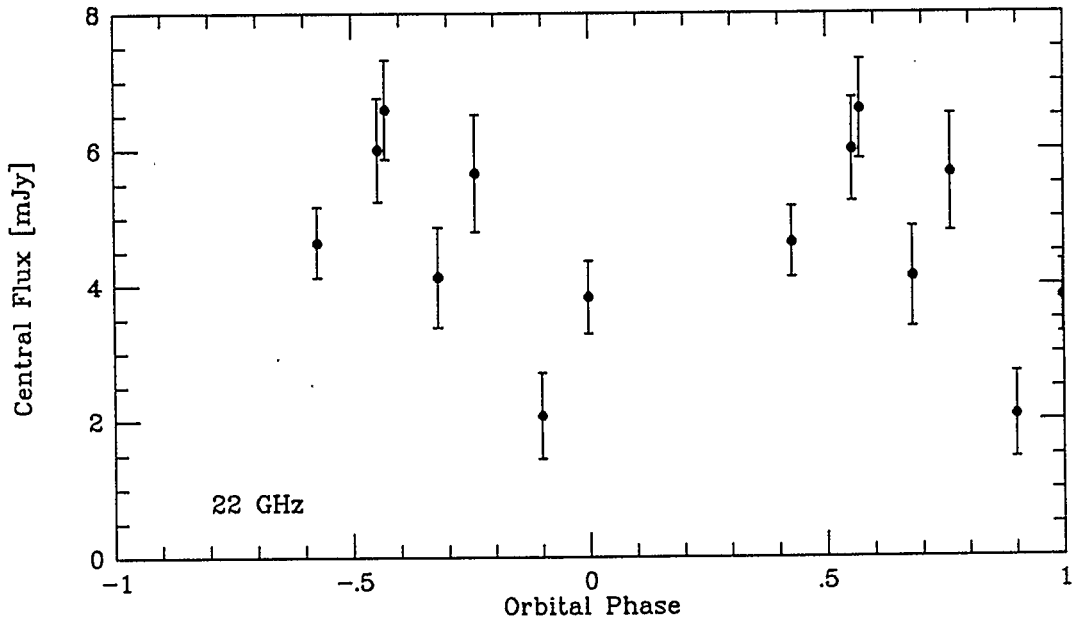
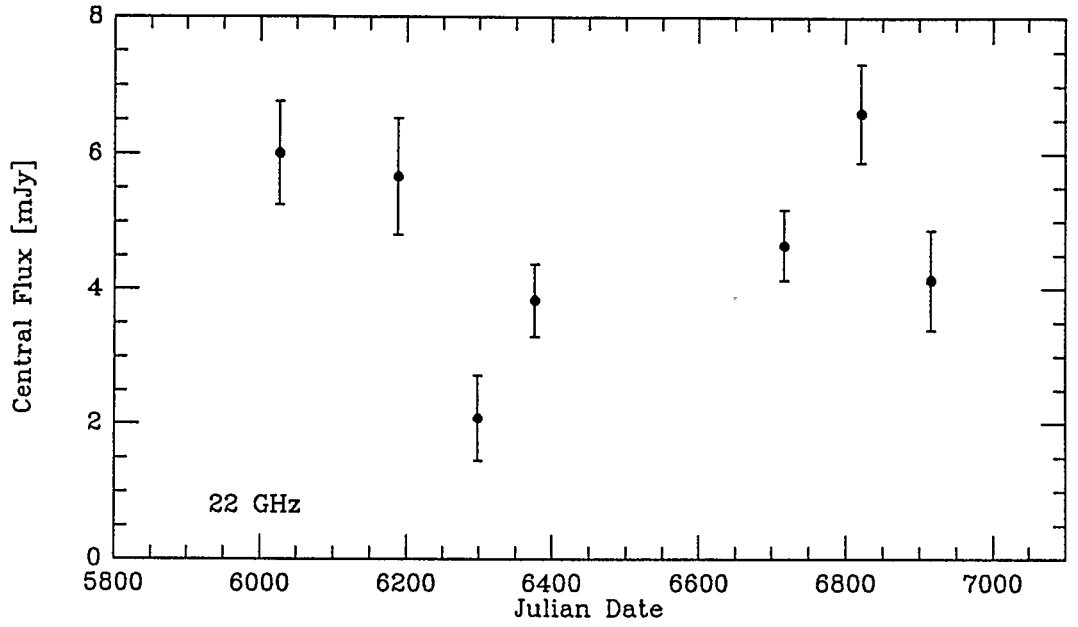
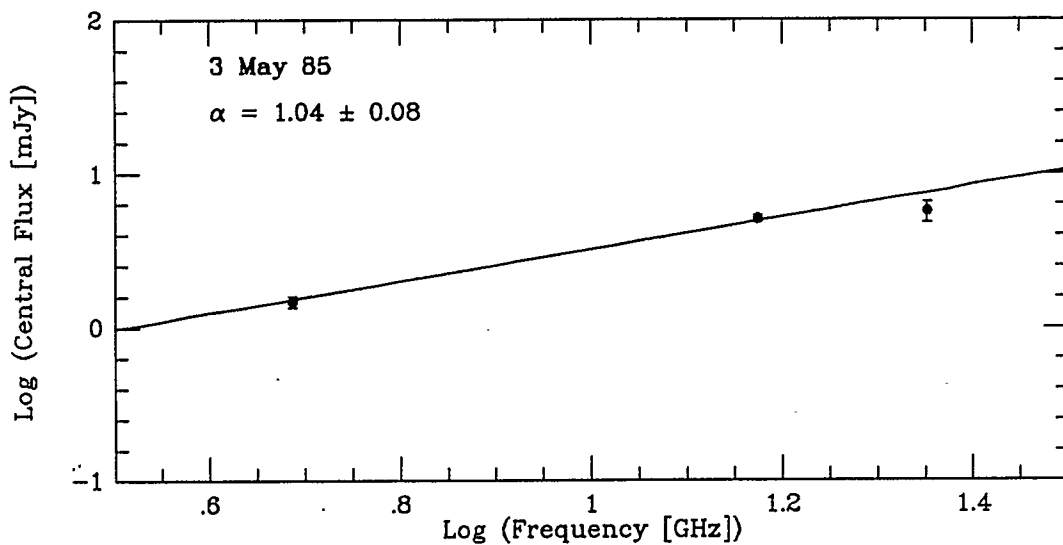
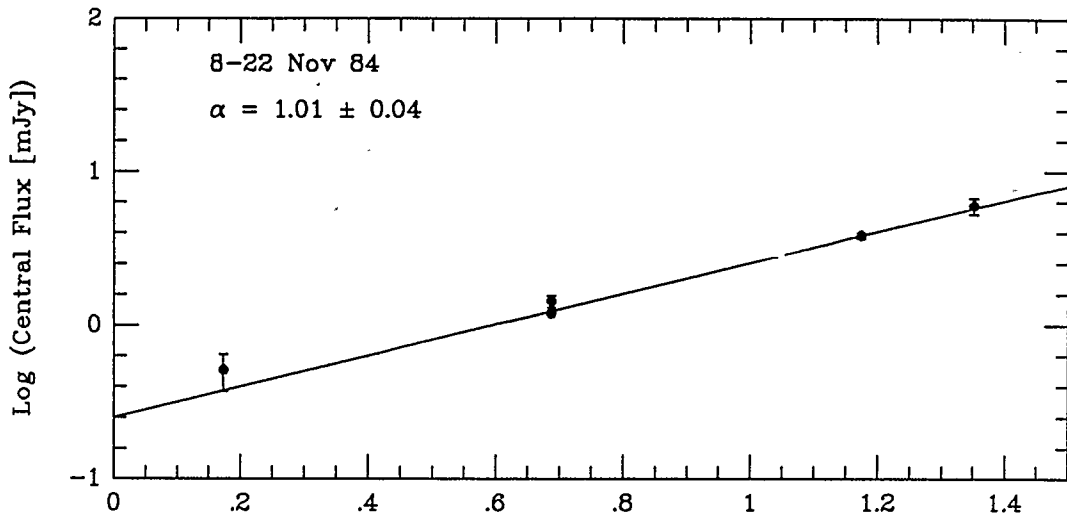


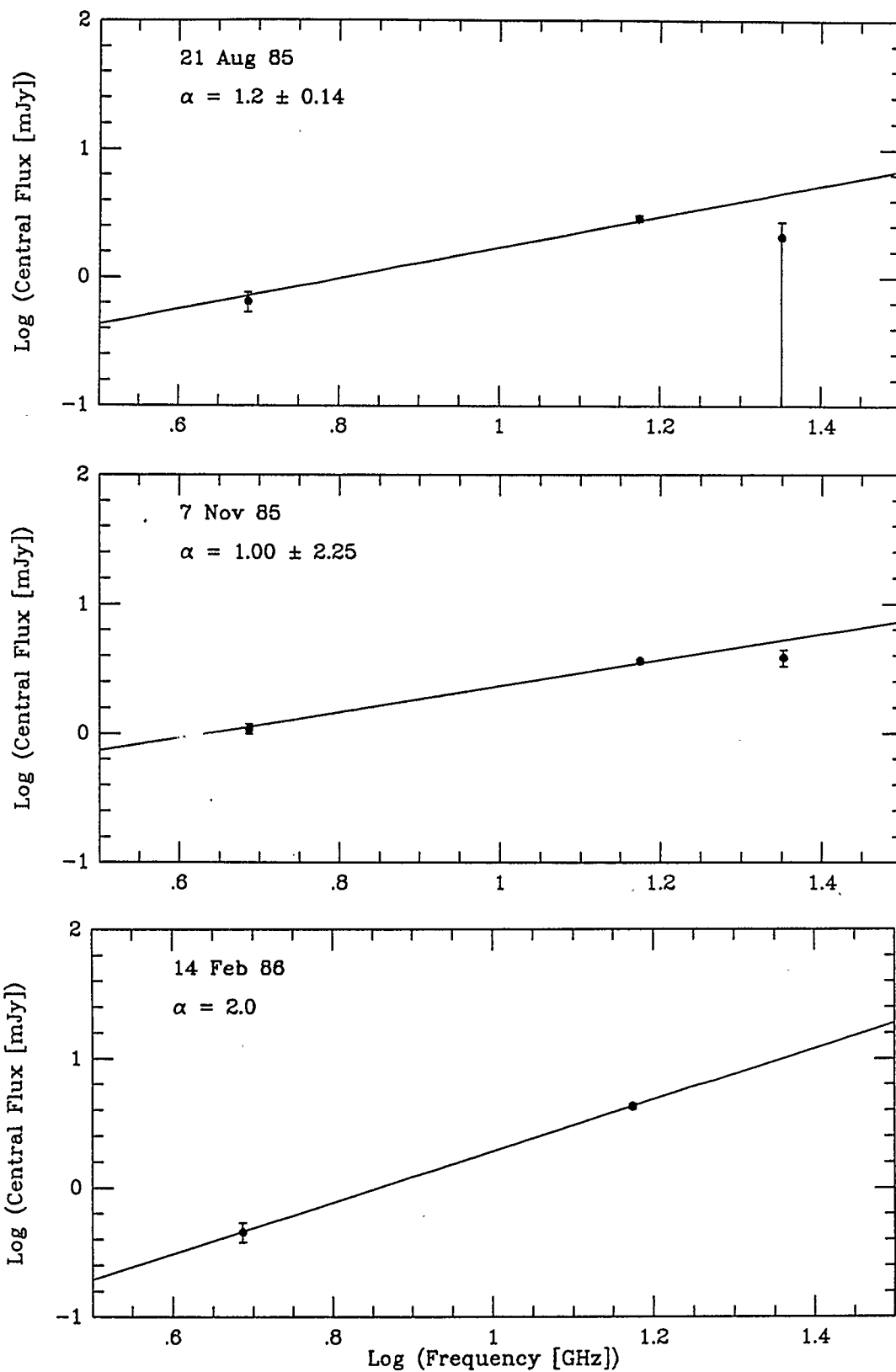
Figure F.2: Central Source Flux: 22 GHz

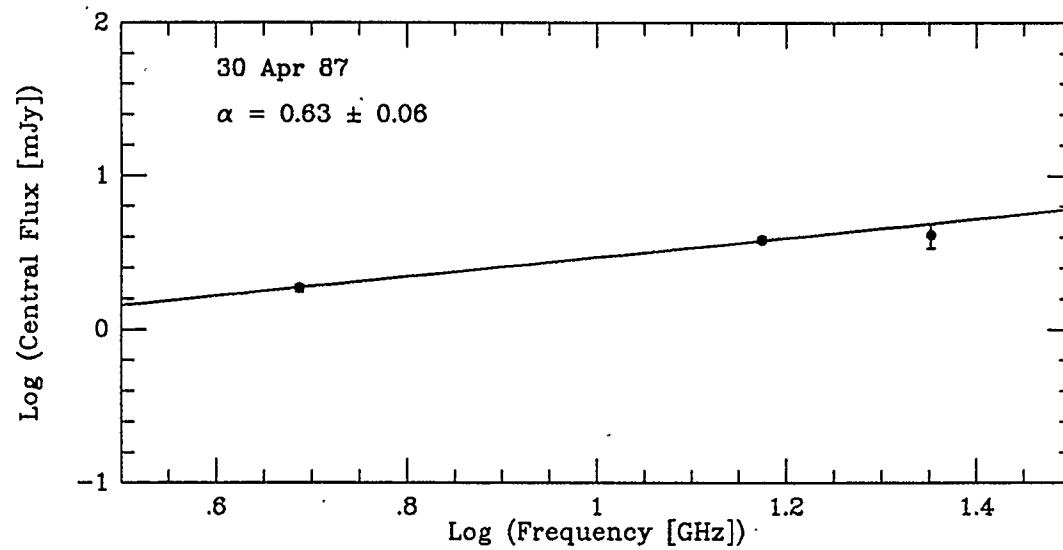
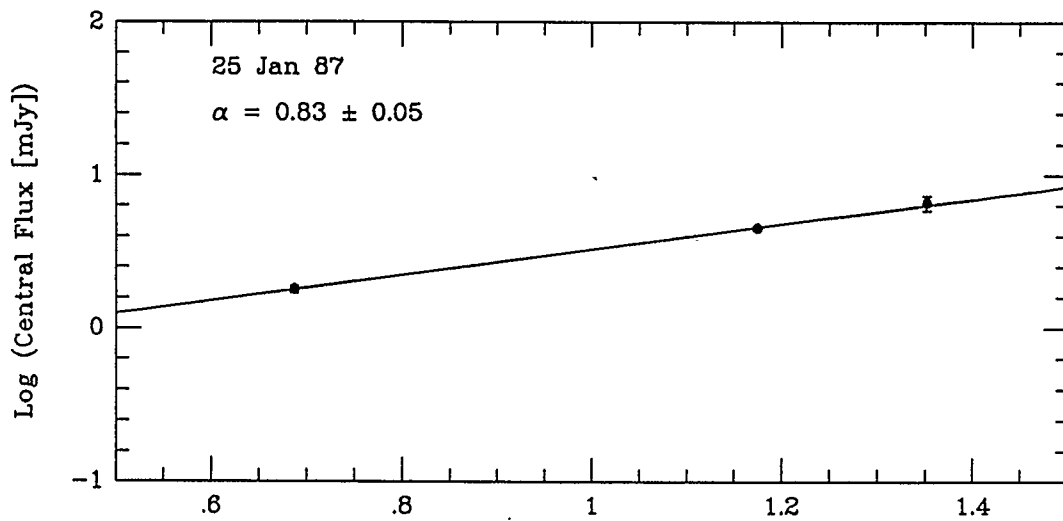
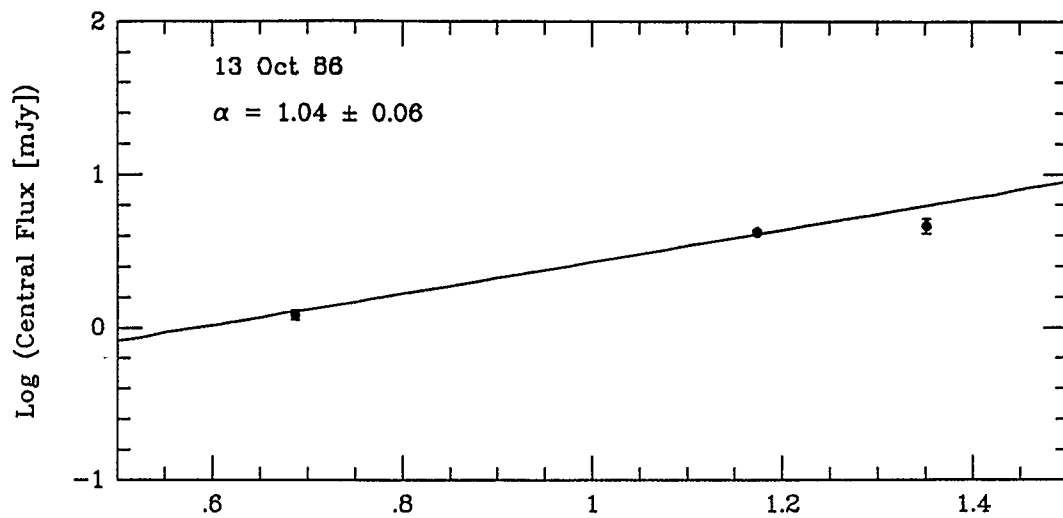
## Appendix G

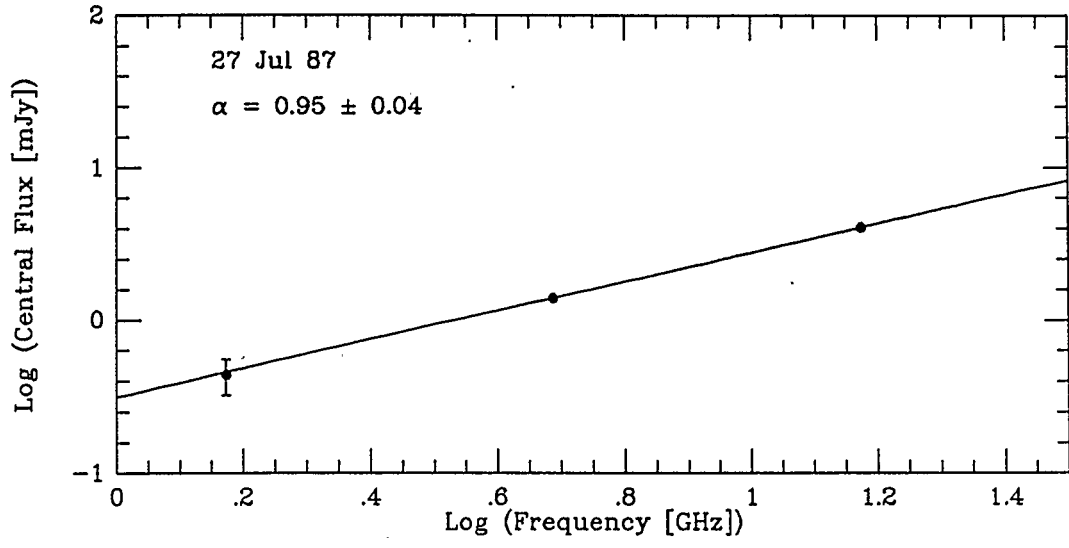
### Spectral Index Determination: Central Source

The plots below show the determination of spectral index,  $\alpha$ , for the epochs of observation. While it has been argued that the result from epoch 2-86 is suspect (Section 4.6), it is presented here for completeness.









## Bibliography

- [1] Aaquist, O. B. 1985, MSc Thesis, University of Calgary, Calgary, Alberta.
- [2] Aaquist, O. B., Kwok, S. 1987, in *Late Stages of Stellar Evolution*, ed. S. Kwok, S. R. Pottasch, (Dordrecht: Kluwer),p. 397.
- [3] AAVSO Quarterly Report, 1962, **25**, 642.
- [4] Abt, H. A., Levy, S. G. 1976, *Astrophysical Journal Supplement*, **30**, 273.
- [5] Abt, H. A., Levy, S. G. 1978, *Astrophysical Journal Supplement*, **36**, 241.
- [6] Allen, D. A. 1979, in *IAU Colloquium 46: Changing Trends in Variable Star Research*, ed. F. M. Bateson, J. Smak, and I. H. Urch (Hamilton, NZ: University of Waikoto),p. 125.
- [7] Allen, D. A. 1980, *Monthly Notices of the Royal Astronomical Society*, **192**, 521.
- [8] Allen, D. A. 1982, in *IAU Colloquium 70: The Nature of Symbiotic Stars*, ed. M. Friedjung and R. Viotti (Dordrecht: Reidel),p. 27.
- [9] Allen, D. A. 1988, in *IAU Colloquium 103: The Symbiotic Phenomenon*, ed. J. Mikolajewska, (Dordrecht: Kluwer),p. 3.
- [10] Altimore, A., Barratta G. B., Cassatella A., Friedjung M., Giangrande A., Viotti R. 1981, *Astrophysical Journal*, **245**, 630.
- [11] Andriolat, Y. 1982, in *IAU Colloquium 70: The Nature of Symbiotic Stars*, ed. M. Friedjung and R. Viotti (Dordrecht: Reidel),p. 47.
- [12] *AIPS Cookbook* 1986, (Socorro: NRAO).
- [13] Archipova, V. P., Dokuchaeva, O. D. 1963, *Soviet Astronomy*, **6**, 483.
- [14] Attenhoff, W. J. 1976, *Astronomy and Astrophysics*, **46**, 11.
- [15] Bath, G. T., Shaviv, G. 1976, *Monthly Notices of the Royal Astronomical Society*, **175**, 305.
- [16] Belyakina, T. S. 1968a, *Soviet Astronomy*, **12**, 110.
- [17] Belyakina, T. S. 1968b, *Izv. Krym. Astrofiz. Obs.*, **38**, 171.

- [18] Belyakina, T. S. 1968c, *Astr. Zh.*, **45**, 139.
- [19] Belyakina, T. S. 1970, *Astrofizika*, **6**, 49.
- [20] Belyakina, T. S. 1985, *Information Bulletin on Variable Stars* **2697**.
- [21] Berman, L. 1932, *Publications of the Astronomical Society of the Pacific*, **44**, 318.
- [22] Bode, M. F. (ed.) 1987, *RS Ophiuchi (1985)*, (Netherlands: VNU Science Press).
- [23] Bowers, R. L., Deeming, T. 1984, *Astrophysics I: Stars*, (Boston: Jones and Bartlett).
- [24] Bowers, P. F., Kundu, M. R. 1979, *Astronomical Journal*, **84**, 791.
- [25] Boyarchuk, A. A. 1967a, *Soviet Astronomy*, **10**, 783.
- [26] Boyarchuk, A. A. 1967b, *Soviet Astronomy*, **11**, 8.
- [27] Boyarchuk, A. A. 1975, in *IAU Symposium 67: Variable Stars and Stellar Evolution*, ed. V. E. Sherwood, L. Plant, (Dordrecht: Reidel), p. 377.
- [28] Boyarchuk, A. A., Belyakina, T. S., Tarasov, A. E. 1987, *Astrophysics and Space Science*, **131**, 775.
- [29] Boyarchuk, A. A., Esipov, V. F., Morov, V. I. 1966, *Soviet Astronomy*, **10**, 331.
- [30] Burbidge, G. R., and Burbidge, E. M. 1954, *Astrophysical Journal*, **120**, 76.
- [31] Bracewell, R. M. 1986, *The Fourier Transform and Its Applications* (USA: McGraw-Hill).
- [32] Cannon, A. J. 1916, *Ann. Harvard Coll. Obs.*, **76**, 31.
- [33] Caputo, F. 1971, *Astrophysics and Space Science*, **10**, 93.
- [34] Ciatti, F., D'Odorico, S., Mammano, A. 1974, *Astronomy and Astrophysics*, **34**, 181.
- [35] Clark, G. C. 1989, in *Synthesis Imaging in Radio Astronomy*, ed. R.A. Perley, (Utah: Brigham Young), p. 1.
- [36] Cowley, A., Stencel, R. 1973, *Astrophysical Journal*, **184**, 687.

- [37] Feast, M. W., Catchpole, R. M., Whitelock, P. A., Carter, B. S., Roberts G. 1983, *Monthly Notices of the Royal Astronomical Society*, **203**, 373.
- [38] Feast, M. W., Robertson, B. S., Catchpole, R. M. 1977, *Monthly Notices of the Royal Astronomical Society*, **179**, 499.
- [39] Fernie, J. D. 1985, *Publications of the Astronomical Society of the Pacific*, **97**, 653.
- [40] Fomalont, E. B. 1973, *Proceedings of the IEEE*, **9**, 1211.
- [41] Fomalont, E. B., and Wright, M. H. 1974, in *Galactic and Extragalactic Radio Astronomy*, ed. K.I. Kellerman, (New York: Springer-Verlag), Chapter 10.
- [42] Fleming, W. R. 1894, *Astronomy and Astrophysics*, **13**, 502.
- [43] Friedjung, M. 1967, *Astrophysical Journal*, **72**, 797.
- [44] Fuensalida, J. J., Rosa F., Fuentes F. J. 1988, *Astronomy and Astrophysics*, **191**, L13.
- [45] Fujimoto, M. Y. 1982a, *Astrophysical Journal*, **257**, 752.
- [46] Fujimoto, M. Y. 1982b, *Astrophysical Journal*, **257**, 767.
- [47] Gallagher, J. S., Holm, A. V., Anderson, C. M., Webbink, R. F. 1979, *Astrophysical Journal*, **229**, 994.
- [48] Garcia, D. A., Kenyon, S. J. 1988, in *IAU Colloquium 103: The Symbiotic Phenomenon*, ed. J. Mikolajewska, (Dordrecht: Kluwer), p. 27.
- [49] Gehrz, R. D., Woolf, N. J. 1971, *Astrophysical Journal*, **165**, 285.
- [50] Ghigo, F. D., Cohen, N. L. 1981, *Astrophysical Journal*, **245**, 988.
- [51] Glass, I. S., Webster, B. L. 1973, *Monthly Notices of the Royal Astronomical Society*, **165**, 77.
- [52] Grant, Gordon, Aller, L. H. 1954, *Astronomical Journal*, **59**, 321.
- [53] Gregory, P. C., Kwok, S., Seaquist, E. R. 1977, *Astrophysical Journal*, **211**, 429.
- [54] Hjellming, R. M., Johnson 1980, *Astrophysical Journal*, **237**, 840.

- [55] Hjellming, R. M. 1985, in *Radio Stars* ed. R. M. Hjellming, D. M. Gibson, (Dordrecht: Reidel),p. 97.
- [56] Hogg, L. 1932, *Publications of the Astronomical Society of the Pacific*, **44**, 328.
- [57] Hollis, J. M., Kafatos, M., Michalitianos, A. G., Oliverson R. J., Yusef-Zadeh, F. 1987, *The Large-Scale Radio Structure of R Aquarii* (NASA).
- [58] Hutchings, J .B., Cowley, A. P., Redman, R. O. 1975, *Astrophysical Journal*, **201**, 404.
- [59] Hutchings, J. B., Redman, R. O. 1972, *Publications of the Astronomical Society of the Pacific*, **84**, 240.
- [60] Iben, I. 1967, *Annual Reviews of Astronomy and Astrophysics*, **5**, 571.
- [61] Iben, I. 1982, *Astrophysical Journal*, **259**, 244.
- [62] Johnson, H. M. 1980, *Astrophysical Journal*, **237**, 840.
- [63] Kenyon, S. J. 1986, *The Symbiotic Stars*, (Cambridge: Cambridge University Press).
- [64] Kenyon, S. J. 1988a, in *IAU Colloquium 103: The Symbiotic Phenomenon*, ed. J. Mikolajewska, (Dordrecht: Kluwer),p. 11.
- [65] Kenyon, S. J. 1988b, in *IAU Colloquium 103: The Symbiotic Phenomenon*, ed. J. Mikolajewska, (Dordrecht: Kluwer),p. 161.
- [66] Kenyon, S. J., Gallagher, J. S. 1983, *Astronomical Journal*, **88**, 666.
- [67] Kenyon, S. J., Truran, J. W. 1983, *Astrophysical Journal*, **273**, 280.
- [68] Kenyon, S. J., Webbink, R. F. 1984, *Astrophysical Journal*, **279**, 252.
- [69] Keyes, C. D., Plavec, M. J. 1980a, in *IAU Symposium 88, Close Binary Stars: Observations and Interpretations*, ed. M. J. Plavec, D. M. Popper, R. K. Ulrich, (Dordrecht: Reidel),p. 535.
- [70] Keyes, C. D., Plavec, M. J. 1980b, in *The Universe at Ultraviolet Wavelengths*, ed. R. D. Chapman, (NASA CP-2171),p. 443.
- [71] Knapp, G. R., Morris, M. 1984, *Astrophysical Journal*, **292**, 640.
- [72] Kraus, J. D. 1986, *Radio Astronomy*, 2'nd Edition, (Ohio: Cygnus-Quasar).

- [73] Kriz, S. 1981, *Bulletin of the Astronomical Institute of Czechoslovakia*, **33**, 302.
- [74] Kutter, G. S., Sparks, W. M. 1980, *Astrophysical Journal*, **239**, 988.
- [75] Kwok, S. 1981, in *Proceedings of the North American Workshop on Symbiotic Stars* ed. R. E. Stencel, (Boulder: JILA), p. 24.
- [76] Kwok, S. 1986, in *Late Stages of Stellar Evolution* ed. S. Kwok, R. Pottasch, (Dordrecht: Reidel), p. 321.
- [77] Kwok, S., Purton 1978, *Astrophysical Journal Letters*, **219**, L125.
- [78] Kwok, S., Purton 1979, *Astrophysical Journal*, **229**, 187.
- [79] Kwok, S., Leahy, D. A. 1984, *Astrophysical Journal*, **283**, 675.
- [80] Lafler, J., Kinman T. D. 1965, *Astrophysical Journal Supplement*, **11**, 216.
- [81] Lambert, D. L., Slovak, M. H., Gregory, A. S. 1980, in *The Universe at Ultraviolet Wavelengths* (Greenbelt: NASA), p. 461.
- [82] Lang, K. R. 1980, *Astrophysical Formulae*, (New York: Springer-Verlag).
- [83] Livio, M., Prialnik, D., Regev, D. 1989, *Astrophysical Journal*, **341**, 304.
- [84] Lundmark, K. 1921, *Astr. Nachr.*, **213**, 93.
- [85] Luthardt, R. 1984, *Information Bulletin on Variable Stars* **2495**.
- [86] MacDonald 1983, *Astrophysical Journal*, **267**, 732.
- [87] Meinunger, L. 1981, *Information Bulletin on Variable Stars* **2016**.
- [88] Merrill, P. W. 1929a, *Astrophysical Journal*, **69**, 330.
- [89] Merrill, P. W. 1929b, *Publications of the Astronomical Society of the Pacific*, **41**, 255.
- [90] Merrill, P. W. 1932, *Astrophysical Journal*, **75**, 413.
- [91] Merrill, P. W. 1942, *Astrophysical Journal*, **95**, 386.
- [92] Merrill, P. W. 1951a, *Astrophysical Journal*, **113**, 605.
- [93] Merrill, P. W. 1951b, *Astrophysical Journal*, **114**, 338.

- [94] Merrill, P. W. 1959a, *Astrophysical Journal*, **129**, 44.
- [95] Merrill, P. W. 1959b, *Sky and Telescope*, **18**, 490.
- [96] Merrill, P. W., Burwell, C. G. 1933, *Astrophysical Journal*, **78**, 87.
- [97] Michalitianos, A. G., Kafatos, M., Hobbs, R. W. 1980, *Astrophysical Journal*, **237**, 506.
- [98] Mouschovias, T. Ch. 1978, in *Protostars and Planets*, ed. T. Gehrels, (Tuscon: University of Arizona),p. 209.
- [99] Nord. Astron. Tidsskr. 1957, **4**, 146.
- [100] Nussbaumer, H., Stencel, R. E. 1987, in *Exploring the Universe with the IUE Satellite*, ed. Y. Kondo, (Dordrecht: Reidel),p. 203.
- [101] Nussbaumer, H., Vogel, M. 1987, *Astronomy and Astrophysics*, **182**, 51.
- [102] *Observ. of Var. Stars* 1963, (Gronigen-Netherlands),**3**, 6.
- [103] *Observ. of Var. Stars* 1963, (Gronigen-Netherlands),**4**, 5.
- [104] *Observ. of Var. Stars* 1964, (Gronigen-Netherlands),**5**, 6.
- [105] Orío, M 1988, in *IAU Colloquium 103: The Symbiotic Phenomenon*, ed. J. Mikolajewska, (Dordrecht: Kluwer),p. 173.
- [106] Pacynski, B., Rudak B. 1980, *Astronomy and Astrophysics*, **82**, 349.
- [107] Pacynski, B., Zytkow A. N. 1978, *Astrophysical Journal*, **222**, 604.
- [108] Payne - Gaposchkin, C. 1957, *The Galactic Novae*, (New York: Interscience Publishers),p. 217.
- [109] Pearson, T. J., Redman, A. C. 1984, *Annual Reviews of Astronomy and Astrophysics*, **22**, 97.
- [110] Penston, M. V., Allen, D. A. 1985, *Monthly Notices of the Royal Astronomical Society*, **212**, 939.
- [111] Rigollet, R. 1947, *Astronomie*, **61**, 247.
- [112] Rigollet, R. 1948, *Astronomie*, **62**, 297.
- [113] Roche, P. F., Allen, D. A., Aitken, D. K. 1983, *Monthly Notices of the Royal Astronomical Society*, **204**, 1009.

- [114] Rohlfs, K. 1986, *Tools of Radio Astronomy* (New York: Springer-Verlag).
- [115] Sahade, J., Brandi, E. 1980, in *The Universe at Ultraviolet Wavelengths* (Greenbelt: NASA),p. 451.
- [116] Seaquist, E. R., Taylor A.R., Button S. 1984, *Astrophysical Journal*, **284**, 202.
- [117] Seaquist, E. R., Taylor A.R. 1989, *Astrophysical Journal*, (in press).
- [118] Slovak, M. H. 1982, *Astrophysical Journal*, **262**, 282.
- [119] Slovak, M. H. 1980, *Bulletin of the American Astronomical Society*, **12**, 868.
- [120] Slovak, M. H., Lambert D. L. 1988, in *IAU Colloquium 103: The Symbiotic Phenomenon*, ed. J. Mikolajewska, (Dordrecht: Kluwer),p. 265.
- [121] Sopka, R. J. 1982, *Astrophysical Journal*, **258**, L35.
- [122] Spitzer, L. 1978, *Physical Processes in the Interstellar Medium* (USA: John Wiley & Sons Inc.).
- [123] Stebbins, J., Huffer, C. M., Whitford, A. E. 1940, *Astrophysical Journal*, **91**, 20.
- [124] Stencel, R.E., Michalitsianos A. G., Kafatos M., Boyarchuk A. A. 1982, *Astrophysical Journal Letters*, **253**, L77.
- [125] Struve, O. 1944, *Astrophysical Journal*, **99**, 210.
- [126] Swenson, G. W., Mathur, N .C. 1968, *Proceedings of the IEEE*, **56**, 2114.
- [127] Swings, P., Struve, O. 1940, *Astrophysical Journal*, **91** , 546.
- [128] Szkody, P. 1977, *Astrophysical Journal*, **217**, 140.
- [129] Taylor, A. R. 1988, in *IAU Colloquium 103: The Symbiotic Phenomenon*, ed. J. Mikolajewska, (Dordrecht: Kluwer),p. 77.
- [130] Taylor, A. R., Seaquist, E. R. 1984, *Astrophysical Journal*, **286**, 263.
- [131] Taylor, A. R., Seaquist, E. R., Mattei J. A. 1986, *Nature*, **319**, 38.
- [132] Taylor, A. R., Seaquist, E. R., Kenyon, S. J. 1988a, in *IAU Colloquium 103: The Symbiotic Phenomenon*, ed. J. Mikolajewska, (Dordrecht: Kluwer),p. 231.

- [133] Taylor, A. R., Hjellming, R. M., Seaquist, E. R., Gehrz, R. D. 1988b, *Nature*, **335**, 235.
- [134] Taylor, A. R., Bode, M. F., Davis, R. J., Porcas, R. W. 1988c, in *IAU Colloquium 103: The Symbiotic Phenomenon*, ed. J. Mikolajewska, (Dordrecht: Kluwer), p. 335.
- [135] Taylor, A. R., Davis, R. J., Porcas, R. W., Bode, M. F. 1989, *Monthly Notices of the Royal Astronomical Society*, **237**, 81.
- [136] Tcheng, M. L. 1950, *Annales d'Astrophysiques*, **13**, 51.
- [137] Tcheng, M. L., Bloch, M. 1946, *Vistas in Astronomy*, **2**, 1412.
- [138] Verschuur, G. L., Kellerman, K. I. (Ed.) 1974, *Galactic and Extragalactic Radio Astronomy*, (New York: Springer Verlag).
- [139] *VLA Observational Status Report 1988*, (Socorro: NRAO).
- [140] Welty, D. E. 1983, *Publications of the Astronomical Society of the Pacific*, **95**, 217.
- [141] Wendker, H. J., Baars, J. W., Altenhoff, W. J. 1973, *Nature: Physical Sciences*, **245**, 118.
- [142] Willson, L. A. 1981, in *Proceeding of the North American Workshop on Symbiotic Stars*, ed. R. E. Stencel, (Boulder: JILA), p. 23.
- [143] Woodsworth, A. W., Hughes, V. A. 1977, *Astronomy and Astrophysics*, **58**, 105.
- [144] Wright, A. E., Allen, D. A. 1978, *Monthly Notices of the Royal Astronomical Society*, **184**, 893.
- [145] Wright, A. E., Barlow, M. F. 1975, *Monthly Notices of the Royal Astronomical Society*, **170**, 41.
- [146] Zuckerman, B. 1980, *Annual Reviews of Astronomy and Astrophysics*, **18**, 263.